Observation of monsoon and typhoon-driven hydro-morphodynamics at a tropical low-tide terraced beach: a case study at Nha Trang, Vietnam

Hai Thuan Duong

THÈSE

En vue de l'obtention du

DOCTORAT DE L'UNIVERSITÉ DE TOULOUSE

Délivré par : *l'Université Toulouse 3 Paul Sabatier (UT3 Paul Sabatier)*

Présentée et soutenue le *05/12/2018* **par :**

DUONG HAI THUAN

Observation of monsoon and typhoon-driven hydro-morphodynamics at a tropical low-tide terraced beach: a case study at Nha Trang, Vietnam

---

JURY

NICK HALL	Professor	Président du Jury
THONG NGUYEN	Associate Professor	Examinateur
THANH BINH LE	Doctor	Examinateur
ERWIN BERGSMA	Doctor	Examinateur

École doctorale et spécialité :
SDU2E : Océan, Atmosphère, Climat

Unité de Recherche :
Laboratoire d'Études en Géophysique et Océanographie Spatiales (UMR 5566)

Directeur(s) de Thèse :
Patrick MARCHESIELLO, *Rafael ALMAR* et *Trung Viet NGUYEN*

Rapporteurs :
Nadia SÉNÉCHAL et *Eric BARTHÉLEMY*

Acknowledgements

Now, when I look back on the journey that I have been able to complete this thesis, I find that I really have gone a long way and have too many people to remember and can hardly describe in words. This thesis began in mid-May 2013, when Dr. Rafael Almar, one of my three thesis supervisors, came to Hanoi to present the shore-based camera interpretation technique. Since then I've been sticking to this field so far. I want to thank Dr. Rafael Almar, who always wanted me to go further in the study with a bit of pressure on the job, yet very friendly.

I am also very grateful to Prof. Nguyen Trung Viet, who gave me the opportunity to participate in the Vietnam-France protocol project, creating a chance for me to meet and work with Dr. Rafael Almar on the camera system installed in Nha Trang. Not only is my dissertation supervisor in Vietnam, to me, Prof. Nguyen Trung Viet is also a mentor, a brother, a person I go to whenever I have difficulties in science and life.

I would like to express my sincere thanks to the IRD's ARTS Fellowship. I would not be writing these lines without the financial support from the IRD. And also thanks to the ARTS scholarship, I was able to go to LEGOS-Toulouse to conduct research. This gave me the opportunity to meet my advisor Dr. Patrick Marchesiello, who is extremely patient about my slow progress. His devotion in guiding me and editing my work was immeasurable.

In addition, I would like to express my sincere thanks to the PI of the protocol research projects between Vietnam and France, supported by the Ministry of Science and Technology of Vietnam (MOST), phase one or MOST1, entitled "Study on hydrodynamic regime and sediment transport in estuarine and coastal zones of Nha Trang bay, Khanh Hoa province", and especially phase two or MOST2, entitled "Investigate morphodynamical processes and propose applied solutions to recreate and upgrade the Nha Trang coast, Khanh Hoa province in the context of climate change", as well as the COASTVAR (Coastal Variability in West Africa and Vietnam) project, for allowing me to use the data and support me financially.

I would also like to thank my colleagues in Vietnam for their field work, who have always accompanied me in the major surveys: Dr. Luis Pedro Almeida, Dr. Le Thanh Binh, Mr. Dien, Mr. Thuong, and of course those I cannot list here.

To be able to attend a Phd course at LEGOS-Université Toulouse III Paul Sabatier, I can not do without the help of my colleagues in Vietnam, so I would like to thank them also.

It would be very difficult to study away from home without the help of people in Toulouse. So I would like to thank LEGOS secretaries such as Brigitte Cournou, Martine Mena, Catherine Donati, and Nadine Lacroux. Thanks also to the community of Vietnamese students studying at LEGOS for curing my home sickness and treating me with many Vietnamese dishes.

Finally, I would like to send my deepest thanks to my family (Dad, Mum, and Brothers) who

are always with me, encouraging me to complete this thesis. And above all, I want to thank my Wife (Mai Ngoc) and my two daughters (Mai Phuong and Kim Ngan) because I know they are always my greatest supporters. This thesis is dedicated to them.

Toulouse, October 18, 2018

Duong Hai Thuan

Abstract

Most of the coast of Vietnam is currently eroding, an imbalance in the sediment budget that may be caused by overuse of river sediments for construction, subsidence associated with overuse of groundwater, over-exploitation of the littoral zone (coastal squeeze), and possibly by an increase in typhoon frequency and winter monsoon events. Assessment of sediment budget is needed and requires accurate evaluation of sediment transport in the coastal environment. In my PhD study, I use two close-range camera systems for nearshore monitoring: a land-based nearshore camera system for observing short-, medium- and long-term coastal hydro-morphodynamics and a drone for monitoring short-term events. Specifically, I used a camera system installed in Nha Trang beach, Viet Nam, from 05/2013 to 08/2016. The cross-shore profiles, shoreline positions and wave characteristics (height and period) extracted from the video data are calibrated with in-situ measurement from two field experiments during the Haiyan typhoon event.

Then, the results on short-term and seasonal shoreline changes are analyzed – and published (Thuan et al., 2016, Almar et al., 2017). The study shows a marked seasonal evolution of Nha Trang shoreline and dramatic impact of cat-5 typhoons Nari and Haiyan with changes of 4 to 8 m in each case. However, the recovery to individual events is fast, as opposed to the effect of winter monsoon events. Our continuous video observations show for the first time that long-lasting monsoon events have more persistent impact (longer beach recovery phase) than typhoons. Using a shoreline equilibrium model, we estimate that the envelope of intra-seasonal events rather than monthly-averaged waves drives the seasonal shoreline behavior. Finally, the shoreline study suggests that the interplay between intensity and duration of intra-seasonal events may be of key significance.

In the second part of this PhD study, a video-based bathymetry inversion technique is applied to long-term data with varying wave environment from swell to wind wave conditions. A main result is the overall stability and high resiliency demonstrated for the low tide terrace (LTT) beach of Nha Trang, with rapid exchange of sediment between the terrace and the upper beach during typhoons, monsoon events or seasonal cycles. The high resiliency of these tropical environments may provide faster beach recovery compared with mid-latitude configurations.

At the same time, the study details the treatment techniques needed for a long-term dataset, and focuses on the limitations of the method in the case of wind waves. For the first time, a tide gauge is used to quantify the error produced by video estimates, which provides a quality criterion. More generally, this study provides guidelines for users of video-based depth inversion methods and a base for standalone error assessment, which is essential for operational and data assimilation systems. A comprehensive error estimate, such as the one proposed here, is thus an excellent step for improving the assimilation approach.

The study is concluded with an exploratory chapter on the use of drones for remotely assessing a continuous profile of topography and bathymetry. Instead of using a fixed-wing drone, which is not best suited for stationary applications, in this study, we use a rotary-wing drone with a very-high resolution camera. The study shows that the technique developed for shore-based video cameras can be successfully applied to a video system attached to a rotary-wing drone. Drone estimates are successfully compared with bathymetric surveys in Nha Trang. In addition, a preliminary sensitivity analysis suggests some guideline for future users.

Résumé

La majeure partie des côtes du Vietnam s'érode actuellement, un déséquilibre dans le bilan sédimentaire qui peut être causé par la surexploitation des sédiments fluviaux pour la construction, l'affaissement associé à la surexploitation des eaux souterraines, la surexploitation de la zone côtière, et peut-être aussi par une augmentation observée des typhons et de la mousson d'hiver. L'évaluation du bilan sédimentaire est nécessaire et nécessite une évaluation précise du transport des sédiments dans l'environnement côtier. Dans mon étude de doctorat, j'utilise deux systèmes de caméras à courte portée pour la surveillance des eaux littorales : une caméra terrestre pour l'observation de l'hydro-morphodynamique côtière à court, moyen et long terme et un drone pour la surveillance des événements à court terme. J'ai utilisé un système de caméra installé sur la plage de Nha Trang, au Viet Nam, du 05/2013 au 08/2016. Certains résultats sur les changements saisonniers et à court terme du littoral ont été analysés et publiés (Thuan et al., 2016, Almar et al., 2017). Les profils transversaux, les positions du rivage et les caractéristiques des vagues (hauteur et période) extraits des données vidéo ont été étalonnés à l'aide de mesures in situ provenant de deux expériences sur le terrain et de mesures bathymétriques effectuées pendant le typhon de Haiyan. L'étude montre une évolution saisonnière marquée du littoral de Nha Trang. L'impact des typhons de catégorie 5 Nari et Haiyan sur le littoral est également dramatique avec des changements de 4 à 8 m dans chaque cas. Cependant, la reprise aux événements individuels est rapide. Nous avons également comparé l'effet des moussons d'hiver avec celui des tempêtes. Nos observations vidéo continues montrent pour la première fois que les épisodes de mousson de longue durée ont un impact plus persistant (phase de récupération de la plage plus longue) que les typhons. À l'aide d'un modèle d'équilibre riverain, nous estimons que c'est l'enveloppe des événements intrasaisonniers plutôt que la moyenne mensuelle des vagues qui détermine le comportement saisonnier du rivage. Enfin, l'étude suggère que l'interaction entre l'intensité et la durée des événements intrasaisonniers peut être d'une importance capitale.

Dans la deuxième partie de cette étude de doctorat, une technique d'inversion bathymétrique basée sur la vidéo est appliquée aux données à long terme avec des conditions de vagues variables, de la houle aux vagues de vent. L'un des principaux résultats est la stabilité globale et la haute résilience démontrées pour la plage de la terrasse à marée basse (LTT) de Nha Trang, avec échange rapide de sédiments entre la terrasse et la plage supérieure pendant les typhons, la mousson ou les cycles saisonniers. La haute résilience de ces environnements tropicaux peut permettre une récupération plus rapide des plages par rapport aux configurations des latitudes moyennes.

En même temps, l'étude détaille les techniques de traitement nécessaires pour un ensemble de données à long terme et se concentre sur les limites de la méthode dans le cas des vagues

de vent. Pour la première fois, un marégraphe est utilisé pour quantifier l'erreur produite par les estimations vidéo et produire un critère de qualité. Plus généralement, cette étude fournit des lignes directrices pour les utilisateurs de méthodes d'inversion de profondeur basées sur la vidéo et une base pour l'évaluation autonome des erreurs, qui est essentielle pour les systèmes opérationnels et d'assimilation de données. Une estimation complète des erreurs, telle que celle proposée ici, est donc une excellente étape pour améliorer l'approche d'assimilation.

Contents

List of Figures

List of Tables

Introduction

Motivations

- **Local context and coastal engineering paradigm**: Most of the coast of Vietnam is currently eroding, an imbalance in the sediment budget that may be caused by overuse of river sediments for construction, subsidence associated with overuse of groundwater, over-exploitation of the littoral zone (coastal squeeze), and maybe also by an observed increase in typhoon frequency and winter monsoon events (strong 1-10 day synoptic events) due to climate variability and climatic change. A better assessment of the long-term coastal response to climate-related storminess changes is required for risk mitigation planning. Current coastal engineering practice in Vietnam generally overlooks physical processes linked to multi-scale ocean forcing, from typhoons to synoptic monsoon events and inter-annual variability due to climatic modes (e.g. ENSO, pacific decadal oscillation - PDO). The thesis subject is a proposition along these lines based on innovative monitoring. During the Vietnamese MOST-PROTOCOL project (2013-2014) and later with French ANR-COASVAR project (2015-2017), in-situ measurements and continuous video imaging have become available at the pilot site of Nha Trang beach, a major touristic location in south-central Vietnam. This study is part of a dynamic France-Vietnam cooperative project (ANR-MOST) for implementing a comprehensive network of beach observation off central Vietnam and for developing models and operational systems for use in coastal management.

- **Ocean forcing at multiple time scales and beach resilience**: Coastal morphology is in a constant process of equilibration at various timescales. Sandy coasts in particular are the most dynamic geological environments on earth. The coastal system is a complex interface between land and oceans and is thus affected by various forcing at various timescales. Evolution results from complex interactions between morphology, sediment fluxes and hydrodynamics. During extreme events, the beach is observed to evolve dramatically, dominated by surf processes that can rapidly lead to an up-state transition through offshore sediment transport by the undertow and sandbar formation. After such extreme event, the beach slowly evolves through transient states while recovering under low or moderate energy wave forcing (Coco et al., 2014, Angnuureng et al., 2017). There is as yet no consensus on whether these events have transient or persistent impact on

beach evolution and on the crucial recovery processes leading to beach resilience (Anderson et al., 2010). Resilience capacity would relate on the extent of departure from equilibrium driven by short events and on recovery timescale, which can be from days to years, depending on the site and severity of events. For isolated storm events, departure from equilibrium is related to storm intensity (Frazer et al., 2009, Davidson et al., 2013). However, no clear conclusion can be drawn when considering sequences of events, since both enhanced and weakened effects are observed (Ferreira, 2005, Karunarathna et al., 2014, Splinter et al., 2014a). It seems that it is the interplay between recurrence interval of events and post-event (low-energy) recovery timescales that matters. For example, a sequence of events with recurrence interval shorter than recovery duration (e.g., strong 2013-2014 winter events in Europe; Masselink et al. (2016), Castelle et al. (2015)) shows greater impact than individual events. The reason is that the system moves sequentially toward a new state of high-energy equilibrium. The sediment transported offshore (below depth of closure) is lost for the sediment cell or is only slowly re-introduced over a long period of time. Recovery timescales is thus a crucial parameter for predicting either an erosive or accretive beach response but it varies significantly with location, ranging from days to months and years. For Nha Trang beach in Vietnam, recurrence interval of typhoons in this region can significantly vary, which would make prediction of beach evolution sensitive to climate modulation of storm occurrence. However, it would be misleading to consider typhoons as the only drivers of shoreline evolution. Winter monsoon brings high-energy conditions in a succession of events of relatively long duration. Is everything said above for typhoons valid also for these events? And how significant are these two types of events on Nha Trang beach evolution? These are fundamental questions for this thesis.

- **Low energy environments and weak wind-wave conditions**: Low-energy beaches remain mainly out of the scope of coastal studies. Recovery processes associated with swash/wind-waves are still poorly known. Jackson et al. (2002) suggestion that morphological features are those of high-energy events is generally assumed. For instance, bars located seaward of low still-water level do not appear to be part of the sediment exchange system with the foreshore. But is it really the case? How does beach recover? Our study aims at understanding the paroxysmal impact of typhoons or monsoon events but also their long-term impact (seasonal) involving low-energy recovery processes. Beaches with steep upper slope sand flat low-tide terraces (LTT) represent a special case of beach where two distinct hydrodynamic regimes (reflective and dissipative) can be observed at different tide stages (Miles and Russell, 2004). Despite their interest and their wide presence in tropical environments, these LTT beaches remained out of the scope of most of the recent studies. Open question still remains on their functionning and dynamics. How this specific morphology influences hydro-morphodynamics and exchanges between upper and lower beach profile sediment cells. How the terrace responds to events and can a shift to different higher or lower energy states be observed ?

- **Participation to the international effort of video-based coastal monitoring: dealing with challenging conditions with frequent typhoons and periods of short wind-waves**: More than other geosciences, nearshore research historically faces

difficulties in observing a complex and high-energy environment. Satellite observations still have low time and space resolution for the beach scale, although significant progress was made (more to come from the SWOT mission). Conventional in-situ measurements remain scarce (e.g., buoys) and intensive field experiments with high spatial and temporal sampling rates are uncommon as they are expensive and hazardous. As a result, bridging the knowledge gap between short-term, small-scale dynamics and long-term evolution is a major challenge. Coastal video monitoring provides an excellent response to this challenge. Owing to their low installation and running cost, a network of video stations is rapidly growing along the world coastlines, including southern countries and remote areas. But they are limitations in the methods with lack of guidelines for users. In particular, what are the limits of validity of depth inversion methods when applied to short waves? Can monitor a small-scale morphological structure such as a low tide terrace at different timescales?

Research questions and objectives

The present thesis addresses essential scientific questions:

- What are the transient and persistent impacts of short term events on a low tide terraced beach? What is the comparative impact of typhoons and monsoon events on shoreline?

- What are the dynamics of low tide terraced beaches ? These beaches are very common in tropical zones but poorly documented. How do LTT beaches recover from high-energy tropical events, in particular during low energy wind wave conditions?

These questions raise a **general objective**: quantifying the resilience capacities of coastal areas – overlooked in coastal engineering studies – in response to short term and synoptic monsoon events, with a focus on low-energy wind wave recovery conditions. The scientific objective is addressed by achieving a **methodological objective**: developing a video camera platform (installation, processing and analysis) for monitoring coastal evolution and wave forcing. This includes validation with field data and assessment of the limits of video depth inversion techniques, particularly when applied to wind wave environments (e.g., closed seas).

This thesis provides a fundamental understanding of storm impact and coastal recovery at tropical low tide terraced beaches.

Organization of the thesis

The organization of the thesis is as follows.

- Chapter 1 is an introduction to wave dynamics, beach dynamics and beach morphology, that were used in the methods and analyses of the study.

- Chapter 2 presents the study site and all field campaigns conducted during the PhD project and used for validation of video analyses.

- Chapter 3 presents the tools and methods for shoreline detection and bathymetry inversion from a shore-based camera system.
- Chapter 4 details the major surveys conducted in Nha Trang from 05/2013 to date, within the framework of the MOST1&2 and COASTVAR projects, and this chapter also presents the validation results of the shore-based cameara system.
- Chapter 5 presents an analysis of shoreline evolution of Nha Trang beach, focusing on the effect of intra-seasonal events, namely typhoons and monsoon events.
- Chapter 6 shows that the inversion of beach profile evolution provides understanding of the fast shoreline recovery observed in Chapter 4, involving the terrace. It also provides guidelines for video users and sets limits of bathymetry inversion techniques.
- Chapter 7 tackles nearshore survey methods based on drones, i.e., topography reconstruction using photogrammetry and bathymetry estimation through wave celerity inversion.
- Chapter 8 gives a summary and a perspective of this thesis.

Introduction en Français

Motivations

- **Contexte local et paradigme de l'ingénierie côtière**: La plus grande partie des côtes du Vietnam s'érode actuellement, un déséquilibre dans le bilan sédimentaire qui peut être causé par la surexploitation des sédiments fluviaux pour la construction, l'affaissement associé à la surexploitation des eaux souterraines, l'aménagement de la zone côtière, et peut-être aussi par une augmentation des typhons et de la mousson d'hiver (forts événements synoptiques de 1-10 jours) due aux variations et changements climatiques. Une meilleure évaluation de la réponse côtière à long terme aux changements de tempêtes liés au climat est nécessaire pour la planification de l'atténuation des risques. La pratique actuelle du génie côtier au Vietnam néglige généralement les processus physiques liés au forçage multi-échelle de l'océan, des typhons aux évènements synoptiques de la mousson et à la variabilité interannuelle due aux modes climatiques (ENSO, PDO: oscillation décennale du Pacifique). Le sujet de thèse est une proposition en ce sens basée sur un suivi innovant. Au cours du projet vietnamien MOST-PROTOCOL (2013-2014) suivi du projet français ANR-COASVAR (2015-2017), des mesures in situ et des images vidéo en continu ont été collectées sur un site pilote: la plage de Nha Trang, un site touristique majeur du centre-sud du Vietnam. Cette étude s'inscrit dans le cadre d'un projet dynamique de coopération France-Vietnam (ANR-MOST) visant à mettre en place un réseau global d'observation des plages au large du centre du Vietnam et à développer des modèles et systèmes opérationnels pour la gestion côtière.

- **Forçage de l'océan à de multiples échelles de temps et résilience des plages**: la morphologie côtière est dans un processus constant d'équilibre à différentes échelles de temps. Les côtes sableuses en particulier sont les environnements géologiques les plus dynamiques de la Terre. Le système côtier est un système complexe entre la terre et les océans et est donc affecté par divers forçages à différents endroits de la planète. Son évolution résulte d'interactions complexes entre la morphologie, les sédiments et la nature. Lors d'événements extrêmes, on observe une évolution spectaculaire de la plage, dominé par des processus de déferlement et transports de sédiments associés. Après un tel évènement, la plage semble évoluer lentement vers son profil initial grâce au forçage de vagues de faible ou moyenne énergie (Coco et al., 2014, Angnuureng et al., 2017). En fait, il n'y a pas encore de consensus sur la question de savoir si les événements énergétiques ont un impact transitoire ou persistant sur l'évolution des plages et sur les processus cruciaux menant à

leur résilience (Anderson et al., 2010). La capacité de résilience dépendrait de l'ampleur de l'écart par rapport à l'équilibre dû à des événements de courte durée et du délai de rétablissement, qui peut aller de quelques jours à des années, selon le site et la gravité des événements. Dans le cas des tempêtes isolées, les écarts par rapport à l'équilibre sont liés à l'intensité des tempêtes (Frazer et al., 2009, Davidson et al., 2013). Toutefois, aucune conclusion claire ne peut être tirée lorsqu'on examine les séquences d'événements, car on observe à la fois des effets accrus et affaiblis (Ferreira, 2005, Karunarathna et al., 2014, Splinter et al., 2014a). Il semble que c'est l'interaction entre l'intervalle de récurrence des événements et les délais de récupération post-événement (basse énergie) qui importe. Par exemple, une séquence d'événements dont l'intervalle de récurrence est plus court que la durée du récupération (e.g., les événements hivernaux de 2013-2014 en Europe; Masselink et al. (2016), Castelle et al. (2015)) ont un impact plus important que les événements individuels. La raison est que le système se déplace vers un nouvel état d'équilibre à haute énergie. Les sédiments transportés au large (sous la profondeur de fermeture) sont perdus pour la cellule sédimentaire ou ne sont réintroduits que lentement sur une longue période de temps. Les délais de rétablissement sont donc un paramètre crucial pour prédire la réaction érosive ou accrétive d'une plage, mais ils varient considérablement d'un endroit à l'autre, allant de quelques jours à plusieurs mois et années. Pour la plage de Nha Trang au Vietnam, l'intervalle de récurrence des typhons dans cette région peut varier considérablement, ce qui rendrait la prévision de l'évolution des plages sensible à la modulation climatique de la fréquence des tempêtes. Toutefois, il serait trompeur de considérer les typhons comme les seuls moteurs de l'évolution du littoral. La mousson d'hiver apporte des conditions de haute énergie dans une succession d'événements d'une durée relativement longue. Tout ce qui a été dit ci-dessus pour les typhons est-il valable aussi pour ces événements ? Et quelle est l'importance de ces deux types d'événements sur l'évolution de la plage de Nha Trang ? Ce sont des questions fondamentales pour cette thèse.

- **Environnements à basse énergie des régimes de vagues et vents**: Les plages à basse énergie restent principalement en dehors du champ des études côtières. Les processus de résilience associés aux vagues de vent, peu énergétiques, sont encore mal connus. On suppose généralement comme Jackson et al. (2002) que les caractéristiques morphologiques d'une plage sont celles des événements à haute énergie. Par exemple, les barres situées au large d'un faible niveau d'eau calme ne semblent pas faire partie du système d'échange de sédiments avec l'estran. Mais est-ce vraiment le cas ? Comment la plage se rétablit-elle ? Notre étude vise à comprendre l'impact immédiat des typhons ou des évènements de moussons mais aussi leur impact à long terme (saisonnier) sur les processus de récupération à basse énergie (mer de vent). Les morphologies de "Low Tide Terrace" (LTT) représentent un cas particulier de plage où deux régimes hydrodynamiques distincts (réfléctif et dissipatif) peuvent être observés à différents stades des marées (Miles and Russell, 2004). Malgré leur intérêt et leur large présence en milieu tropical, ces plages LTT sont restées hors de portée de la plupart des études récentes. Il reste clairement des intérrogations sur leur fonctionnement et leur dynamique. Comment cette morphologie spécifique influence

l'hydro-morphodynamique et les échanges entre le haut et le bas de plage. Comment la terrasse réagit-elle aux événements et peut-on observer un passage à des états d'énergie différents, plus ou moins élevés ?

- **Participation à l'effort international de surveillance côtière par vidéo : le cas de conditions complexes avec moussons, typhons et périodes calmes**: Plus que les autres géosciences, la recherche littorale se heurte historiquement à des difficultés dans l'observation d'un environnement complexe et à haute énergie. Les observations satellitaires ont encore une faible résolution temporelle et spatiale à l'échelle de la plage, bien que des progrès significatifs aient été réalisés (la mission SWOT devrait permettre d'en faire davantage). Les mesures in situ conventionnelles demeurent rares (e.g., bouées) et les campagnes de terrain intensives sont peu courantes, car elles sont coûteuses et dangereuses. Par conséquent, combler le fossé des connaissances entre la dynamique à court terme et l'évolution à long terme est un défi majeur. La vidéosurveillance côtière constitue une excellente réponse à ce défi. En raison de leur faible coût d'installation et d'exploitation, un réseau de stations vidéo se développe rapidement le long des côtes du monde, y compris dans les pays du Sud et les zones reculées. Mais ce sont des limites dans les méthodes avec un manque de lignes directrices pour les utilisateurs qui peuvent poser problème. En particulier, quelles sont les limites de validité des méthodes d'inversion de la bathymétrie appliquées à la mer de vent? Peut-on surveiller l'évolution d'une fine structure morphologique telle que celle de LTT?

Questions et objectifs de la recherche

La présente thèse aborde des questions scientifiques essentielles:

- Quels sont les impacts transitoires et persistants des événements à court terme sur une plage en terrasse LTT? Quel est l'impact comparatif des typhons et des évènements de mousson sur le littoral?

- Quelle est la dynamique des plages en terrasses LTT? Ces plages sont très fréquentes dans les zones tropicales mais peu documentées. Comment les plages LTT se remettent-elles d'événements énergétiques tropicaux durant les périodes calmes?

Ces questions soulèvent un **objectif général**: quantifier les capacités de résilience des zones côtières – négligées dans les études d'ingénierie côtière – en réponse à des typhons et des événements de mousson, en se concentrant sur les conditions de récupération durant les périodes calmes où l'état de mer est dominé par la mer de vent. L'objectif scientifique est atteint par la réalisation d'un **objectif méthodologique**: le développement d'une plateforme de caméra vidéo (installation, traitement et analyse) pour le suivi de l'évolution côtière et du forçage des vagues. Cela comprend la validation à l'aide de données de terrain et l'évaluation des limites des techniques d'inversion de la bathymétrie, en particulier lorsqu'elles sont appliquées aux environnements de vagues de vent (e.g., les mers fermées).

Cette thèse fournit une compréhension fondamentale de l'impact des tempêtes et de la résilience côtière sur les plages tropicales, spécifiquement les plages LTT.

Organisation de la thèse

L'organisation de la thèse est la suivante:

- Le chapitre 1 est une introduction à la dynamique des vagues, à la dynamique et à la morphologie des plages, qui sera utilisée dans les méthodes et analyses de l'étude.
- Le chapitre 2 présente le site d'étude et l'ensemble des campagnes de terrain menées dans le cadre du projet doctoral et utilisées pour la validation des analyses vidéo.
- Le chapitre 3 présente les outils et les méthodes de détection du trait de côte et d'inversion bathymétrique à partir d'un système de caméras fixes.
- Le chapitre 4 détaille les principales études menées à Nha Trang du 05/2013 à ce jour, dans le cadre des projets MOST1&2 et COASTVAR; ce chapitre présente également les résultats de la validation du système de cameras fixes.
- Le chapitre 5 présente une analyse de l'évolution du littoral de la plage de Nha Trang, en mettant l'accent sur l'effet des événements intrasaisonniers, notamment les typhons et les évènements de moussons.
- Le chapitre 6 montre que l'inversion de l'évolution du profil de la plage permet de comprendre le rétablissement rapide du littoral observé au chapitre 4, qui concerne la terrasse. Il fournit également des lignes directrices pour les utilisateurs de cameras et fixe les limites des techniques d'inversion bathymétrique.
- Le chapitre 7 traite des méthodes de mesures littorales basées sur les drones, c'est-à-dire la reconstruction topographique par photogrammétrie et l'estimation bathymétrique par inversion de la vitesse des vagues.
- Le chapitre 8 donne un résumé et les perspectives de cette thèse.

Chapter 1

Background

Contents

This chapter gives a brief overview of common knowledge on wave characteristics, sediment transport, beach erosion and recovery, which will be useful for our study of video-base shoreline extraction and bathymetry inversion.

1.1 Wave Properties

Coastal processes affecting coastal geomorphology are generally initiated by wave movements. Therefore, it is important for a coastal oceanographer and engineer to acquire knowledge of wave

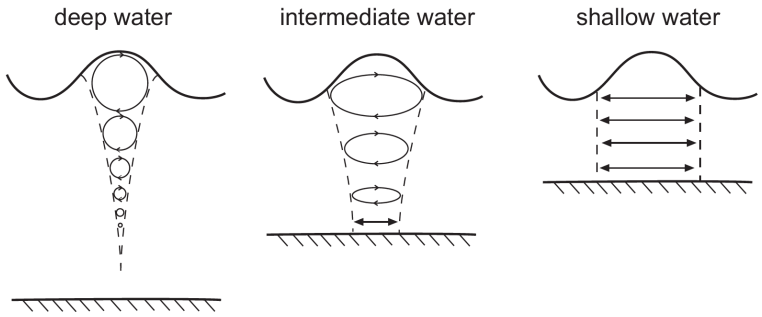

Figure 1.1: Motion of water particles under waves according to linear wave theory. In deep water, water particles follow a circular motion with the radius of the orbits decreasing with depth beneath the surface. In intermediate water, the orbits are elliptical and become flatter as the sea bed is approached. In shallow water, all water motion consists of horizontal movements to-and-fro which are uniform with depth (Masselink and Hughes, 2014).

dynamics and to be able to evaluate its effect on shore (Dean and Dalrymple, 2004). In addition, video-based observation makes use of theoretical solutions of the wave equations, particularly the linear Airy wave theory, which will be recalled here.

1.1.1 A Wave Description

As the wind blows over the water surface the shear stress creates higher resistance for the streamlines close to the water surface than the ones further away. Eventually the parallel streamlines will try to balance the force field and shift into circular streamlines, forcing the water to oscillate. During this process, wind energy is transferred to the wave, which carries the energy by iterating its form between kinetic to potential as the wave propagates (Davidson-Arnott, 2010). It continues until it reaches shallow water where it eventually breaks and dissipates the energy along the shoreline. The motion of the waves induces the water particles beneath the wave to move in an orbital path with a positive net movement forward causing a slight transportation force. In deep water the oscillation is composed of circular movements all the way down to the bottom, while at transitional and shallow water depths the oscillation path becomes elliptical and almost completely horizontal at the sea bed (Figure 1.1).

1.1.2 Wind Waves and Swell

Waves are generally described by wave height, period and direction that depend on wind speed, duration, fetch and water depth in the wave generation area (Dean and Dalrymple, 2004). Wind waves are those generated close to the shoreline by local winds. They have short wave periods, broad directional and frequency spectrum bands. Swell are waves generated remotely during storms and propagate towards the coast where they are observed. They are not related to local wind conditions at the observation site. They often have longer wave periods than wind waves, narrow directional and frequency spectrum bands. Swells are longer than wind waves because during their propagation, smaller wavelength dissipates faster. Video-based bathymetry inversion is generally used during swell conditions as small wind waves present a bigger challenge as will be seen.

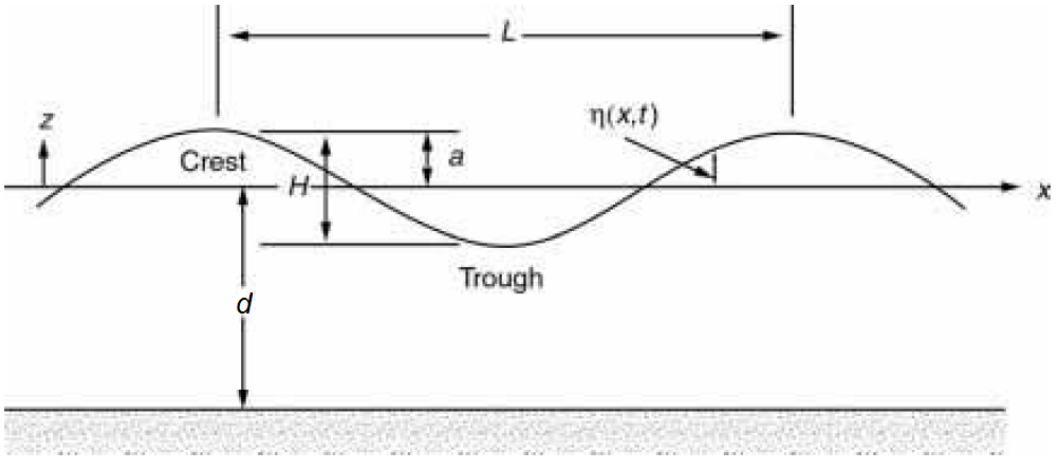

Figure 1.2: An ideal sinusoidal wave can be defined by its properties wave height (H), wavelength (L) and wave period (T) at a certain water depth d (Dean and Dalrymple, 2004).

1.1.3 Dispersion Relation and Wave Celerity

In ideal conditions, a wave would oscillate as a perfect sinusoidal curve. In reality the wave field is a complex mixture of waves of various shape and direction (Davidson-Arnott, 2010). This complexity is hard to describe mathematically because of nonlinearity effects, three-dimensional characteristics and random behaviour. There are three different theories that combine and calculate basic wave properties; Airy wave theory, Stokes wave theory and solitary wave theory. The most commonly used linear wave theory is the one derived by Airy in 1845 which is applicable for waves with a small wave height in relation to the wavelength and the water depth (Masselink et al., 2010). In this study all calculations were based on Airy's linear wave theory. Therefore, waves are assumed to act as simple waves, i.e. a sinusoidal waves with a dispersion relation given by linear equations (Dean and Dalrymple, 2004).

For a propagating wave of a single frequency – a monochromatic wave – the surface elevation (η), i.e. the elevation of the free water surface over the still water level (SWL), is given by:

$$\eta = \frac{H}{2} \cos\left(\frac{2\pi x}{L} - \frac{2\pi t}{T}\right) \tag{1.1}$$

where H is the wave height [m], L is wavelength [m], T is wave period [s], d is water depth [m], x is horizontal direction [m] and t is time [s] (see Figure 1.3). The wavelength is the horizontal distance between corresponding points in two consecutive waves. The height of the wave represents the vertical height between the crest and the trough of the wave. The wave period is the time it takes for corresponding points in two consecutive waves to pass a fix point. And finally, the water depth is the vertical distance from the still water level to the sea bed (Dean and Dalrymple, 2004).

The wave celerity (C) is the ratio of wavelength and wave period, since the travelled distance by the wave during one wave period is equal to the wave length:

$$C = \frac{L}{T} = \frac{\omega}{k} \tag{1.2}$$

ω is radial frequency and k is wavenumber. The relation between L and T (or ω and k) is the dispersion relation that is estimated for linear waves by the Airy theory. The wave celerity is then given as a function of wavelength (or period) and water depth:

$$C = \sqrt{\frac{g}{k}\tanh(kd)} = \sqrt{\frac{gL}{2\pi}\tanh\left(\frac{2\pi d}{L}\right)} \tag{1.3}$$

where g is the gravitational acceleration 9.81 m/s^2 and d is the water depth in metres. Note that waves are generally dispersive, meaning that waves with different periods travel at different speeds. This expression for C is the basis of bathymetry inversion as video images provide information on celerity and period (leading to wavelenth). The bathymetry is then given by:

$$d = \frac{L}{2\pi}\tanh^{-1}(\frac{2\pi C^2}{gL}) \tag{1.4}$$

Note that the wave height is not related to other wave properties in the linear theory and has to be found from measurements.

1.1.4 Wave Classification With Depth

There are many different perspectives to consider when classifying a wave. Some of the classifications which waves might be divided into consider the movement of the water particle beneath the wave, the water depth, the spectrum or how they are generated. For our purpose, a classification with respect to water depth is the most relevant because the bathymetry cannot be inverted in the deep water limit.

Shallow and Deep Water Limits

As bathymetry throughout the ocean can vary suddenly and drastically, it is of importance to have a clear definition of the difference between a deep water wave and a shallow water wave, as different rules applies for them. The linear wave theory simplifies in the deep and shallow water limits. It is therefore natural to use three zones: deep water, shallow water and a transitional water zone where no simplification is possible. A wave is said to be a deep water wave when the depth is higher than half the wavelength, i.e., depth to wavelength relationship is 0.5 (Table 1.1), while a shallow water wave is defined as such when depth divided by wavelength is lower than 1/25.

Classification	d/L	C
Deep water	$> 1/2$	$\sqrt{\frac{g}{k}}$
Transitional water	1/25 to 1/2	$\sqrt{\frac{g}{k}\tanh(kd)}$
Shallow water	$< 1/25$	$\sqrt{gd}$

Table 1.1: Classification of water depth is defined by the relationship between the water depth (d) and the wavelength (L). Wave phase speed C is given in each case. Shallow and deep water relations are limits of the complete relation (transitional water).

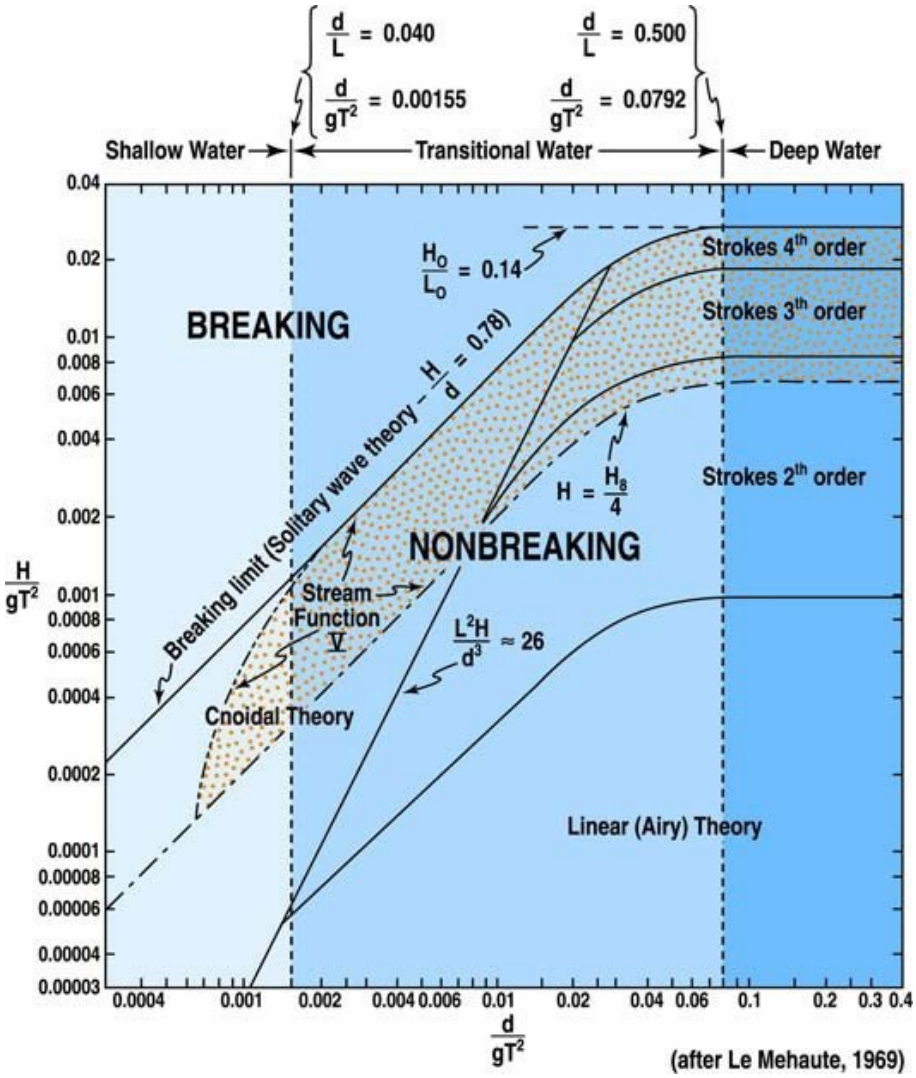

Figure 1.3: Wave category theory

There is a simple relationship between celerity and depth in shallow water, but most importantly for us, in the deep water case, waves are not affected by depth – neither the dispersion relation, nor wave celerity is depth-related (Table 1.1). This is a problem for computing depth inversion from wave characteristics, and the usual limit $d/L > 1/2$ should be questioned for the purpose of depth inversion. This is a question that will be addressed in this study (see chapter on bathymetry inversion).

Another question is whether the linear theory is generally valid and if the error made using the linear dispersion relation for depth inversion is dominant. Figure 1.3 is an illustration of the validity of the different theories in the wave parameter space. We will come back to it.

1.1.5 Wave Transformation and Breaking

Before breaking, a deep water wave propagating into shallower water is exposed to wave transformation processes: shoaling, refraction, reflection and diffraction. Wave shoaling affects the wave height while wave refraction affects the celerity and wavelength and thus also the direction of the wave. Reflection and diffraction occur when the wave encounters a barrier which

influences the pattern of the wave crests.

Shoaling

The law of conservation of energy states that energy cannot be created nor lost but can change form. This means that the energy of a deep water wave crest must be equal to the energy of the same wave crest in shallow water. As waves enter shallower waters, they slow down by interaction with the bottom, so that their celerity and wavelength decreases. Therefore to conserve energy, the wave height must increase, i.e. the kinetic energy of the wave is converted into potential energy. The wave period remains unchanged during this process called shoaling. Eventually the wave crest becomes too steep and unstable and thus transforms into a breaking wave. The wave shoaling process distributes the energy along the profile of the wave train (Dean and Dalrymple, 2004, Holthuijsen, 2010).

Refraction

As a wave moves shoreward with a certain angle to the shore, it has part of its crest closer to shore in shallower water. Due to the relationship between wave celerity and water depth, the more seaward part of the crest moves with a higher velocity and eventually catch up to form a crest that tends to be parallel to the shoreline (Dean and Dalrymple, 2004).

The same wave refraction process occurs in situations where waves approach headlands, embayments and islands, as land contours and bathymetry will produce a spreading out or a contraction of the wave rays. Wave rays are contracted and the energy is concentrated at headlands, while wave rays are spread out and the energy is dispersed at embayments, which is shown in Figure 1.4. With this follows that the wave height increases near headlands and decreases in bays, due to energy conservation (Davidson-Arnott, 2010). The wave refraction process distributes the energy along the coast (Dean and Dalrymple, 2004, Holthuijsen, 2010) and limits the angle between wave crest and shore, which has consequences for the distribution of cross-shore and longshore currents (see nearshore currents below).

Reflection

Natural or man-made vertical barriers, e.g. harbour walls or seawalls, may have a great influence locally on wave processes (and vice versa). As the incoming wave hits the barrier the energy of the wave is reflected instead of being dissipated along the shore. Depending on the material of the barrier waves can be partially or fully reflected. An impermeable wall which fully reflects the wave corresponds to a reflection coefficient equal to 1.0 and the total energy of the wave is reflected. This means that the reflected wave will have an equal wave height as the incident wave (Holthuijsen, 2010). A permeable barrier, e.g. rouble mound breakwater, will partly let through the wave energy and less energy will be maintained in the reflected wave.

An incoming wave crest perpendicular to a vertical, impermeable barrier is reflected in the opposite direction and receives the same frequency, period and amplitude as the incident wave. The resulting wave becomes a so called standing wave and the water surface profile can easily be estimated by superposing the two identical waves with opposite propagation direction (Dean

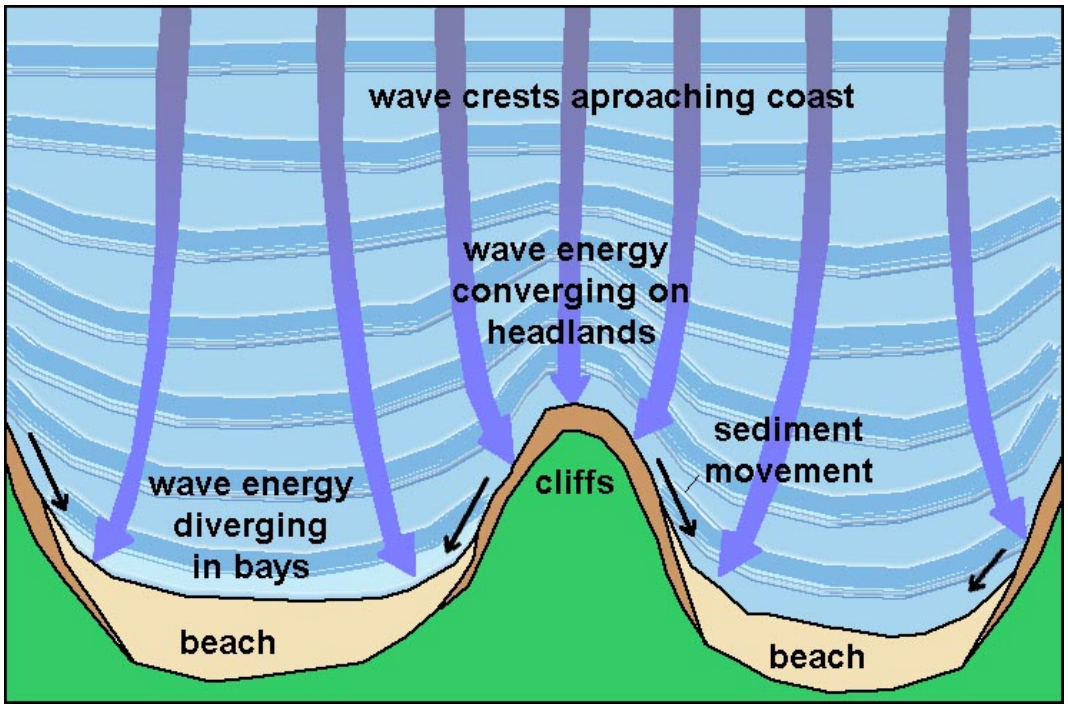

Figure 1.4: Wave refraction focuses wave energy on headlands and deposits sand in quieter bay settings (Komar, 1999).

and Dalrymple, 2004, Holthuijsen, 2010). On the other hand, if the incoming wave angle to the normal from the vertical barrier is equal to α, then the angle of the reflected wave will be equal to α on the opposite side of the normal (Masselink and Hughes, 2014).

This kind of reflection phenomenon induced by man-made constructions has a great impact on not only the construction itself but also on the sediment transport. For example, in a harbour multiple reflections can build-up energy which can result in disturbance and surging within the harbour area, which in turn affects the harbour construction and anchored ships (Dean and Dalrymple, 2004, Holthuijsen, 2010).

Diffraction

Propagating water waves are also transformed when encountering obstructions, for example breakwaters or islands, by transferring the wave energy sidewise along the wave crest (Holthuijsen, 2010). As the waves approach the obstruction, three regions will be formed; a shadow region, a short-crested region and an undisturbed region, see Figure 1.5. The region in front of the obstruction will be affected by both the incident waves and the waves that are reflected against the barrier creating a region with short-crested waves. When the wave passes the barrier, the lateral dispersion of wave energy will force the wave to bend around the tip of the barrier and form a circular wave crest with centre at the tip of the barrier. In reality though, this wave transformation process is much more complicated since the waves that are reflected by the barrier in the short-crested region will diffract into the undisturbed region. Hence, the short-crested region will be extended into the undisturbed region (Masselink and Hughes, 2014, Holthuijsen, 2010).

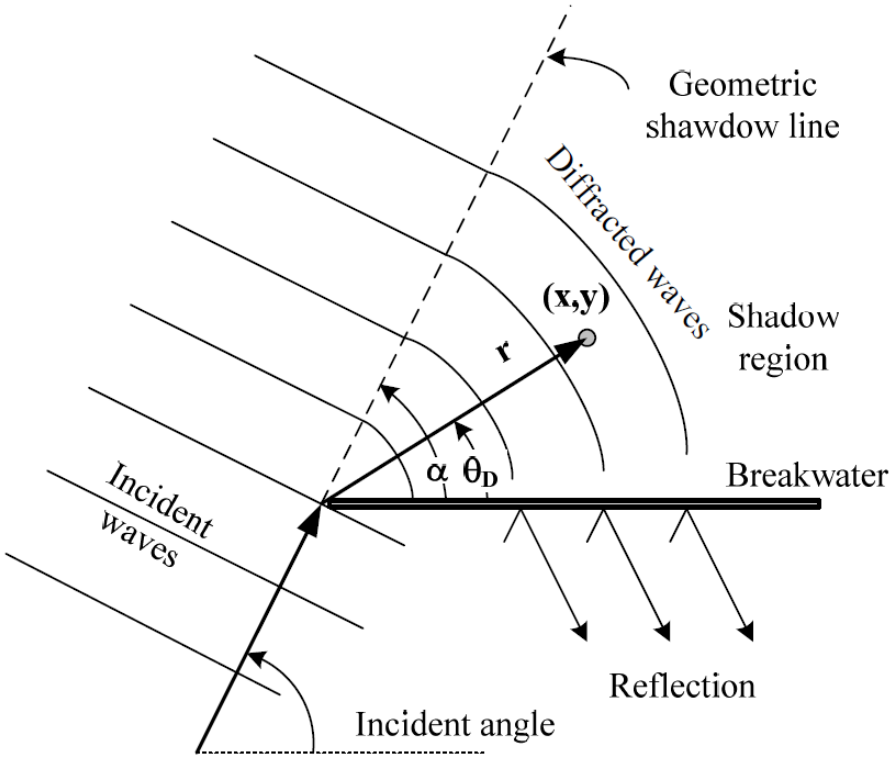

Figure 1.5: Diffraction of waves after encountering an infinity breakwater (Reeve et al., 2012).

Breaking Waves

In deep water, waves theoretically break when wave height divided by wavelength is equal to 1/7 – although breaking actually occurs earlier. In shallow water waves theoretically break as the ratio of wave height to water depth H/d reaches 0.78. At breaking point, the wave crest is usually so steep that water particles in the crest have higher velocity than in the waveform, causing the wave to break (Komar, 1999, Masselink and Hughes, 2014, Holthuijsen, 2010).

Breaking waves are classified in different categories depending on their features. The different types are spilling, plunging, surging and collapsing waves, see Figure 1.6. A spilling wave usually occurs on beaches with little slope and happens when the crest slowly reaches its peak and then falls down as foam and bubbles. A plunging wave approaches the beach, which usually is steep, with a vertical crest that rolls over with a big fountain of water. A surging wave is almost like a plunging wave but differs in the sense that the wave base reaches the beach before the crest and thus makes the wave collapse. Surging waves most often occur on very steep beaches when they are a quite small.The collapsing wave is a mix of a surging and plunging waves. Many ocean waves are a mixture of the explained categories of breaking waves, which makes it difficult to distinguish between them (Komar, 1999, Masselink and Hughes, 2014, Holthuijsen, 2010).

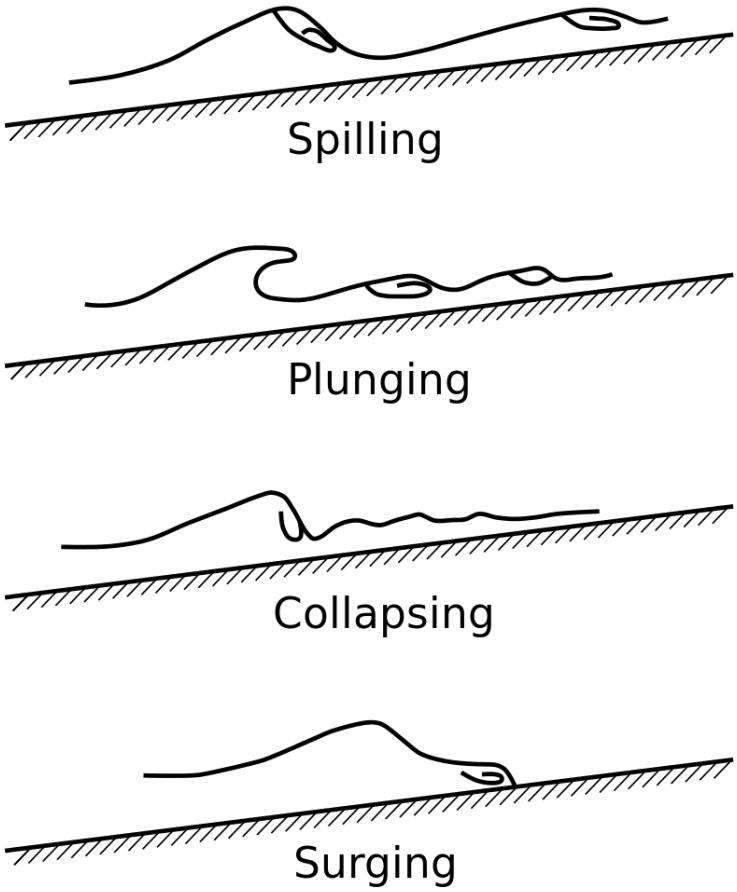

Figure 1.6: Illustrative sketches of the four different types of breaking waves on slopes; spilling, plunging, collapsing and surging. Redrawn by S.L. Douglas and J. Krolak (FHWA).

1.2 Radiation Stress and Nearshore Currents

Radiation stress is the flux of momentum, which is carried by the ocean waves. In the Airy theory, the radiation stress is determined from the properties of surface gravity waves as:

$$S = (2\frac{C_g}{C_p} - \frac{1}{2})E \tag{1.5}$$

C_g and C_p are phase speed (ω/k) and group speed ($\partial\omega/\partial k$) of the waves. E is the wave energy given by:

$$E = \frac{1}{8}\rho g H^2 \tag{1.6}$$

As a progressive wave approaches shore and the wave height increases due to wave shoaling, the radiation stress increases. Momentum conservation requires this additional flux to be balanced and causes a decrease in the mean water level (and a decrease of pressure) called wave setdown. On the contrary, wave setup (and pressure increase) occurs after the waves break as radiation stress decreases and causes the surface level to increase. Wave setup is particularly of concern during storm events, when the effects of big waves from the storm are able to increase the mean sea level by wave setup.

Another important consequence of wave breaking is that the wave momentum is transferred to the water column, forcing nearshore currents. These persistent currents (in a wave-averaged sense) have a high capacity of transport and thus play an important role in coastal environments. Most commonly, we consider two types of nearshore currents: cross-shore and longshore currents, whether they flow in a direction normal or parallel to the shoreline.

During wave breaking, a current is generated in the same direction as the wave. If the wave is shore normal, an onshore surface flow is created. Then, an offshore current is also generated along the lower water column (called undertow) to compensate for the onshore flow, satisfying the requirement of flow continuity (for incompressible fluid). These currents are referred to as cross-shore currents as they flow in a direction perpendicular to the shoreline.

Longshore currents are formed in the surf zone when the crest of the incoming breaking wave has an angle with the shoreline. In this case, currents are generated parallel to the shoreline. The strength and direction of the longshore currents depend on the angle between the crest and the shoreline. For maximal current strength the incoming wave crest should be 45 degrees to the shoreline.

Wave setup can also participate to nearshore currents. They produce rip currents when breaking is variable in the longshore direction. For example, if normally incident waves are breaking on each side of a channel, pressure forces created by alongshore variations of wave setup can drive currents that converge into the channel and turn as seaward rip currents. This creates a cell circulation of the currents in the nearshore zone, potentially important for sediment transport (Dean and Dalrymple, 2004, Holthuijsen, 2010).

1.3 Littoral Sediment Transport

Most of the beach morphological change occurs in the littoral zone because of the dissipation of energy along the shoreline as waves break. If it were not for the waves there would be no littoral processes. Sediment transported by waves and currents in the littoral zone, i.e. the zone between the backshore and the most seaward breaking waves, is defined as littoral transport. The sediment may be transported by three different transport modes, bed load, suspended load and sheet flow. Bed load is when the grains are moving along the bottom caused by the shear stress induced by the moving water above the sediment bed, while suspended load are the grains lifted upward from the bottom by turbulent fluid motion. Sheet flow transport occurs when the grains move collectively as a layer along the bottom surface. Further, the littoral transport can be divided into two categories depending on the direction of the sediment movement in relation to the shore. Transport of sediment parallel to the shore is referred to as longshore transport, while transport of sediment perpendicular to the shore is called cross-shore transport. The cross-shore transport is the significant transport process in the offshore zone, while both cross-shore transport and longshore transport are significant in the surf zone (Davidson-Arnott, 2010, Masselink and Hughes, 2014).

The computation of net transport is important when investigating if a beach remains stable, eroding or, to the contrary, accreting. The difficulty is to properly accounts of the different processes that affects the budget. These is discussed further in this section.

Cross-shore sediment transport

Ideal deep water waves generate a circular movement of the water particles perpendicular to the wave crest (orbital currents). The strength and scale of this circulation decrease with depth and is non-existing at the sea bottom. Therefore, deep water waves have low impact on bottom sediment. As the wave propagates onshore, the water depth becomes shallower and the circular movement elliptical. The elliptical movement also decreases with depth, but has a greater impact on the bottom sediment, and the water at the bottom begins to move. In shallow water, the elliptical movement stretches and becomes almost a horizontally straight line. These horizontal water movements transport sediments shoreward and seaward, and can produce a net transport if the waves are asymmetric or skewed (bedload transport). The action of orbital currents is also to lift up sediments that can then be transported by wave-averaged cross-shore currents in the water column. This process of suspended load transport (e.g., by undertow and rip currents) is generally considered dominant in nearshore regions, although bedload transports are not well understood.

Longshore sediment transport

Cross-shore sediment transport is mainly affected by wave steepness, sediment grain size and the beach slope. High and steep waves tend to move more and coarser material offshore, while lower waves of long period move finer material onshore (Davidson-Arnott, 2010, Masselink and Hughes, 2014). If the amount of sediment transported with the swash up on the beach slope equals the amount being transported with the backwash out to the sea again, the slope is said

to be in dynamic equilibrium (Komar, 1999, Masselink and Hughes, 2014).

Longshore transport is a suspended load transport process. As the waves break, energy is supplied to the sediment, which stirs up from the sea bottom. The longshore current generated parallel to the shore, catches the free drifting sediment and transport it along the shoreline. This transport of sediment may only be local rearrangement, or it may be transported for several kilometres (Davidson-Arnott, 2010, Masselink and Hughes, 2014). The longshore transport rates may vary from nearly nothing up to several million cubic meters per year. Hence, this process is essential for the long-term change of beach morphology (Davidson-Arnott, 2010, Masselink and Hughes, 2014).

Sediment can also be transported in the longshore direction by the swash. Broken waves transport sediment up on the beach with the swash, but at the same time the longshore current makes the wave run down with the backwash in an angle different to the incoming angle of the swash. This creates a positive net transport of the sediment in the longshore current direction.

1.4 Coastal Morphodynamics

1.4.1 Definition of Coastal Zones

The beach profile and the shoreline can look very different at various locations and seasons, which makes it hard to have precise definitions of the different areas in the coastal zone. The water closest to the shoreline and the immediate land next to it is referred to as the littoral zone, while the water area closest to the shoreline is called the nearshore zone, i.e., a section of the littoral zone (Figure 1.7).

The nearshore zone can further be divided into three zones: breaker zone, surf zone and swash zone. Waves start breaking in the breaking zone, but the process continues in the surf zone. The surf zone is usually wide where the beach consists of fine sediments and narrower in areas with coarser sediment. This is a result of wave energy because waves with higher energy, which would start breaking in deeper water, can carry coarser and consequently heavier sediment. In the swash zone, waves subject the beach to run-up and backwash as the waves hit the beach face (Komar, 1999, Masselink and Hughes, 2014).

The foreshore in the littoral zone has almost the same definition as the beach face, but is the area between the berm and the lowest point at the low tide swash. The berm is a flat area on the beach and is part of the backshore, located next to the foreshore in the onshore direction. It can exist more than one berm on a beach and it can be hard to identify. The backshore stretches all the way out to a change in the physical setting, which can be a cliff, a sand dune or a construction etc. (Komar, 1999, Masselink and Hughes, 2014).

Beach states and classification

The diversity of environmental conditions (hydrodynamic, sedimentary, morphological) to which beaches are exposed around the world can give the appearance of diversity. Observations show that beaches actually take on a relatively limited number of appearances. Starting from the hypothesis that the beach is in balance with wave climate, state classifications have been proposed. First, these classifications were developed only for the single bar beach type, in microti-

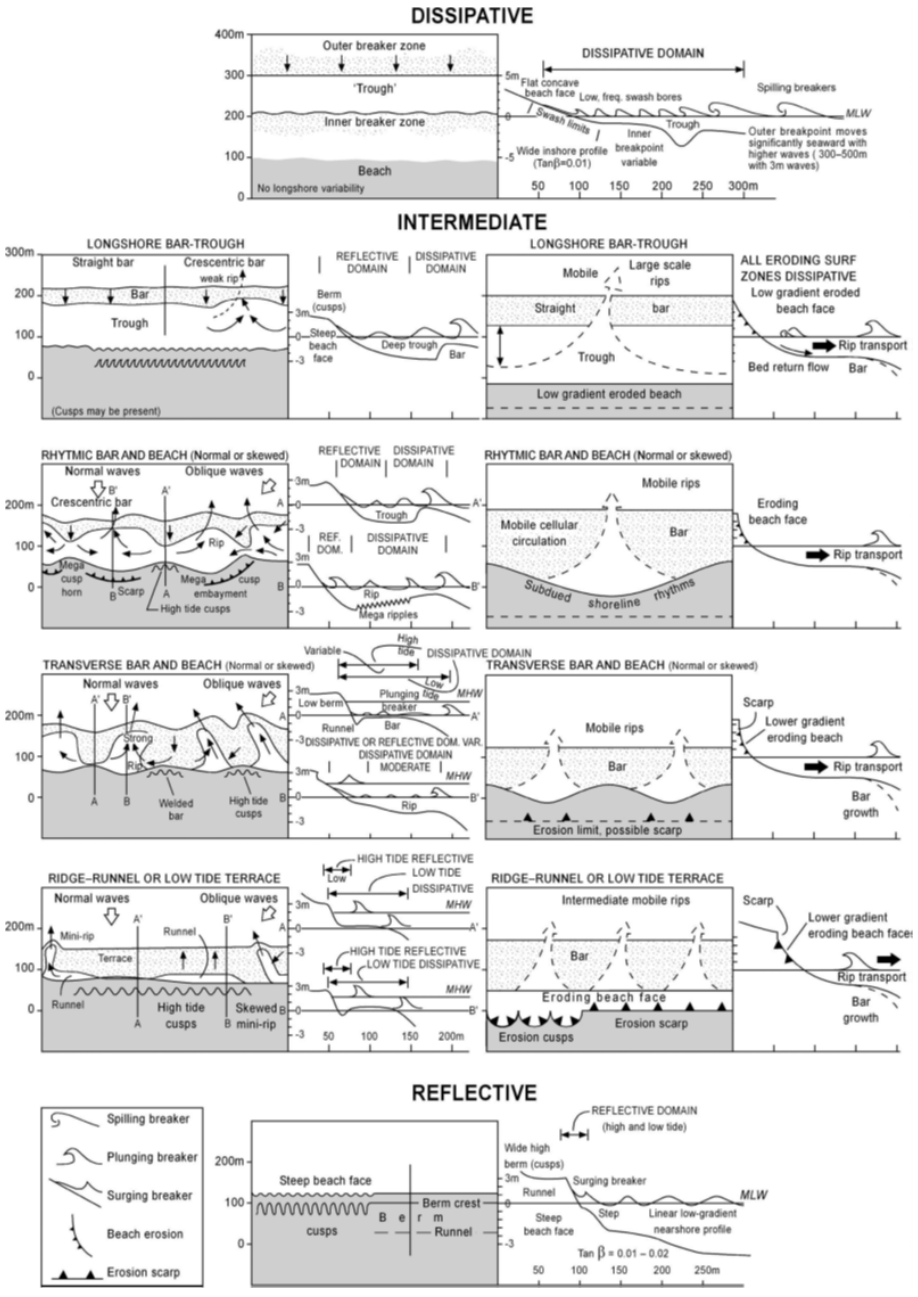

Figure 1.7: Beach states and classifications (Short, 2006).

dal environment. The Gourlay parameter Ω (Gourlay and Meulen, 1968) which depends on the granulometry of the site and wave forcing, allows to describe three distinct classes of beach:

$$\Omega = \frac{H_b}{w_s T} \tag{1.7}$$

where H_b is the height of breaking waves, w_s the fall rate of the sediment – associated with the timescale of morphological response to forcing – and T the period of the waves. The classes are:

- Dissipative ($\Omega > 6$): a beach is said to be dissipative when the sand is relatively fine and waves are short and powerful. The equilibrium profile has generally a mild slope. The beach may have one or more bars, usually straight. In the literature, this state is often associated with the "storm profile".

- Reflective ($\Omega < 1$) : A beach is reflective when the sediment is fairly coarse and that she's exposed to low-energy waves. This profile is generally associated with "calm weather".

- Intermediate ($1 < \Omega < 6$) : This range is the most common. The beach is characterized by high temporal variability and diversity of appearance. To describe this diversity, four sub-states are defined (Wright and Short, 1984, Lippmann and Holman, 1990, Masselink and Short, 1993, Short, 2006) for which the sandy bar (only considered in these classifications) can present a 3D geometry (Masselink and Hughes, 2014). These four sub-states depend mainly on the position of the sandy bar in relation with the top of the beach: from the furthest offshore position associated with the most dissipative states up to a bar connected to the upper beach for reflective states. The presence of 3D structures is also associated with a reflective intermediate state whereas a 2D geometry corresponds to a more dissipative state. From dissipative to reflective, these states are "Longshore Bar and Trough" (LBT), "Rhytmic Bar and Beach" (RBB), Transverse Bar and Rip (TBR) and Low Tide Terrace (LTT).

Low Tide Terraced beaches

A Low Tide Terrace (LTT) is generally defined as a flat area of a beach adjacent to the low-water line. They occur on the open coast where sand is fine to medium and wave height averages between 0.5 and 1.0 m. On high energy coasts they occur where nearshore reefs and headlands lower waves to less than 1.0 m at the shore. Low tide terrace beaches are characterized by a moderately steep beach face, which is joined at the low tide level to an attached bar or terrace, hence the name low tide terrace. The bar usually extends between 20 m and 50 m seaward and continues alongshore, attached to the beach. It may be flat and featureless, have a slight central crest, called a ridge, and may be cut every several tens of metres by small shallow rip channels, called mini rips.

At high tide when waves are less than 1.0 m, they may pass right over the bar and not break until the beach face, behaving much like a reflective beach. At spring low tide, however, the entire bar is usually exposed as a ridge or terrace. At mid tide, waves usually break right across the shallow bar and a small surf zone is produced. The water is returned seaward, both by

reflection off the beach face, especially at high tide, and via the mini rips, even if no rip channels are present. The rips, however, are usually weak, ephemeral and shallow. Low tide terrace beaches are the least hazardous of the intermediate beaches, because of their characteristically low waves and shallow terrace. One of the safer beach types when waves are below 1.0 m high, especially at mid and high tide. Higher waves, however, generate dumping waves, strong currents and ephemeral rips, called side drag, side sweep and flash rips by lifesavers (Castelle et al., 2014, Almar et al., 2018).

Abundance of coarse sediments, often associated with drift geology in higher latitudes (Orford et al., 2002), also influences the R/LTT transition. If a large amount of coarse sand or gravel is available, a steep and reflective profile can be maintained throughout the intertidal region, resulting in a reflective beach type . But if the supply of coarse material is limited, the steep and coarse upper beach will be fronted by a sandy low tide terrace, resulting in the LTT beach type . The amount of coarse sediment available is only partly related to wave conditions and is mainly attributable to geological factors.

Questions on LTT beach evolution

In this PhD study, we are most concern with a beach located in a semi-enclosed bay, exposed to seasonal modulation of moderate energy waves, which can be defined as a low energy environment (Jackson et al., 2002). In such environment, major morphological changes are generally attributed to events of moderate to high-energy waves, with long periods of inactivity in between. Transfers between the subtidal region and upper beach are assumed weak or non-existent since the depth-of-closure (beyond which the depths do not change with time) is small. These assumptions have not been challenged until recently and low-energy environments have remained beyond the scope of major research interest. Yet, they raise important issues: how can a beach recover if the subtidal and upper beach sediment cells are disconnected? Are morphological features only generated during high-energy events or do low-energy wave conditions have a role to play in the recovery process?

During extreme events, the beach is observed to evolve dramatically, dominated by surf processes that can rapidly lead to an up-state transition through offshore sediment transport by the undertow and sandbar formation. After such extreme event, the beach slowly evolves through transient states while recovering under low or moderate energy wave forcing (Coco et al., 2014, Angnuureng et al., 2015). There is as yet no consensus on whether these events have transient or persistent impact on beach evolution and on the crucial recovery processes leading to beach resilience (Anderson et al., 2010). Resilience capacity would relate on the extent of departure from equilibrium driven by short events and on recovery timescale, which can be from days to years, depending on the site and severity of events. For isolated storm events, departure from equilibrium is related to storm intensity (Frazer et al., 2009, Davidson et al., 2013). However, no clear conclusion can be drawn when considering sequences of storms, since both enhanced and weakened effects are observed (Ferreira, 2005, Karunarathna et al., 2014, Splinter et al., 2014a). It seems that it is the interplay between recurrence interval of events and post-event (low-energy) recovery timescales that matters. For example, a sequence of events with recurrence interval shorter than recovery duration (e.g., strong 2013-2014 winter events in Europe; Castelle et al.

2015, Masselink et al. 2016) shows greater impact than individual events. The reason is that the system moves sequentially toward a new state of high-energy equilibrium.

The evolution of a beach can be characterized at different time scales, i.e., interannual, seasonal or event scales (Quartel et al., 2008). The most dramatic changes occur occasionally during a storm event and high-frequency assessment is needed in this case. Traditional observation tools are designed for low frequency monitoring (bi-monthly with satellites and monthly with GPS) or are sporadic during measurement campaigns. Key parameters of coastal morphodynamics may be missed. To circumvent the problem, low cost systems of coastal video imaging (Holland et al., 1997, Holman and Haller, 2013) were designed. They are particularly well suited to monitor the shoreline evolution in various parts of the world, covering timescales from seconds to years and spatial scales from meters to kilometers. It allows a monitoring of beach morphology as well as hydrodynamic factors governing its evolution. The present PhD study will present some analysis of shoreline seasonal evolution, typhoon and monsoon events in LTT beach in Vietnam using the video camera technique. It will provide an example of the patterns and interplay between intra-seasonal events and seasonal recovery in a low-energy environment.

1.5 Causes of Shoreline Erosion

A beach and its shoreline are not a fixed state, but nature has a tendency to change and adapt to new conditions. Some shores are subjected to growth and expansion while other might be subjected to erosion and contraction. Both of these shoreline changes could be caused by natural processes, but anthropogenic impact have increased, sometimes dramatically.

1.5.1 Natural Variation

When a beach is exposed to higher waves than normal, sediment from the beach is transported out into deeper parts of the sea with the cross-shore currents. Often bars are formed in the ocean this way. When a calmer period comes, sediments are transported back to the beach again by the waves (presumably through bedload transport). Higher waves often occur during winter storms in Europe or winter monsoon in Southeast Asia and a summer calm period comes in between. This makes it a seasonal loop that alters the beach appearance from season to season. Rough weather during winter implies that the beach retreats while the beach accretes during the gentle summer weather (Davidson-Arnott, 2010, Masselink and Hughes, 2014). Such system can be in balance and do not have to imply that erosion is taking place. But sediment may be lost to deeper parts of the ocean where it is lost from the sediment loop, resulting in a negative net transport of sediment and hence erosion. This is the reason why an assessment of subtidal morphological evolution during and after intra-seasonal events is so critical.

Longshore currents can also influence the natural variation of the complete shoreline orientation. Depending on the angle and strength of the incoming wave, which vary with the seasons and low frequency climate variations, the shoreline alternates at various scales. With waves coming from a north direction, the shoreline might retreat in the southern part and accrete in the northern part. If waves instead come from a south direction, the reverse will occur. This makes the shoreline to naturally shift in gradient from a plan view. It is usual to assume that

cross-shore transports vary at high-frequency (intra-seasonal to seasonal), while longshore transports vary at lower frequency (seasonal to lower). Around the Pacific Ocean and particularly in Southeast Asia, ENSO (El Nino Southern Oscillation) is a major climate forcing (see next chapter) that strongly affects both tropical cyclone activity and the winter monsoon. This can impact the coastal sediment budget through two major processes coming either from the ocean as wave forcing or the continent as river sediment flux associated with precipitation changes. Strong winds can also carry sediment from the beach and thus change the sediment budget. The role of ENSO on coastal erosion is poorly known as it requires long-term monitoring along the coast and rivers.

A beach can also be affected by climate change. With sea level rises, the beach would try to adjust to the same profile. This will make the beach retreat and sediment will be lost (Davidson-Arnott, 2010, Masselink and Hughes, 2014). Sea level rise occurs naturally around the world, but there is also a fear of higher speed of such a rise due to global warming.

1.5.2 Human Impact on Erosion

Humans can interrupt the stability of beaches around the world. One example of this is the mining of sand. Since sand is an ingredient in building material it is coveted in today's society when population growth is increasing and thereby also more properties are built. Often the sand comes from rivers, floodplain and terrace deposits and removal of sand from these places will unbalance the system as the sediment budget is altered and the hydraulics of the channel is changed (Padmalal and Maya, 2014). If less sand is transported in the rivers, it will be harder for the beach to renourish.

Constructions of dams in river systems are also changing sediment budget for many rivers. The dams could be built to act as, for example, water source for hydropower or irrigation and fresh water source. The sediment is trapped inside the dams and thus it is hindered from its transport further down in the river and eventually to the coast. However, compensation processes can also take place in rivers. As the dam ponds the water, it retains a large part of the sediment. The water subsequently released is almost devoid of sediment. This "Hungry water" has the tendency to pick up sediment as it moves downstream (Kondolf, 1997), thus accelerating river bank erosion but in the same time mitigating coastal erosion.

In harbours or channels, sediment will often get stuck and hinder the flow of water. Therefore dredging of material in harbours and channel is often done. The sediment is then removed and relocated at some other place in the sea, and the material can be lost from the sediment balance of the coast (Davidson-Arnott, 2010, Masselink and Hughes, 2014). When dredging bars outside the beaches, the wave pattern will be changed and if waves are not breaking at the bar any longer they will continue their way towards the beach with higher energy and thus the risk for erosion at the beach will increase.

The beach can also be subjected to human change for example by removing vegetation that binds sediment with its roots. Also flattening of the beach to make it more attractive for sunbathers will affect the sediment transport processes. Building pavements and hardening the surface are also working in favor of erosion (coastal squeeze). Other constructions along the coastline, like sea groins and seawalls, can also increase the risk of erosion by changing srround-

ing wave conditions (Davidson-Arnott, 2010, Masselink and Hughes, 2014). Sometimes these measures protect the nearby shores but will change the sediment budget for areas downstream, resulting in a movement of the erosion problem.

Another growing concern in Southeast Asia is land subsidence due to massive groundwater extraction (Syvitski et al., 2009). Land subsidence is a major process of land retreat in the Mekong delta, where groundwater is largely overused, but recent studies also attribute beach retreat in central Vietnam to the same process. Subsidence is part of the relative sea level rise but can be of much higher amplitude than global sea level rise in the coastal area (a few mm per year against a few cm for subsidence in the Mekong delta).

Chapter 2

Study area

Contents

2.1 General Background about Vietnam

Vietnam is located between 9 and 23 degrees north in Southeast Asia with neighbouring countries being China, Laos and Cambodia (Figure 2.1). The country is oblong with some parts as narrow as approximately 50 kilometres wide, but in total the land area covers an area of 170,000 square kilometres with a population of 90.7 million people. A great part of the land border, more precisely 3,260 kilometres, is located along the coast and adjacent to the South China Sea (SCS) in the east and to the Gulf of Thailand in the south. The country is mountainous in the northwest and in the central highlands facing the South China Sea, with peaks reaching up to 2450m. In

the north around Hanoi and in the south around Ho Chi Minh City, there are extensive low-lying regions in the Red River delta and the Mekong delta respectively. The coastline is irregular with many headlands and embayments (INMAN and Harris, 1966, Dahlström and Böös, 2015).

2.1.1 Climatology

Vietnam's climate can be divided into three different zones: north, central and south Vietnam. The climate in north Vietnam is humid and subtropical, while south Vietnam has a tropical climate all year round, with the central region in-between. As Vietnam is a long, narrow country, climatic conditions vary considerably with temperatures ranging between $20°C$ and $35°C$. Due to higher altitudes, it is coolest in the mountains.

Overall, Vietnam has a tropical monsoon type of climate. From May to September, the south monsoon sets in, and the country is dominated by south to southeasterly winds. From October to April, the north monsoon is dominant with northerly to northeasterly winds affecting the country (Figure 2.2). During the north monsoon, northern Vietnam has cloudy days with occasional light rain, while southern Vietnam tends to be dry and sunny, sheltered by the central mountain range. Between each monsoon season lies a transition month when winds are light and variable.

The onset of northeast winter monsoon (October-April) resulting from the formation of winter anticyclones over the Siberian region leads to high wind conditions, particularly off northern and central Vietnam. As new Siberian anticyclones form every 3 to 10 days, surges of northeast winds set in then wane with this cycle. These events – known for sudden drop of temperature in Hong Kong – are called winter monsoon events or surges. They are important in our study for they effect on waves, which have never been emphasized before.

The annual precipitation in Vietnam ranges from 1,000 mm to over 3,000 mm (INMAN and Harris, 1966, Dahlström and Böös, 2015). The country has an actual rainy season during summer monsoon (May to September). Rainfall is light and infrequent for the remainder of the year. Even so, annual rainfall can be considered abundant and exceed 1000mm almost everywhere. This figure is even higher in the hills, especially those facing the sea, in the range of 2000-3000mm (the greatest coastal rainfall appears in Hue, located in central Vietnam). For coastal areas and the parts of the central highlands facing northeast, the season of maximum rainfall is between September to January. During this period, these regions also receive torrential rain from typhoons which move in from the South China Sea.

The average temperature in Vietnam ranges from 24 to 30 degree Celsius. Temperatures are high all year round for southern and central Vietnam. Northern Vietnam, however, has a definite cooler season as the north monsoon occasionally advects cold air in from China. Frost and some snow may occur on the highest mountains in the north for a few days a year. The lowlands in southern Vietnam are sheltered from outbreaks of colder northerly air. These areas have a dry season that is warm to hot, with much sunshine.

2.1.2 Wave Climate

Wave height and direction in the sea are related to wind strength and direction. During the northeast and southwest monsoons the waves come from northeast and southwest, respectively.

Figure 2.1: Vietnam is located in Southeast Asia with the adjacent countries China, Laos and Cambodia and oceans South China Sea and Gulf of Thailand.

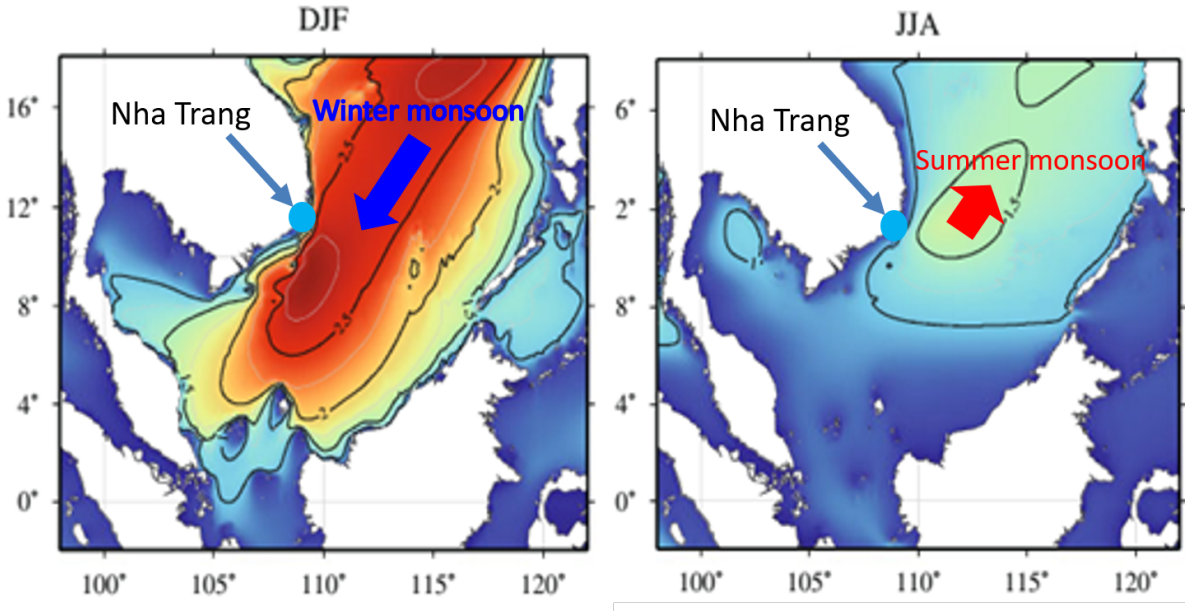

Figure 2.2: Seasonal mean wind velocity over Vietnam and Southeast Asian waters during winter time (left) and summer time (right), when the northeast and southwest monsoons, respectively, occur. After Mirzaei et al. (2013)

Summer monsoon drives relative weak, short-period southwesterly waves, which contrasts with the severity of tropical storms. However, the onset of northeast winter monsoon and associated monsoon events leads to high wave conditions, particularly off northern and central Vietnam. The winter mean significant wave height is in excess of 2.5 m off the central area (Chu et al., 2004) and the 90th percentiles can even reach 4 m (Mirzaei et al., 2013). Heavy swell during strong surges in the northeast monsoon can cause significant wave heights to rise to more than 6 m for one to a few days. Winter monsoon surges can also be reinforced by the occurrence of low-pressure typhoons by increasing the pressure gradients between the Southeast Asian continent and the ocean. However, coastal waves are generally lower than offshore waves due to sheltering and dissipation effects over the continental shelf (Mirzaei et al., 2013).

2.1.3 ENSO Impact on Vietnam Climate

There is high interannual variability observed in winter over central Vietnam, which is forced in part by coherent large-scale phenomena, such as ENSO (El Nino Southern Oscillation). Anomalous anticyclonic winds over the SCS are largely modulated by ENSO (Juneng and Tangang, 2005). There is weaker winter monsoon winds over the SCS during El Nino (and stronger during La Nina). Weaker winds also correspond to weaker waves and lower significant wave heights. However, in summertime (JJA), positive correlation values are observed in southern SCS due to strengthening of summer monsoonal winds over the southern SCS during El Nino years.

Seasonal rainfall and heavy rainfall months are significantly higher during La Niña than during El Niño episodes. It helps explain flooding anomalies: flooding is at least twice as frequent during La Niña compared with El Niño conditions, particularly in Central Vietnam. Because ENSO cycles have an impact on flooding, it provides prospects for early warning, differentiated for different zones and rainfall regimes.

2.1.4 Typhoons

The Northwest Pacific Ocean is the most active tropical cyclone basin on the planet. Annually, an average of about 26 tropical cyclones in the basin acquire tropical storm strength or greater and 16 of them become typhoons (Joint Typhoon Warning Center database). The risk of landfall of a typhoon or tropical storm depends on its trajectory, varying strongly with the season, as well as on interannual (Chan, 1985) and interdecadal time scales (Ho et al., 2004). Cyclogenesis over the tropical northwest Pacific takes place in a broad region west of the date line. Most of these tropical cyclones (TCs) follow rather straight west-northwestward tracks, but about one-third of these Northwest Pacific TCs continue in a westward direction and make landfall in Southeast Asia (Camargo et al., 2007a). There are about 5 landfalls in Vietnam on average, mostly over the northern provinces.

These numbers were shown to vary significantly from year to year, partly due to the influence of El Niño–Southern Oscillation (ENSO; e.g., Camargo et al. (2007b)). There is a tendency in El Niño years toward tropical cyclones that turn northward while avoiding the South China Sea, as opposed to La Niña years, when Vietnam is statistically more affected than in normal years.

The year 2013 (when our video camera started recording) was qualified as a normal year but followed long-lasting La Niña events from 2010 to 2012. As a result, large positive anomalies of subsurface waters were still observed in 2013, which is particularly favorable to TC intensification. Whether this can explain the exceptional 2013 Pacific typhoon season is an open question. In any case, with 51 named systems, it was the most active typhoon season since 2004, as well as the deadliest since 1975. The first two-thirds of the season were weak but the season became dramatically active starting from mid-September. 10 named systems crossed the South China Sea and landed in Vietnam, most noticeably Typhoon Nari in October and in early November, Typhoon Haiyan, which became one of the most intense tropical cyclones on record.

2.1.5 Tides

Tides in the South China Sea have been studied since the 1940s (see Minh et al. 2014). The four most important tidal constituents (O1, K1, M2 and S2) give a relatively complete picture of the tidal pattern of the region and are sufficient for a general description. However, the co-tidal and co-range charts (tidal phases and amplitudes of the main tidal constituents) shown before the 1980s had large discrepancies over the shelf areas. Numerical model later allowed substantial improvements.

Tides in the South China Sea are essentially maintained by the energy flux of both diurnal and semidiurnal tides from the Pacific Ocean through the Luzon Strait situated between Taiwan and Luzon (Luzon is the largest island in the Philippines, located in the northernmost region of the archipelago). The major branch of energy flux is southwestward passing through the deep basin. The branch toward the Gulf of Tonkin is weak for the semidiurnal tide but rather strong for the diurnal tide. Semi-diurnal tides are generally weaker than diurnal tides in the South China Sea.

2.1.6 Geomorphology

The northern two thirds of Vietnam are covered by semi-mountainous areas, while the inland consists of high plateaus with elevations up to 2,000 meters. Between inland and coastline, the environment consists of inter-mountain and alluvial plains. The southern one third of Vietnam is a low-lying area with dominating alluvial deltas, which often is exposed to flooding. The continental shelf along Vietnam slopes gently from the shoreline out to the edge of the shelf down to 200 meters then continues more steeply down to depths of 3,000 meters and more in the South China Sea (INMAN and Harris, 1966, Dahlström and Böös, 2015).

The geological setting of Vietnam is dominated by hard rocks of the Annamite Range, which is an extended mountain chain from the Himalayan Mountains. The hard rocks contain coarse-grained, intrusive rocks (granite), older sedimentary formations (largely metamorphosed to limestones, quartzites and schists) and volcanic rocks (basalt and rhyolite). The south part of the Annamite Range has eroded, which led to the formation of the high plateaus in the northern and central Vietnam (INMAN and Harris, 1966, Dahlström and Böös, 2015).

Many of the headlands along the irregular coastal areas of the north and central Vietnam are composed by former islands in a Holocene sea and were created by littoral deposition. There are many sandy beaches along the coast stretch that do not exceed the length of ten kilometres, with the exception of the 128 km long beach at Hue. Old barriers of beach ridges, dated up to between 2,500 and 4,000 years, indicate the former coastlines. They show that an extensive amount of littoral deposited along the Vietnamese coast. In some places the deposits have blown inland and created great sand dunes (INMAN and Harris, 1966, Dahlström and Böös, 2015).

The sediments of the deltas in the southern areas consists of fine-grained fluvial deposits (muds and sands), which are transported by rivers like the Mekong river, and covers the hard Annamite rock with at least a 400 m thick layer (INMAN and Harris, 1966).

2.1.7 Contemporary erosion

A great part of the Vietnamese land-frontier is located by the coast and is exposed to the interactions between land and sea, and natural and human processes. Hence, Vietnam is facing the issue of coastal erosion, which results in morphological changes and may have a strong and negative impact on not only nature itself but also on facilities. Between the years of 1990 and 2003, 263 sites spread along the Vietnamese coastline exposed to erosion were recorded with a total eroded area of 8,839 ha. Some of the stretches experience only local and short-section erosion problems, while other stretches are exposed to severe erosion (Cat et al., 2006).

2.2 Nha Trang Bay

Nha Trang bay is located in the province of Khanh Hoa, which is situated in the south central part of Vietnam, approximately 500 kilometres northeast from Ho Chi Minh City, see Figure 2.1 and 2.3. Nha Trang bay covers 507 square kilometres and diving is a popular attraction as the bay provides an ecosystem with coral reefs, especially along the islands where the conditions are favourable (Viet, 2014). Two rivers enter the bay, Cai in the middle and Tac in the south. There are nineteen islands located in the bay, the biggest among them being the island of Hon

Figure 2.3: Satellite image of Nha Trang bay where the location of Nha Trang city is marked.

Tre (Mau, 2014, Dahlström and Böös, 2015). The bathymetry in the bay is quite complex due to the presence of the islands. The islands provide sheltered areas which have made anchoring easy and were probably the reason why Nha Trang has functioned as an important harbour for many years. There is a fishing harbour located in the Cai river entrance (INMAN and Harris, 1966, Dahlström and Böös, 2015) but also an international and bigger harbour in the south of the bay (Viet, 2014).

2.2.1 Nha Trang City

The city of Nha Trang is located in the bay and the population was in the year of 2010 estimated to be 304,200 people. The city stretches along the 16 kilometres long beach located in the bay (Figure 2.3). The beach is divided into north and south, separated by the river mouth of Cai river. The main attraction of the city is the southern sandy beach (Figure 2.4) running along Tran Phu street, which covers a length of 7 kilometres (Mau, 2014, Dahlström and Böös, 2015). In contrast, the northern beach has suffered from severe erosion and is at present lacking a beach on large stretches, only leaving the groins visible (Figure 2.5).

Before the year 2000, the region got most of their income from fishery, agricultural and forestry activities. Today the tourist brings capital to the area and plays an important role in the local economy of the region – tourism and industrial construction is making 80% of the total gross domestic in the region of Khanh Hoa (Viet, 2014, Dahlström and Böös, 2015). To meet the increasing demand, new facilities and services must be built to deliver the need of the growing interest in the region. The building industry increases and generates work when new

Figure 2.4: The sandy beach south of Cai river mouth in Nha Trang. The photo was taken at 11h04 19/05/2013.

Figure 2.5: The beach of Cai river mouth has suffered from severe erosion and today the beach is absent and only the seawall is visible. Photo taken at 16h51 24/05/2013.

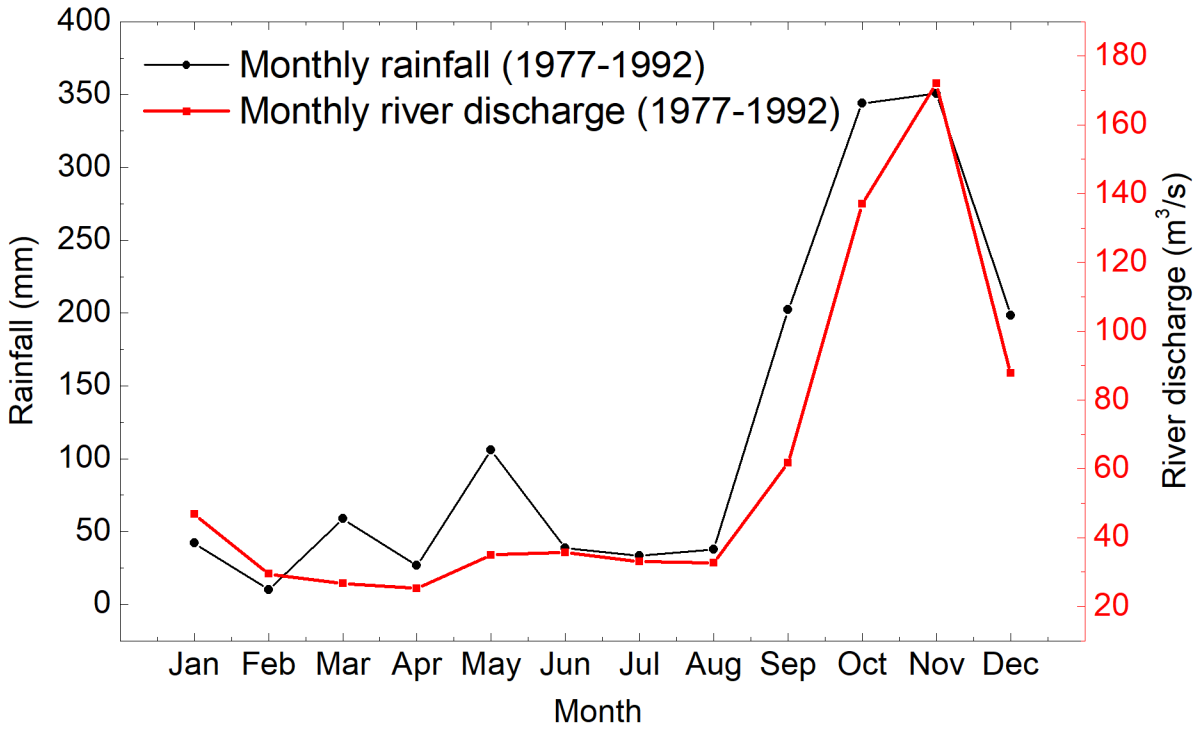

Figure 2.6: Monthly discharge (red) from Cai river and monthly rainfall (black) in Nha Trang in the years 1977-1992 (red).

roads and hotel complex are built. Most of the new constructions are located along the southern beach and Tran Phu street. This may come at the price of disrupting the beach natural cycles of evolution, which is poorly known. The recent Vietnamese and French projects for monitoring and study Nha Trang beach came in response to this problem.

2.2.2 Climatology

In Nha Trang the year is divided into two seasons, the dry season and the wet season. The precipitation is around 1,500 millimetres per year. The dry season usually occurs in the months of January until August. Between the years of 1977-1992 the mean precipitation was 8.40 millimetres in February, which makes it the driest month of the year (Figure 2.6). The months of September to December represent the wet season, with the largest precipitation appearing in November, which has a mean value of 1450 millimetres of rain during the time period 1977-1992 (Mau, 2014, Dahlström and Böös, 2015).

The large amount of rainfall leads to a higher river discharge through Cai river, which is visualized in Figure 2.6. A larger volume of water being transported in the river generates a larger force, which in turn manage to transport a greater amount of grains through the river and out to the sea (Mau, 2014, Dahlström and Böös, 2015). Large precipitation also coincides with the time of year when the northeast monsoon is taking place, i.e. in the months of October to March (Lefebvre et al., 2014), and is associated with large waves that impact coastal sediment transport.

Nha Trang is affected by two monsoons: the northeast and southwest monsoons. The north-

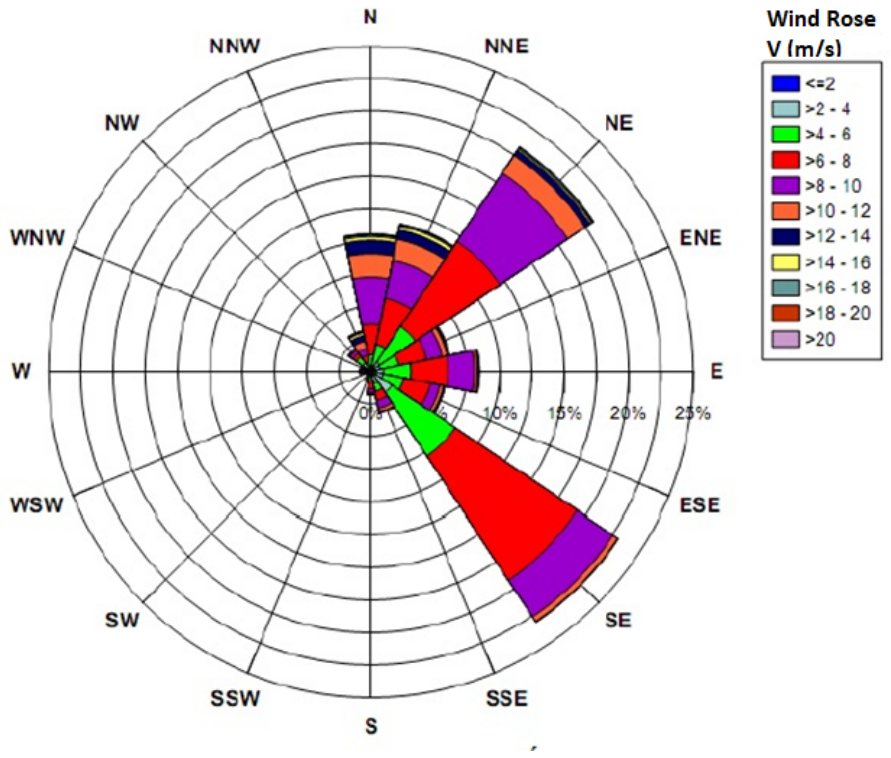

Figure 2.7: Variation of wind amplitude and direction during the years 1990-2006.

east monsoon is the strongest one and is most dominant in the months of November to January. In the years 1988 to 2007 the maximum recorded wind velocity was measured at 28 m/s in November 1988. The southwest monsoon is most dominant in the months of June to September. The maximum recorded wind velocity between the years of 1988 to 2007 was 16 m/s and occurred in September 1992 (Mau, 2014, Dahlström and Böös, 2015). Figure 2.7 show the amplitude and direction of the winds during the years 1990-2006. Weather data, i.e., precipitation and wind data, were measured at the meteorology station of Nha Trang at the latitude 12°13' and longitude 109°12'.

The temperature in Nha Trang is fairly constant throughout the year. It only varies slightly between the highest temperature of 29 degrees Celsius during the summer months of June, July and August and the lowest temperature of 24 degrees Celsius occurring during the winter months of December and January (Mau, 2014, Dahlström and Böös, 2015).

2.2.3 Wave climate and tides

Nha Trang beach is located in a semi-closed bay oriented north-south and facing the fetch limited South China Sea. A group of islands located in the southeast corner of the bay partially shelters it from short to moderate southeast wind waves during summer monsoon. During winter monsoon, however, Nha Trang bay is exposed to long, high-energy northwest swell waves (Lefebvre et al., 2014, Thuan et al., 2016). The offshore annual mean significant wave height H_s is 0.95 m, with an associated averaged peak period T_p of 6.2 s. Waves show seasonal variability: during fall and winter seasons (October to April), mean H_s is 1.2 m and T_p is 6.8 s, while during spring and summer (May to September) mean H_s is reduced to 0.6 m with a shorter T_p below

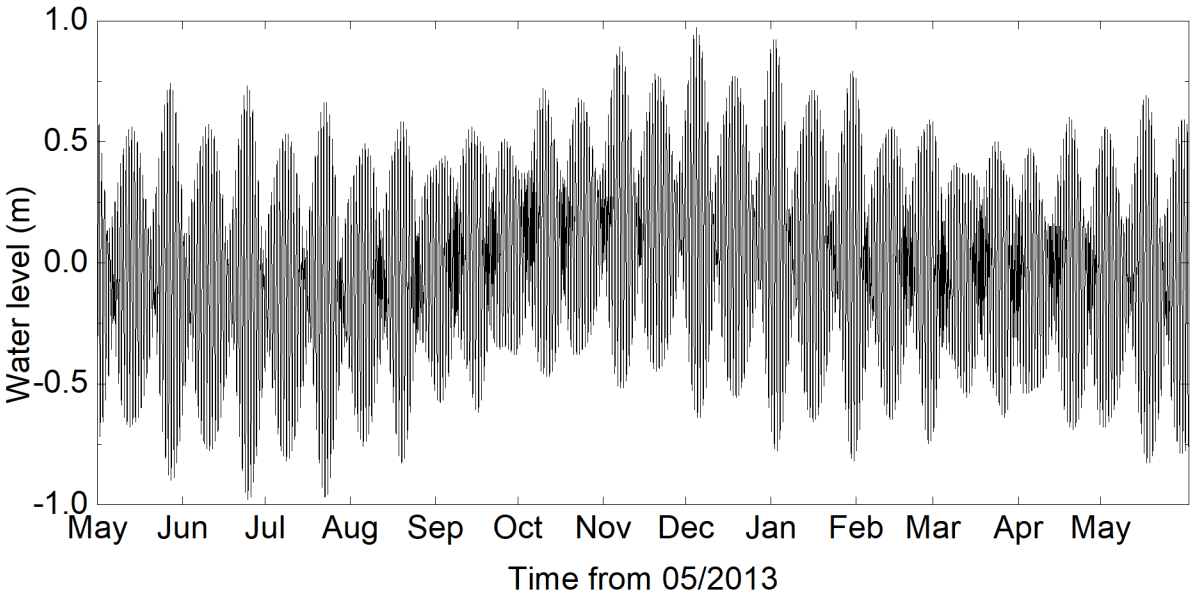

Figure 2.8: Tidal level variation in the Nha Trang bay measured at Cau Da station at Institute of Oceanography, Nha Trang.

5 s. Waves generally hit this sheltered embayed beach with near shore-normal incidence due to refraction.

Nha Trang experiences a mix of the diurnal and the semi-diurnal tide. In Nha Trang, spring tide can reach 1.7 metres and neap tide can be as low as 0.4 metres (Thuan et al., 2016). The tidal level for one year obtained at Cau Da tidal station can be seen in Figure 2.8.

To sum up, the beach is a wave-dominated mixed micro-tidal environment (Relative Tidal Range, i.e., tidal range modulated by wave height: RTR∼1).

2.2.4 Geomorphology

At the city of Nha Trang the geology is made up from granitic rock but in some areas the bedrock also consists of volcanic rock. The geology in Nha Trang and the surrounding islands in the bay differ to some extent (INMAN and Harris, 1966, Mau, 2014, Dahlström and Böös, 2015).

The main contributor to sediment in Nha Trang bay is the river Cai. It deposits sediment in the bay and forms ridges essentially made of terrigenous background. Only 2% of the material on the beach at Nha Trang is made up from biogenous material, that contains a lot of calcium carbonate like shells, corals etc. The situation is different in small sheltered bays of the islands in the bay, where the calcium carbonate content in the sediment reaches a much higher level, due to the higher distance to the river mouth (INMAN and Harris, 1966, Mau, 2014, Dahlström and Böös, 2015).

Most of the sediment discharge from the river Cai is made up of sand (Mau, 2014) and this sand is light in color and have irregular surface (INMAN and Harris, 1966, Dahlström and Böös, 2015). Sediment on the shoreface is medium sized ($D50 \sim 300$). Only a minor part of the sand is made up from darker and slightly more reddish sand. (INMAN and Harris, 1966, Mau, 2014) suggest that this is remains from previous sedimentation cycles. The city of Nha Trang is

built on old beach ridges which have coarse sand. Below this layer of approximately 10 metres, another layer of more silty sand is located. It is believed to be the remains of the beach existing prior to the modern beach of Nha Trang (INMAN and Harris, 1966, Mau, 2014, Dahlström and Böös, 2015).

The beach morphology presents some variability but remains mostly in **alongshore uniform, intermediate low-tide terrace, reflective upper beach state (Gourlay parameter $\Omega \sim$ 1.5)**. See LTT description in Chapter 1.

2.2.5 River sediment flux

In Khanh Hoa province, there are two main river systems called Cai Nha Trang river system and Cai Ninh Hoa river system. In this study, Cai Nha Trang river system is referred to as the Cai river, which is the one flowing into Nha Trang bay. The Cai river mouth is the main outlet and the Tac river mouth is a minor downstream branch of Cai river. With a catchment area of only 72km^2 compared with about 2000km^2 of the catchment area of Cai river, the impact of Tac river on Nha Trang bay can be neglected (Viet, 2014). The Cai River (also known as Cu River or Phu Loc River and upstream as Thac Ngua River) has a length of 79 km, originating from the high mountains from 1500m to 2000m high but a very short distance to the sea. The river basin has a large slope with the ability to concentrate water quickly.

The flow of rivers in Khanh Hoa province is correlated with precipitation. Therefore, the sharp seasonal difference in rainfall during dry and rainy seasons reflects on the Cai River flow. Variations are not only seasonal but also very different from year to year. Water discharge during the three months of the flood season from October to December accounts for 65% of the total water discharge in the year. For example, according to reports by Viet (2014), based on monitoring data from 1992 to 2000 at Dong Trang hydrological station, the average water transport in the rainiest year can be as high as 156m^3/s, while the driest year has only 30m^3/s.

Based on the study by (Viet, 2014), the average annual turbidity of Cai river is about 6g/m^3 and the average suspended sediment transport of Cai river is about 8kg/s. Therefore, the amount of sand that can flow into the bay is about 0.25MTons/year or about 160,000 cubic-metres of sediment per year. This value is close to that of 195,000 cubic-metres of sediment per year given in Dahlström and Böös (2015), and the difference reflects the uncertainty in these estimations.

2.2.6 Sediment transport in the bay

The flow and sediment transport are mostly dependent on the wave and current climates inside the bay. The wave and current climates are in turn affected by the local winds, the monsoons and the bathymetry of the bay (Mau, 2014).

The flow from Cai varies considerably due to the uneven occurrence of precipitation. As the sediment is transported by the water, the amount of sediment reaching the bay varies with the precipitation. The sediments reaching the bay settle in part inside the bay while some, normally finer particles, are transported seaward or further south down the coast and are deposited in for example Cam Ranh, a city about 40 kilometres from Nha Trang. When there is little or low wind speed (especially in summer), the freshwater from the river remains on top of the seawater due to the difference in density. Thus the sediment has lower tendency to settle and the beach

will have less nourishing of sand (INMAN and Harris, 1966, Mau, 2014, Dahlström and Böös, 2015).

As seen in Chapter 1, waves are an important player for sediment transport (resuspension and nearshore transport). High-energy northeast winter monsoon waves can resuspend heavier sediment and promote their transport by tides or wind-driven currents. Nearshore transports (cross-shore and alongshore) are also at their maximum in winter. The islands in the area play a substantial role in causing waves to reflect and diffract along their contours, especially in summer.

The tides present in the bay can also transport sediment in the cross-shore direction. Even when the amount of water flowing towards the coast during rising tides equals that flowing off the coast during falling tide, a net onshore sediment transport is explained by a number of asymmetries in the water movement (tidal asymmetry) and sediment behavior.

Onshore winds can also participate in coastal sediment accretion. Ekman drift is a process that tends to carry water to the right of the wind (less so in shallow water). During winter, northeastern monsoon winds thus provide some ways of accumulating sediments to shore. We expect that tidal and wind-driven currents can mostly transport very fine material – particularly that coming from the river –, although wind-driven currents may explain the relatively deep 24 m channel between Hon Tre island and the mainland (INMAN and Harris, 1966, Mau, 2014, Dahlström and Böös, 2015). Here, we assume little impact from these currents on the evolution of the beach. High-resolution modeling of the bay would give us more certainty.

2.2.7 Coastal protection Measures

Waves and sediment transport in the bay are affected by constructions along the shore as well as constructions built upstream of the river Cai. Along the shoreline of Nha Trang city, many protections such as seawalls, piers and harbours, were built during the last two decades, some of which can be seen in Figure 2.9.

At the abutment of Cau Tran Phu bridge (at the mouth of Cai river), built in 1999 to 2002, approximately 450 metres of hard concrete surfaces surrounds the Alexandre Yersin Park and continues around the restaurant Nha Trang View cafe (Figure 2.10, 2.11 and 2.12). The concrete surfaces were built after 2009 when the sand spit at the river mouth started to erode. South of the cafe there are also two jetties made of tetrapods, constructed during the years 1990-1992, protecting the structure (Figure 2.13; Viet (2014)).

To the south, a vertical seawall stretches for approximately 2,000 metres along the beach from the Nha Trang View restaurant to the structure Hoa Bien. The seawall was initially made of steel but in the years between 1996 to 1999 a concrete construction was made. In front of the vertical seawall nearby Nha Trang View restaurant a lower concrete seawall sloping seawards was constructed in 1999.

Near the south end of the bay, the Vinpearl ferry terminal was built in 2003 and served as a ferry terminal to transport people to the island Hon Tre. It is a L-shaped groin, with a 60 metres long cross-shore pier and a 50 metres wide arm attached to it (Figure 2.14). It only served as a terminal for a few years, until the cable car to Vinpearl Island was built north of Tac river mouth and used in 2007. Approximately 600 metres further down the coastline of the

Figure 2.9: Location of some of the constructions along the shoreline of Nha Trang beach (Google Earth Pro).

Figure 2.10: Concrete constructions around the northern section of Yersin Park at the river mouth of Cai river. From Google Earth Pro.

Figure 2.11: The groins are visible on the east stretch of Yersin Park. Photo taken by drone at 11:36 AM 24/12/2016.

Figure 2.12: The seawall and the groins at the beach south of Nha Trang View restaurant. Photo taken at 11h14 12/03/2015.

Figure 2.13: Two jetties made from tetrapods at the south of Nha Trang View restaurant. Photo taken at 09h22 06/12/2015.

Figure 2.14: A part of the vertical and sloping seawall along the stretch between Nha Trang View restaurant and the structure Hoa Bien.

Vinpearl ferry terminal lies the Army port. It was built by the US Army in 1965-1966 and was further extended in later years. It was originally 80 metres long across-shore, but then extended 100 metres further out into the sea. Nowadays, the pier is used by the Naval Academy.

Dredging has been done in Nha Trang bay. Both in the channel of the Army port and in the Tac river mouth, but also when building hotel and resort complexes on the islands in the bay. Since the year 2000 approximately 2 million cubic metres of dredging material were removed and dumped outside the bay at the sea (Viet, 2014).

Figure 2.15: Vinpearl ferry terminal. Photo taken at 12h48 03/12/2015.

Chapter 3

Coastal video monitoring technique

Contents

The shore-based camera system in Nha Trang is exactly the same as the ARGUS system (Holman and Stanley, 2007) that has existed for more than 30 years. The methods of shorelines detection or nearshore depth inversion are also quite similar to that used in many other studies (Aarninkhof et al., 2003, Almar et al., 2012b, Bos, 2006, Almar et al., 2008). However, the system developed for Vietnam as part of a collaboration between IRD and TLU is open source and freely available, contrary to ARGUS. For this reason, the present system is fully adapted to developing countries such as Vietnam and can be used for coastal research, engineering or management. This section will detail the camera system installed in May 2013 in Nha Trang, and also the methods applied to the system, with their specific application to Vietnam.

3.1 Video monitoring station

On May 23rd, 2013, during the NT1 field experiment under the MOST1 research project, a system consisting of 2 color cameras with a resolution of 2Megapixel was installed on a public light pole on the walkway at about 15 m height, and connected to a PC on site in the local post office (Figure 3.1). One camera facing North was named NNT and the other facing South was named SNT. They are Internet Protocol (IP) cameras of Vivotek Inc. (IP7361) with the highest resolution of 1600×1200 pixels. Studies for ARGUS systems (e.g., SIRENA - Nieto

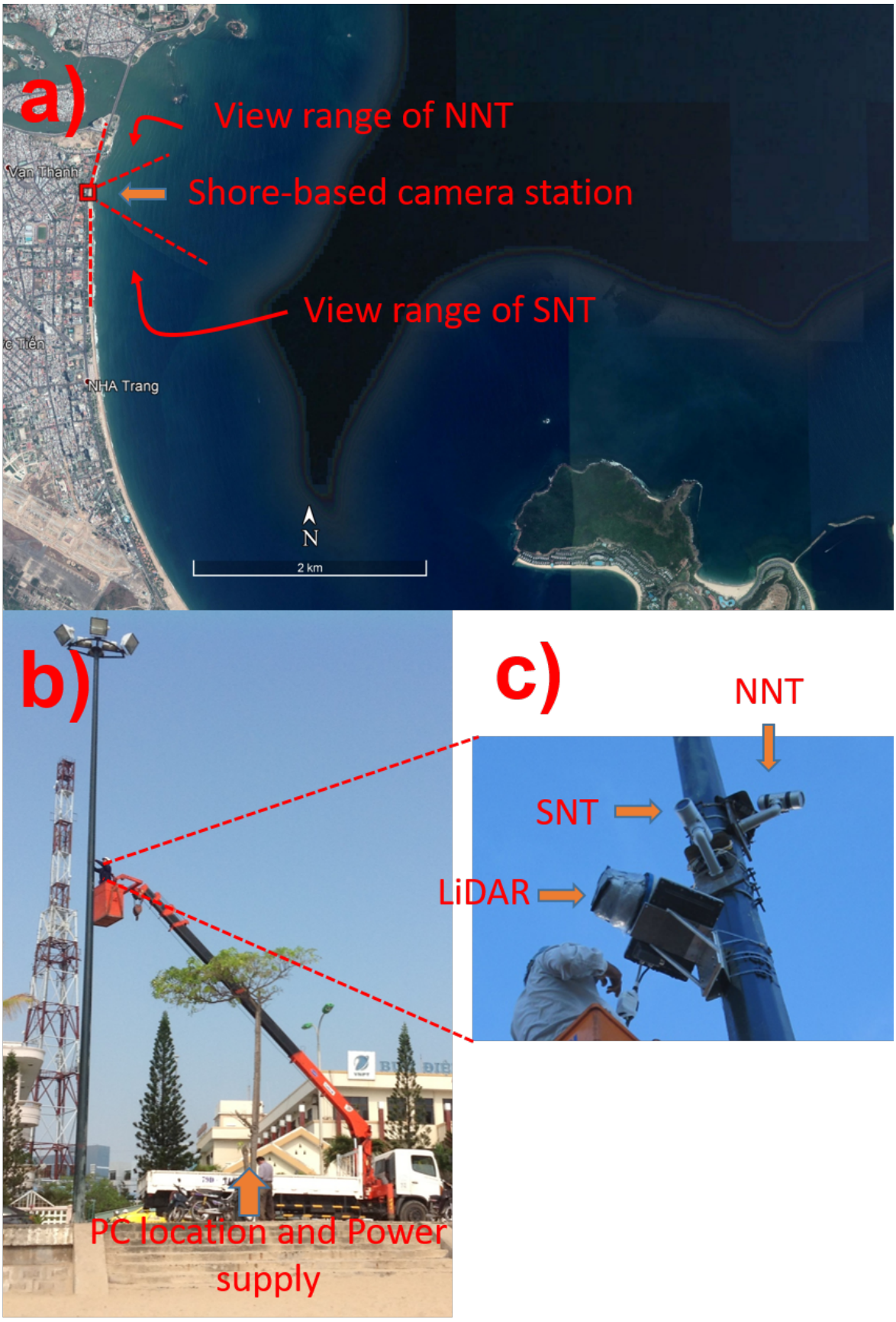

Figure 3.1: a) Camera system position on Google map indicating monitoring range. b) Public light pole structure holding the cameras and c) Zoom on the two cameras named NNT and SNT pointing respectively North and South. The cameras are located at a height above mean sea level of 14.80 m for NNT and 14.03 m for SNT

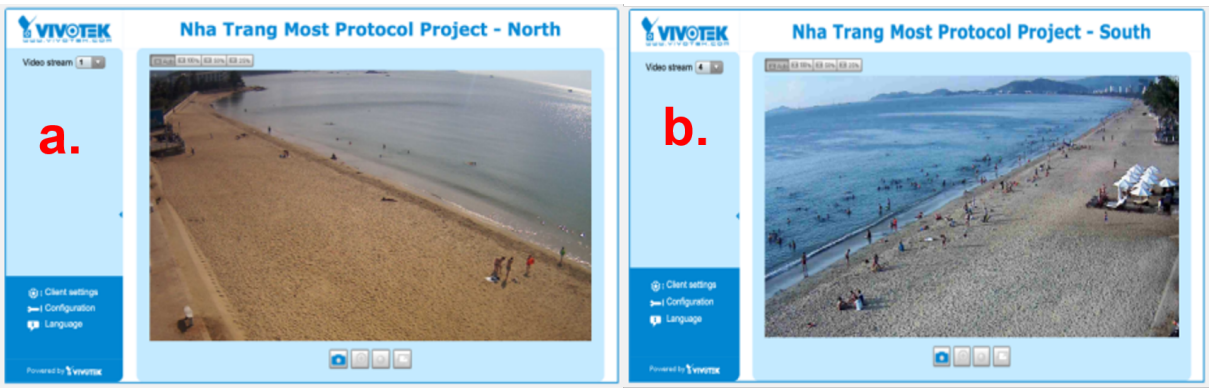

Figure 3.2: The web interface is used to access images of two cameras online a) For NNT camera and b) for SNT camera

et al. (2010); COSMOS - Taborda and Silva, 2012) show that Internet Protocol (IP) camera lines are one of the affordable options for research compared to expensive dedicated camera lines. The IP camera line has the advantage of being a universal camera so it's easy to replace or repair. In addition to the ability to communicate over the internet or local line it can be easily connected to transmit data on a PC where it can be stored easily. The IP7361, Vivotek's relatively inexpensive outdoor surveillance camera line, with excellent moisture resistance (IP61) (Vivotek User's Manual IP7361), is adapted to coastal monitoring because electronic devices are sensitive to oxidation. The camera supports memory cards in micro SD up to 64Gb, allowing comfortable storage. For short-term studies, the data can be extracted directly from the memory card and no connection is needed.

The cameras are powered by the post office across the street. The power of the post office is generally stable 24/7 because it has its own generator. Each camera is assigned a static IP address as follows: NNT camera is http://113.252.160.107 and SNT camera is http://113.252.160.106. The network and power supplies are located in the post office's security office and are easily accessible for inspection or repair. From there it is easy to access the cameras via the internet to check its performance 24/7, ensuring data integrity. For example, in Figure 3.2, a web interface is used to access images of the two cameras online. This interface can be used to set all the features and operation schedule of the cameras.

Although the IP7361 camera is capable of recording 1600×1200 pixels at 10Hz (10 frames per second), to minimize the cost of storing data, the frame of NNT camera was cropped to 1456x840 pixels and SNT frame to 1504×784 pixels (i.e., removing sky and inland areas). Both cameras are set to MPEG compression mode, with a 2Hz recording rate (2 frames per second). One minute of video is stored in one file, and a specific hour folder will contain 60 files. Hour folders are sorted in date directories. Organizing such data simplifies the archiving process. The initial video files are recorded directly to the Sandisk microSD card 64Gb, then sent by internet. The camera is connected to the server located in ThuyLoi University using FileZilla Client free software. Raw video files are then backed up to 2Tb-4Tb external hard drive before processing, i.e., extracting frames, creating average images (time-exposure image), or creating time-stack images. This means that raw video files are stored and can used again with more advanced data processing expected in the future (e.g., data assimilation in numerical models).

Both cameras are set to record only during daytime, specifically from 5:30 am to 6:30 pm. When the memory card is full, it automatically erases the oldest data. A 64Gb memory card can hold up to 6 days. With high speed internet access, downloading one day of data requires 2 hours, and data is downloaded every 3 days. This semi-manual protocol has the advantage that the cameras are often checked. In some cases, the camera may well show images on the web browser, but due to a problem with the internal memory card they may not be recorded. To ensure continuity, the data was checked every day at around 7-8 am. The test is carried out quickly, and if problem a remote reboot of the cameras would solve it.

However, that is just the simplest problem encountered with this camera system. A more serious problem affecting data is the instability of electrical equipment. Due to the inherent quality of the AC-DC converter, it is often used outdoors (for proximity to the cameras). Unfortunately, on July 26, 2014, after more than a year of operation (starting in May 25, 2013), the whole system was struck by lightning. After checking and replacing, only the NNT camera could operate, and SNT data is only available from 25 May 2013 to 26 July 2014 for a total of 388 days of data. The remaining NNT camera operated until August 27, 2016 with 939 days of data. Then the camera was inoperative and no funds were available for replacement.

3.2 Image processing

The downloaded video files at the ThuyLoi University server are processed to create image files containing instant images (frame), average images (timex) and timestack images. These is discussed in detail below.

3.2.1 Secondary images

Instant image

These instant frames are saved as a quality check, in case of dust, fog, sun glint in the images as shown in Figure 3.3 for a video file of SNT camera at 12h on July 1, 2013. As seen in Figure 3.3a a video file is extracted into frames. Since the video files are recorded at 2Hz and each file contains one minute of video data, each video file contains 120 frames (60 sec $\times$ 2Hz). An exact time is thus given for each frame and the time lag between measurements can be checked, as the camera timer do not coincide with the real time.

TIMEX or average image

TIMe-EXposure images (Timex, Figure 3.3b) or average images are created by the mathematical average of individual frames collected over a pre-selected sampling period (Holman and Stanley, 2007). In this study, this period was chosen to be 15 minutes.

Taking an average of 15 minutes of pixel intensity in the average image file will smooth out the moving objects (i.e., waves) during that time and stress out the repetitive phenomena that appear on the frame. This leads to the phenomenon of enhancing the white bright intensity pattern in the breaking zone on the Timex image, so that one of the first applications of the

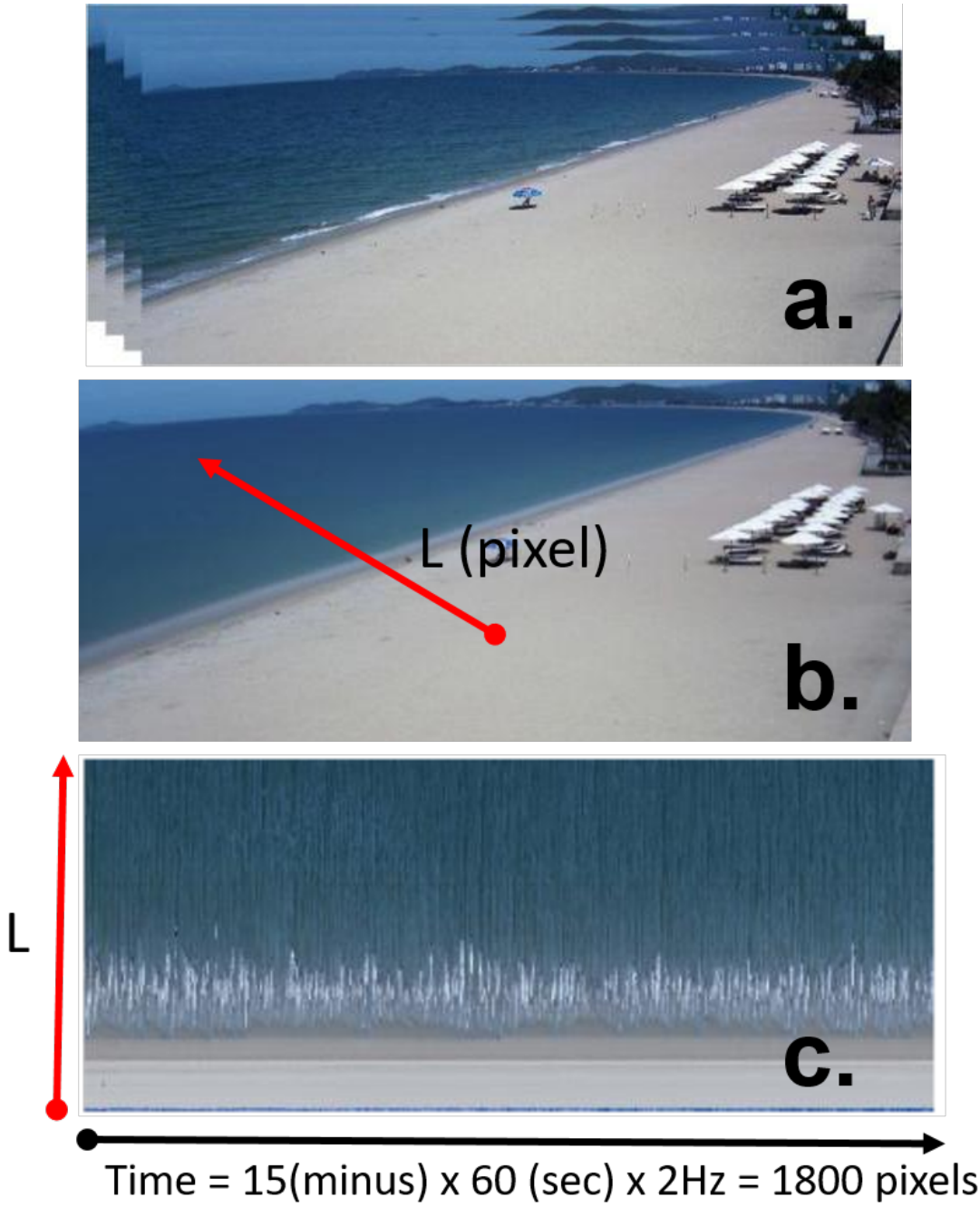

Figure 3.3: An example of video files processed into image files commonly used from shore-based camera systems. a) Extraction of video file into frames, one for each instant image. b) TIMe-Exposure images (or average images) are created by taking the average of all frames at step a) for the given time period, e.g., 15 minutes in this case. The red arrow line is the cross-sectional location for creating the timestack image. c) The timestack image is created with a period of 15 minutes, with the horizontal axis being the time and the vertical axis being the section location in b).

TIMEX images is to determine the breaking zone (Lippmann and Holman, 1989). It can be indicative of nearshore submerged sand bars as waves often break at the bar crest, and Timex images are often used to study the morphodynamics of submerged sandbars (**??**) including with numerical models (Marchesiello et al., 2015).

At the same time, the swash movements on the foreshore slope are filtered. For this reason, Timex have been also widely used for shoreline detection (e.g., Aarninkhof et al. (2003), Almar et al. (2012b)) and for a long-term monitoring of shoreline evolution (e.g., Pianca et al. 2015, Angnuureng et al. 2017, Abessolo Ondoa et al. 2016, 2017a). However, shoreline detection on Timex was often observed as being affected by beach saturation color and can lead to a wrong shoreline position, e.g., on a low terrace and/or during low tide conditions (Huisman et al., 2011).

For the shore-based camera system installed in Nha Trang, in the initial design, the shoreline was extracted from TIMEX images according to the method proposed by Almar et al. (2012b) and will be discussed in detail in Section 3.3. In addition to this technique, the shoreline can also be extracted from the timestack images, which will be presented in Section 3.3.

Timestack image

A timestack image is generated by collecting all pixels along a fixed line on the frame. Each frame provides a column of pixels on the timestack image, so that when arranged sequentially in chronological order (frame order) a two-dimensional timestack image is formed corresponding to the axis of time and location. In Figure 3.3c, a timestak image is generated by taking all pixels along the red line for a period of 15 minutes. Therefore, one dimension of timestack image must contain 15(min)×60(sec)×2Hz = 1800 pixels and the second must be equal to L pixels (length of the transect). In general, the duration time for creating the timestack image plays an important role because if it is too large, the image file is excessive, leading to a time consuming process and often overflows memory. Meanwhile, if the time is too small, statistical significance is lost when calculating wave bulk informations (i.e., due to groups and infragravity waves). So the reasonable duration time for creating a timestack image is usually about 10-20 min. In this study, the timestack was created at the same time as Timex for a 15 min time frame, meaning that the video recording continuously for 1 hour produces 4 timestack images.

Since its introduction in 1989 (Aagaard and Holm, 1989), timestack images have been widely used in numerous studies of nearshore hydrodynamics and morphology, e.g., for the study of wave runup (Holman et al., 1993, Stockdon et al., 2006, 2014), wave period (Lippmann and Holman, 1989, Almar, 2009), wave spectrum (Zikra, 2012). Further reading can be found in Holman and Stanley (2007) or references listed in Andriolo (2018).

In the present study, timestack images are used to determine:

- wave period Tp, following Almar (2009),
- wave breaking height Hb, following Almar et al. (2012a),
- shoreline position by runup averaging,

- wave celerity, from which nearshore bathymetry is inverted using the linear wave dispersion relation.

The method of shoreline detection is detailed in Section 3.3 and the method of nearshore bathymetry inversion in Section 3.6.

In addition to the three types of secondary images mentioned above, a popular secondary image type in shore-based camera community is variance image, created by calculating the standard deviation of each image over a sampling period (Holman and Stanley, 2007). This type of image usually enhances wave breaking and swash regions because these areas are very variable. However, the camera system in Nha Trang was not design to produce that type of image, and it will not be discussed further. For more information refer to Holman and Stanley (2007).

3.2.2 Camera calibration

In order to exploit the images acquired by a coastal video-system for quantitative studies, an accurate procedure must be applied to the raw video data to obtain geo-referenced images (e.g., Hartley and Zisserman (2003)). This section describes the necessary steps to obtain geo-referenced images from coastal video-monitoring systems.

Camera calibration is the process that estimates the georeferencing parameters in order to transform the physical coordinates of objects into the coordinates of the image and vice versa. The set of georeference parameters, usually divided into two groups: a first group called intrinsic parameters, including focal length f, image center coordinates (u_C, v_C), and/or radial and tangential distortion coefficients k_j; and the second group called extrinsic orientation parameters consisting of 6 parameters including 3 camera optical center coordinates (X_C, Y_C, Z_C) and 3 camera rotation angles (azimuth α, tilt τ, roll θ).

There are many suitable calibration methods such as computer vision (Hartley and Zisserman, 2003), photogrammetry (Kraus, 2011), or close range photogrammetry (Luhmann et al., 2007). Specifically for shore-based video camera systems (Holman and Stanley, 2007), the calibration process proposed by Holland et al. (1997) is widely accepted and used. It is derived from a pinhole camera model with the direct linear transformation (DLT) approach proposed by Abdel-Aziz and Karara (1971), as shown in Figure 3.4. From the collinearity condition, the object point $\mathrm{O}(X_O, Y_O, Z_O)$ and its projection on the image frame (u_O, v_O) and the camera optical center (X_C, Y_C, Z_C) must be on a single straight line. Considering the object-space reference frame (the XYZ-reference system), we have the following collinearity equations:

$$\begin{bmatrix} u_O - u_C \\ v_O - v_C \\ -f \end{bmatrix} = b \begin{bmatrix} r_{11} & r_{12} & r_{13} \\ r_{21} & r_{22} & r_{23} \\ r_{31} & r_{32} & r_{33} \end{bmatrix} \begin{bmatrix} X_O - X_C \\ Y_O - Y_C \\ Z_O - Z_C \end{bmatrix} \tag{3.1}$$

or

$$\begin{aligned} u_O - u_C &= b\,[r_{11}(X_O - X_C) + r_{12}(Y_O - Y_C) + r_{13}(Z_O - Z_C)] \\ v_O - v_C &= b\,[r_{21}(X_O - X_C) + r_{22}(Y_O - Y_C) + r_{23}(Z_O - Z_C)] \\ -f &= b\,[r_{31}(X_O - X_C) + r_{32}(Y_O - Y_C) + r_{33}(Z_O - Z_C)] \end{aligned} \tag{3.2}$$

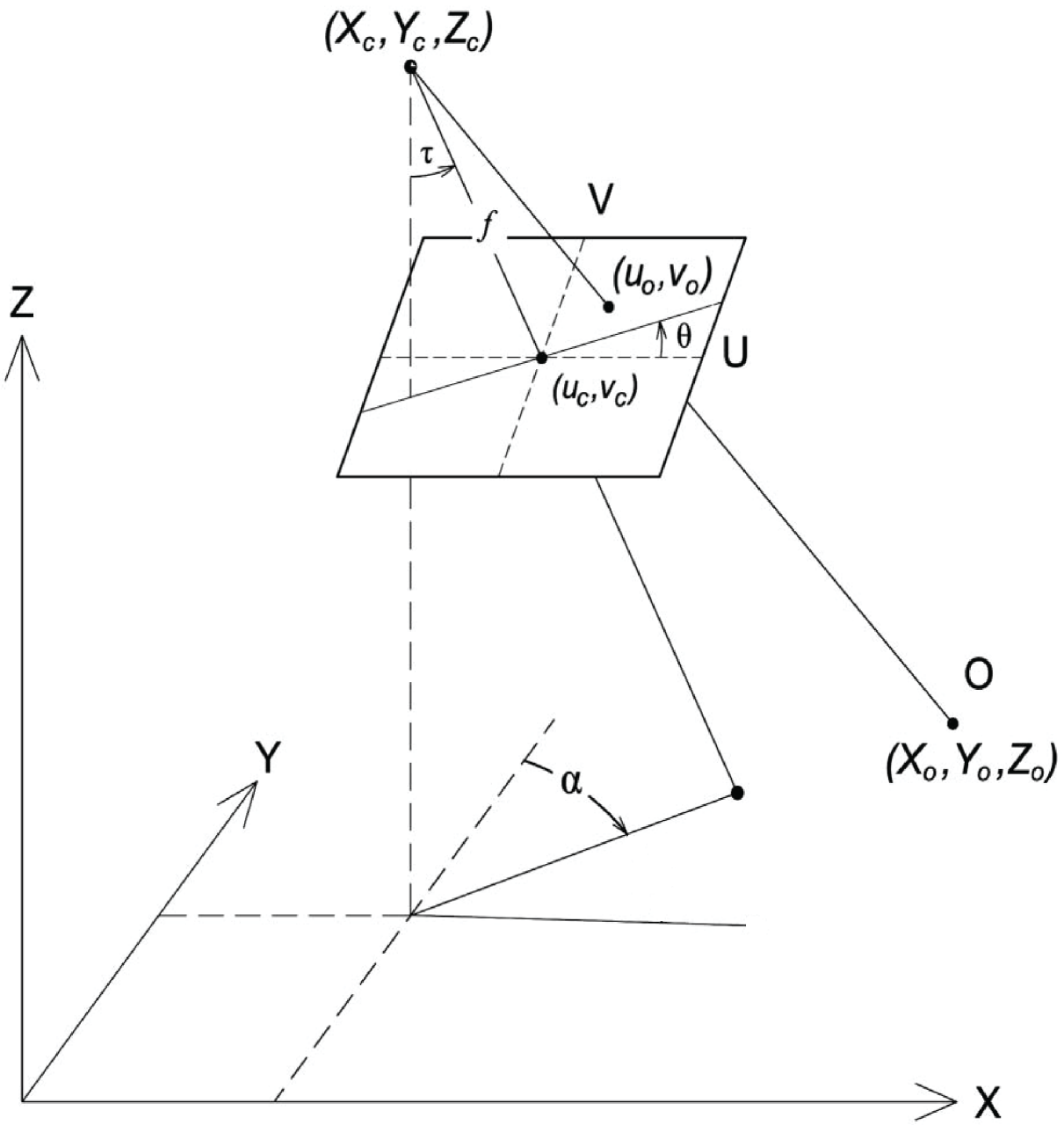

Figure 3.4: Pinhole camera model demonstrating the collinearity relationship between the object (X_O, Y_O, Z_O), the image point (u_O, v_O), the camera optical center (X_C, Y_C, Z_C) and camera rotation angles (azimuth α; tilt τ and roll θ). Adapted from Bechle et al. (2011).

Where, b is a scaling coefficient, the coordinates (u_O, v_O), (X_O, Y_O, Z_O), (X_C, Y_C, Z_C), and (u_C, v_C) are explained in Figure 3.4, r_{ij} are elements of the transformation matrix to convert the object-space reference frame to the image-plane reference frame:

$$\begin{aligned}\mathbf{R} &= \begin{bmatrix} r_{11} & r_{12} & r_{13} \\ r_{21} & r_{22} & r_{23} \\ r_{31} & r_{32} & r_{33} \end{bmatrix} \\ &= \begin{bmatrix} \cos(\alpha) & \sin(\alpha) & 0 \\ \sin(\alpha) & \cos(\alpha) & 0 \\ 0 & 0 & 1 \end{bmatrix} \begin{bmatrix} 1 & 0 & 0 \\ 0 & \cos(\alpha) & -\sin(\alpha) \\ 0 & \sin(\alpha) & \cos(\alpha) \end{bmatrix} \begin{bmatrix} -\cos(\alpha) & -\sin(\alpha) & 0 \\ -\sin(\alpha) & \cos(\alpha) & 0 \\ 0 & 0 & 1 \end{bmatrix}\end{aligned} \tag{3.3}$$

From the third equation in the equation system 3.2, we obtain:

$$a = \frac{-f}{r_{31}(X_O - X_C) + r_{32}(Y_O - Y_C) + r_{33}(Z_O - Z_C)} \tag{3.4}$$

Substituting Equation 3.4 for a in the equation system 3.3:

$$\begin{aligned} u_O - u_C &= -f \frac{r_{11}(X_O - X_C) + r_{12}(Y_O - Y_C) + r_{13}(Z_O - Z_C)}{r_{31}(X_O - X_C) + r_{32}(Y_O - Y_C) + r_{33}(Z_O - Z_C)} \\ v_O - v_C &= -f \frac{r_{21}(X_O - X_C) + r_{22}(Y_O - Y_C) + r_{23}(Z_O - Z_C)}{r_{31}(X_O - X_C) + r_{32}(Y_O - Y_C) + r_{33}(Z_O - Z_C)} \end{aligned} \tag{3.5}$$

Remember that both (u_O, v_O) and (u_C, v_C) are in the real reference (object reference) so they will have the same units as (X_O, Y_O, Z_O). Thus, it may be in millimeters (mm), while in fact, (u_O, v_O) and (u_C, v_C) are usually in pixel units. Introducing two unit conversion factors λ_U and λ_V corresponding to the axes U and V, the left hand size of Equation 3.5 can be rewritten:

$$\begin{aligned} u_O - u_C &\Rightarrow \lambda_U (u_O - u_C) \\ v_O - v_C &\Rightarrow \lambda_V (v_O - v_C) \end{aligned} \tag{3.6}$$

Then Equation 3.5 is written as follows:

$$\begin{aligned} u_O - u_C &= -\frac{f}{\lambda_U} \frac{r_{11}(X_O - X_C) + r_{12}(Y_O - Y_C) + r_{13}(Z_O - Z_C)}{r_{31}(X_O - X_C) + r_{32}(Y_O - Y_C) + r_{33}(Z_O - Z_C)} \\ v_O - v_C &= -\frac{f}{\lambda_V} \frac{r_{21}(X_O - X_C) + r_{22}(Y_O - Y_C) + r_{23}(Z_O - Z_C)}{r_{31}(X_O - X_C) + r_{32}(Y_O - Y_C) + r_{33}(Z_O - Z_C)} \end{aligned} \tag{3.7}$$

Here, it is important to emphasize that the coordinates (u_O, v_O) and (u_C, v_C) in Equation 3.7, although denoted similarly to Equation 3.5, are given by pixel units. Also note that the two unit conversion factors λ_U and λ_V in Equation 3.7 can be different from each other. Usually, they are calculated based on the camera sensor specifications provided by the manufacturer. Actually, their precise values are not necessary, because they are linearly dependent on the effective focal length f and the scale factor S_u (Heikkila and Silven, 1997). For instance, with the Vivotek camera IP7361 used in this study, according to the manufacturer's specifications (Vivotek User's Manual IP7361), the camera has a 1/3.2inch CMOS sensor, which means that the sensor size is 4.54×3.42 mm, in 1600×1200 pixels resolution. Thus, the conversion factors

can be calculated by the formula:

$$\begin{aligned} \lambda_U &= \frac{4.54}{1600}(\text{mm/pixel}) \\ \lambda_V &= \frac{3.42}{1600}(\text{mm/pixel}) \end{aligned} \tag{3.8}$$

Rearranging Equations 3.7 for X_O, Y_O, and Z_O:

$$\begin{aligned} u_O &= \frac{L_1 X_O + L_2 Y_O + L_3 Z_O + L_4}{L_9 X_O + L_{10} Y_O + L_{11} Z_O + 1} \\ v_O &= \frac{L_5 X_O + L_6 Y_O + L_7 Z_O + L_8}{L_9 X_O + L_{10} Y_O + L_{11} Z_O + 1} \end{aligned} \tag{3.9}$$

where,

$$\begin{aligned} [f_U, f_V] &= \left[\frac{f}{\lambda_U}, \frac{f}{\lambda_V}\right] \\ L &= -\left(X_C r_{31} + Y_C r_{32} + Z_C r_{33}\right) \\ L_1 &= \frac{u_C r_{31} - f_U r_{11}}{L} \\ L_2 &= \frac{u_C r_{32} - f_U r_{12}}{L} \\ L_3 &= \frac{u_C r_{33} - f_U r_{13}}{L} \\ L_4 &= \frac{(f_U r_{11} - u_C r_{31}) X_C + (f_U r_{12} - u_C r_{32}) Y_C + (f_U r_{13} - u_C r_{33}) Z_C}{L} \\ L_5 &= \frac{v_C r_{31} - f_V r_{21}}{L} \\ L_6 &= \frac{v_C r_{32} - f_V r_{22}}{L} \\ L_7 &= \frac{v_C r_{33} - f_V r_{23}}{L} \\ L_8 &= \frac{(f_V r_{21} - v_C r_{31}) X_C + (f_V r_{22} - v_C r_{32}) Y_C + (f_V r_{23} - v_C r_{33}) Z_C}{L} \\ L_9 &= \frac{r_{31}}{L} \\ L_{10} &= \frac{r_{32}}{L} \\ L_{11} &= \frac{r_{33}}{L} \end{aligned} \tag{3.10}$$

Distortion in Camera Calibration

The camera matrix does not account for lens distortion because an ideal pinhole camera does not have a lens. To accurately represent a real camera, the camera model includes the radial and tangential lens distortion.

Radial Distortion

Radial distortion occurs when light rays bend more near the edges of a lens than they do at its optical center. The smaller is the lens, the greater the distortion. IP security cameras such as the Vivotek camera used in Nha Trang have large distortion.

Determination of camera internal parameters is necessary to correct the image distortion inducted by the lens curvature. Recall that internal parameters are the focal length f, the position of the image center (u_C, v_C), radial and tangential distortion coefficients k_j. Focal length is defined as the distance from the center of the lens to the focal points of the lens. It is a measure of how strongly the optical sensor converges or diverges light. It is usually specified in millimetres (mm) and is inversely proportional to the field of view of a lens. The position of the image center coincides around the center of the image in pixels. Finally, the distortion coefficients quantify the deformation that might be inducted on the image by the lens curvature.

In this work, a freely available Camera Calibration Toolbox for Matlab (Heikkila and Silven, 1997, Bouguet, 2015) is used to perform camera calibration. The toolbox guides the user through the camera calibration process step-by-step to determine the camera intrinsic parameters. Two

Figure 3.5: Camera calibration results of NNT camera, applying field calibrations using 59 in situ GCPs. The actual pixel coordinates (open red circle) of the object are determined manually. The pixel coordinates (red cross) were projected using georeference calibration parameters in Table 3.1.

methods for computing camera intrinsic distorsion parameters are tested:

- Using chessboard method with regular grid to compute parameters,
- Using Ground Control Points measured with a differential GPS and computing distortion with an iterative method to minimize error.

Parameter ( ) [unit]	Value
Scale factor S_u [ ]	1.048499
Effective focal length (f) [mm]	3.8849
Principal point (u_C; v_C) [pixel,pixel]	835.588634 ; 446.812486
Radial distortion (k_1; k_2) [mm^{-2},mm^{-4}]	-2.655717 $\times 10^{-02}$; 7.587641 $\times$ 10^{-04}
Tangential distortion (k_3, k_4) [mm^{-1},mm^{-1}]	7.021100 $\times 10^{-03}$; -8.489986 $\times 10^{-05}$
Camera optical center (X_C; Y_C; Z_C) [m,m,m]	0 ; 0 ; 14.799
camera rotation angles (α ; τ ; θ) [deg,deg,deg]	114.2744 ; -32.5015 ; -13.0875

Table 3.1: Georeference calibration parameters for NNT camera.

3.3 Shoreline position

In this section, the method used to determine the shoreline location for the shore-based camera system installed in Nha Trang. It is based on timex images. We also tried another method based on timestack images to determine the shoreline position at a fixed transect, but we will not describe it here, as the first one was suited to Nha Trang beach and successful.

The shoreline determined from timex images can be constructed from the inter-tidal bathymetry (Aarninkhof et al., 2003). Comparison between the 3D inter-tidal bathymetry obtained from the Timex image with in-situ measurements conducted by theodolite or DGPS can be considered as an evaluation of the method chosen for shoreline detection. Therefore, this comparison is given in Section 4.2, and can be found in publications of the COASTVAR group such as Duc et al. (2014a), Viet et al. (2014), Thuan et al. (2016). An analysis of the shoreline evolution obtained from timex images is also given in Chapter 5, or can be found in Thuan et al. (2016), Almar et al. (2017), Thanh et al. (2018).

Despite its common usage, the shoreline has been given several definitions based on different approaches: physical, geological, biological, or coastal engineering. Boak and Turner (2005) describe a wide variety of shoreline definitions. Depending on the definition, the shoreline position can vary up to hundreds of meters. The choice of the period over which the waterline is averaged to determine the shoreline will also cause some differences between shoreline definitions.

Here, it is derived from optical variables (Aarninkhof et al., 2003) as the interface between water and beach in timex images, the shoreline is determined following the two-step method of Almar et al. (2012b) as follows:

- First, a region of interest (ROI) defined in the Timex images must cover both wet and dry pixels (Figure 3.6a). A histogram is generated by the Red:Green ratio of the pixels in ROI with bin size = 7 pixels. The histogram generally shows a bimodal distribution (Figure 3.6b) where the lower and higher R:G peaks are expected to be associated with water and beach, respectively.

- After that, the local minimum, i.e., the transition zone between the two peaks, is calculated. It is the refined shoreline as represented by the red dot line in Figure 3.6c.

Compared to other methods using timex images to define shorelines, such as Shoreline Intensity Maximum (SLIM) (Plant and Holman, 1997), or Channel Color Divergence (CDD) (Turner et al., 2001), the Minimum Shoreline Variation (MSV) method (Almar et al., 2012b) is stable and suitable for Nha Trang beach, which is characterized by steep slopes, including in the low tide area which is generally the most challenging, and large seasonal variation, from summer to winter monsoon, with sudden reshaping typhoons. This is discussed in the next Chapters where the application of the method is compared to ground truth.

3.4 Wave breaking height

In addition to being used to determine celerity and invert nearshore bathymetry (next section), the timestack image is also used to determine wave height at the breaking point Hb at wave by wave scale. Because wave breaking height Hb is one of the key parameters for nearshore hydrodynamics and longshore sediment transport, a number of researchers have attempted to identify Hb from shore-based camera systems (Hilmer, 2005, Kim et al., 2008, Gal et al., 2014, Robertson et al., 2014).

In this study, Hb is determined from timestack images according to the method proposed by Almar et al. (2012a). This section briefly introduces the method and its step by step appli-

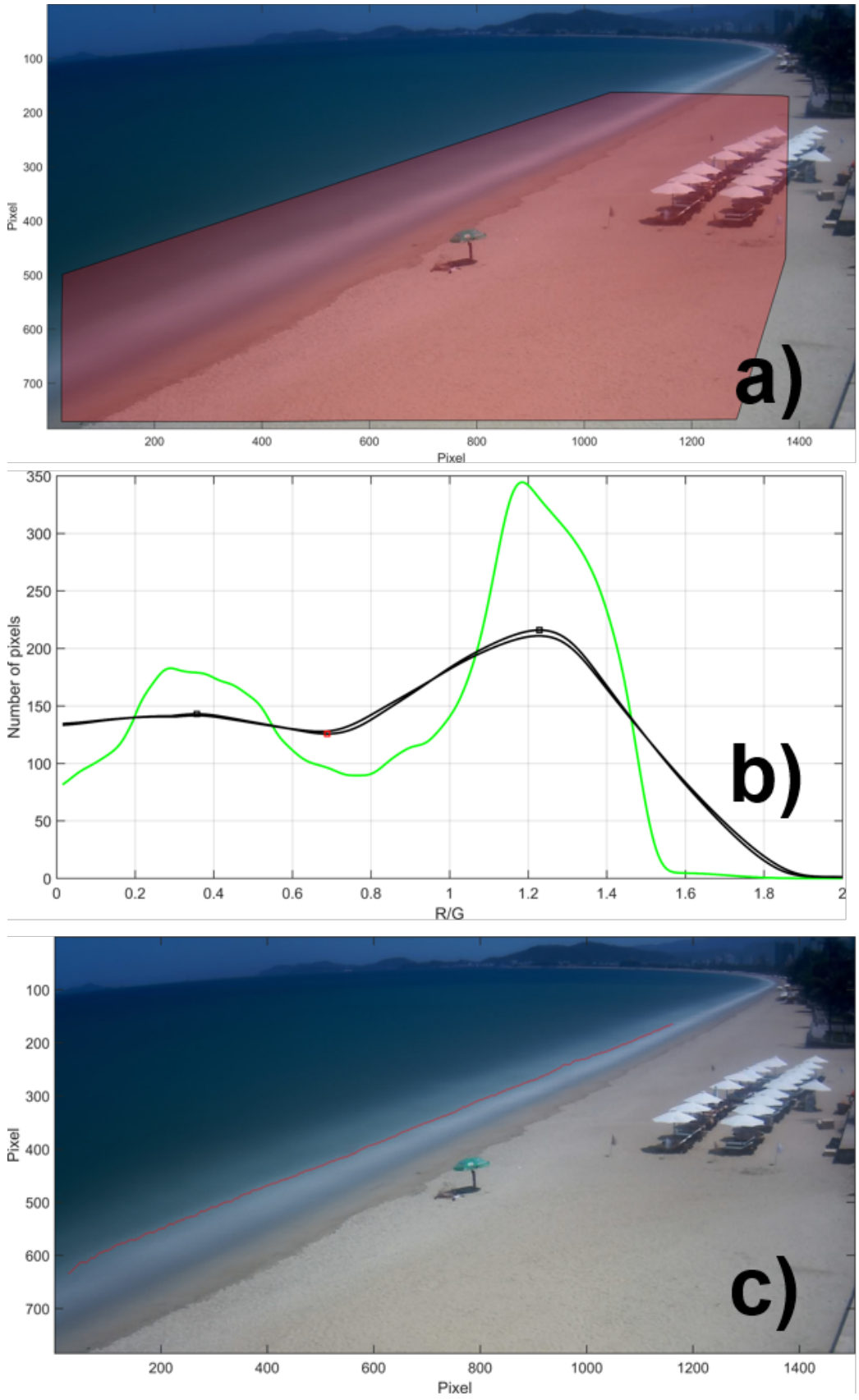

Figure 3.6: An example of a two-step shoreline detection method, applied to SNT Timex image. a) The background image is the Timex image and the red filled pattern is the region of interest (ROI). b) The histogram of all pixels in the ROI, calculated with a bin size of 7 pixels. The green line is the initial result and the black lines are iterative steps. c) The shore line results are represented by red dots.

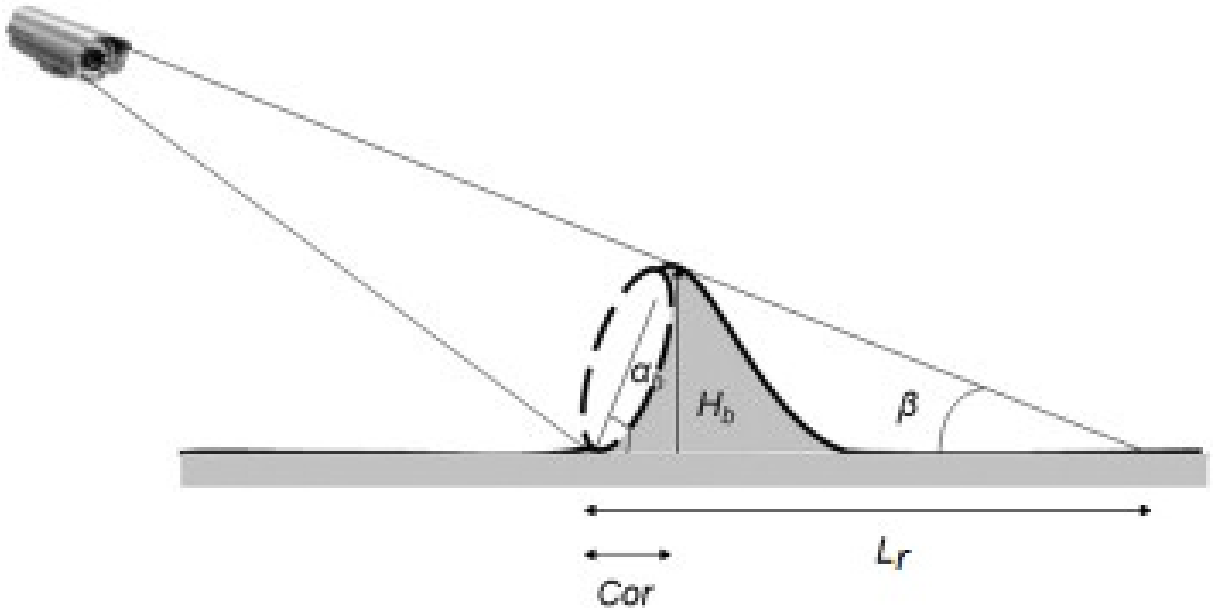

Figure 3.7: Principle of the method for Hb estimation. Camera view angle is β and α_b is the wave front face slope. Roller appears as a dashed oval. L_r is the wave roller horizontal projection, Cor a correction taking into account αb and Hb is the actual breaker height. Adapted from Almar et al. (2012a).

cation in Nha Trang. The method proposed by Almar et al. (2012a) is chosen because it gave good results in laboratory experiments (Almar et al., 2012a) as in the field (Angnuureng, 2016, Abessolo Ondoa et al., 2017b,a). It is essentially based on the geometrical relation between the breaking point location, the wave length roller and the camera position as shown in Figure 3.7.

With the parameters defined in Figure 3.7, we have trigonometric equations:

$$H_b = Cor \tan \alpha_b \tag{3.11}$$

$$H_b = (L_r - Cor) \tan \beta \tag{3.12}$$

Using the two equations 3.11 and 3.12 gives:

$$Cor = \frac{L_r \tan \beta}{\tan \alpha_b + \tan \beta} \tag{3.13}$$

The angle α_b can be considered as the model parameter and β is determined by the relative position between the camera location and the breaking point. Given the angles α_b and β, once the horizontal projection of the wave face covered by the roller (L_r) is determined, we can compute the correction coefficient Cor from Equation 3.13 and then calculate Hb using Equation 3.12 or 3.11.

The steps to determine Hb from timestack images are: first determine the location of wave breaking inception based on abrupt changes of wave optical characteristics at the breakpoint. At the breaking point, there is a large jump in intensity (Catalán et al., 2011). Thus, the breaking point location for each wave can be directly determined by calculating the intensity difference between two consecutive pixels on the same time axis (Figure 3.8c).

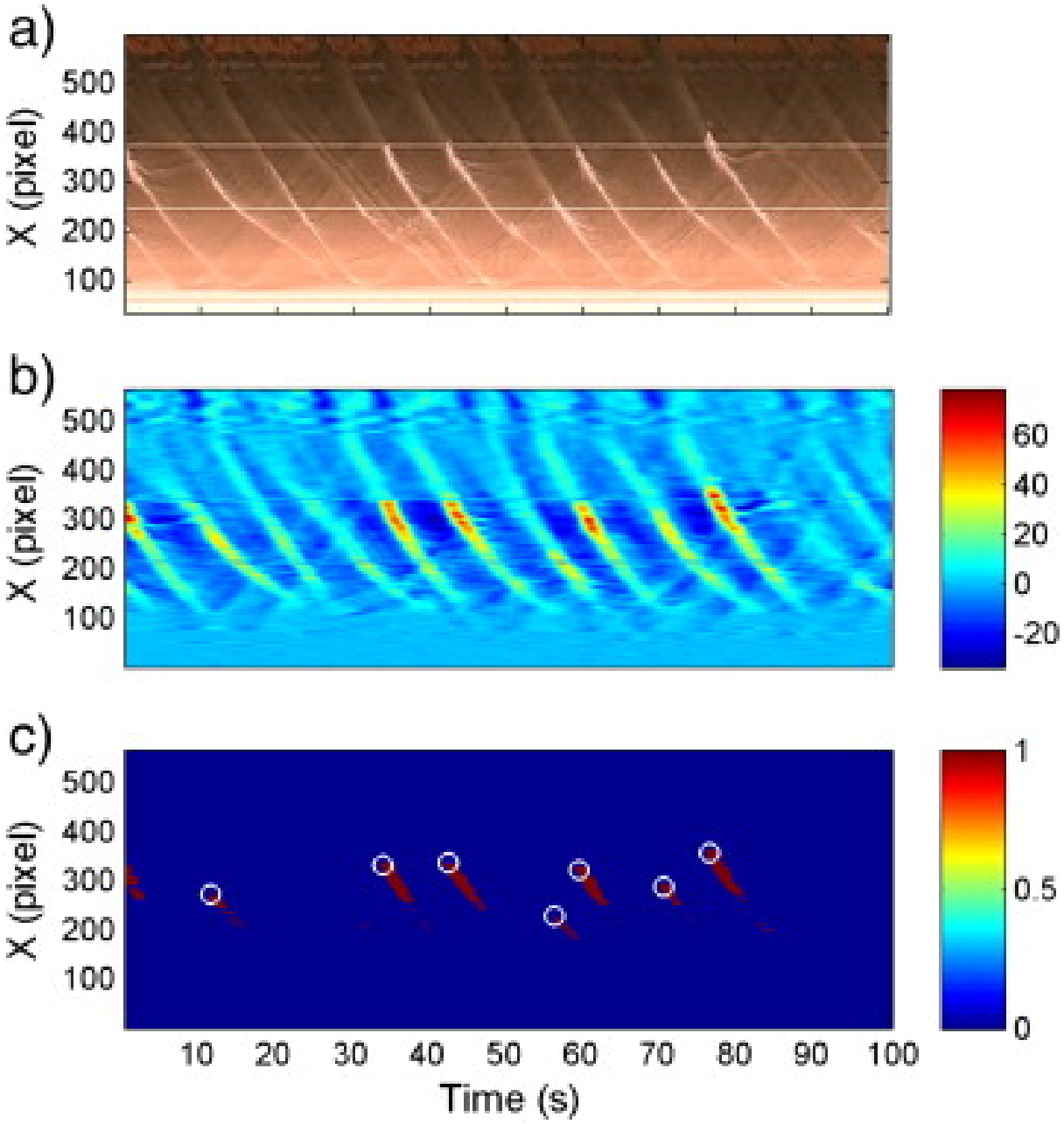

Figure 3.8: (a) Raw cross-shore timestack image of SNT camera. Wave propagation is apparent from deep water (up) to the beach (down) over time (from left to right). (b) Filtered timestack image. (c) Roller identification (red zones) by application of a pixel intensity threshold. White circles represent the location of identified breakpoints. Adapted from Almar et al. (2012a).

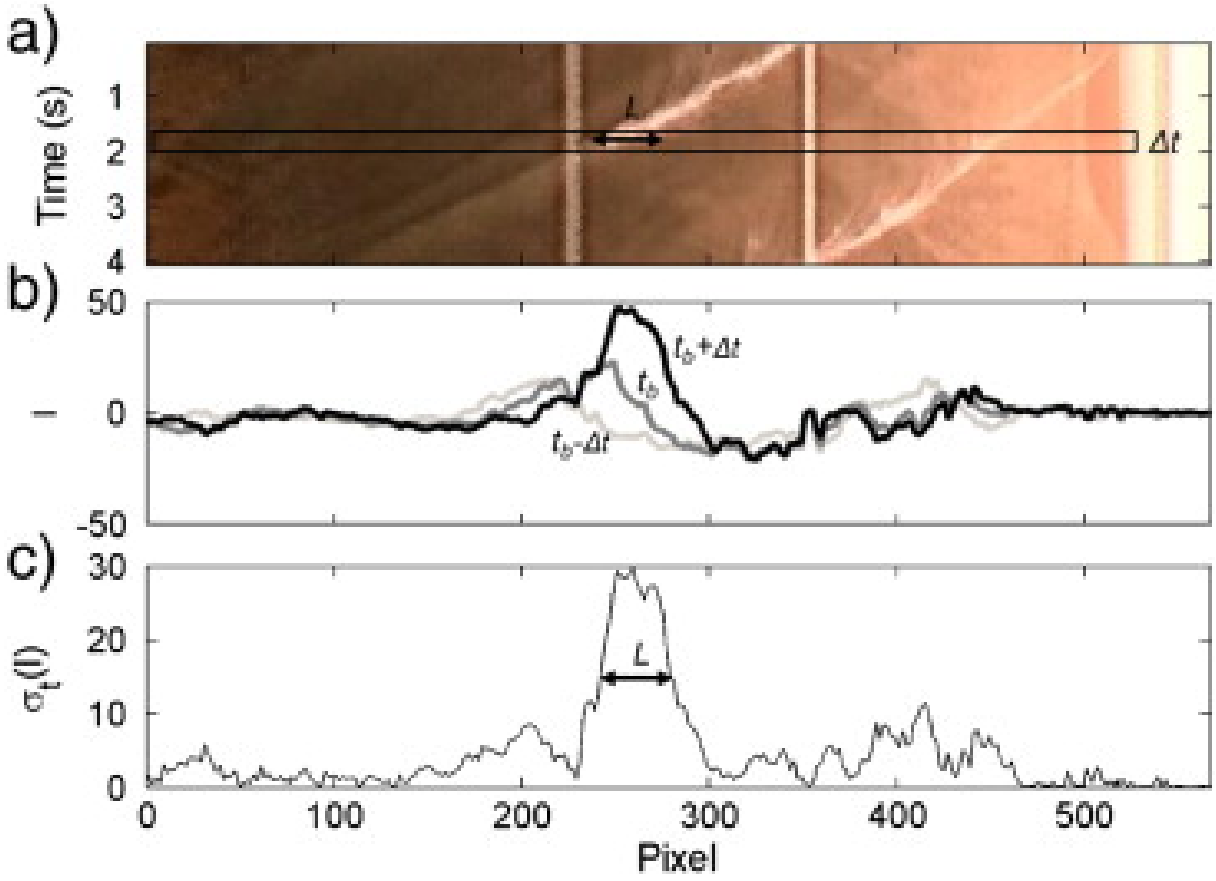

Figure 3.9: (a) Timestack image centered around an individual breaking event; (b) pixel intensity anomaly (c) Standard deviation in a). L_r represents the horizontal projection of the wave face covered by the roller. Adapted from Almar et al. (2012a).

However, applying the method to the raw cross-shore timestack image may get more breaking points than the number of waves during the sampling period (15 minutes). Therefore, the raw cross-shore timestack images (Figure 3.8a) are pre-processed to enhance the wave intensity signal. A pass-band filter between 0.05 and 0.5 Hz is used to remove low-frequency (light variations due to clouds) and high-frequency components (rapid adjustment of the camera "auto-iris"). The result are shown in Figure 3.8b. Then, the waves are clearly intensified, and the foam region is effectively eliminated. In addition, the pixels associated with breaking waves clearly stand out with intensity values $Ipix > 80$, while the rest is only $Ipix \sim 10$. Therefore, similarly to Catálan and Haller (2008), an arbitrary threshold ($Ipix = 30$) can be used to discriminate between breaking and non-breaking pixels. The result is shown in Figure 3.8c.

It should be noted that Hb can only be calculated at the breaking point because once breaking initiates a clear intensity peak appears at the wave crest. Next, as the roller develops and foam slides toward the wave trough, the pixel intensity at the peak increases. As the wave continues to break, the horizontal extension of the intensity peak is no longer only associated with the wave face but to roller propagation and remaining foam. So, from the break-point location moving shore-ward, the intensity continues to rise and peak at the white incipient roller, after that the intensity decreases and reaches a local minimum at the wave trough. Therefore, the distance from the local minimum to the break-point location can be simply considered as the approximation

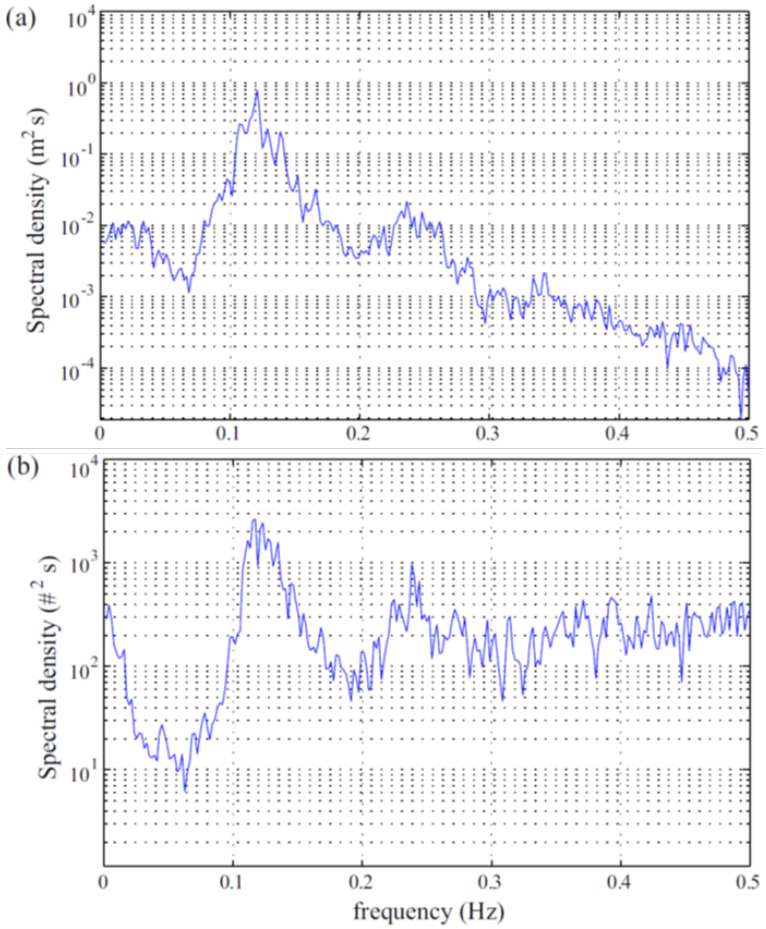

Figure 3.10: Spectral analysis of in-situ measured pressure sensor and video image intensity data (a) frequency spectrum of the measured pressure sensor, (b) frequency spectrum of video image intensity. (Figure 29 in Yoo 2007)

of L_r (in pixels) (Figure 3.9b). Compared with Almar et al. (2012a), this method is simpler and does not loose any generality because α_b is used to calibrate the model. The length L_r in pixel units is then converted to the physical length by the coefficients obtained in the camera calibration step (Section 3), and Hb can be computed.

With this method, we determine the wave height at break-point at a wave by wave scale. Then, we can compute the mean wave height of the highest third of the waves to determine the significant wave height at breaking point (Hs). The results are validated in Section 4.2.

3.5 Wave period

Another important wave parameter that the timestack image can provide is the dominant near-shore wave period. The spectral analysis of video image pixel intensity and in-situ pressure sensor data shows very high similarity (Lippmann and Holman, 1991, Stockdon and Holman, 2000, Yoo, 2007, Almar, 2009). An example of similarity of the spectrum of these two signals is shown in Figure 3.10.

This study also uses the time series of intensity signals from video images to determine the wave period. Generally, the near-shore dominant wave period is obtained from the peak fre-

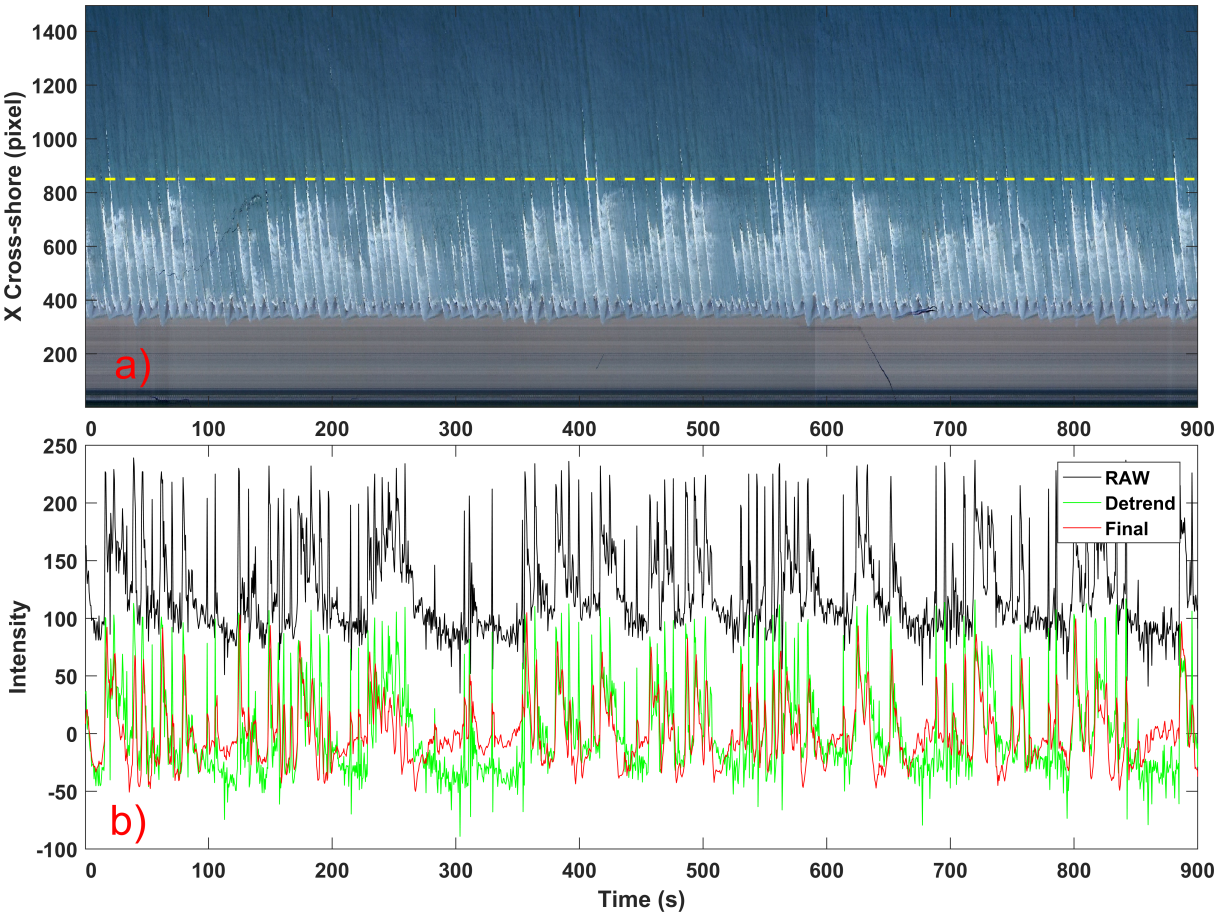

Figure 3.11: Example of intensity time series from a SNT camera timestack image used for wave period estimation. a) the background is a timestack image, with the yellow dashed line being the location for intensity sampling. b) signal processing: the black solid line represents the time series of "Raw" intensity of all pixels along the yellow dashed line in the top panel; the green solid line is the result of detrending; the red line is the result of filtering (of the detrended signal); the resulting intensity time series can then be used to determine the wave period.

quency in the spectral analysis of intensity signal (Lippmann and Holman, 1991)), or averaging all cross-shore points (Stockdon and Holman, 2000), or from the peak period in the wavelet spectrum analsysis (Yoo, 2007). In this study, instead of using these spectral methods, following Almar (2009) I applied the wave upward zero-crossing method (Davidson-Arnott, 2010) commonly used in statistical analysis of intensity signals.

First, a time series of intensity at a pre-selected location on the cross-shore section is obtained by taking intensity of all pixels on a straight line, such as the yellow dashed line shown in Figure 3.11a. The initial intensity is shown in Figure 3.11b labeled "Raw". The time series is detrended as shown by the green solid line in Figure 3.11b. Next, to enhance the wave intensity signal, a pass-band filter between 0.05 and 0.5 Hz is applied to the detrended signal to obtain the desired wave signal now called "Final" (red solid line in Figure 3.11b).

Finally, the upward zero-crossing method is applied to the "Final" intensity signal to estimate the wave period as shown in Figure 3.12. The distance between two intersections of the baseline (zero) and the intensity signal with same trend (upward) gives the wave cycle (Figure 3.12a). With this method we can determine the wave period at the wave by wave scale. Then, we can

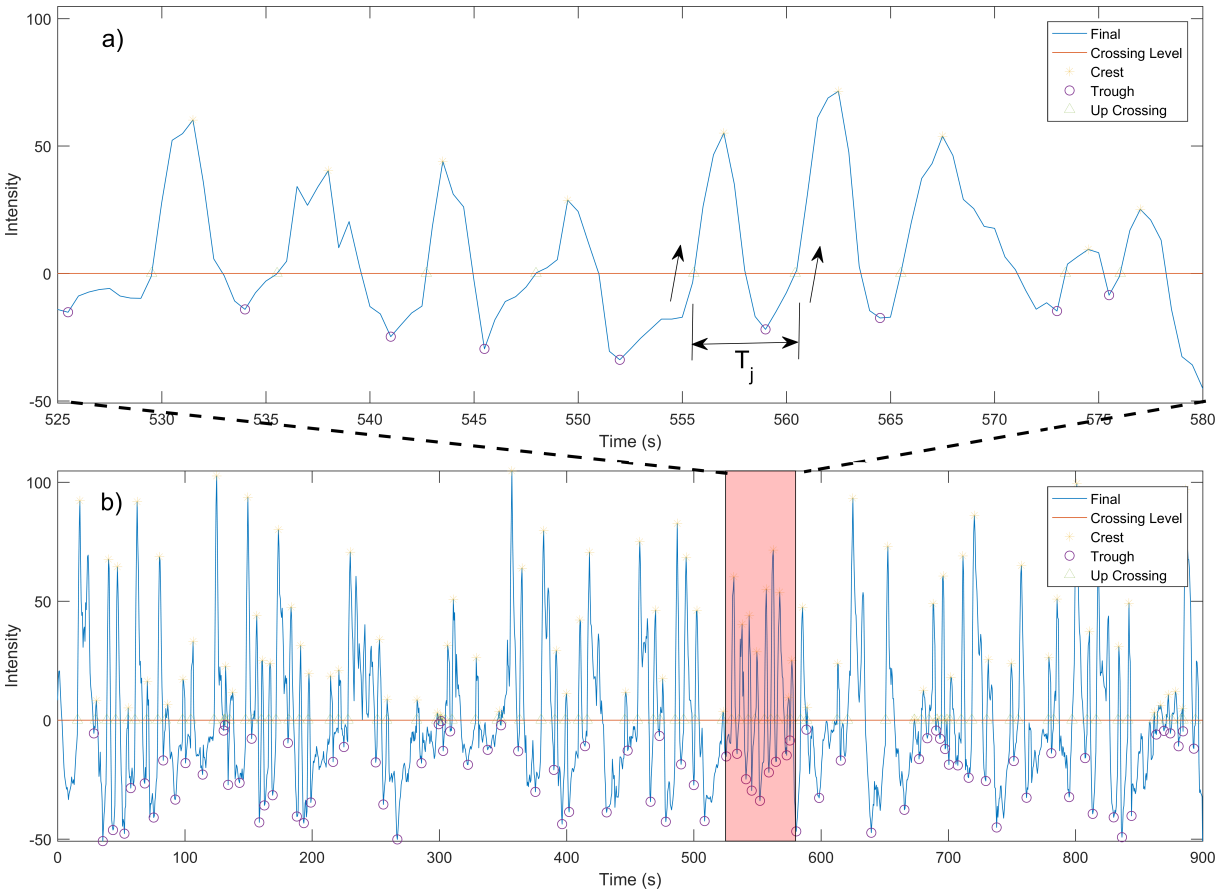

Figure 3.12: The filtered "Final" time series of pixel intensity is used to determine the wave period using upward zero-crossing method.

calculate the mean wave period (T_{mean}) and significant wave period ($T_{1/3}$) as follows:

- Mean wave period:

$$T_{mean} = \frac{1}{N}\sum_{j=1}^{N} T_j \tag{3.14}$$

- Significant wave period ($T_{1/3}$) as the mean of the period of the highest one third waves:

$$T_{1/3} = \frac{3}{N}\sum_{j=1}^{N/3} T_j \tag{3.15}$$

  Where, N is the number of waves counted in 15 minutes (the timestack image is generated with a sampling interval of 15 minutes). T_j is the cycle of each wave.

This method of determining the wave period is suitable for the wave climate in Nha Trang bay, especially during the low-energy wave regime in summer when the wave spectrum becomes wider and peak frequency is difficult to identify in the spectral analysis. The good agreement between video-based wave period and direct AWACs in-situ measurements during the NT1&2 surveys will confirm that in Section 4.2.

3.6 Nearshore bathymetry estimation

Two main approaches exist to estimate bathymetry from video-derived wave parameters: temporal and spectral methods. The difference between the temporal and spectral methods is in the estimation of wave celerity within the time or spectral domain:

- The temporal method correlates time-varying wave signals at different positions to find the best correlation, which is related to the celerity (Bos, 2006, Almar et al., 2008, Catálan and Haller, 2008).

- The spectral method correlates pixel intensity phases at different positions (Stockdon and Holman, 2000, Plant et al., 2008, Holman and Stanley, 2013). The spectral method (Plant et al., 2008, Holman and Stanley, 2013) assesses the celerity by deploying a cross-spectral correlation to find the most coherent frequencies which are associated with a cross-shore spectral phase ramp, hence a wavenumber k leading to celerity C. Holman and Stanley (2013) combined the earlier techniques used in Stockdon and Holman (2000) and Plant et al. (2008) and added a Kalman filter for robustness and error reduction.

Choosing a method determines the setup of the video camera systems that will offer a tailor-made format to the method. The temporal method (Bos, 2006, Almar et al., 2008) uses the full set of available pixels while Argus systems (Holman and Stanley, 2007) greatly reduce the data by coarsening the grid of pixel intensities. The tailored video settings might play a significant role in depth inversion accuracy. Recently, a comparison of the two methods by Bergsma and Almar (2018) suggests that they produce similar results given the same image quality. Therefore, in this study we chose the temporal method. The results, analyzes and error estimates are presented in

Chapter 6. Here, we describe in detail the temporal method for nearshore bathymetry inversion. For additional information, the reader may refer to Bos (2006), Almar et al. (2008), Bergsma and Almar (2018).

It is useful here to briefly recall the Airy wave theory, giving the depth inversion equation (Chapter 1). The propagating wave form or water surface elevation (η) is:

$$\eta(x, y, t) = a \cdot \cos(k \cdot x \cdot \cos\theta + k \cdot y \cdot \sin\theta - \sigma \cdot t) \tag{3.16}$$

where a is wave amplitude, k is wave number, θ is incident wave angle, σ is wave frequency, (x, y) is horizontal location. The relationship between the wave phase speed (or celerity) C, wave number k, wave frequency σ, wave length L, and wave period T are:

$$k = \frac{2\pi}{L} \;;\; \sigma = \frac{2\pi}{T} \;;\; C = \frac{L}{T} \;;\; C = \frac{\sigma}{k} \tag{3.17}$$

In deep water, the dispersion relation gives the celerity as:

$$C_0 = \frac{g \cdot T}{2\pi} \tag{3.18}$$

And wavelength:

$$L_0 = \frac{g \cdot T^2}{2\pi} \tag{3.19}$$

Then, the general dispersion relation relating wavelength L, wave celerity C, wave frequency σ, and wavenumber k for waves propagating in the nearshore (finite depth) is given by:

$$L = L_0 \cdot \tanh(k \cdot h) \tag{3.20}$$

$$C = C_0 \cdot \tanh(k \cdot h) \tag{3.21}$$

$$\sigma^2 = g \cdot k \cdot \tanh(k \cdot h) \tag{3.22}$$

And depth inversion h follows:

$$C^2 = \frac{\mathrm{g}}{k}\tanh(k \cdot h) \quad \Rightarrow \quad h = \frac{\tanh^{-1}\left(\frac{C^2 k}{g}\right)}{k} \tag{3.23}$$

To test the method with a more controlled dataset than video signal, noisy by nature, a monochromatic wave pattern including incident wave angle θ was generated by computing the wave trajectory in space-time. In this case, wave refraction must be accounted for and is given by Snell's law:

$$\frac{\sin\theta_1}{C_1} = \frac{\sin\theta_2}{C_2} \tag{3.24}$$

Synthetic case study

The monochromatic wave patterns and timestack images were created using the following

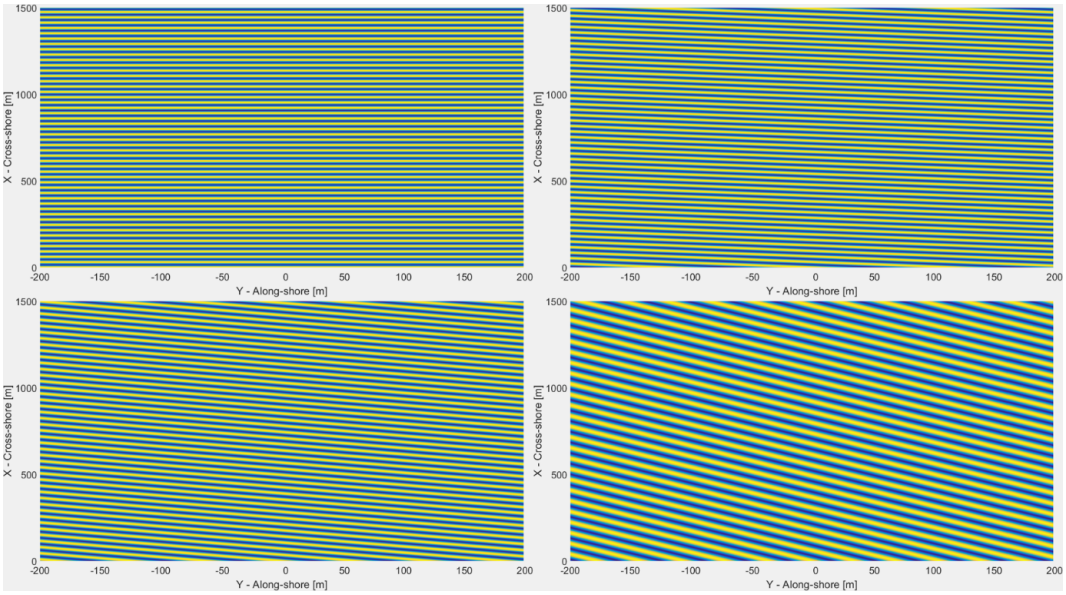

Figure 3.13: Wave pattern in flat view in the case with $h = 3m$, $slope = 0$, and $\theta_0 = 60°; 30°; 15°; 0°$ from right to left and bottom to right.

parameters:

- Wave amplitude $a = 0.8m$; Wave period $T = 6\,\text{sec}$, $dt = 0.25\,\text{sec}$, $dx = 0.25m$, $dy = 0.25m$
- For the simplest case of constant depth, the depth is set to $h = 3m$ or $h = 6m$
- For the case with depth variation, the bed slope is set to $1/40$
- For the case with wave angle, the offshore incident wave angle $\theta_0 = 60°; 30°; 15°; 0°$

Figures 3.13, 3.14, and 3.15 show the synthetic wave patterns produced. Figures 3.13 and 3.14 represent simple test cases with constant depth $h = 3m$ and $h = 6m$, respectively, and Figure 3.15 presents the depth-variable case with bed $slope = 1/40$. Each Figure has four cases corresponding with variation of different offshore incident wave angles $\theta_0 = 60°; 30°; 15°; 0°$.

The results of Figures 3.13 and 3.14 confirms that a constant depth gives a constant celerity C. In contrast, the wave crest pattern in Figure 3.15 shows a variation celerity C and wave angle θ associated with variable depth.

Celerity estimation from temporal method

The timestack images of the 12 cases previously shown were created at section $Y = 0m$ (Equation 3.16). Figures 3.16, 3.17, and 3.18 present the timestack in three simple cases without depth variation or incident wave angle $\theta_0 = 0°$.

We explain here the principle of the temporal method as well as important parameters directly influencing the cross-correlation matrix (**R2M**): the peak vector (**R**), the maximum correlation range $Dc[pixel]$ and the phase time lag $n = \frac{dpha}{dt}[pixel]$. We first consider a simple case with constant depth ($h = 6m$ and/or $slope = 0$) and neglect incident wave angle ($\theta_0 = 0°$), which is a reasonable assumption in the surf zone (Tissier et al., 2011). Figure 3.17 is in pixel coordinates (unit) and its conceptual sketch is represented in Figure 3.19.

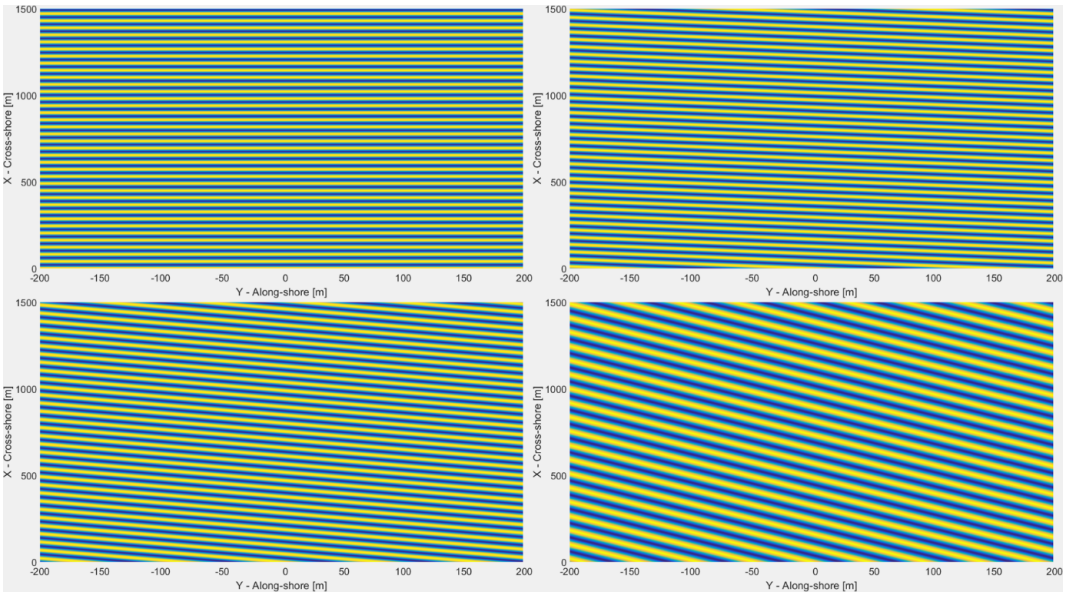

Figure 3.14: Same as Figure 3.13 but for $h = 3m$

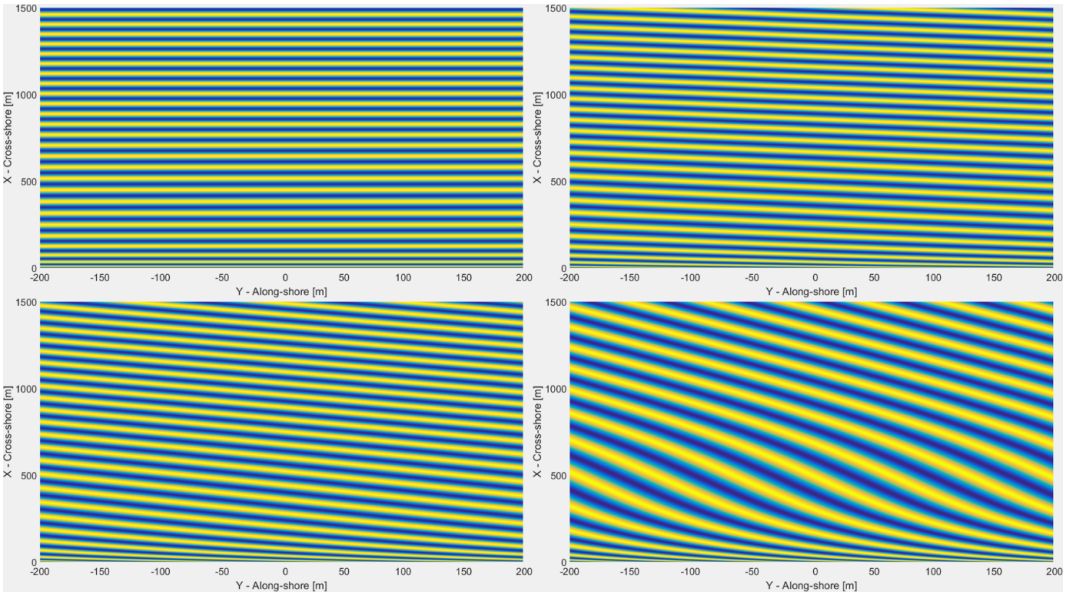

Figure 3.15: Wave pattern in flat view in the case with $h = f(x)$, $slope = 1/40$, and $\theta_0 = 60°; 30°; 15°; 0°$.

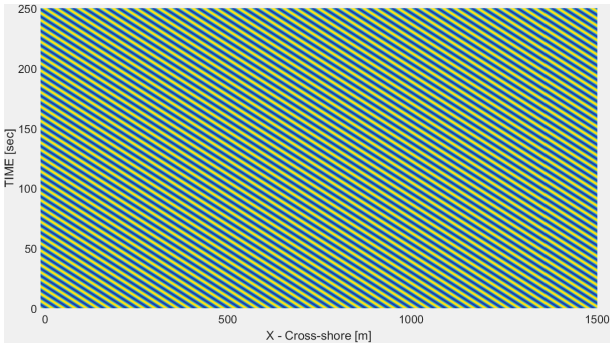

Figure 3.16: Time-stack image pattern in the case with $h = 3m$, $slope = 0$, and $\theta_0 = 0°$.

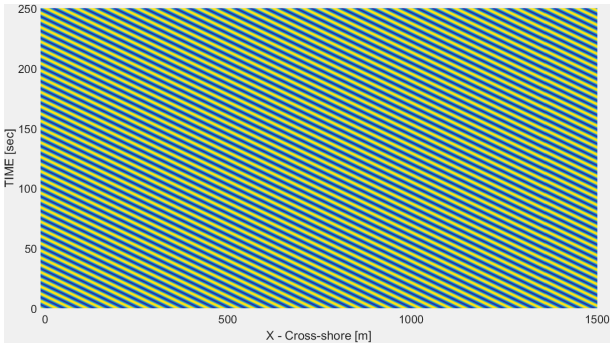

Figure 3.17: Time-stack image pattern in the case with $h = 6m$, $slope = 0$, and $\theta_0 = 0°$.

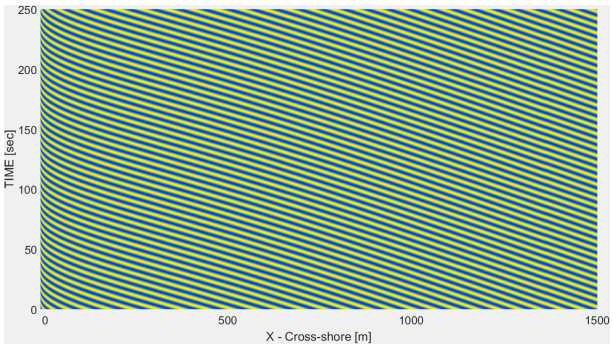

Figure 3.18: Time-stack image pattern in the case with $h = f(x)$, $slope = 1/40$, and $\theta_0 = 0°$.

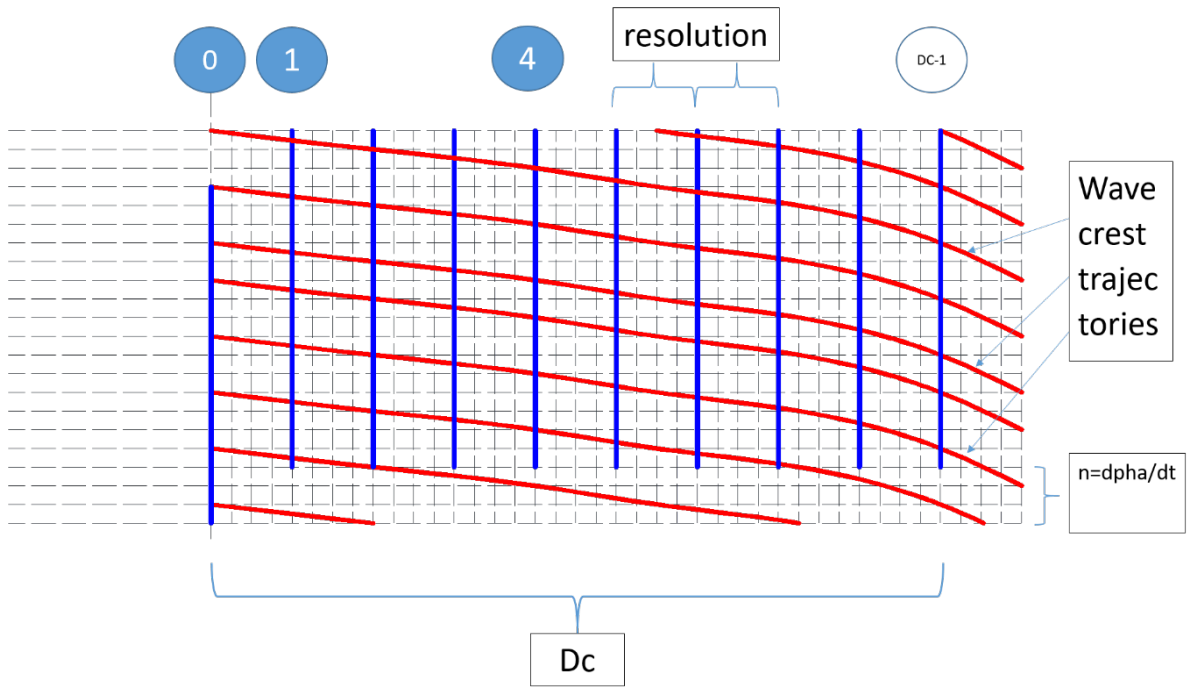

Figure 3.19: Sketch of time-stack image pattern in the case with $h = 6m$, $slope = 0$, and $\theta_0 = 0°$ illustrating the wave crest trajectory detection using the temporal method.

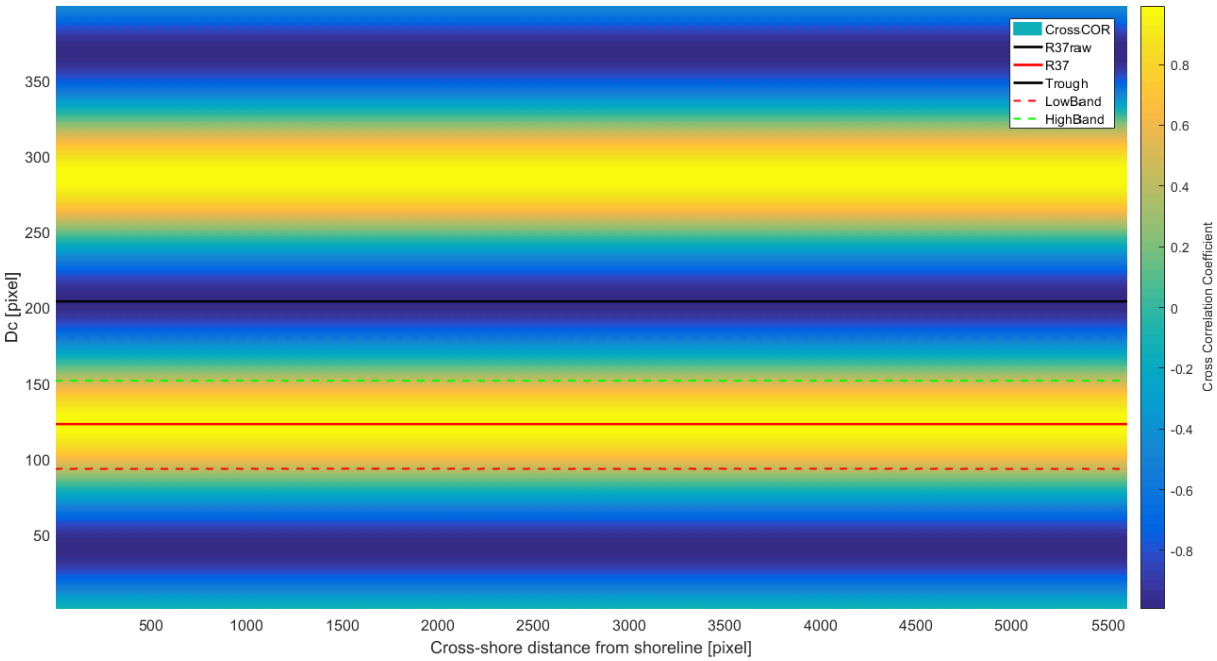

Figure 3.20: Cross-correlation matrix (**R2M**) and peak correlation coefficient vector (**R**- red solid line) in the case with $h = 6m$, $slope = 0$, and $\theta_0 = 0°$.

Figure 3.19 shows how the temporal method is used to detect wave crest-trajectories in the stack images. The solid red lines show an example of the wave crest trajectories. The solid blue lines show the sampling location, with horizontal distance between them representing the resolution; the phase time lag in pixel $n = \frac{dpha}{dt}[pixel]$ calculated from pre-selected time lag ($dpha[sec]$), usually less than the wave period T; and temporal resolution (dt[sec]). The cross-correlation of intensity collected at a reference with the neighbors ($\overline{1..Dc}$) is calculated. The maximum of the correlation coefficient represents the time-integrated distance made by the waves during ($dpha$). Figure 3.20 and Figure 3.21 show the cross-correlation matrix (**R2M**) and the peak of cross-correlation coefficients vector (**R**). Figure 3.20 shows **R2M** and **R** for a constant depth case and Figure 3.21 in case of variable depth. In order to convert the vector **R** into celerity C (or water depth h), it is necessary to explain the meaning of **R2M** matrix, **R** vector and the influence of phase time lag n and maximum range Dc on **R2M** and **R**.

The meaning of Dc and $n = \frac{dpha}{dt}$ and their impact on cross-correlation matrix R2M and peak correlation coefficient vector R

Considering variable water depth with $slope = 1/40$, and neglecting the incident wave angle $\theta_0 = 0°$, we obtain the timestack in Figure 3.22. Before creating the matrix **R2M** and extracting the vector **R**, we need to select the parameter Dc and phase time lag $n = \frac{dpha}{dt}$, for example $Dc = 400$ [pixel] and $n = 7$ [pixel]. Let's consider an arbitrary location, for example at point **A** (red dot) in Figure 3.22. We first get the pixel intensity along the red line from **A** (length of time series – n) called **Avec**; we then get the pixel intensity along the black lines called **Evec** and calculate the cross-correlations <**Avec**,**Evec**> until the distance Dc [pixel] is reached, which serves to construct matrix **R2M**. It means the size of the matrix **R2M** will

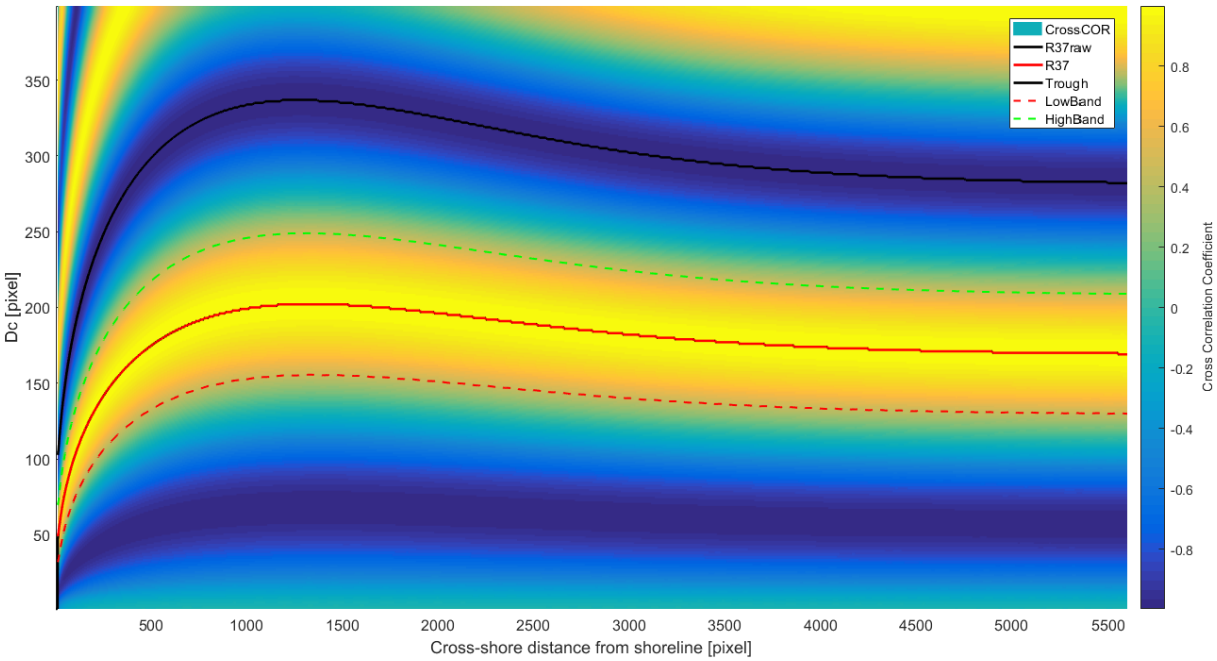

Figure 3.21: Cross-correlation matrix (**R2M**) and peak correlation coefficient vector (**R**- red solid line) in the case with $h = f(x)$, $slope = 1/40$, and $\theta_0 = 0°$.

be $Dc \times (X_{\max}^{image} - Dc)$, and the value of the vector $\mathbf{R}$ is the maximum of cross-correlation coefficients. For the example shown in Figure 3.22, $\mathbf{R}(x = x_{\mathbf{A}}) = \overline{EB}$

Wave celerity C and wavelength L

Wave celerity C is then converted into water depth using the wave dispersion equation 3.23. As can be seen in Figure 3.23, at the position $\mathbf{A}$, $x = x_{\mathbf{A}}$. Wave period $T = \overline{\mathbf{AD}}$ [s] and in pixels (Figure 3.23) $\overline{\mathbf{AD}} = \frac{T}{dt}$ [pixel]. The phase time lag in pixel $\overline{\mathbf{AE}} = n$ [pixel] and in seconds $\overline{\mathbf{AE}} = n \cdot dt$ [s]. It can be seen that the values of the maximum correlation coefficient $\mathbf{R}(x = x_{\mathbf{A}})$ at location $\mathbf{A}$ is the length of $\overline{\mathbf{EB}}$. Since the water depth varies along the cross-shore section then the wave celerity C varies with x, and the vector $\mathbf{R}(x = x_{\mathbf{A}})$ also varies across-shore.

The wavelength L can also be estimated directly in the $R2M$ matrix as the distance between two peaks of correlation. This offers another way of estimating the depth. The difference between the two methods can be used as an estimation of uncertainty in the temporal method. This is clearly an advantage in comparison with the spectral method, which cannot offer such error estimate (Bergsma and Almar, 2018).

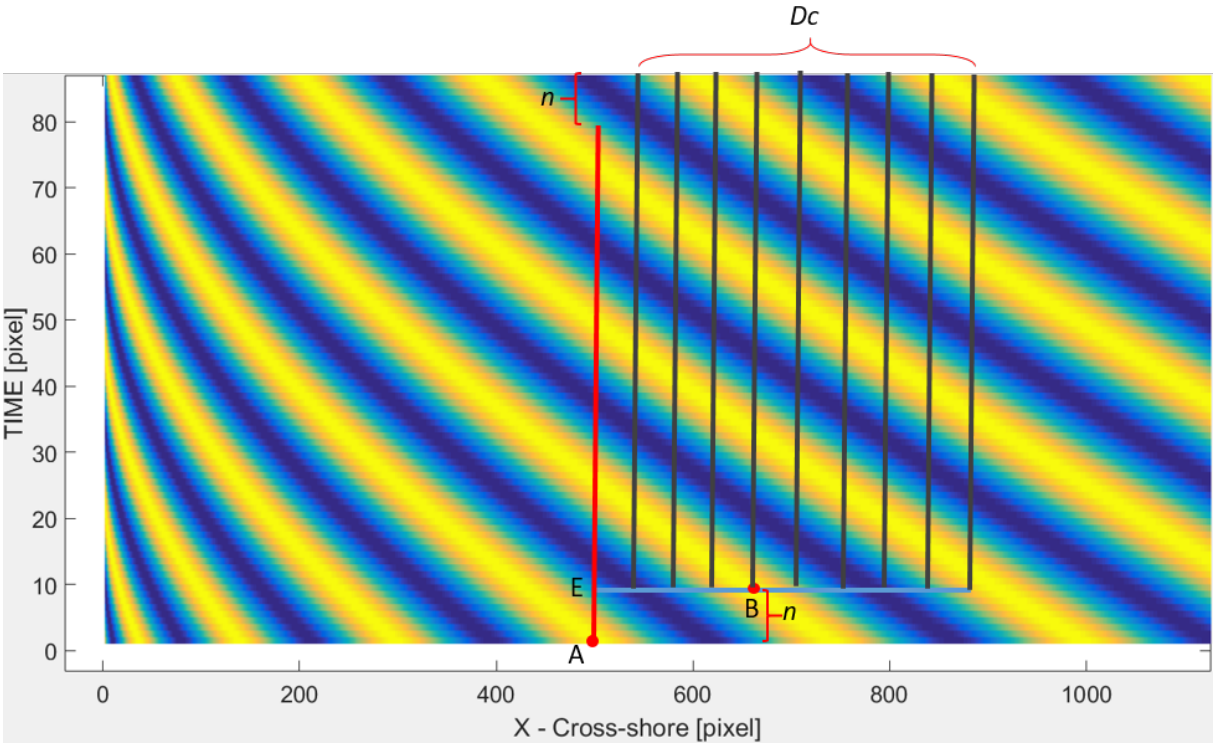

Figure 3.22: Zoom-in of time-stack image presented in Figure 3.18, in the case with $h = f(x)$, $slope = 1/40$, and $\theta_0 = 0°$.

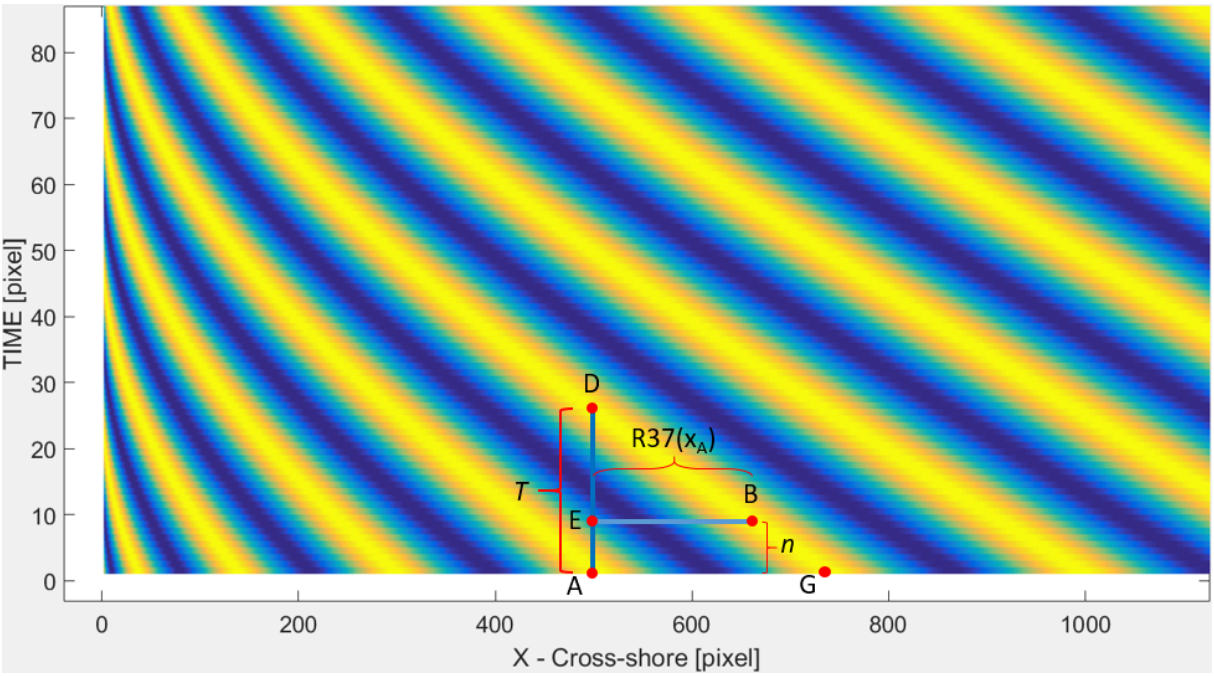

Figure 3.23: Zoom-in of timestack image presented in Figure 3.18, in the case with $h = f(x)$, $slope = 1/40$, and $\theta_0 = 0°$. The figure presents the meaning of phase time lag $n[pixel] = \frac{dpha}{dt}$, related to $\mathbf{R}$ vector.

Chapter 4

Field measurements and validation of video-based observations

Contents

As pointed out in the previous chapters, Nha Trang beach is affected by a complex seasonal wave field. The summer wave regime is dominated by southwest wind waves from March to September, and by northeast swell waves during winter monsoon from October to February. The country is also part of the most important cyclogenesis region in the world and 4 to 6 typhoons hit the coast every year from October to December (Thao et al., 2014). It appeared as an ideal location to set up project studies like MOST1&2 and COASTVAR, that were focused on tropical beach hydro-morphodynamics. MOST1&2 are Protocol research projects between Vietnam and France, supported by the Ministry of Science and Technology of Vietnam, and entitled: "Study on hydrodynamic regime and sediment transport in estuarine and coastal zones of Nha Trang bay, Khanh Hoa province"; and "Investigate morphodynamical processes and propose applied solutions to recreate and upgrade the Nha Trang coast, Khanh Hoa province in the context of climate change". The duration of the MOST1 project was 2 years in 2013-2014, and the MOST2 project is for 3 years in 2015-2019. The COASTVAR project (Coastal Variability in West Africa and Vietnam project) ran for 3 years in 2016-2018 with the purpose of advancing our understanding of tropical nearshore hydro-morphodynamic processes, from event to inter-annual scales. Emphasis was given to extreme events and to the fundamental processes underlying the swash-surf-shelf exchanges and their long-term effect on the equilibrium of nearshore morphology.

As a full member involved in the cooperation projects MOST1&2 and COASTVAR between Vietnam and France, that includes this PhD study, I participated in the projects from beginning to end. I participated in all major field surveys (apart from the first NT1 survey), designing the deployment strategy, responsible for data managing, storage and especially maintaining the shore-based camera system installed during NT1 survey. Therefore, I have an detailed knowledge of the data produced during MOST1&2 and COASTVAR. Since this is the data used in the PhD study, this chapter begins with presenting the project's existing data. Then, the data is used for assessment and calibration of the camera system that will be used in subsequent chapters.

4.1 Field experiments

Figure 4.1 shows the time line of the four major surveys of MOST1-2 and COASTVAR projects from the start in 2013 to date. These are intensive and detailed surveys with groups of national and international experts and a diverse set of equipment. Here, each major survey is presented including objectives, general conditions, equipment installation, and data quality and purpose. It should be noted that I was not responsible for all the data processing, of course, but I was fully involved in the surveys and actively participated in the data processing team work.

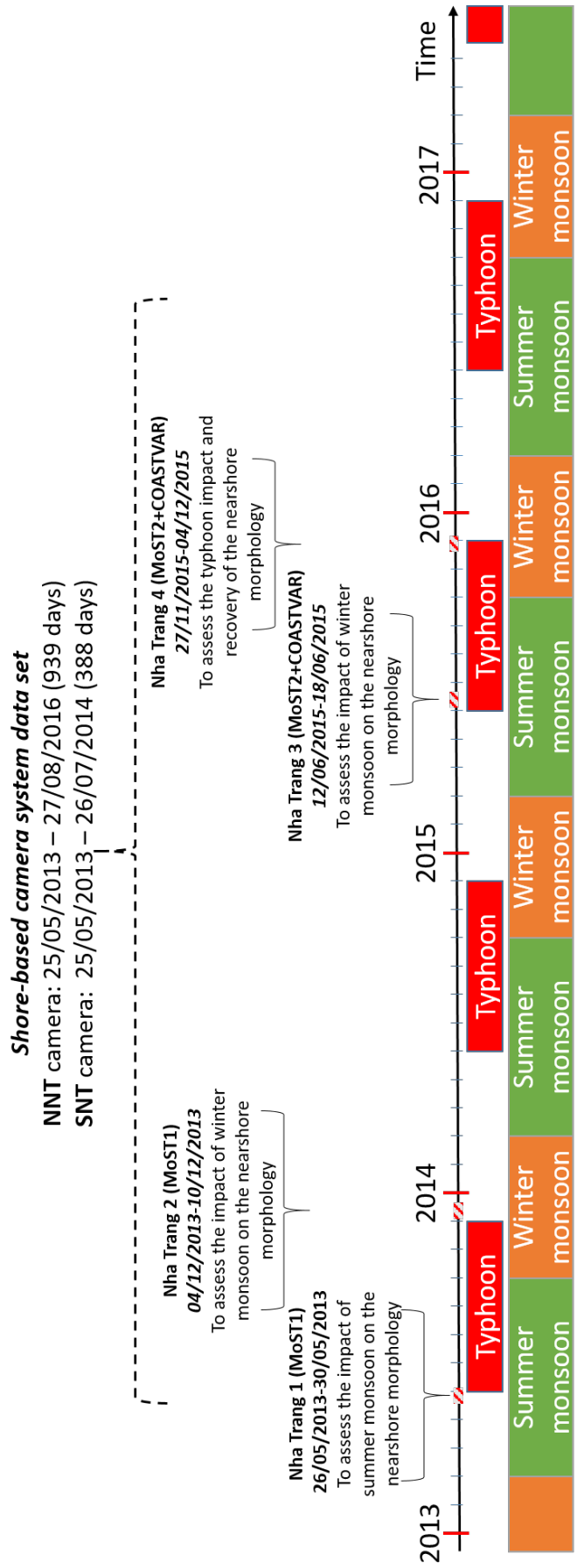

Figure 4.1: Time line of all major field experiments (I participated in almost all of these surveys).

4.1.1 Nha Trang 1 experiment (May 2013): Summer monsoon conditions (MOST1)

Objective

The first field experiment was conducted during May 23 - June 01 (NT1) (Figure 4.1). The aim of the survey was to observe the bathymetry, geomorphology of the upper beach, hydrodynamics of the bay and dynamics of southwest summer monsoon wind-waves (Almar et al., 2014, Lefebvre et al., 2014).

General Conditions

During the NT1 experiment, tide range varied from 0.8 to 1.5 m, while the diurnal modulated (i.e., by afternoon sea breeze) wind-waves remained roughly persistent over the experiment with $H_S = 0.25$ m, $Tp = 3.3$ s from southeast. Beach profiles (Figure 4.10a) showed no substantial variation, with a spring high-tide mark beach step and a rather linear swash zone, presenting a reflective large 0.17 slope. Sediment on the shoreface is medium sized ($D_{50} = 300\mu$m). Apart from storm events, the beach is impacted by waves locally generated by moderate southeast winds and it is a low-energy wave-dominated micro-tidal environment (Relative Tidal Range RTR ~ 1). Beach morphology presents an alongshore uniform, intermediate low-tide terrace reflective upper beach state (Wright and Short, 1984) with Gourlay parameter $\Omega\sim 1.5$. The average slope in the swash zone is of approximately (6°), and approximately (3°) in the surf zone.

Instruments and Measurements

A suite of instruments were deployed along a cross-shore transect from beyond the depth of closure to the swash zone and the measuring devices were located at the stations marked A, B, C, D and E as shown in Figure 4.2. In particular, station A located 1075 m offshore at a depth of 9.2 m and station B located 795 m offshore at a depth of 7.0 m have similar equipment. At stations A and B, incident wave parameters were measured by two AWAC (Nortek) and suspended sediments by two grain size analyzers LISST-25X (Sequoia Scientific, Inc) shown in Figure 4.3a. Station C located 370 m offshore and station D located 262 m offshore was set up with an electromagnetic current meter COMPACT and released at a depth of 4.8 m and 2.6 m, respectively. Station C is equipped with a pressured type wave gauge DNW-5M while station D is equipped with a multi-parameter sensor (water height and period, turbidity) OBS-3A (OSIL) shown in Figure 4.3b. At station E, a micro-profiler ADV - Vectrino II (Nortek) was deployed in the vicinity of the swash-poles, at either end of the surf zone or at the highest point of runup, following the tide-induced displacement of the swash zone.

In order to investigate the role of the swash zone in the recovery phases generated by low energy waves, different techniques were used to collect data at different time scales (swash event, tidal and monthly). A new method based on video monitoring of swash and surf zone was also tested for low-energy, high-frequency conditions by coupling **Swash-poles** and **Swash-camera**, at station E. Swash-poles consisted of 20 black painted metallic poles each with a 30mm wide red tape adhered near their tops. They were deployed across-shore from the back-shore to the surf zone; the 13 poles closest to shore were spaced one meter apart and the last 7, two meters apart (Figure 4.2). The actual position and elevation of the top of each pole was measured with a theodolite GTP101 (Topcon). Swash-camera is a high definition (1920×1080 pixels) video

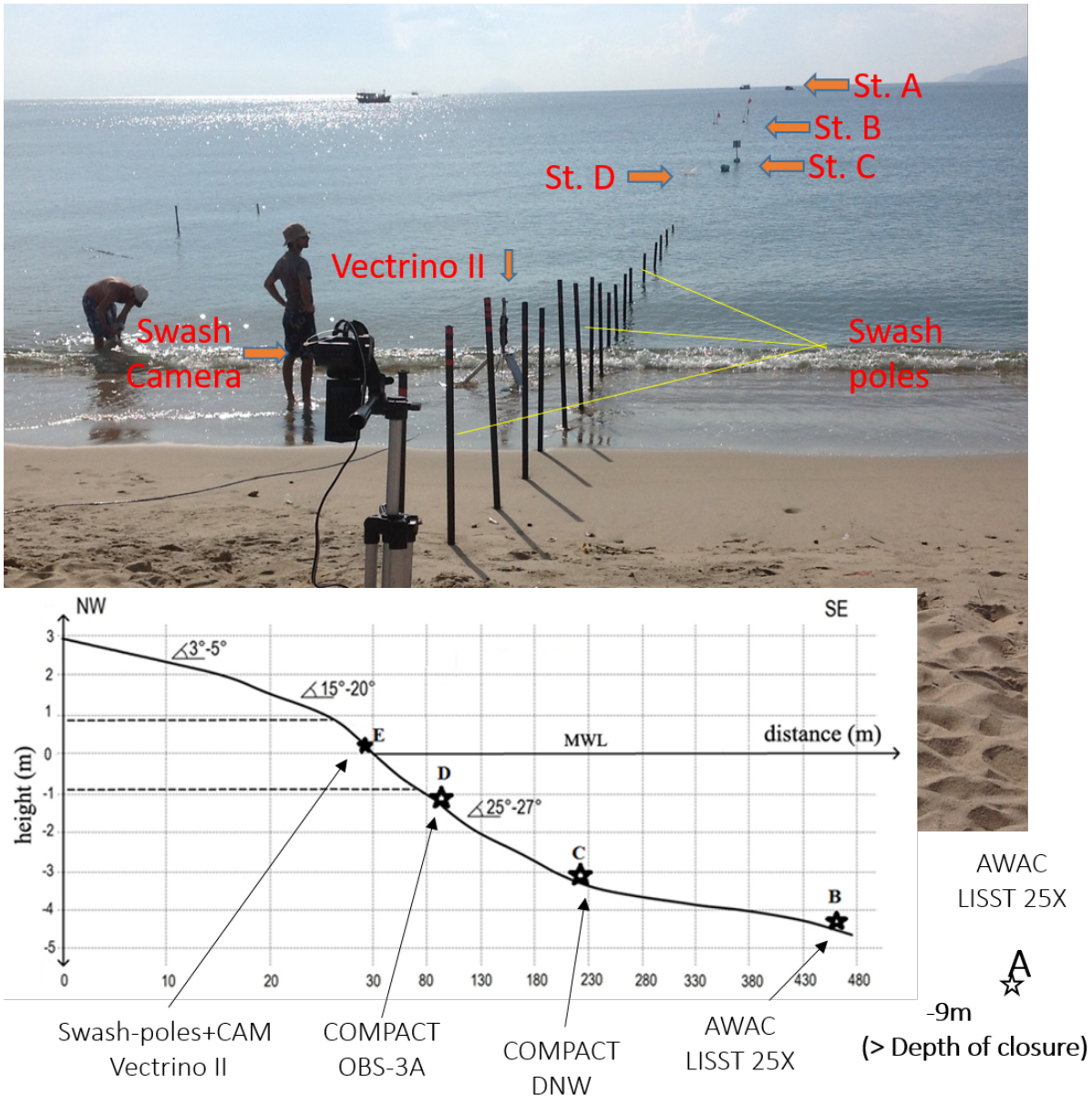

Figure 4.2: NT1 deployment with indication of the location of each instrument.

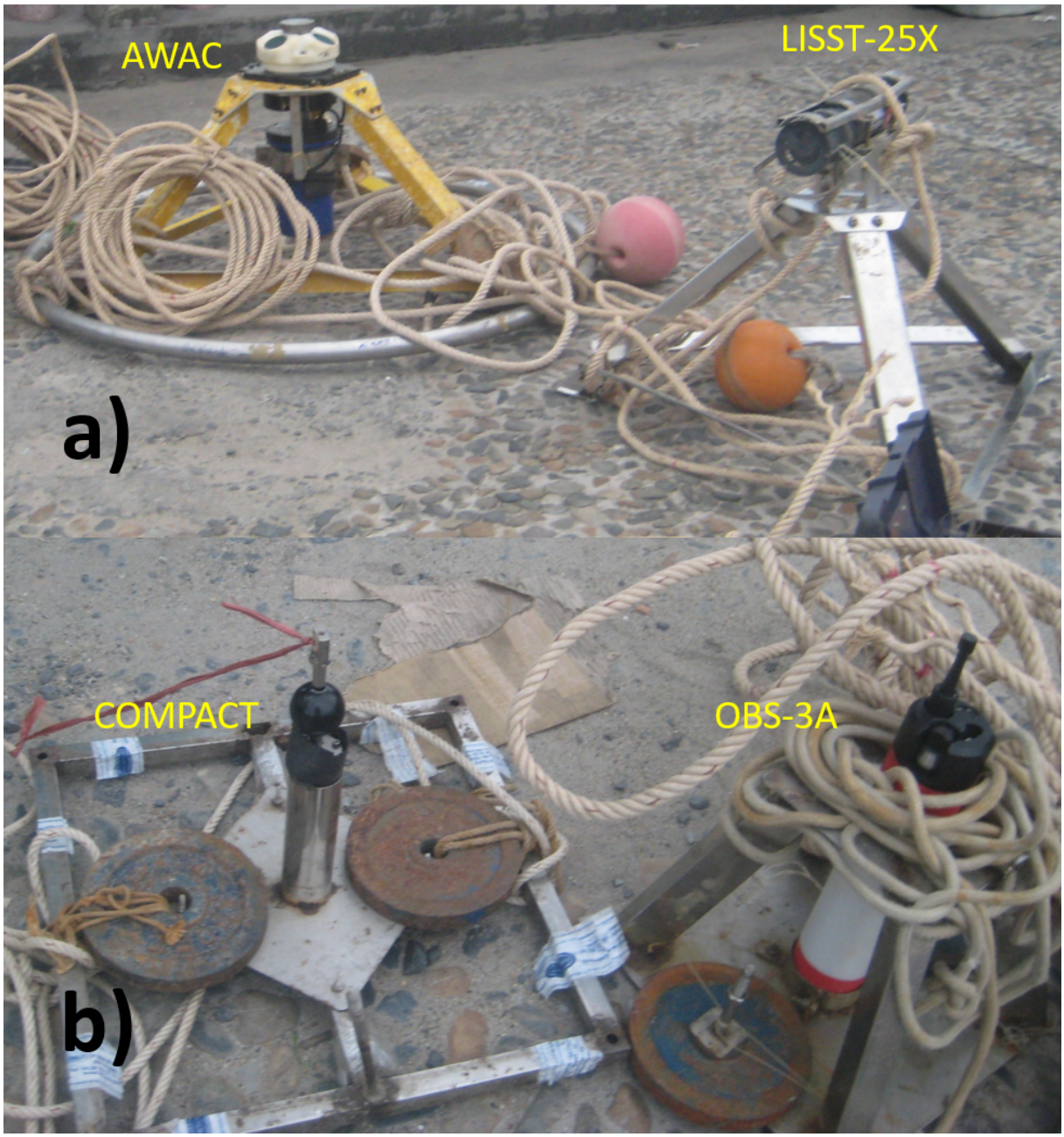

Figure 4.3: Measurement devices used at station A, B, C and D.

Figure 4.4: Field photo showing the course of a bathymetric survey during NT1.

camera HDR-CX 250 (Sony) used to monitor waves along the poles over daylight hours with an acquisition rate of 25 Hz. Therefore, it offers an unsupervised method to obtain the wave height in the swash and surf zone simultaneously at each pole and at a sample rate of 25 Hz. The methodology and preliminary results of swash-poles and swash-camera system are presented in Lefebvre et al. (2014) with validation obtained by comparing with 4 pressure sensors deployed during NT2 (see Figure 8 in Almar et al. (2014)).

During the first day of field experiment, May 26, the bathymetry of the bay was measured by coupling a dual frequency echo-sounder and a differential GPS (DGPS) ProMark2 (Thales Navigation) shown in Figure 4.4. The DGPS transmitter station was located in front of the device's cross-shore transect, with elevation and coordinates of the station previously transmitted from the reference point installed at the National Institute of Oceanography of Nha Trang, using a theodolite GTP101 (Topcon). The DGPS system was later also used to measure the GCPs for the camera calibration of the shore-based camera system described in detail in Chapter 3.

Daily topographic measurement of the beach were conducted with a theodolite (Topcon, GTP101) and differential GPS. Topographic surveys were carried out three times a day with a theodolite from the back-shore up to approximately 1.5 m depth. During two days, hourly surveys of bed elevation at each pole, was conducted by manually measuring the elevation between the top and the base of each pole. This pole-related measurement was referenced with

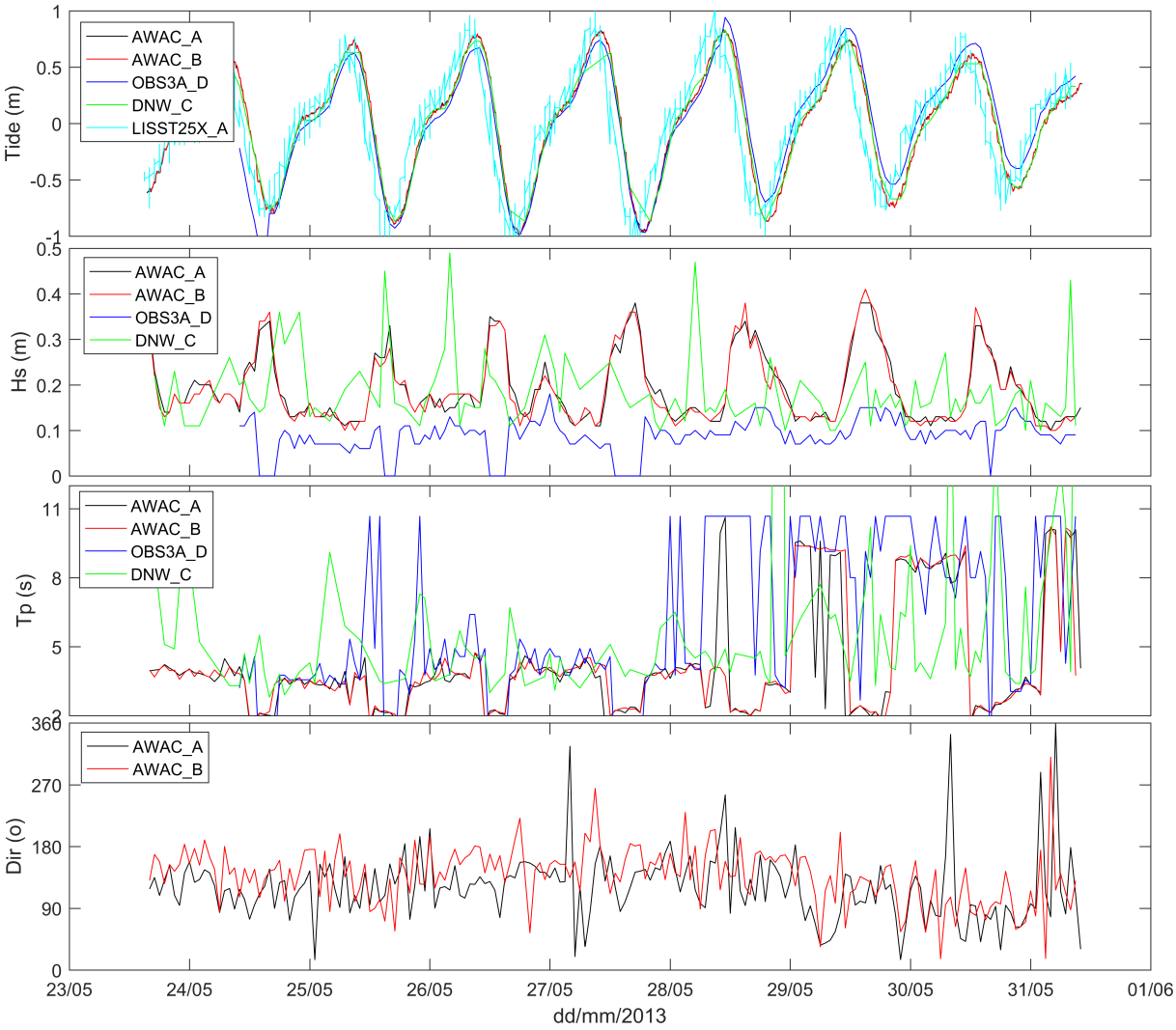

Figure 4.5: Examples of field measurements showing tidal (water level) and wave characteristics (Hs and Tp) at stations A, B and D using AWAC and DNW.

the three-dimensional position of the top of the pole.

In addition to the above mentioned stations, for the purpose of providing river flow data as boundary conditions for the proposed models for Nha Trang bay, a hydrological station was implemented at Ngoc Hoi bridge. In particular, water discharge of the Cai river was measured every three hours with an acoustic Doppler current profiler ADCP (Notek). Hourly water level was also measured.

To complete these intensive short-term experiments, a two-camera permanent video system was deployed at the beginning of NT1 field trip. The description of the system is detailed in Chapter 3 and published papers by the project's research group Almar et al. (2014), Viet et al. (2014), Duc et al. (2014a), Thuan et al. (2016).

Achievement

In general terms, the monitoring equipment in this survey worked as intended. The method used for deploying and retrieving data is safe and accurate. For example, Figure 4.5 shows measurement of tide level and wave characteristics (Hs, Tp and wave direction) at stations A, B, C and D using AWACs and DNW. The results show that tide measurements at stations A

and B with AWAC and station C with DNW are consistent, serving as validation. Significant wave height (Hs), wave period (Tp) and wave direction at offshore stations A and B are an exact match, while they depart from DNW measurement at nearshore station C as expected.

In-situ measurements (Figure 4.5) used in Lefebvre et al. (2014) and Almar et al. (2014) indicate that NT1 had achieved its initial purpose of assessing the basic hydrodynamic and morphodynamic conditions of Nha Trang beach during summer monsoon. In addition, NT1 saw the successfully installation of a shore-based camera system – first in Vietnam for scientific purpose – and provided initial data on upper beach topography and bathymetry of the whole bay. The long-term video data initiated during this campaign will be presented in detail in this PhD study, and published elsewhere (Duc et al., 2014a, Almar et al., 2017). The dataset made of upper beach topography and bay bathymetry constitutes an important achievement of its own. It was used to generate grids for hydrodynamic models such as FVCOM (Duc et al., 2014b) and EFDC (Duc, 2016), and for the wave model SWAN (Yen, 2018). The dataset also served to estimate the depth of closure of the bay (Binh, 2017), and provided preliminary results on swash studies (Lefebvre et al., 2014, Almar et al., 2014).

Note that presenting all the survey data is obviously beyond the scope of this PhD report. However, as data manager of the Vietnamese group, I organized the data so that they can easily be shared with other scientists for future studies.

4.1.2 Nha Trang 2 experiment (December 2013): Winter monsoon conditions (MOST1)

Objective

The second field experiment (NT2) was conducted from December 4-10 2013 (Figure 4.1). The aim of the survey was to describe the geomorphology of the upper beach and hydrodynamics of the bay during the northeast wave regime associated with winter monsoon with moderate to high-energy shore-normal swell waves (Almar et al., 2014).

General Conditions

During the NT2 experiment, tide range varied from spring to neap tides, from 1.7 m to 0.6 m. Swell waves showed fairly persistent characteristics with $Hs \sim 1m$ and $Tp \sim 8s$ from shore-normal East direction. It is noteworthy that the mega typhoon Haiyan hit the coast on November 14, about 2 weeks before the beginning of the experiment and even if wave energy during NT2 was moderate, the beach was recovering. The alongshore-averaged beach profile (Figure 4.10b) shows an almost constant 0.15 slope throughout the experiment, while morphology changed from linear to convex shape.

Instruments and Measurements

The measurement strategy were basically similar to that of NT1 survey. Measuring instruments were similarly deployed at stations named A, B, C, D, and E (Figure 4.6). However, there are important changes that need to be noted. Most importantly, the cross-transect of aligned measurement stations was moved about 70 m to the north from the NT1 cross-transect. The reason was to be closer to the shore-based camera as to have coincidence of the measurement transect with the time-stack transect line of the camera. Therefore, validation of video observation with field measurements would more appropriate during this survey.

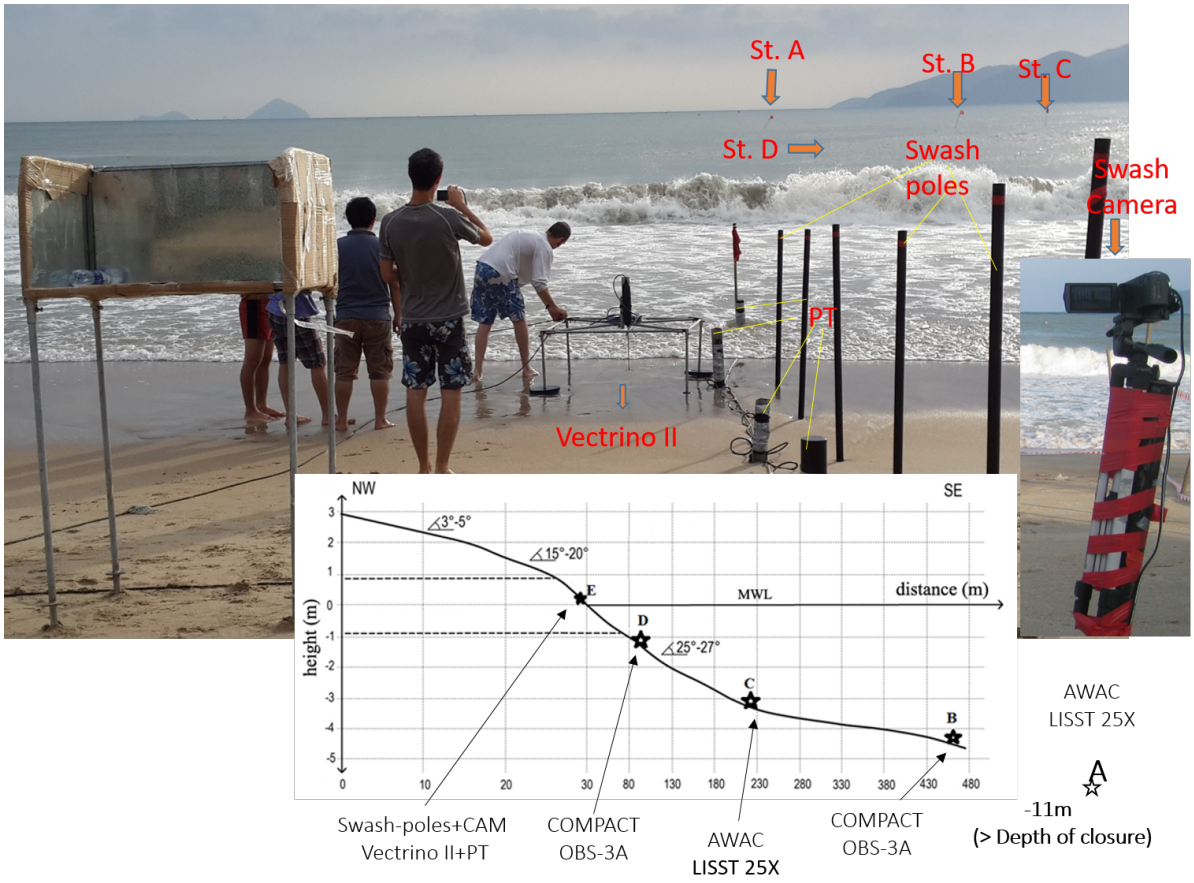

Figure 4.6: NT2 deployment with the indication of location of each instrument.

The equipment used at station A remains unchanged from NT1, consisting of an AWAC and a LISST-25X deployed 892 m offshore and 11-m depth. The equipment used at station B is different from NT1, now including a COMPACT and OBS-3A, deployed 615 m offshore at 8-m depth. The equipment used at station C is similar to station B in NT1, consisting of an AWAC and a LISST-25X, deployed 180 m offshore at 5.5-m depth. The equipment used at station D remains unchanged from NT1, consisting of a COMPACT and a OBS-3A, deployed now 58 m offshore at 1.5-m depth. At station E, for the study of swash processes, Vectrino II devices, swash-poles and a swash-camera is still used in the same arrangement as during NT1. In addition, 4 pressure sensors named PT (Wave Gauge Blue - Ocean Sensor Systems, Inc) were deployed for for swash pole technique validation.

In NT2, for the purpose of studying surfzone bathymetry and hydrodynamics, a device called "Bathymeter" is used as shown in Figure 4.7. A 3-m high triangular metal frame with a GPS (Garmin) and a mirror of theodolite mounted together on top, and an AQUAPRO (Notek) mounted at the base. The theodolite provide an accurate position and altitude of the top of the frame from which to infer the bed elevation. However, the implementation of this equipment in the surfzone is very dangerous when even moderate waves are breaking, as shown in Figure 4.8. This highlights the significant advantage of shore-based camera technology for nearshore wave monitoring.

In the river section, water level fluctuations and river discharge as well as sediment sampling were conducted in the same way as in NT1 survey. The upper beach topography was measured daily in the early morning at the lowest tide of the day by the theodolite. The theodolite was also used hourly to measure the top and bottom elevation of swash-poles between 07h to 17h. However, the bathymetry of the whole bay was not measured during this time. Instead, selected transects were measured until the depth of closure (depth $>$ 11m) (Binh, 2017). The entire cross-sectional profile was obtained by combining topography and bathymetry but it required interpolation in the surfzone, where data was missing.

Achievement

Figure 4.9 shows measurement of tide level and wave characteristics (Hs, Tp and wave direction) at stations A, B, and C using AWACs and OBS-3A. Again, the tide measurements at stations A and C with AWAC and station B with OBS-3A are consistent. Significant wave heights (Hs) measured at stations A, B and C are now much higher, which is expected. The OBS-3A values (station B between A and C) shown in blue solid line are markedly lower. This can be explained by dissipation of the waves as they approach the shore before shoaling. The wave period (Tp) measurements shown in the third panel of Figure 4.9 confirm that all three devices performed well during the measurement period. Surprisingly, the two AWACs in station A and C showed similar values of water level, Hs and Tp, but the wave direction given by the AWAC at station C went wrong. We expect from the northeast winter monsoon that swell direction be perpendicular to the shore, which is confirmed at station A (fourth panel in Figure 4.9). The faulty measurement at station C can be explained by the unsteady AWAC orientation. As reported by the diver when removing the equipment, the counterweight was probably too light to hold the equipment frame steady in the high-energy wave environment.

As for the Bathymeter, although deployment was difficult, as shown in Figure 4.8, the team

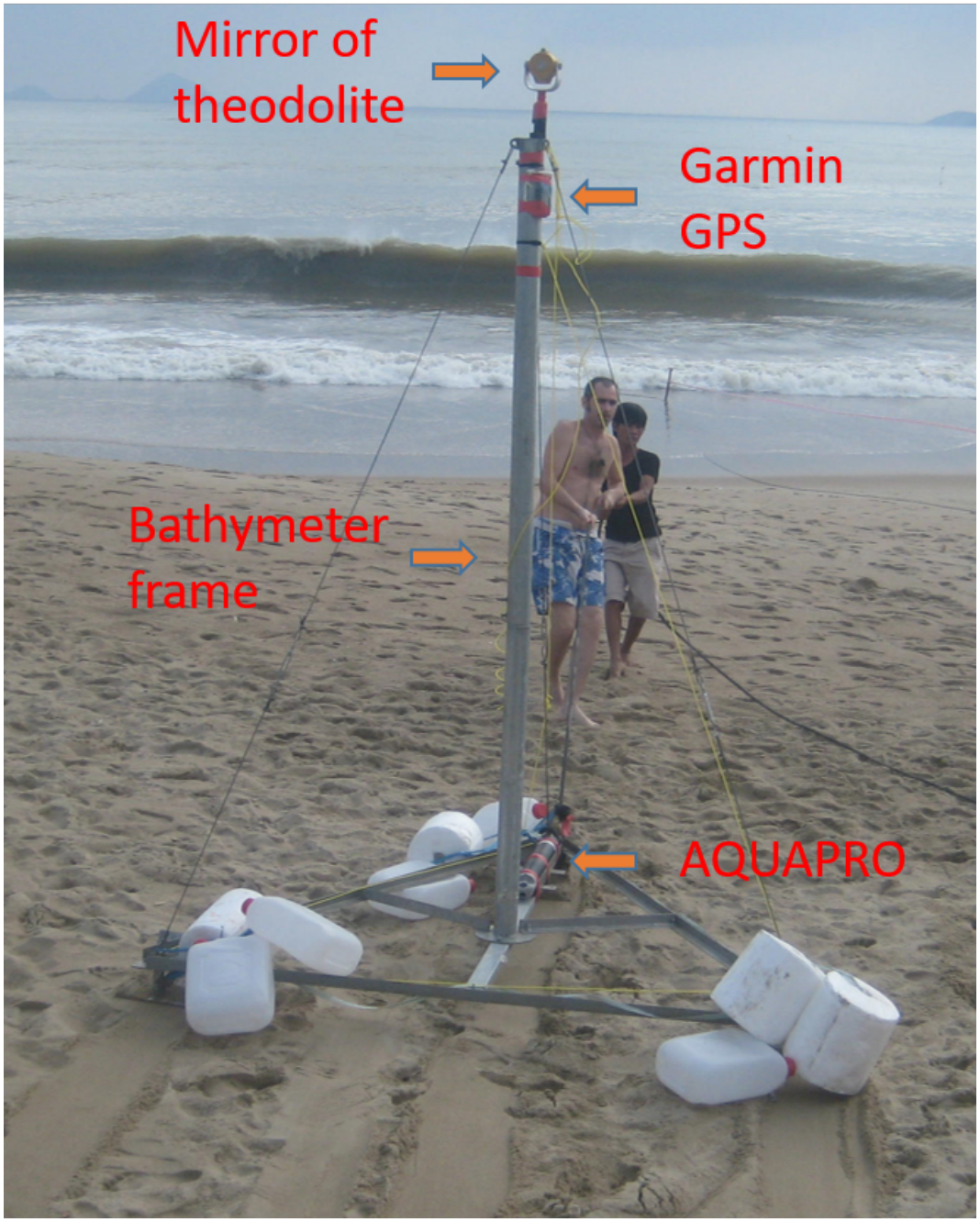

Figure 4.7: The "Bathymeter" prototype designed by Jean-Pierre Lefebvre, LEGOS, Toulouse.

Figure 4.8: An example of how to deploy the Bathymeter. In the upper picture shows to take Bathymeter out of the surf zone, then drag shorward to get the entire profile in lower picture

tried hard to make four measurements, at 14h28-15h39 06/12/2013, 15h50-16h30 07/12/2013, 16h00-16h50 08/12/2013 and 16h57-17h34 09/12/2013 going as far offshore as possible (40 m offshore). However, up to now, the Aquadopp Profiler data has not been evaluated and analyzed. This is a pity but, hopefully, analyzes will be done in a near future. However, our impression is that this Bathymeter prototype does not provide enough stability. With wave energy as high as in winter monsoon, the deployment and accuracy of the Bathymeter is questionable.

Swash-driven alongshore current

Beach reconstruction under mild wind wave conditions is an open question for the research community. This is addressed here. The wave incidence was oblique during NT1 and mostly shore-normal during NT2 (Figure 4.11). In the swash, where the level of turbulence and sediment in suspension are high, this is of high importance for alongshore transport. An ensemble average of the wave field provides a description of currents over a normalized period (Figure 4.12). The oblique incidence observed during NT1 (Figure 4.12.a) generates a northward component of velocity during a swash period whereas no such component is observed for NT2 (Figure 4.12.b). This swash-driven alongshore transport may play a key role in Nha Trang beach recovery during the low-energy summer monsoon, whereas waves are too small to produce any significant longshore drift in the surfzone.

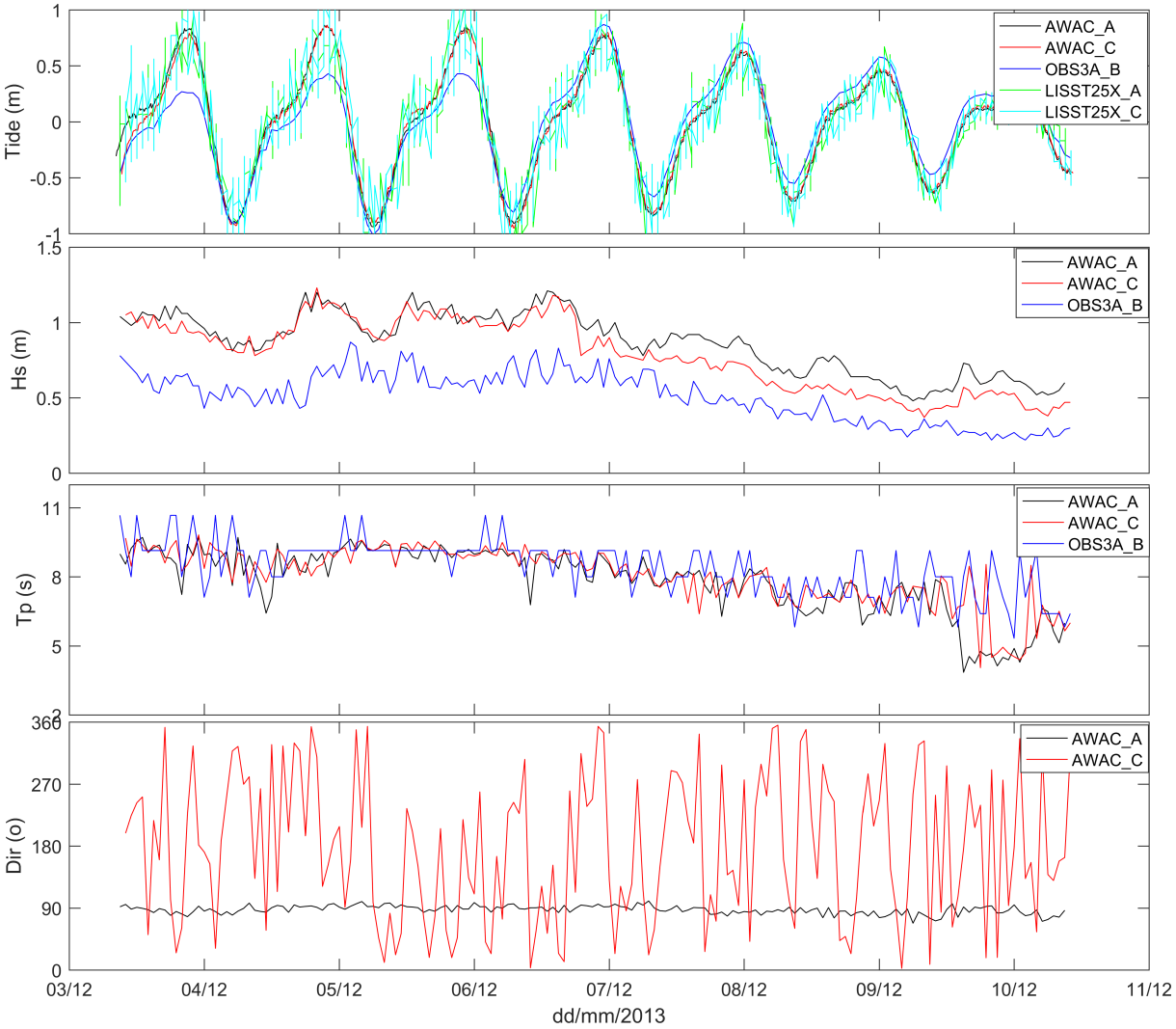

Figure 4.9: Examples of field measurements of tidal (water level) and wave characteristics (Hs and Tp) at stations A, B and C using AWAC and OBS-3A

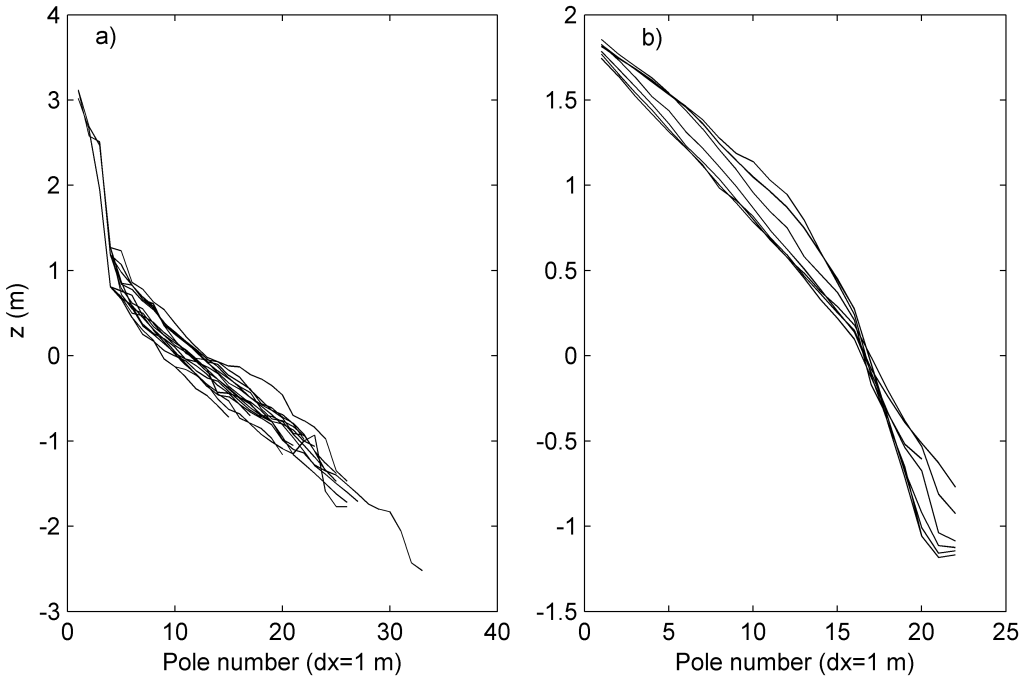

Figure 4.10: Daily theodolite topographic profiles during a) NT1 and b) NT2. After Almar et al. (2014).

4.1.3 Nha Trang 3 experiment (June 2015): Seasonal transition (MOST2/COASTVAR)

Objective

The third field experiment (NT3) was conducted from June 12-18 2015 (Figure 4.1). The aim of the survey was to describe the geomorphology of the upper beach and wave dynamics of the bay during a seasonal transition for a complete assessment of the seasonal cycle. This was the first in-situ wave field monitoring conducted in Nha Trang bay over a continuous period of 6 months (using ADCP). It was also probably the first time that a LTT sandy beach was measured continuoulsy using a LIDAR for more than 6 months.

Installation Instruments

Unlike the other three field surveys, NT3 was the only attempt at establishing long-term monitoring: LIDAR at the shore and in-situ ADCP in Nha Trang bay. On June 12, 2015, a LIDAR system was set up as shown in Figure 4.13. The system consists of a LIDAR (SICK 2D LiDAR sensor LD-LRS3601), mounted on the same street lamp as the shore-based camera system. Internet cable receivers and power lines are provided by wire ropes, connected to the power supply system located in the security office of Nha Trang post office. The signal cable was connected to a desktop PC located in the security office across the street. Electricity is taken through the electricity system of the post office, which has its own private power generation system independent of civilian electricity. This setup ensures stability and continuity, particularly during natural hazards like typhoons. LIDAR operates continuously through the SOPAS software that comes with it, and data is written directly to the desktop PC's 2Tb hard drive. The LIDAR records continuously and writes the data in the computer hard drive via

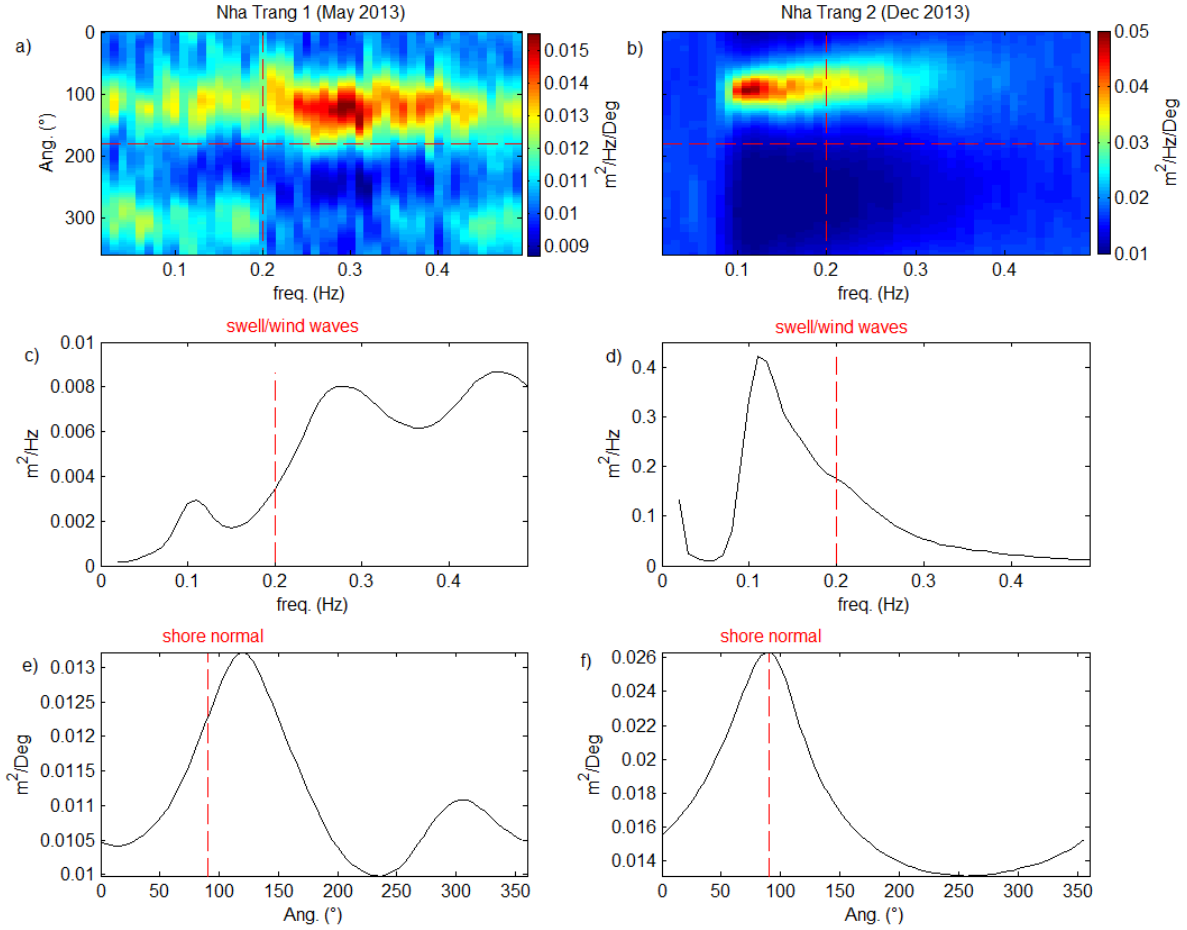

Figure 4.11: Wave energy spectra during NT1 (left column) and NT2 (right column) from 10-m depth AWAC measurements. Upper panels are directional wave spectra, mid panels are frequency spectra, and bottom panels direction spectra. After Almar et al. (2014).

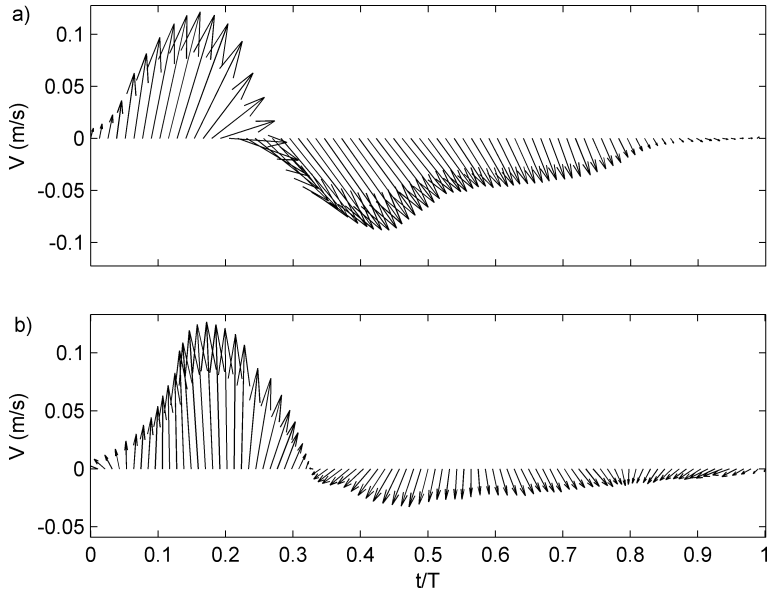

Figure 4.12: Swash ensemble-averaged velocity V (in m/s) from micro-ADV profiler over a normalized swash period for a) NT1 and b) NT2. After Almar et al. (2014).

Figure 4.13: Field photo showing the setting of a long-term LIDAR station at Nha Trang beach.

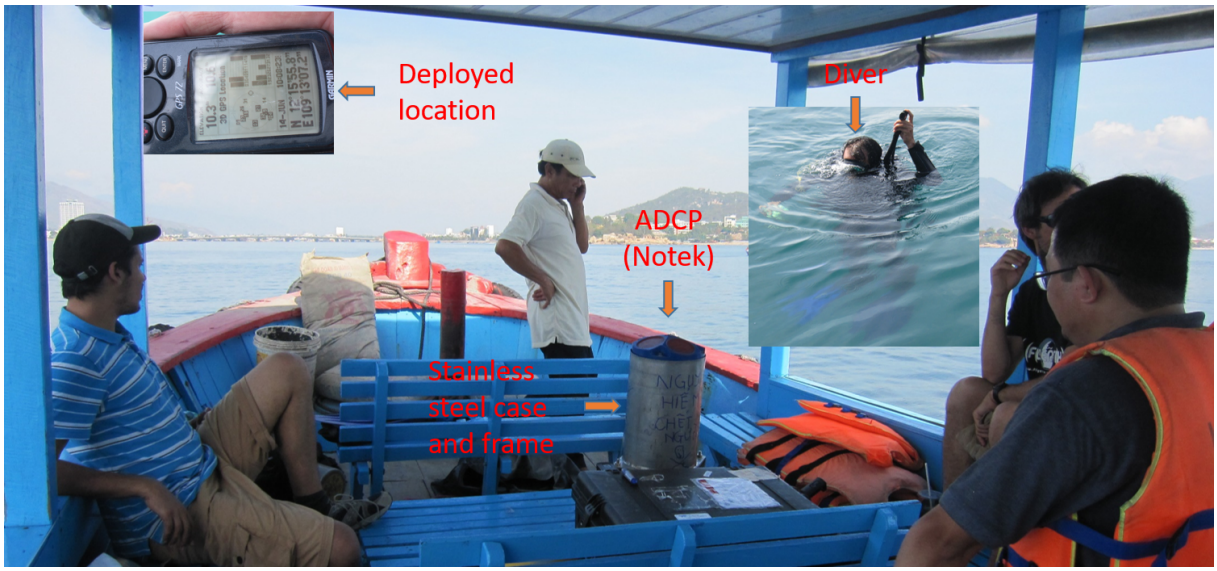

Figure 4.14: Field photo showing the setting of a long-term ADCP station in Nha Trang bay.

the SOPAS management software. With a scan of up to 250 m, the LIDAR scan range covers the whole upper beach until the leg of terrace. The LIDAR activity is monitored daily via the internet and TeamViewer remote control software. Thanks also to local personnel who are post office employees that ensure continuity of internet connections and power supplies, the LIDAR was able to operate continuously for the intended purpose.

For the purpose of getting initial data for LIDAR long-term observations and as a reference for further analysis, on June 10 and 11, 2015, the entire upper beach topography was measured by the theodolite at the lowest tide in the early morning by the same team as for NT1 and NT2. For LIDAR calibration, its transect profile was also measured by the theodolite.

On the morning of June 14, 2015, the ADCP was moored for continuous long-term monitoring as shown in Figure 4.14. The drop position is set at coordinates N12°15′55.8; E109°13′07.1 as shown in Figure 4.14. The ADCP is inserted into a stainless steel tube, and the tube is welded to the frame. The frame was then weighted by eight bags of cement or about 400 kg. Proper installation of the ADCP was supported by two professional divers. Waves were measured continuously for every hour in 15 minutes burst. Batteries were expected to last for 1.5 months so that 4 replacement were operated so as to provide continuous wave data for 6 months.

Achievement

The LIDAR system was not fully automatic, but the experimental designed allowed for remote control at any time. Therefore, the LIDAR recorded from June 13 to October 27, 2015, giving 59 days of data available. The data was generally collected daily during 2 to 3 continuous hours with a sampling frequency of 10 Hz and variable sampling duration. In the typhoon season of 2015 (from August to October) the record was more frequent. In September, particularly, there are 23 days of active LIDAR. unfortunately, the LIDAR data is still in raw form is awaiting for a research team and project to exploit the information.

On July 24, 2015, as part of a survey (July 22-28) after more than a month since installation, I returned to Nha Trang to retrieve data and replace the ADCP battery. Unfortunately, the ADCP had disappeared. Despite our effort at searching for three consecutive days with the help

of professional divers, the ADCP equipment was not found. There are several explanations for the disappearance, e.g., it may have been stolen or unintentionally moved around in the bay by fishermen. But whatever the reason, in the end it was unlucky not to have this data. This is a very important issue because it is extremely difficult to obtain long-term data in the South China Sea (Vietnam East Sea). Most of the equipment is lost if there is no 24/7 live guard at the field, which impossible during harsh conditions such as typhoons or strong winter monsoon events. Here again, remote monitoring methods appear very attractive and can play a very important role in Vietnam marine sciences. This was one of my motivations for conducting this study.

4.1.4 Nha Trang 4 experiment (December 2015): typhoon impact and recovery (MOST2/COASTVAR)

Objective

The fourth field experiment (NT4) was conducted from November 25 to December 4, 2015 (NT4) (Figure 4.1). The aim of the survey was to address the impact of high-energy events (e.g., Typhoons) on the nearshore morphology of Nha Trang beach. The main experiment took place on the usual location in the southern bay (COASTVAR study site). However, in parallel to the main experiment some work was performed at the northern bay (MOST2 project study site). On the 9th day (Dec 3), a workshop was organized on the COASTVAR project to synthesize the results of previous surveys. For NT4, the survey concentrated on measurements of swash zone hydrodynamics (run-up and run-down position, swash depth and flow velocity) and morphological response (bed vertical changes) at wave-by-wave time scale.

General Conditions

The wave and tide conditions during this experiment varied substantially. The first days of the experiment were characterized by large swell with offshore waves recorded by the moored ADCP showing Hs between 0.9 and 1.3 m, and Tp between 8 and 12 seconds, during spring tides. The sustained high waves resulted from a combination of a typhoon and winter monsoon event formed in the northern South China Sea (a not so rare occurrence in this period but poorly recorded for its effect in Vietnam). The remaining four days of the experiment were characterized by mild wind waves, with offshore Hs under 1 m, Tp between 5 and 8 seconds and the tidal range gradually reduced to neap conditions (tidal range $<$ 1 m) (Almeida et al., 2016a, 2017).

Instruments and Measurements

NT4 was the most detailed survey from the largest group of participants among all NT surveys. Apart from the members who were hired by the MOST2 project, there was 20 participants, most of them from France (13) followed by Vietnam (5) and England (2). The equipment used in this field trip and their relative installation positions are shown in Figure 4.15. In particular, the aligned transect of equipment was close to the transect in NT2, only about 10 m to the south.

Unlike NT1 2, during NT4 offshore waves were measured only by one ADCP deployed about 1500 m offshore at a depth of about 15 m. Nearshore waves characteristics such as wave shape at breaking, wave reflection on the inner surf zone, wave dissipation, wave-induced currents and bed

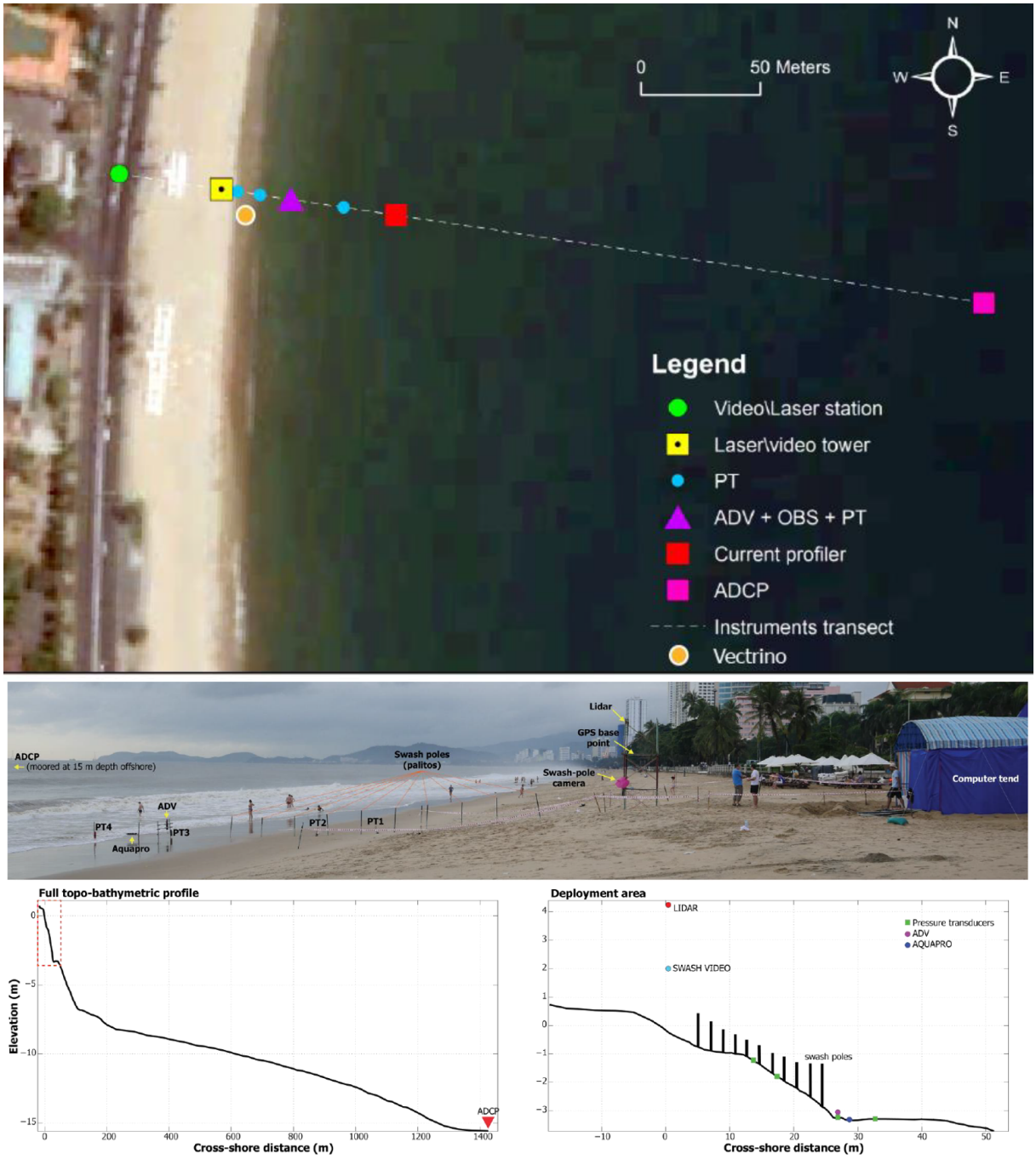

Figure 4.15: Aerial photo of Nha Trang beach with overlaid field instruments locations during NT4. After Luis Pedro Almeida's report

Figure 4.16: Location of equipment in the field

changes on the intertidal terrace were measured at wave-by-wave time scale by a combination of remote sensing and in-situ instruments.

As part of remote sensing, a swash-camera coupled with a system of swash-poles were deployed similarly to NT1&2 (Lefebvre et al., 2014, Ibaceta et al., 2018). In addition, a low-range LIDAR (SICK LMS511-20100) name LIDARlr was attached to a 6-m high iron frame installed on the beach. Power and signal cables for LIDARlr were supplied 24/7 from tents installed on the beach (see for example the middle panel of Figure 4.15). Of course, during this survey two cameras of the shore-based camera system were operating normally and were set to record 24/7 to complement the survey.

Instruments for measuring swash and inner surfzone hydro- and morphodynamics include 4x pressure transducer, an Aquapro and an ADV, in which the vectrino II device was also used in the last two days. The equipment is arranged as shown in Figure 4.16.

During NT4, low tide topographic surveys were performed along cross-shore transects (approximately 10 m spacing) only on the area of interest (about 700 m) of the experiment. Low-tide surveys covers a profile from the top of the beach to the "dry" zone of the intertidal terrace. Topographic surveys were performed using real time kinematic GPS system (RTK-GPS), by walking with a GPS staff with a GPS receiver (Figure 4.17) following pre-installed lines.

RTK-GPS devices were also used to measure the GCPs for drone and shore-based cameras, top and bottom of swash-poles, positions of ADV, PTs, and Aquapro in the early morning at low tide.

In NT4, no bathymetry survey of the whole bay was conducted, but one bathymetry profile was measured on December 3, 2018. The bathymetric surveys were performed using a single beam echo-sounder synchronized with a DGPS system using Hypack software similar to NT1-2 (Figure 4.4). The gap of measurements between the topographic survey and bathymetric survey was manually corrected. However, the gap was not too large because the strategy was to measure topography at the lowest tide of the day (at 6AM on December 3, 2015), while bathymetry was measured at the highest tide of the day.

Figure 4.17: Field photo showing a surveyor performing a topographic survey with a RTK-GPS mounted on a walking staff.

Figure 4.18: The two drones used during NT4.

In addition, the upper beach topography was monitored by cameras mounted on two drones. One is a DJI phantom 3 pro, which is presented in detail in Chapter 7 and the other one is an Hexa drone with a professional Nikon D800 camera for 40 Mpixel images (maximum resolution 7424x4924 pixels) as shown in Figure 4.18. Applying the depth inversion method (Chapter 3) to the video images obtained from DJI Phantom 3 Pro, provided nearshore bathymetry as detailed in Chapter 7.

In order to characterize the sediment bed in the intertidal zone of Nha Trang beach, about 80 sediment samples at the surface and sub-surface (-15 cm) were analyzed. The samples were collected from November 25 to December 4, 2015, at locations shown in Figure 4.19. In the main study site, i.e., south of Cai River, 27 surface and subsurface wet samples were analyzed on site and 6 replicas were analyzed in the laboratory by dry method. North of the river, 12 samples were analyzed and five replicas were left for laboratory analyzes. Two surface samples were collected in the near subtidal zone (0 and -2 m) and analyzed post-mission with a Coulter LS320 laser granulometer (Morio et al., 2016). To study the sedimentary structure of the beach and its variability within 20-30 cm from the surface, vertical sections were also made at the end of the mission (December 4, 2015) at various points of the survey transect (Morio et al., 2016).

In addition to the above field survey, the LEGI team conducted a study on longshore transport in the swash zone by fluorescent sand tracer technique (Komar and Inman, 1970) in combination with a sand-mixing technique (Ciavola et al., 1997) and a method of determining sand dye by camera imagery (Gallagher et al., 2011). The sand mixing depth experiment was con-

Figure 4.19: Location of sediment samples collected during the NT4 field campaign. After Morio et al. (2016)

ducted with a combination of bamboo sticks and rings by Yen (2018) on November 30, 2015. At 8 am on December 1, 2015, at the lowest tide of the day, 200 kg of sand were deposited at the berm in Nha Trang beach (near the main transect) after being dyed and dried. Then at the lowest tide at 8h30 on December 2, 2015, sand dye was determined by camera technique with the aid of UV lamps. Detailed experiments, results and conclusions of experiments are detailed in Appendix D of Yen (2018).

Achievement

Overall, this survey was very successful. In spite of losing one PT on the first day, the rest of the devices worked well and provided good data. The experimental protocol was standardized. For example, the location and implementation time of all equipment, such as ADV, Aquapro, and PTs were carefully recorded and inserted in the data structure. The data from the instrument were digitized into Matlab's mat files and are easy for different teams to use. This survey data has already been used to publish articles on swash zone dynamics and beach recovery during post-typhoon events (Almeida et al., 2016b,a, 2017), combining LIDARlr data with the shore-based video camera to increase the accuracy of 3D intertidal bathymetry (Andriolo et al., 2018).

The fluorescent sand tracer experiment did not proceed as expected. The dyed sand was quickly buried in place rather than transported alongshore. This shows that onshore sediment transport was much stronger than alongshore transport during the survey and this is a characteristic of moderate waves during the northeast monsoon season that are favoring accretion after the combine high-energy typhoon/monsoon event.

4.2 Validation of video estimates with field observations during NT1&2

The results of this section were published in *Journal of Coastal Research* **2016**, 75, 263-267.

In this section, video-based observations of surfzone cross-shore profiles, shoreline positions and wave characteristics (height Hs and period Tp) are calibrated and validated with in-situ measurements from the two first field experiments NT1(from 23/05/2013 to 01/06/2013) and NT2 (from 03/12/2013 to 10/12/2013), including the Haiyan typhoon event (09/11/2013 and 11/11/2013).

In particular, as mentioned in Section 4.1.1) and 4.1.2), The first experiment (NT1) targeted summer monsoon wind-wave dynamics, and the second (NT2) the more powerful winter monsoon swell dynamics. It is also noteworthy that the mega-typhoon Haiyan, which notoriously devastated central Philippines on November 8, hit the Vietnam coast on November 14, about 2 weeks before the beginning of our experiment. Even though wave energy during NT2 was still moderately high, the beach was recovering from the storm. The longshore-averaged beach profiles showed an almost constant slope of 0.15 throughout the experiment, but the morphology changed from a linear to convex shape.

The shoreline location can be obtained using various definitions (Boak and Turner, 2005). Here, it is derived from optical variables (Aarninkhof et al., 2003) as the interface between water

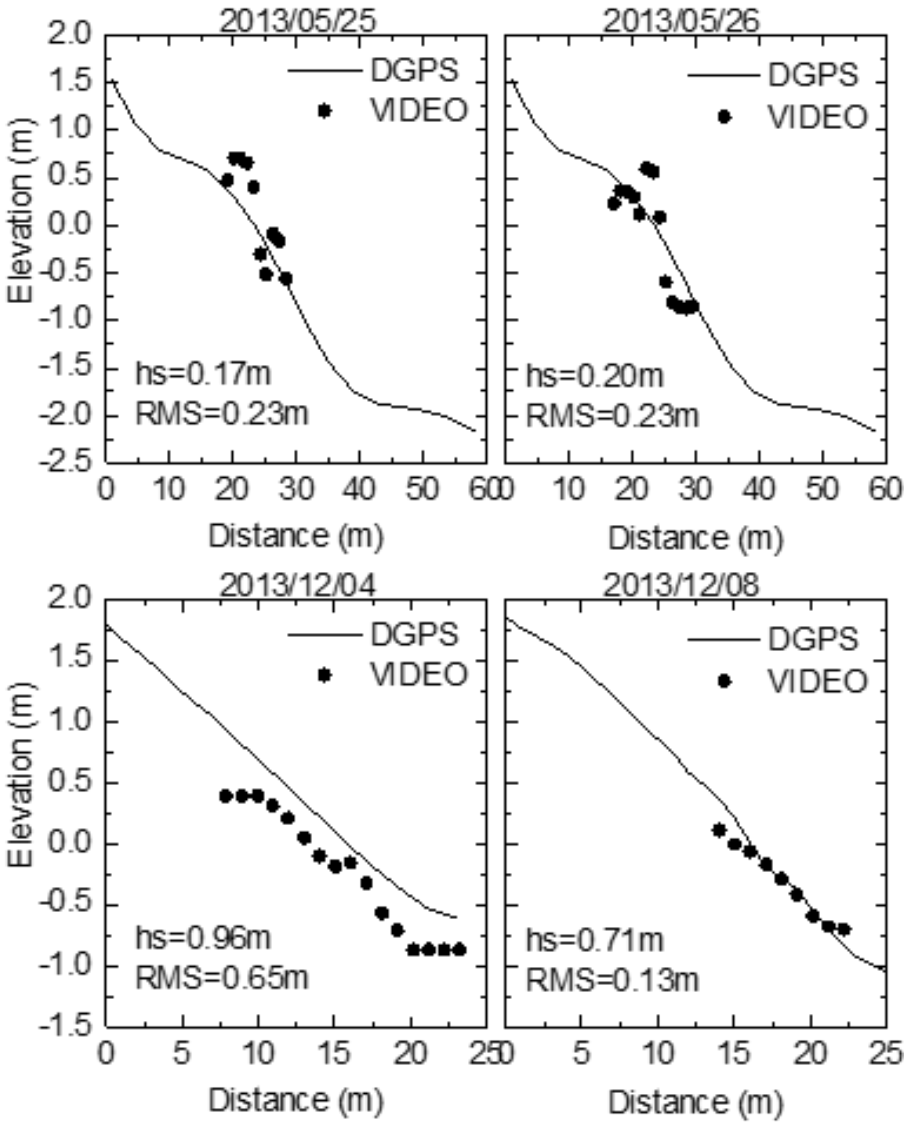

Figure 4.20: Comparison of beach profiles detected by camera and measured by DGPS.

and beach in average images following the two-step method of Almar et al. (2012b) described in details in Chapter 3: a first detection of the red to blue and green pixel transition and refinement by minimizing the variation of shoreline length around its location. This method showed good skills at beaches with complex intertidal zones. Determination of the intertidal beach profile involved the delineation of the shoreline at different tidal levels (Aarninkhof et al., 2003) and interpolation between low and high tides.

Breaker wave height (Almar et al., 2012a), period and surface elevation were determined from space-time images. Surface elevation requires the inversion of total depth from wave celerity (Chapter 3) and removal of the time-mean value over 3 days, assuming that the bathymetry is unchanged during this period of time. More is said about this method in Chapter 6, where tide computation is introduced as the basis for a new error estimation method for video cameras.

In Figure 4.20, video-based and surveyed intertidal profiles are compared. The RMS error is 30 cm in average over NT1 and NT2, which is within the usual uncertainty shown by video techniques (e.g., Aarninkhof et al. (2003)).

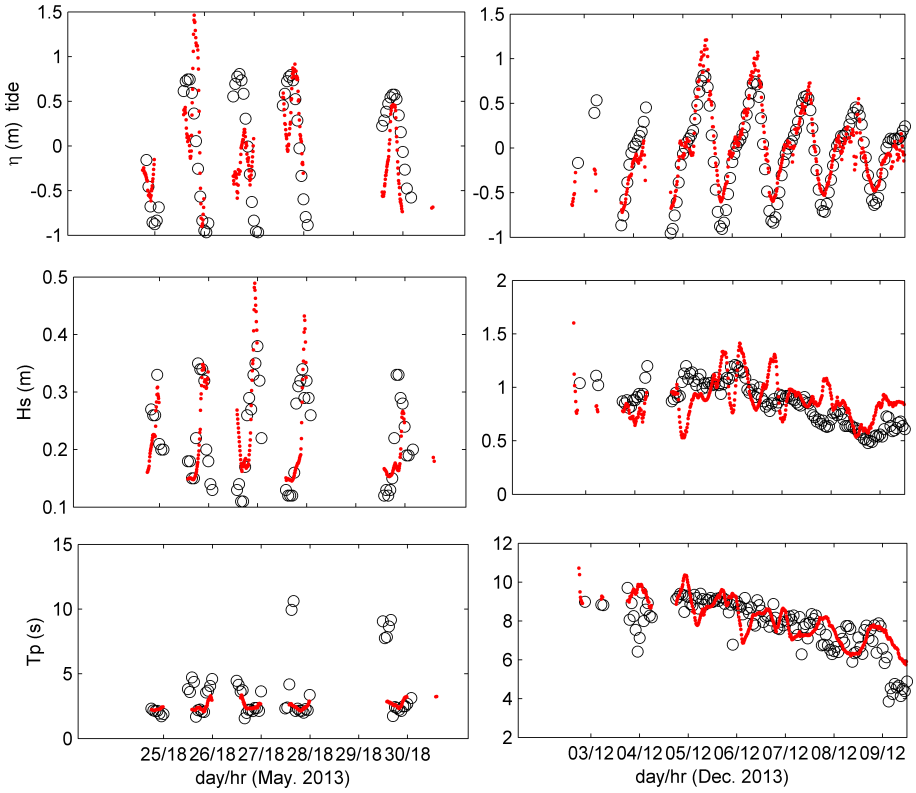

Figure 4.21: Comparison of hydrodynamic properties (tidal elevation, Hs and Tp), from video (red dots) and from in-situ measurements (black circles), for NT1 (left) and NT2 (right).

In Figure 4.21, video estimates of hydrodynamic properties near the breaker point (wave height Hs, period Tp and tidal elevation) are compared with in-situ AWAC measurements during NT1 and NT2. An overall good agreement is found for tidal elevation (RMSE = 34 cm, bias 5 cm), Hs (RMSE = 6 cm, bias 2 cm) and Tp (RMSE = 1.18 s, bias 0.82 s). The skills are better for NT2, probably because of the clearer wave signature (swell waves during NT2 versus wind waves during NT1).

The validation for tidal elevation actually came as a good surprise because it hinted at the possibility of using tides to estimate the error made in inverting bathymetry from wave celerity. This is developed in Chapter 6.

Chapter 5

Shoreline response to a sequence of typhoon and monsoon events

Contents

Abstract

Shoreline continuously adapts to changing multi-scale wave forcing. This study investigates the shoreline evolution of tropical beaches exposed to monsoon events and storms with a case study in Vietnam, facing the South China Sea, over the particularly active 2013—2014 season, including the Cat-5 Haiyan typhoon. Our continuous video observations show for the first time that long-lasting monsoon events have more persistent impact (longer beach recovery phase) than typhoons. Using a shoreline equilibrium model, we estimate that the seasonal shoreline behavior is driven by the envelope of intra-seasonal events rather than monthly-averaged waves. Finally, the study suggests that the interplay between intra-seasonal event intensity and duration on the one hand and recovery conditions on the other might be of key significance. Their evolution in a variable or changing climate should be considered.

Published in *Water* ***2017***, 9, 364

5.1 Introduction

It would be a mistake to consider the vulnerability of coastal regions as a simple response to sea level change, assuming static coastal morphology (Ashton et al., 2008, Davidson et al., 2013). On the contrary, coastal morphology is in a constant process of equilibration at various timescales. It is generally assumed that waves are the main driver of coastal evolution but their role is strongly non-linear, and the coastal response to unsteady forcing is unclear (Cooper and Pilkey, 2004).

Beach recovery to extreme events is also still debated as there is not even agreement on their transient or persistent impacts (Anderson et al., 2010, Ranasinghe et al., 2012). For isolated events, departure from equilibrium is related to the event's intensity and duration (Davidson et al., 2013, Kriebel and Dean, 1993, Frazer et al., 2009). However, no clear conclusion can be drawn when considering a sequence of events, since both enhanced (Ferreira, 2005) and weakened effects are observed (Coco et al., 2014, Karunarathna et al., 2014, Splinter et al., 2014b), e.g., during the particularly stormy winter of 2013–2014 in Europe, e.g., Masselink et al. (2016). The timescales' interplay between recurring events and recovery conditions appears determinant.

Existing shoreline equilibrium models (among others: Davidson et al. 2013, Yates et al. 2009, Splinter et al. 2014a) show appreciable skills in predicting shoreline location from wave energy at monthly or longer time-scales for mid-latitude,storm-dominated coasts. However, these skills may be at fault in a so-called low-energy environment as often encountered in the tropics. There, the beach is mostly active during occasional events and is generally found in equilibrium with the preceding energetic event rather than current conditions (Jackson et al., 2002). Existing equilibrium models might not be able to describe such behavior, in particular when energetic wave events do not occur concomitantly with the seasonal peak of wave energy.

Tropical beaches are exposed to infrequent short (1–3 days) but paroxysmal storms such as cyclones (typhoons in the western Pacific) and can rapidly adapt to these very energetic conditions (Chen and Curcic, 2016). They slowly recover under persisting low to moderate waves during the rest of the year. However, all the tropical environments are not strictly low-energy, and this is particularly true in Southeast Asia as it is affected by monsoons (Chang et al., 2006). Typical winter monsoon events last from three days to three weeks and can bring strong persistent swells of somewhat lower energy but longer duration than tropical storms. There is substantial literature on the atmospheric cold intrusion affecting the Southeast Asian coastal states every winter, e.g., Wu and Chan 1995, but the role of these energetic events on shoreline evolution has not been investigated. Clearly, they are active processes for shoreline erosion and must be compared with the effect of short-term storms. Their particularly long duration may be a crucial element of their beach response as the beach may have sufficient time to adjust to the energetic conditions and reach equilibrium.

In this thesis, we investigate the video-derived shoreline evolution of Nha Trang beach, Vietnam, over the particularly active 2013–2014 season, with numerous winter monsoon events and storms, including the Cat-5 Haiyan typhoon. We first investigate the role of monsoon events on shoreline evolution compared with storms, and secondly the seasonal behavior of the beach in response to both monthly-averaged wave forcing and wave events using a shoreline equilibrium model (Davidson et al., 2013).

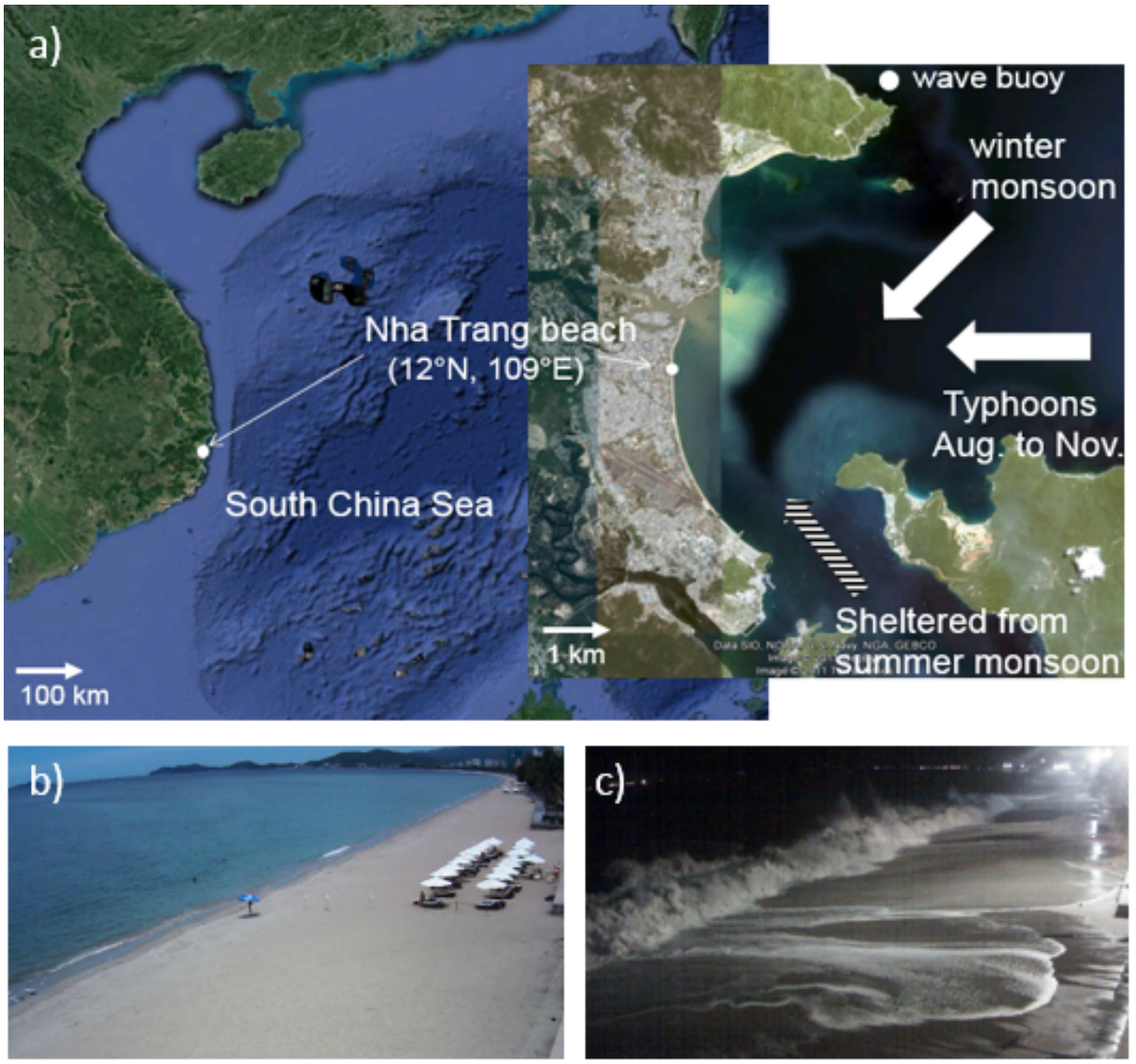

Figure 5.1: Study site, (a) Nha Trang beach, Vietnam, facing the South China Sea (Vietnam East Sea). Images from the video system during (b) calm summer season and (c) Cat. 5 Haiyan typhoon.

5.2 Study Site

Nha Trang is an embayed beach located in southeastern Vietnam coast, facing the South China Sea (Figure 5.1, upper panel). This 6 km bay is oriented north–south and is partially sheltered from waves by a group of islands at its southern end. This medium-sized ($D_{50} = 0.4$ mm) sandy beach is rather uniform along the shore, and is characterized by a steep (slope $\sim$ 0.1) upper face and a flat low-tide terrace ($\sim$ 40 m wide). The tide is a mix of diurnal and semi-diurnal, with a small tidal range ($<$ 1.6 m).

5.2.1 Typhoons

The Northwest Pacific is the most cyclogenetic region on earth. Of the 16 tropical storms that turn into typhoons (JTWC 2013) annually, about one-third propagate westward to South China

Sea (Camargo et al., 2007a). Every year, 4–6 typhoons hit Vietnam (Nicholls et al., 1999), typically between August and December, but the risk of landfall varies strongly at seasonal and interannual scales, e.g., Camargo et al. 2007a, Chan 1985. The year 2013 came after two years of La Niña conditions, resulting in strong sea surface temperatures, which favored cyclone generation (Nakamura et al., 2016a). As a consequence, 2013 was observed to be the most active typhoon season since 2004, and the one with most casualties since 1975. Among the 10 typhoons landing in Vietnam in 2013, Cat. 5 Haiyan in early November turned into one of the world strongest recorded tropical cyclones (Nakamura et al., 2016b).

5.2.2 Monsoons

Summer monsoons (May to September) drive relatively weak, short-period southwesterly waves in the South China Sea. The inception of winter monsoon (October to April), caused by high-pressure systems in Siberia, drives strong northeast winds. Because these pressure systems form every three days to three weeks, wind pulses occur at these timescales. As a result, the winter monsoon generates energetic waves larger than 2.5 m off the Vietnamese coast (Chu et al., 2004), reaching values up to 4 m, which stands for the 10% exceedance level of wave climate (Mirzaei et al., 2013).

From its orientation, Nha Trang region is mainly sheltered from summer monsoon which consists in very calm conditions. It can be considered that this stretch of coast is under the influence of winter monsoons and typhoons only (Lefebvre et al., 2014, Thuan et al., 2016).

5.3 Methods and Data

A video station was installed in May 2013 (Lefebvre et al., 2014) in the central part of Nha Trang Bay, is considered far enough from the influence of the edges of the bay and is predominantly influenced by cross-shore rather than by longshore dynamics (Thuan et al., 2016, Almeida et al., 2016a). Hydrodynamic (waves, currents, tides) and morphology (intertidal and submerged bathymetry and shoreline) can be extracted from secondary images, timestack, and average images (Thuan et al., 2016, Abessolo Ondoa et al., 2016). In this study, the shoreline was extracted manually at a single cross-shore section of the beach. It is estimated as the video-based average between maximum and minimum runup excursions over 15-min images and during daylight and night hours. Hourly tidal modulation of the shoreline location was averaged out using daily means. Wave fields were extracted from ERA-interim global reanalysis provided by the European Centre for Medium-Range Weather Forecasts (resolution of 0.5°, every 6 h [30]) at the closest node off Nha Trang, and validated over a two month period using a local wave gauge. This validation was successful (coefficient of determination $R^2 = 0.87$, RMSE = 0.26 m) down to event scale, which made it possible to extend our study over a full annual period, from 1 August 2013 to 1 August 2014. The period starts from summer monsoon conditions until October, and then winter monsoon lasts until April when a new summer monsoon begins.

Observations of waves and shoreline changes were used to calibrate the parametrical model of equilibrium shoreline position ShoreFor (Davidson et al., 2013, Davidson and Turner, 2009) accounting for cross-shore transport processes. This model was chosen as it was applied success-

fully at various sites for predicting the daily to seasonal shoreline response to waves compared to other models more dedicated to long-term interannual evolution (Ruggiero et al., 2010). This one-dimensional shoreline prediction model has the form

$$\frac{dx}{dt} = b + c(F^{+} + rF^{-}) \tag{5.1}$$

where b and c are calibrated coefficients, r the ratio between erosive and accretive shoreline change, and $F\pm$ is the shoreline forcing, which depends on disequilibrium with anteceding wave conditions

$$F^{\pm} = P^{0.5}(\Omega_{eq} - \Omega) \tag{5.2}$$

where P is wave power ($\propto H_s^2\, T_p$), with H_s and T_p as the deep water significant wave height and peak period, Ω and Ω_{eq} are the instant and time-varying dimensionless fall velocity such as

$$\Omega_{eq} = \left[\sum_{i=1}^{2\phi} \Omega_{eq}\, 10^{-i/\phi}\right] \tag{5.3}$$

with Ω defined as $\Omega = \frac{H_s}{\omega T_p}$, where ω is the settling velocity and is a function of the site-specific median grain size (D_{50}). In Equation (5.3), i is the day prior to present, ϕ the number of past days where the decaying exponential function reaches 10% (more details in Davidson et al. 2013, Splinter et al. 2014a).

5.4 Results

The offshore wave forcing for the one year study period is presented in Figure 5.2a. The southeast coast of Vietnam is partly sheltered from summer monsoon low-energy wind-waves (H_s < 1m, T_p < 4s). The winter season presents more energetic swell ($H_s \sim$ 1.7m, T_p = 7-8s) and larger variability, with largest values ($H_s \sim$ 3m, T_p = 10s) during monsoon events. Waves during typhoon events have similar magnitude but shorter duration (<3 days). The shoreline (Figure 5.2a) is stable or even slightly in accretion till the end of summer monsoon in October, and then begins an erosive phase during winter monsoon until February when it reaches its most landward location, before migrating seaward again.

This seasonal pattern (duration > 30 days) hides important intra-seasonal (or synoptic scale, i.e., winter monsoon events) variability with shoreline variations reaching 10 m during typhoon events and during long-lasting winter-monsoon events with durations from three days to three weeks. Even though the magnitude of shoreline retreat of these events is similar, Figure 5.2a shows that monsoon events have a more persistent impact with longer recovery (i.e., 10 to 20 days) than typhoons which takes a few days at most (sometimes within less than a day). While typhoon events were frequent at the beginning of the winter season, from October to December 2013, the magnitude of monsoon events increased and peaked in January to February of 2014. This coincided with already decreasing monthly-mean wave height but, surprisingly, the monthly-mean shoreline still eroded.

To investigate this two-month lag between monthly-mean waves and shoreline, the empirical

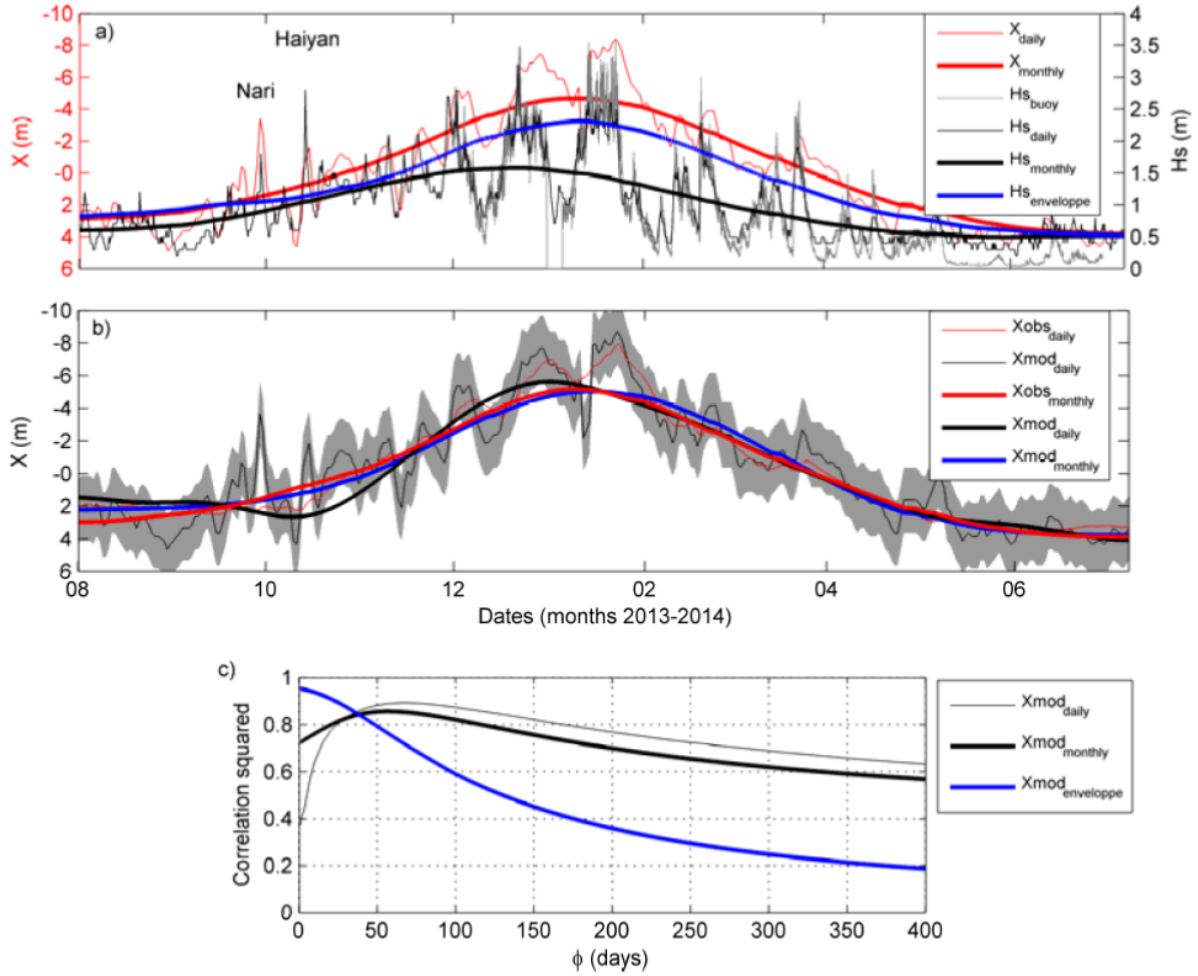

Figure 5.2: (a) Video-derived shoreline location X (red), wave height H_s from Era-Interim (black) and from buoy (gray) off Nha Trang, with the monthly envelope of intra-seasonal H_s (from 3 to 30 days) in blue. (b) Results from the shoreline equilibrium model ShoreFor (black, with uncertainty as shaded area), compared with the observed daily shoreline position (red) and in (c) the respective correlations squared for different ϕ values. In panels a,b, negative and positive X values stand for erosion and accretion from the mean, respectively. In a-c, thin and thick lines are daily and monthly data respectively.

shoreline equilibrium model ShoreFor (Equation (5.1)) was applied on daily wave and shoreline data. In Figure 5.2b the model shows good skills (R^2 = 0.8, RMS = 1.2 m) at intra-seasonal (larger than three days) and seasonal scales but miss short-lived storm impacts. The best correlation appears for a lag ϕ of 50 days (Figure 5.2c), which is much larger than the actual morphological response time of a few days observed at this beach. To investigate this point further, the model was forced with monthly-averaged waves and with the monthly envelop of intra-seasonal events (Figure 5.2b). The latter is done by means of the Hilbert transform, already applied successfully to study wave groupiness (Veltcheva, 2002, Ortega and Smith, 2009), $|H_s^{hf}(t) + \mathrm{H}\{H_s^{hf}(t)\}|^{lf}$ where H denotes the Hilbert transform operator and $||^{lf}$ a low-pass filter operator, taking 30 days as the cutoff period separating short term (hf) and monthly (lf) timescales. Both monthly estimates well predict the seasonal shoreline behavior (Figure 5.2b), although that using the envelope gives more accuracy (R^2 = 0.8 and R^2 = 0.9, RMS = 0.5 and RMS = 0.3 m for monthly-averaged and envelope cases, respectively). Interestingly, the main difference rises from ϕ value in Figure 5.2c, which is similar (52 days) for monthly-averaged and daily data, but 0 for the envelope, indicating that the shoreline is in phase with the monthly envelope of energetic intra-seasonal events. Therefore, the shoreline is in better equilibrium with wave intra-seasonal events than monthly mean wave energy.

5.5 Discussion

One of the most striking points of this study is the wave energy provided by monsoon events and their dominant role on shoreline evolution. In contrast, while typhoons have large ephemeral impacts, our results show that the shoreline recovers rapidly. There is no evidence for a persistent influence, as suggested for short-lived storms by Douglas and Crowell 2000 and Zhang et al. 2002. This is confirmed here using the ShoreFor model that presents good skills at predicting intra-seasonal and seasonal scales but poorly describes short-term typhoon-induced dynamics (see Figure 5.2b, October to November). Recurrence of typhoons is more than 10 days so that they can be considered isolated and without cumulative effect (Ranasinghe et al., 2012). Winter monsoon events have impacts of similar magnitude to typhoons but with longer recovery, which is close to their observed recurrence period. Therefore, they can be considered as a sequence, as the beach cannot fully recover between events and is constantly moving towards a high energetic equilibrium. Note that the ratio of erosion and accretion rates for typhoons is nearly constant over time, but not so for winter monsoons: while the erosion rate is constant, the accretion rate decreases after each new event. This result highlights the importance of the wave event duration, to the extent that the erosive potential will be satisfied only if the event lasts the necessary time for the beach to establish a new equilibrium (Kriebel and Dean, 1993). Thus for short-lived typhoons, the full erosion potential is not achieved. Despite the significant shoreline retreat, the beach profile is likely to be far from a new equilibrium. As a consequence, the shoreline recovery to its previous state (and shoreline position) occurs within a few days and does not affect longer term evolution (Hansen and Barnard, 2010). On the other hand, winter monsoon events have enough duration to achieve their full erosion potential, thus modifying the beach to a fully new equilibrium. The return of the shoreline to its previous position takes longer, leaving the beach more vulnerable and for longer.

It was previously observed that Nha Trang's embayed beach has a seasonal rotation with modulation of waves incidence (Thuan et al., 2016), from northward summer to winter southward transport: the north end of the beach enlarges in summer and erodes in winter, the center of rotation being localized in the central part of the beach (Thanh et al., 2015). It is noteworthy that, even if summer monsoon has only a weak influence compared to the energetic winter monsoon, locally generated wind-waves induce this northward transport (Lefebvre et al., 2014). The shoreline at the central part of the beach close to the video system mainly experiences translation due to cross-shore dynamics and is rather dominated by event scale. This is similar to what has been observed elsewhere (Turki et al., 2013) where rotation and translation of the shoreline were quantified separately.

A main outcome of this study is the long lag (50–60 days) observed between monthly waves and shoreline location, while the envelope (Hilbert transform) of intra-seasonal monsoon events is in closer phase with the shoreline. This suggests that, contrarily to shoreline equilibrium model paradigms (Davidson et al., 2013, Yates et al., 2009), the Nha Trang shoreline is actually in equilibrium with energetic wave conditions. This is in line with observations by Jackson et al. 2002 at low-energy environments where the beach is assumed to be in equilibrium with previous energetic wave events rather than with current conditions. The beach is considered inactive the rest of the time. Here, it is the particularly long duration of winter monsoon events that presumably drives most of the shoreline changes, with very gentle wave conditions in between which limit the recovery potential, as observed elsewhere by Karunarathna et al. 2014. In this sense, the phase-lag observed here between seasonal means and the intra-seasonal envelope is crucial for shoreline equilibrium.

5.6 Conclusions

In this thesis, we addressed the shoreline evolution of the tropical Nha Trang beach, Vietnam, over the particularly active 2013–2014 season. Our results show for the first time that long-lasting (3–10 days) monsoon events have more persistent impact than typhoons (less than 3 days), of similar amplitude but rather transient with fast recovery. The ShoreFor shoreline equilibrium model shows good skills in predicting seasonal shoreline behavior. The seasonal shoreline appears driven by the intra-seasonal event envelope (from Hilbert transform) rather than monthly-averaged waves. Finally, this study suggests that the interplay between intra-seasonal event intensity and duration, on the one hand, and recovery conditions, on the other, might be of key significance. Therefore, their evolution in a variable or changing climate should be considered.

Chapter 6

Video sensing of nearshore bathymetry evolution with error estimate

Contents

Abstract

Although coastal morphology results essentially from underwater sediment transports, the evolution of underwater beach profiles along the diverse coastlines of the world is still poorly documented. Bathymetry inversion from shore-based video cameras set forth a more systematic evaluation and is becoming more commonly used. However, there are limitations to this profiling method that are insufficiently assessed, undermining confidence in operational applications. In this study, we investigate the daily evolution of a Low Tide Terrace (LTT) in Nha Trang beach, Vietnam, under strong seasonal forcing: from weak wind waves during summer monsoon to intermediate swell waves during winter monsoon. A new error estimation for depth inversion is presented based on tidal evaluation. The method compares video-based estimate and direct measurement of tidal amplitudes to provide a quality criterion. It reveals three types of errors, the main one being a deep water error associated with physical limits – loss of celerity-bathymetry relationship in deep water. This error is dependent on wave period and thus has a strong seasonal pattern in Vietnam. It is generally detrimental to depth inversion where wind waves are dominant (in summer here). On the contrary, the second error type is larger for larger waves and is located at breakpoint, altering wave detection. The last error type is due to nonlinear effects and wave setup in shallow water. After removing the faulty data, we finally present the first reliable three-year time-series of a beach profile in Nha Trang, Vietnam. A main result is the overall stability demonstrated for the LTT beach, with rapid exchange of sediment between the terrace and the upper beach during typhoons, monsoon events or seasonal cycles. These tropical environments may provide faster beach recovery compared with mid-latitude configurations.

Published in *Journal of Marine Science and Engineering* ***2019***, 7, 233

6.1 Introduction

Low Tide Terrace (LTT) beaches are a common type of sandy beach but is one of the least documented Abessolo Ondoa et al. (2017a). It can be seen both in low-tide (microtidal) (Wright and Short, 1984, Short, 1996) and high-tide (macro- and meso-tidal) regimes (Short and Jackson, 2013, Karunarathna et al., 2012). While the flat lower terrace area is generally alongshore-uniform, the steeper upper part often presents rhythmic cusps (Troels Aagaard, 2017). The terrace formation is due to a coupling process between the effects of tides and waves. At low tide, waves plunge heavily on the outer terrace, but at high tide, they may pass across the terrace unbroken to surge up the beach face, producing reflection (Miles and Russell, 2004, Masselink and Short, 1993, Almar et al., 2016). LTT beaches belong to the lowest energy of intermediate beaches (Short and Jackson, 2013, Short, 2006); theoretically, it can transform into a transverse bar and rip state (TBR) when wave energy increases and into the lowest energy beach state, which is a reflective beach, when energy decreases. LTT beaches commonly features weak waves and coarse sand.

After more than 30 years of development, many coastal studies produced results using video systems, including for long-term morphological evolution (Holman and Stanley, 2007, Holman and Haller, 2013). However, most are limited to the description of shoreline or submerged-bar location because these are possible in all conditions. Beach profiling from bathymetry inversion is another challenge, and is not commonly tackled even though it is in high demand. Image quality has several sources of error: validity of modulation transfer function, breakpoint discontinuities, wave conditions, weather (lighting), geometrical conditions. Automated extraction techniques are thus known to produce high noise levels (Brodie et al., 2018) that can make physical interpretation difficult. If first-rate data is beyond reach, we need at least to estimate their quality. Recent results from *cBathy* – an inversion method using a Kalman filter (Bergsma et al., 2016) – show that the methodological error can be estimated directly from video techniques (Bergsma and Almar, 2018). However, other error types are due to physical assumptions used in depth inversion. Inversion relies on the linear wave theory that provides a dispersion relation between wave propagation and bathymetry for shallow and intermediate depths. Even though a few studies produce video-based bathymetry estimates – from drones (Holman et al., 2011, Aarnink, 2017) or shore-based cameras (e.g. Brodie et al. (2018), Bergsma et al. (2018a)) – little attention is assigned to error estimates, even though the method is often applied from very shallow to deep waters, without much consideration to the theory's validity.

Quantifying beach morphodynamics requires monitoring beach profiles on a wide range of timescales. Conventional measurement techniques have obvious limitations because they are time consuming, costly and hazardous. These disadvantages do not apply to remote techniques such as shore-based video systems and LiDAR or satellite imagery. Continuous video monitoring now reveals the beach response to wave forcing at different timescales (Pianca et al., 2015, Bergsma and Almar, 2018). In particular, video-based estimation of shoreline position is now rather straightforward, which makes it possible, for example, to estimate the timescales of beach recovery after a storm – about 9 days in Biscarrosse (southwest France), (Angnuureng et al., 2017) and 3 days in Nha Trang, central Vietnam (Thuan et al., 2016, Almar et al., 2017). But these studies miss the full beach profile evolution. For the reasons discussed above, high-

frequency estimates of beach profiles are subject to high noise levels that are often simply filtered. For example, Liu et al. (2012) produce a dataset covering more than 3 years but its time resolution is limited to 7 days after averaging over the tidal cycle and removing poor-quality data due to light intensity. This makes it difficult to study short-term events. But even at seasonal scale, the validity of video-based depth inversion during a low-energy season is not demonstrated.

In the present study, we present the 3-year morphological evolution of a low tide terrace sandy beach in Nha Trang, Vietnam, based on bathymetry inversion from a shore-based camera system. Special care is given to the validity range of data inversion and removal of faulty data based on a new method for error estimate. Then, an analysis of morphodynamics is given at different scales from seasonal to short-term events. The results show that the width of a low tide terrace is an important parameter of beach evolution. The discussion section finally provides guidelines on the limits of video-based inversion for future applications in the diverse coastlines of the world.

6.2 Methods

6.2.1 Study area

Nha Trang beach is a sandy beach located in a semi-closed bay in the south of Vietnam (Figure 6.1). This bay of about 6 km is oriented north-south, facing the fetch limited South China Sea. A group of islands located in the southeast corner of the bay partially shelters it from short to moderate southeast wind waves during summer monsoon. During winter monsoon, however, Nha Trang bay is exposed to long, high-energy northwest swell waves (Almar et al., 2017, Almeida et al., 2016a, Lefebvre et al., 2014, Thuan et al., 2016). The offshore annual mean significant wave height H_s is 0.95 m, with an associated averaged peak period T_p of 6.2 s. Waves show seasonal variability: during fall and winter seasons (October to April), mean H_s is 1.2 m and T_p is 6.8 s, while during spring and summer (May to September) mean H_s is reduced to 0.6 m with a shorter T_p below 5 s. Waves generally hit this sheltered embayed beach with near shore-normal incidence. Nha Trang bay experiences mixed diurnal and semi-diurnal tides (Almar et al., 2017, Almeida et al., 2016a) with a micro-tidal range from 0.4 m to a maximum of 1.7 m.

Several extensive in-situ surveys were conducted between 2013 and 2016 (May 26-30 2013; Dec 3-10 2013; Jun 12-19 2015; Nov 28 to Dec 3 2015; and Dec 20-24 2016), along with more than three years of video monitoring. This dataset revealed the characteristics of Nha Trang beach as a low tide terrace sandy beach with a steep upper beach face (slope ~ 0.1) and a narrow, alongshore-uniform, flat terrace of slope ~ 0.01 and width 10-40 m (Almeida et al., 2016a, Almar et al., 2017). The mean sediment size varies significantly within the bay, with coarse sand in the North ($D_{50} = 0.9$ mm) reducing to medium-to-coarse in the South ($D_{50} = 0.4$ mm) (Almeida et al., 2016a, Morio et al., 2016). Based on three years of 15-min image analyses of the shoreline (Almar et al., 2017), the beach state of Nha Trang beach did not appear to change from year to year. During high-energy conditions beach cusps and mini-rips occurred but the shoreline rapidly straightened after less than 3 days. The submerged beach was not analyzed in these

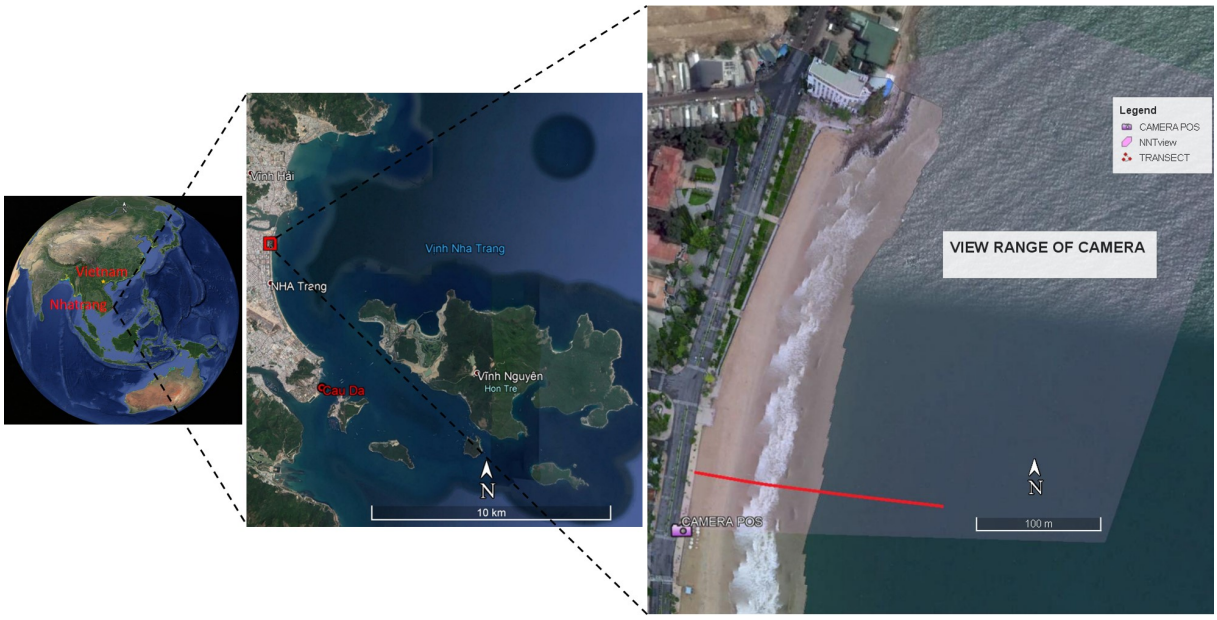

Figure 6.1: Study area in the central part of Nha Trang bay, Vietnam. The Camera view range is represented by transparent pink color, the red solid line presents the profiling location where cross-shore time stack images are created for depth inversion.

studies.

Figure 6.1 presents the configuration of Nha Trang bay and the beach profiling location (cross-shore transect) in the central part of the bay where cross-shore time-stack images are created for depth inversion.

6.2.2 Video data

A shore-based video system (Lippmann and Holman, 1989, Holman et al., 1993, Plant and Holman, 1997) was installed in May 2013 in the central part of Nha Trang bay by researchers of Thuy Loi University in collaboration with LEGOS/IRD-France (Viet et al., 2014, Duc et al., 2014a, Lefebvre et al., 2014, Thuan et al., 2016, Almar et al., 2017). The video station contains two color cameras (VIVOTEK IP7361, max-resolution 1600x1200 pixels) fixed on an existing beach light pole near to the central post office, and are located 70 m from shore and at 14.3 m above mean sea level (MSL). The power of the system was supplied by the post office. The camera recorded data at a frequency of two frames per second stored first in a 64GB SanDisk memory card. The raw video data was then downloaded through Internet connection to a server at Thuy Loi University. From the raw images, three types of secondary images were created every 15 minutes (snapshots, cross-shore time-stacks, and 15 minutes time exposure images). A total of 931 days of data, from 25/05/2013 to 27/08/2016, were used for analysis. Rectification of images from pixel to real world coordinates is accomplished by direct linear transformation using 59 RTK-GPS ground control points (Holland et al., 1997) after correction for the lens radial and tangential distortions (Heikkila and Silven, 1997). With some variation over the field of view, the pixel footprint for cross-shore and alongshore directions is about 0.25 m and 0.05 m, respectively, in the region of interest (surfzone of the instrumented zone). Time-stack images are interpolated on a regular grid using MSL reference and parameters obtained in the

rectification step, with the native time resolution (2 Hz) and a regular space resolution of 0.5 m. The error in celerity caused by floating pixel-position is considered negligible. This is especially true for micro-tidal environments such as Nha Trang beach but probably less for meso- to macro-tidal environments (Bergsma et al., 2016). Tidal data was obtained at Cau Da station at the southern end of the bay. The offshore wave field was extracted from ERA-interim global reanalysis provided by the European Centre for Medium-Range Weather Forecasts (resolution of 0.5° and 6-hourly; Dee et al. 2011) at the closest node off Nha Trang. This assimilated model product was validated over a two-month period using a local wave gauge (Almar et al., 2017). Land and sea morphological surveys were conducted over the study period, and are also used in this study to validate video estimates.

6.2.3 Depth inversion along a cross-shore transect

First, cross-shore timestack images are pre-processed to improve the wave intensity signal. A pass-band filter between 0.05 and 0.5 Hz is used to remove low-frequency (light variations due to clouds) and high-frequency components (rapid adjustment of the camera "auto-iris"). Then, the signal is normalized by dividing the intensity wave signal with the local intensity maximum (Almar et al., 2008).

Second, a temporal cross-correlation method (Almar et al., 2008, Bergsma and Almar, 2018) is applied to invert time stack images for water depth. This method derives wave celerity from temporal cross-correlations. At each location X, a correlation is computed between time series of neighbor locations ΔX, adding a time lag $\Delta\phi$ to neighbor time series. A matrix of resulting correlation coefficients M is obtained as a function of X and ΔX:

$$M(X, \Delta X) = cor(\eta(X, t), \eta(X + \Delta X, t + \Delta\phi)) \tag{6.1}$$

The maximum correlation value of M for a selected range of ΔX gives the average distance ΔX_0 made by the waves within $\Delta\phi$ at each location X. This can be converted to a celerity C:

$$C = \frac{\Delta X_0}{\Delta\phi} \tag{6.2}$$

The use of a time lag $\Delta\phi$ is preferred to a direct cross-correlation, which gives the wavelength L for an associated period T, then $C = L/T$. This is motivated by a better spatial resolution ($C\Delta\phi$ instead of L) that allows resolving smaller-scale bathymetric features. $\Delta\phi$ must be chosen less than or equal to T. $\Delta\phi = 3$ s is a reasonable value for most wave conditions.

6.2.4 Using tide as a quality proxy

As discussed in the introduction, a major challenge for depth inversion is to assess the validity of the method associated with methodological and physical errors, which varies with wave and tide conditions. A rational approach is needed to identify erroneous data and extract a useful dataset. Here, we propose a novel way to quantify the quality of daily data based on the availability of a local tidal gauge.

Figure 6.2 shows an example of image analysis for the morning and afternoon of May 15

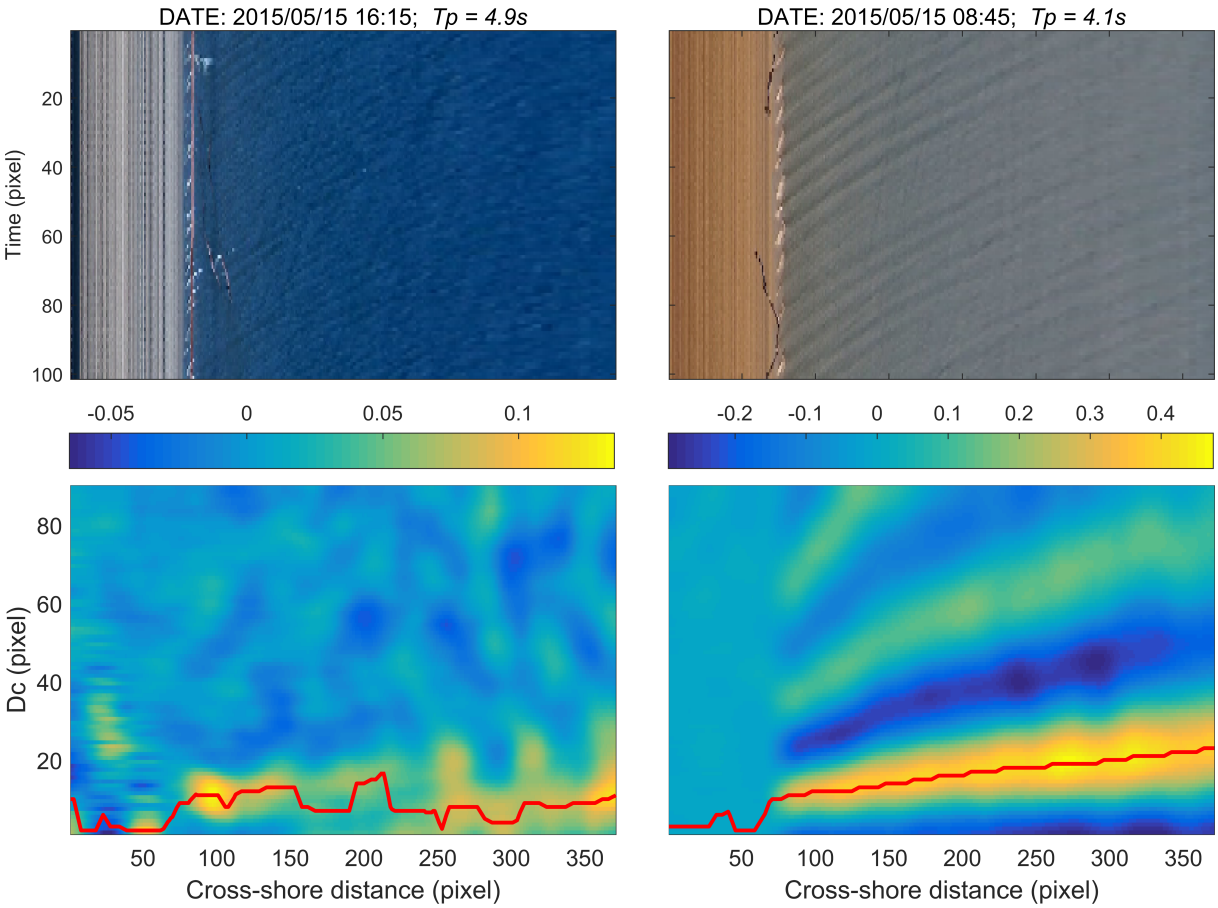

Figure 6.2: Example of image analysis for the morning (right) and afternoon (left) of May 15 2015 where short wave conditions prevailed. In the afternoon, choppy local wind waves are superimposed on the morning spectrum. Top and bottom panels, respectively, present cross-shore time stack images and cross-correlation matrices used for celerity extraction. The lower left axis label Dc is the maximum searching range (in pixels) and the red solid line is the first peak of cross-correlation that gives the distance traveled by waves in $\Delta\phi$ seconds at each location.

2015, where short wave conditions prevailed. The morning presents clear swell conditions on the cross-shore time stack image, leading to a smooth cross-correlation matrix and straightforward celerity estimation. The afternoon presents more choppy conditions with local wind waves perturbing the sea state to the point where the cross-correlation matrix cannot be of any use. Higher frequency cameras could improve the detection of wave propagation from that image but correcting noise level is not sufficient for proper depth inversion. The problem is deep water limitation (see Discussion section) as the waves here are too short to interact with the sea bed, unless they get very close to shore. As a result, both morning and afternoon images are unfit for depth inversion, independently of noise level. To cope with the physical validity of depth inversion and more generally with any sources of error, we designed a simple method.

Assuming little morphological evolution during one day, any variability of water depth within this day can be associated with tides. In this case, the video-based depth estimate D can be split into a daily averaged component, i.e., the bathymetry h varying with sediment transport

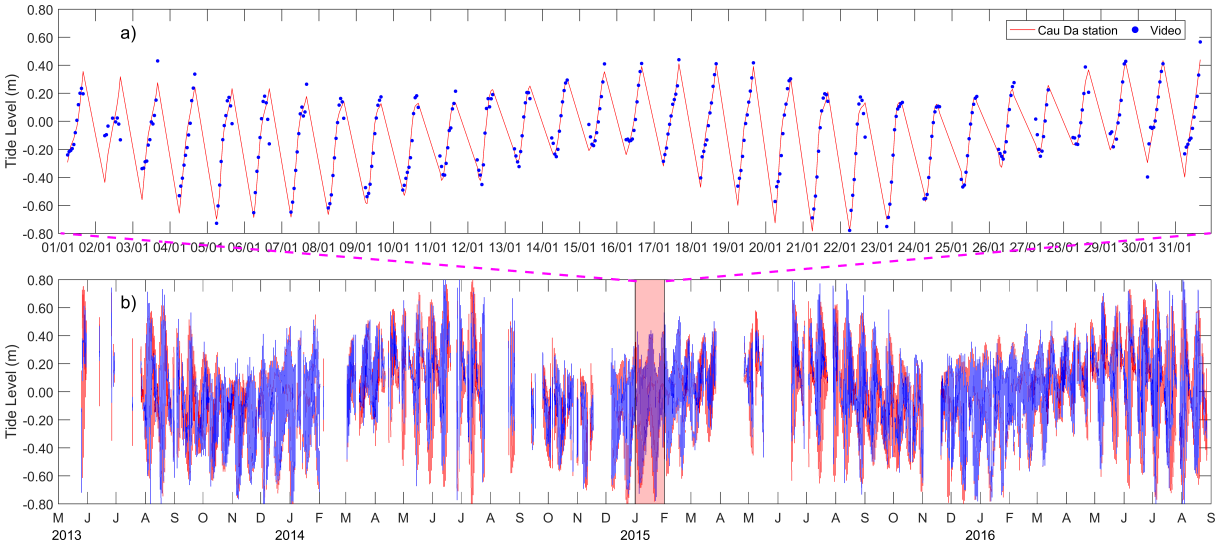

Figure 6.3: Comparison of tides between the signal recorded at Cau Da station (red) and video-based sea level (blue). Panel a) shows the zooms of the time series during selected days and panel b) shows the time series of whole data set.

according to the Exner equation[1] , and an anomaly η varying with tides:

$$D = h + \eta \tag{6.3}$$

We extracted the video-based tidal signal η as a time anomaly of the inverted depth:

$$\eta = D - \overline{D} \tag{6.4}$$

where $\overline{D}$ is a 3-day moving average of D, assumed to equal h. The extracted tidal signal from depth inversion is shown in Figure 6.3 together with tidal gauge measurement. Abessolo Ondoa et al. (2018) recently evaluated sea level from video inversion at Grand Popo Beach (Benin, West Africa), but did not use it to construct a simple error estimator, which is our present proposition. For the tide gauge time series, we also remove a 3-day moving average, similarly to the video data, for consistent removal of atmospheric effects on sea level (inverse barometer and Ekman drift). The comparison with tidal measurements in Figure 6.3 shows generally good agreement, particularly in winter and away from breakpoint and very shallow waters (the three error types that will be discussed in more details later). For error estimation, we compute the root mean squared errors (RMSE) between video and tide gauge measurements of high-frequency (tidal) sea level for each day in the time-series. The good days are assumed to be those with RMSE less than 0.2 m. We will come back to the error estimate in more details in the Discussion section.

6.3 Analysis of beach profile evolution

Here, we present a beach profile analysis for Nha Trang during the three year measurement period. We will focus on the terrace width and its evolution at seasonal scale and as a response

[1]The Exner equation states that the time change of bed elevation h varies with the divergence of sediment flux q_S: $\frac{\partial h}{\partial t} = -\frac{1}{\epsilon_0}\nabla q_S$, where ϵ_0 is the grain packing density

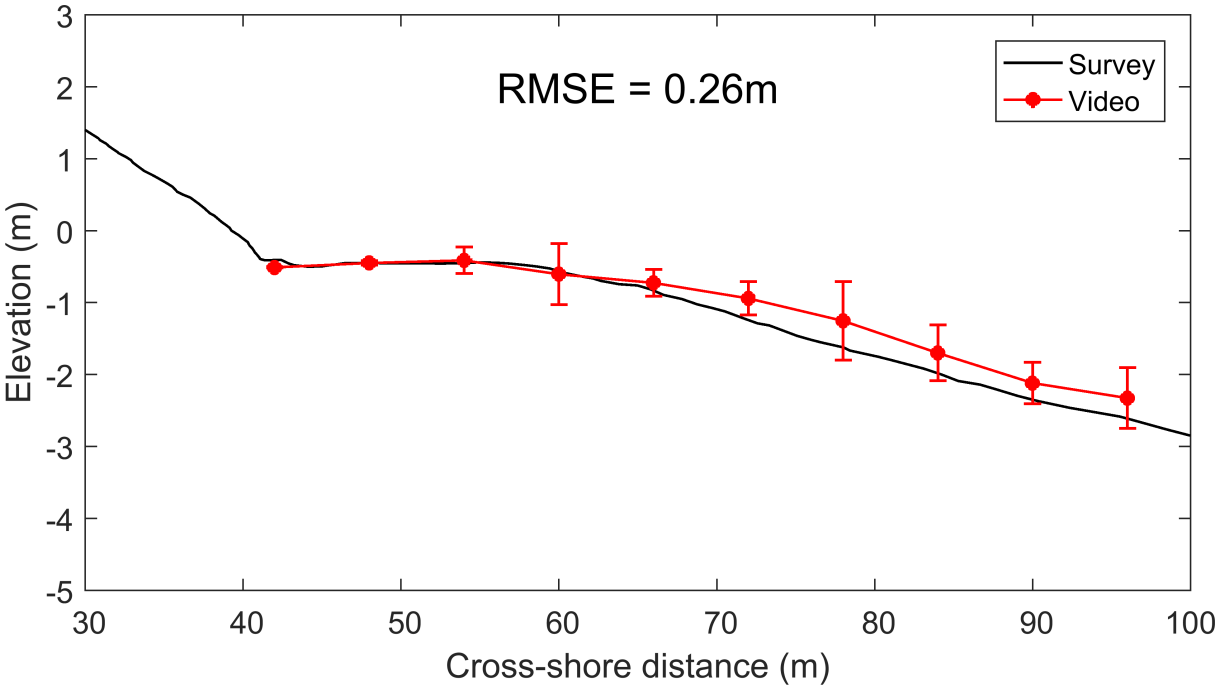

Figure 6.4: Comparison between observed beach profiles during NT4 field survey (Nov 28 to Dec 4 2016) and video-based depth inversion. The solid black line represents the measured profile in Dec. 3 2016 and the dots represents the 7-day average video-based ground-true elevation with error bars that are 4 × standard deviation.

to intense winter monsoon events. As explained in the previous section, data quality control is essentially provided by the error estimate based on tides. But some comparison with bathymetry surveys were also done for validation. The example of Figure 6.4 during the NT4 survey of fall 2016 shows that the main aspect of the profile, i.e., the terrace, is captured by the inversion method.

6.3.1 Bathymetry evolution

Figure 6.5 shows wave forcing and beach response over the 3.5 years of the study period for the profiling location presented in Figure 6.1.

Wave forcing exhibits variability at multiple scales. Wave height H_s is provided by ERA-I while the peak period T_p is derived from the video images and thus better accounts for local waves. The seasonal scale clearly stands out with high-energy northeast swell waves during winter monsoon (October to April; $H_s = 1.7$ m, $T_p = 6$ s) and small local wind waves during summer monsoon (May to September; $H_s = 0.5$ m, $T_p = 3$ s). Interannual variability is also present but largely as a result of intrinsic variability of strong winter monsoon events (3 days to 3 weeks; $H_s = 3$ m) that largely imprints the signal in winter. Short-term events (< 3 days) are associated with typhoon landing but their imprint is more sporadic (from October to December essentially) and not considerably stronger than monsoon events.

Cross-shore time stack composite images are useful to visualize and understand the evolution of shoreline position (red line). This has been analyzed in detail in Almar et al. (2017) and the results will be summarized in the following for interpretation of beach profile evolution. The

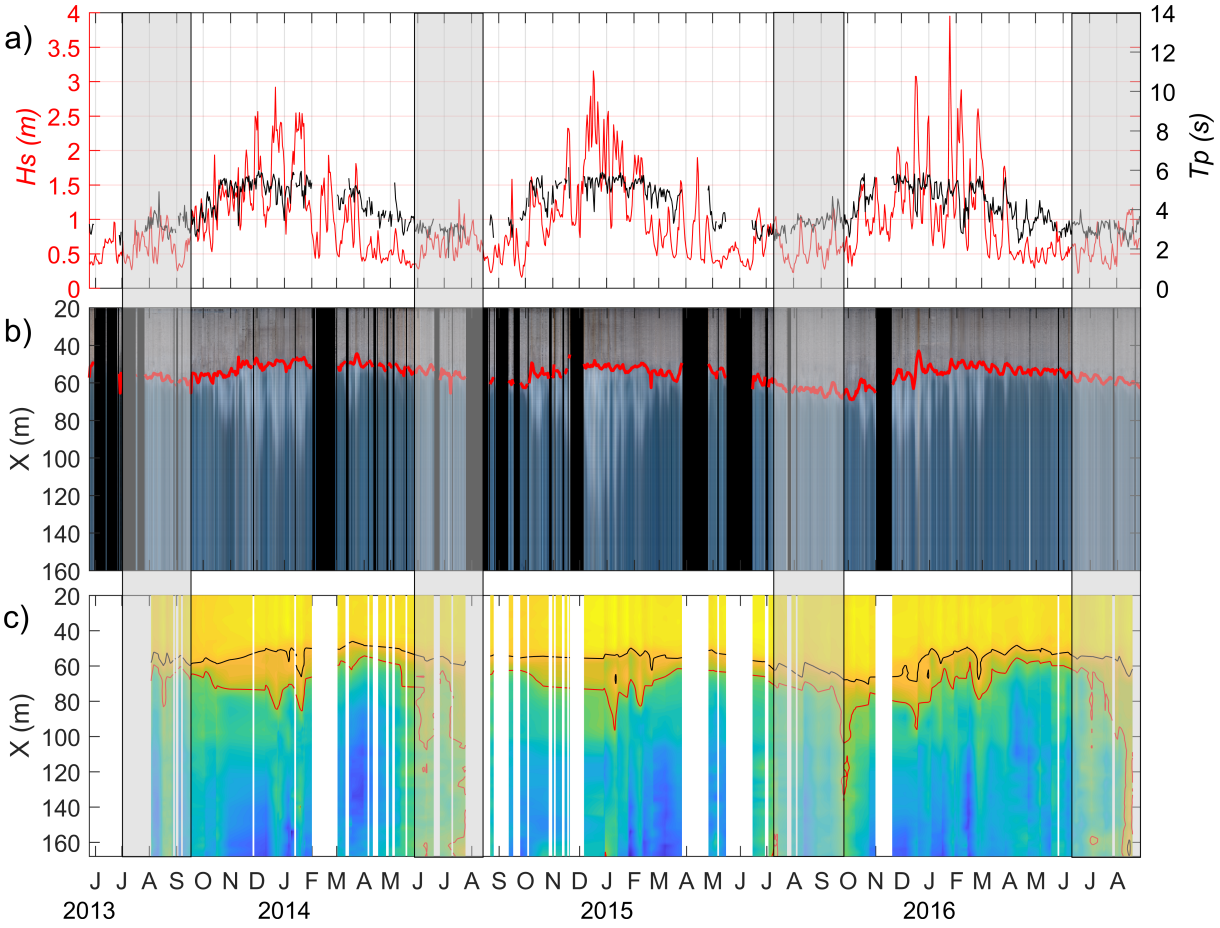

Figure 6.5: Long-term evolution of a) off-shore wave forcing: the red line represents significant wave height H_s from ERA-I and black line the peak wave period T_p computed from video images; b) daily mean cross-shore time stack video images in RGB band color, where a red line marks out the shoreline; c) Daily bathymetry from video inversion (colors), where the low tide terrace area is indicated between a black contour at -0.5 m and red contour at -1.3 m. Note the shaded bands covering the summer season. These were drawn from our error estimate analysis and roughly indicate that wind waves with period less than 3-4 seconds cannot be used for depth inversion.

last panel is a cross-shore time stack composite of video-based depth inversion and presents the evolution of beach profile. The low tide terrace is represented by contour lines of -0.5 m and -1.3 m depth. In the following, we concentrate on the response to seasonal and monsoon events.

6.3.2 Seasonal pattern

Figure 6.6 shows wave forcing and beach response over a mean annual period over the 3.5 years of the study and a low-pass filter reveals seasonal patterns (time scale > 30 days). Unfortunately, during summer, the amount of "good" bathymetry data is too little to allow any reliable observation (see Discussion). Nevertheless, the end and beginning of winter monsoon (with decreasing and increasing wave energy) provides useful information on the transition to summer period, so that a sense of seasonal evolution can be extrapolated. Shoreline evolution — which is available all year long — can help complete the picture.

From February to the end of summer monsoon in October, the shoreline position is stable at first, then accreting more rapidly. In September, it begins an erosive phase due to winter monsoon conditions until February when it reaches its most landward location, 10 m from its summer position (Almar et al., 2017).

The terrace follows an opposite behavior, with a terrace width becoming narrower with decreasing wave energy and wider with increasing energy. There is thus good correlation at the seasonal scale between the evolution of wave energy, shoreline and terrace width. From September to December, when wave energy increases the shoreline erodes at the same time that the terrace expands. Then, from January to April, wave energy decreases while the shoreline begins its recovery and the terrace width decreases from 18 m (January) to 9 m (April). Interestingly, the speed of terrace evolution is much faster in this period than that of shoreline recovery, which is maximum in summer. This can be explained by different sediment fluxes during the periods of increasing and decreasing wave energy. During increasing energy, the terrace expands at the expense of the shore face, while during the decreasing energy, the terrace appears to loose sand to the offshore slope as much as to the shore face.

6.3.3 Impact of winter monsoon events

Besides a strong seasonal cycle, the coast of Vietnam is largely impacted by intense winter monsoon events that last from 3 days to 3 weeks (Almar et al., 2017). Typhoon events are also present but they are less numerous and of shorter duration (see next section). To identify the events, the Peak Over Threshold method (POT) (Dorsch et al., 2008, Angnuureng et al., 2017, Castelle et al., 2015, Abessolo Ondoa et al., 2017a) was applied on the offshore significant wave height (H_s) provided by Era-interim. The 2% exceedence threshold was used to identify strong events. Then, to characterize their general impact, we construct a composite beach profile as an ensemble mean of all events, thereby providing statistical reliability. Note that the composite hides some of the variability associated with winter monsoon events. For example, shoreline variations can reach 10 m during the strongest winter events but only half of that remains in the composite. Figure 6.7 presents the composite event for the periods before and after occurrence (day 0): wave forcing (wave height and period), shoreline position, and terrace width.

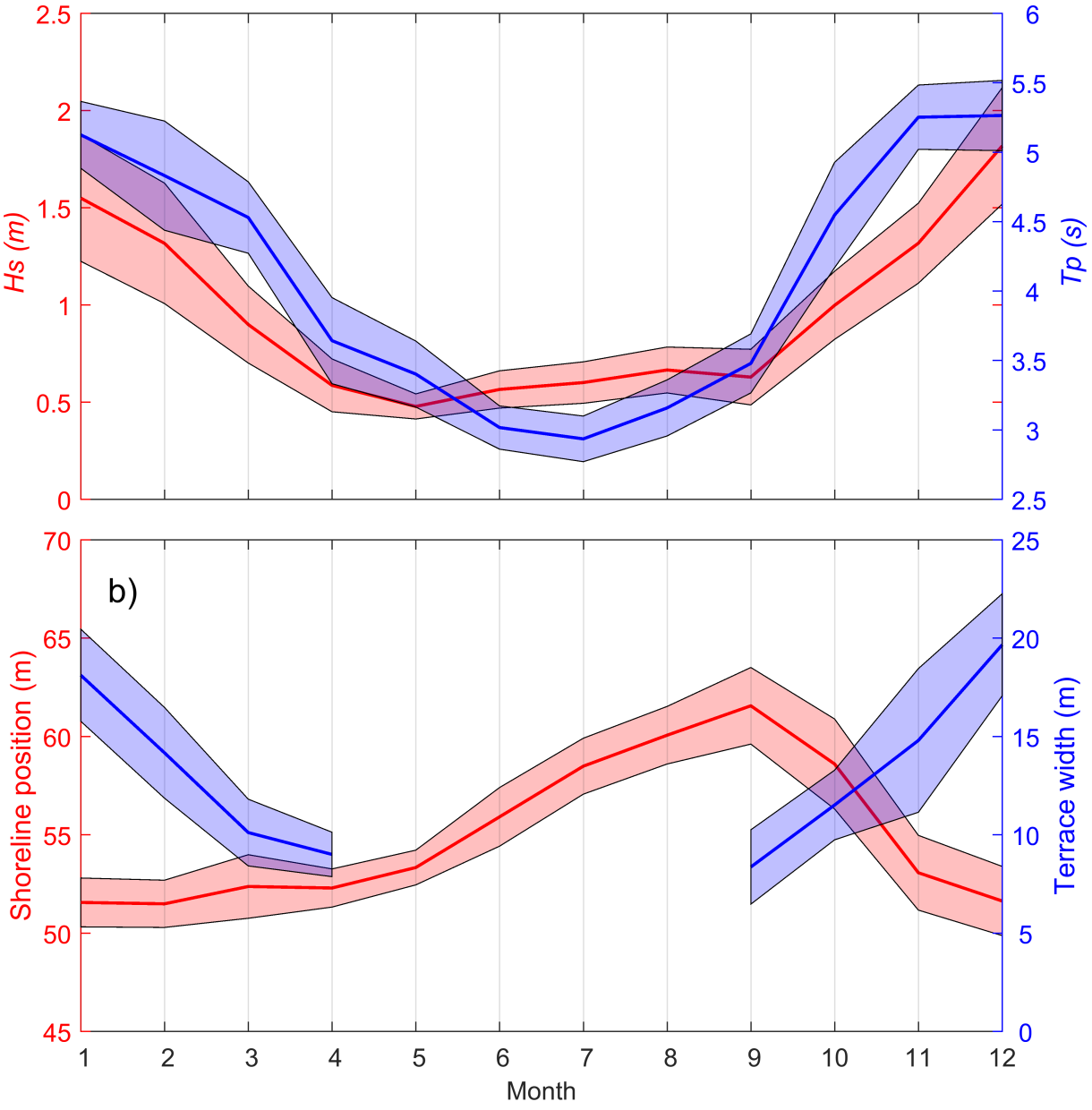

Figure 6.6: Monthly-mean climatology of a) offshore significant wave height (red) and nearshore peak wave period (blue); and b) Shoreline position (red) and terrace width (blue), where solid lines indicate monthly average and the standard deviation represented by shaded zones in all the plots.

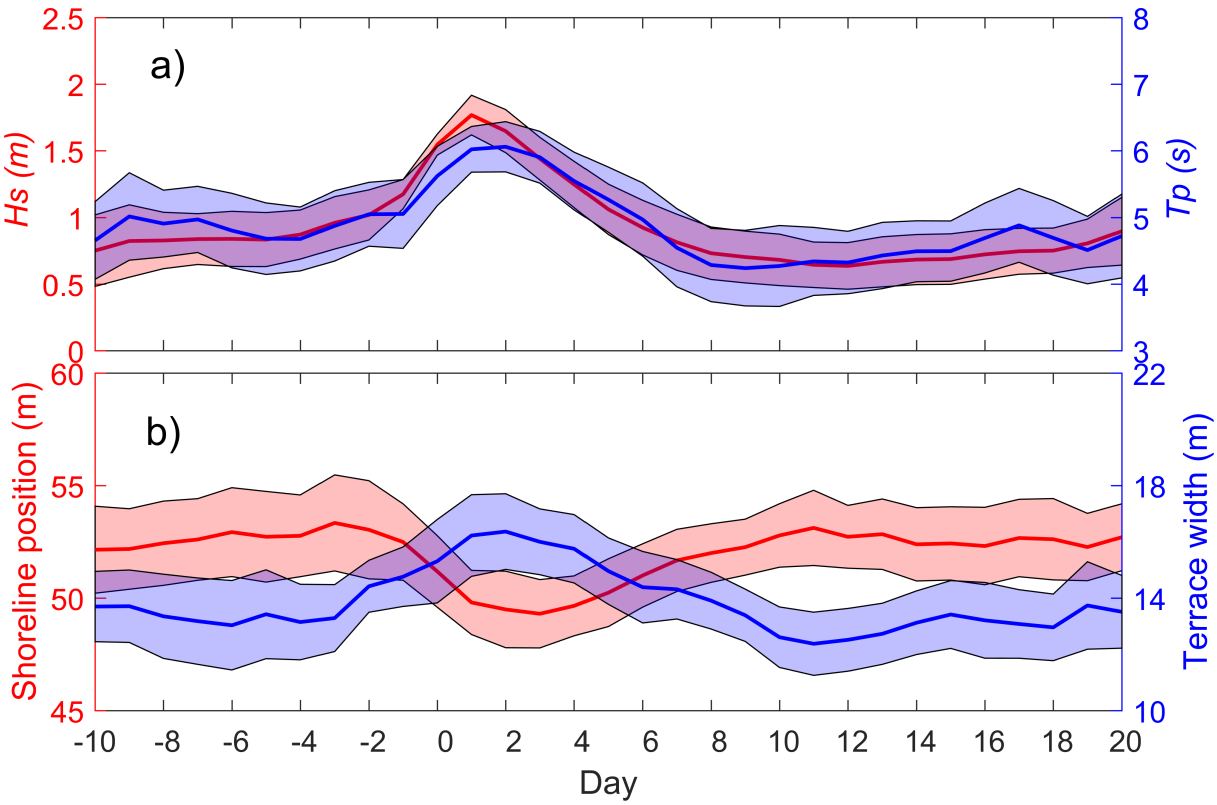

Figure 6.7: Ensemble-mean of all winter monsoon events: a) offshore significant wave height (red) and video-based nearshore wave period (blue); b) shoreline position (red) and terrace width (blue). Standard deviation is represented by a shaded area in all cases.

Day 0 for each event is defined as the time when wave height crosses a given threshold that must be high enough to be considered an event. For that reason, the composite event appears to start a bit earlier around day -2. The wave height rises during 3 days from the onset of the event where it reaches a peak value of a bit less than 2 m. At the same time, the peak period rises as well, indicating the presence of longer swell that has developed across the South China Sea. The wave height and period then slowly reduces over about a week.

As the swell picks up the shoreline quickly retreats about 4 m in 3-4 days and then slowly recovers in about 9 days. The terrace width follows a very similar pattern, but with a negative relationship. It first rapidly increases about 4 m following the rise of wave height and then slowly recovers as waves decline. The average post-event beach recovery duration is thus about 9 days both for the shoreline and terrace, i.e., the whole beach profile. Clearly, shoreline erosion is a process that provides sand to the terrace and inversely, shoreline accretion feeds on the terrace during recovery. The low tide terrace is thus the sand reservoir of the beach and is easily accessible.

6.3.4 LTT beach state dynamics and recovery

Interestingly, while the beach shoreface adapts to changing wave conditions, it never changes its state as a low tide terrace. For example, transition to a barred beach could be expected during high energy conditions, but does not seem to occur. This suggests that LTT beaches are a stable type and can handle a large variety of waves and tides. One of the most striking properties of

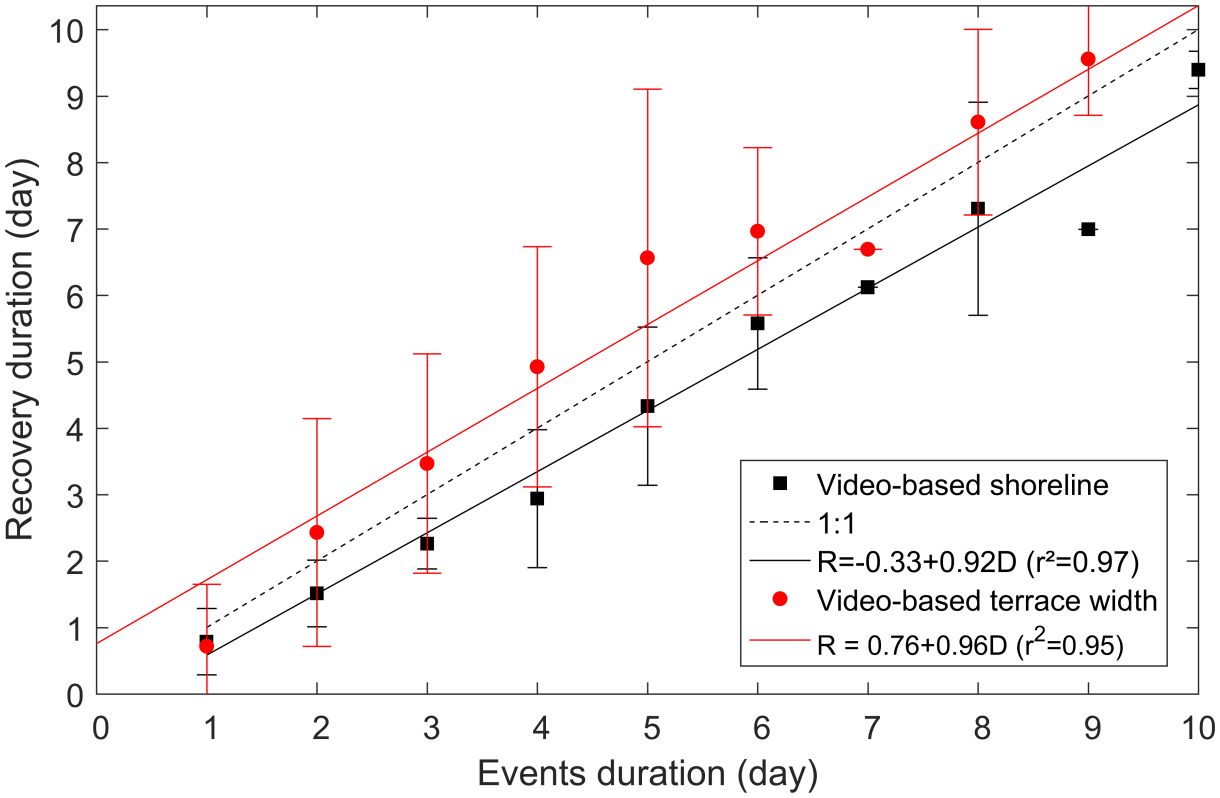

Figure 6.8: Relationship between events duration and recovery duration. Error bars indicate the dispersion within events of same duration.

LTT is its rapid response time. This can be attributed to the fast exchange of sediment between the upper beach part and the terrace. It can be compared to a barred beach, which typically exhibits a response time larger than 10 days (Angnuureng et al., 2017), due to slow exchange of sediment between the bar and upper beach.

The relation between event duration and recovery is presented in Figure 6.8. It shows that long-lasting monsoon events have a more persistent impact on both shoreline position and beach profile, with longer recovery (i.e., up to 10 days), than short-term typhoons (1-3 days), which takes a few days to recover at most (sometimes less than a day). This result is striking at Nha Trang beach, compared with more documented barred beaches in mid-latitudes (Angnuureng et al., 2017, Masselink et al., 2016), where a larger range of high-energy wave event durations are observed. Interestingly at Nha Trang, recovery duration R is almost linearly related to event duration D (see details in legend of Fig. 6.8), albeit with substantial dispersion illustrated by error bars in the figure. This result illustrates again the plasticity (resiliancy) of the terrace due to rapid sediment exchange with the upper beach. It should have important consequences for shoreline modeling. A single beach decay value is often used in models (Davidson et al., 2013, Splinter et al., 2014a) whereas this parameter should account for variable storm durations.

6.4 Discussion on error estimate

Video-based bathymetry inversion has been developed for more than 20 years (Bell, 1999, Holman and Stanley, 2013, Almar et al., 2008, Bergsma and Almar, 2018, Holman et al., 2013),

with a range of errors between 0.2 - 2.0 m (RMSE) and -0.01 to -1.0m (bias). The method was calibrated and validated in various environments and often showed acceptable results compared with traditional in situ measurements. However, little attention was given to the general characterization of errors. A proper criterion was probably missing. Here, the comparison of tides between in situ and video-based inversion provides an estimator that seems to cover most of the reported types of errors in a single result.

Two different approaches for depth inversion are generally applied in near-shore camera systems Bergsma et al. (2018a). The spectral method of cBathy is two-dimensional while the cross-correlation temporal method used in this study is one-dimensional. The latter is adapted to the acquisition strategy at the Nha Trang site, which was designed to save on storage capacity for long-term monitoring purpose, only storing relevant information along a few transects. Bergsma et al. (2018a) show that the two methods give similar results with similar entry data, although applying a one-dimensional method to a cross-shore transect can be an issue for an oblique wave incidence angle and can affect the depth estimate. However, this issue is minor in our case of an embayed beach with near shore-normal incident waves and large refraction (Tissier et al., 2011). The incident wave direction does not significantly affect the accuracy of wave celerity determination and we estimate that for a wave angle less than 15 deg, the error is less than 3.5%. In the following, we concentrate on more dominant sources of error that are shared by both 2D and 1D approaches.

Figure 6.9 shows the cross-shore time stack composite of error estimate for the whole time series and profiling section. Three sources of error are clearly standing out in the figure (middle panel) and time series of each error type are extracted in the bottom panel. The three types of errors were decomposed based on visual inspection of their spatial patterns that show contrasting signatures. A more generic approach is left for future work. By order of importance, they are: deep water limitation (DW), breakpoint optical effect (BP) and surfzone nonlinear effect (NL). They have contrasted spatial patterns (see time-mean cross-shore patterns in the outset attached to the second panel): NL is localized at the shore and largest in the shallowest area; BP is distributed along the breakpoint, which has large temporal variability (top panel); and DW is in deep water with an error that seems to increase linearly with distance to shore. A diagram is given in Figure 6.10 to synthesize the location and processes behind the different error types, which are discussed below, along with their peculiar seasonal patterns.

6.4.1 Nonlinear effects during shoaling and in shallow water

The source of error with least intensity and cross-shore extent (but largest persistence all year long) is physical and concerns the use of linear wave dispersion in a nonlinear nearshore environment. Bergsma and Almar (2018) show that nonlinear processes become important in the shoaling zone and in shallow water (depth to wave length ratio $\frac{d}{L} < \frac{1}{20}$), producing an overestimation of inverted depth based on linear theory. In theory, for wave height to depth ratios $\frac{H_s}{d}$ greater than 1, a nonlinear dispersion relation should be used. However, H_s is not currently available from video systems, as opposed to LiDAR systems, which thus provide improved accuracy for bathymetry inversion. In addition, wave setup in the surf zone and very shallow water, which increases with wave height, can have substantial contribution to the total depth and is

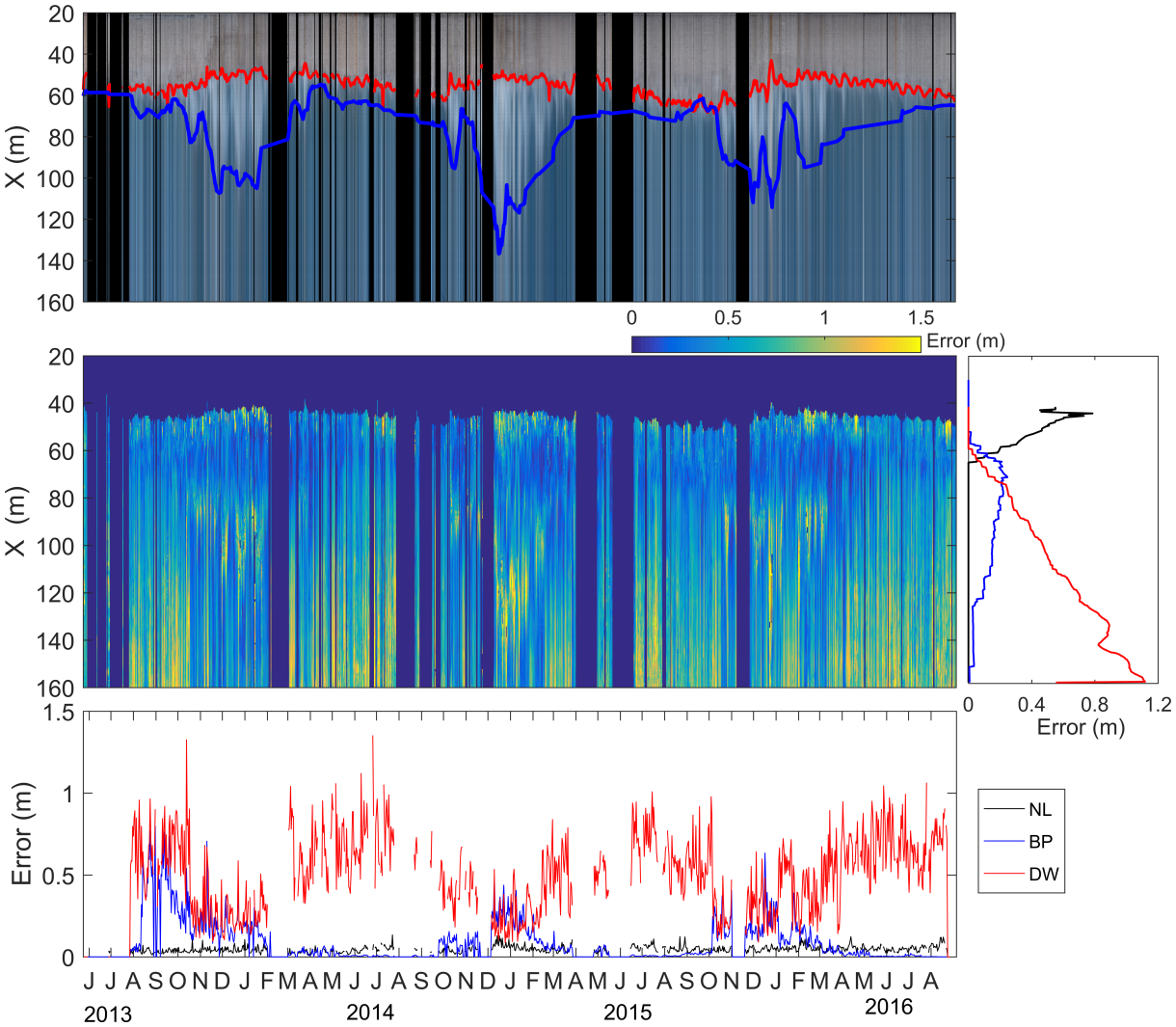

Figure 6.9: Error estimate for video-based depth inversion. Top) Cross-shore time stack image (space-time evolution of pixel intensity) where shoreline (red) and breakpoint (blue) are indicated. Middle) RMS Error of tidal differences between tide gauge observation and video-based inversion. Three error types are identified: deep water limitation (DW), breakpoint optical effect (BP) and surfzone nonlinear effect (NL). They are time-averaged in the outset panel to show their cross-shore extent. Bottom) Time evolution of the three types of errors, integrated across-shore over their respective zone of occurrence.

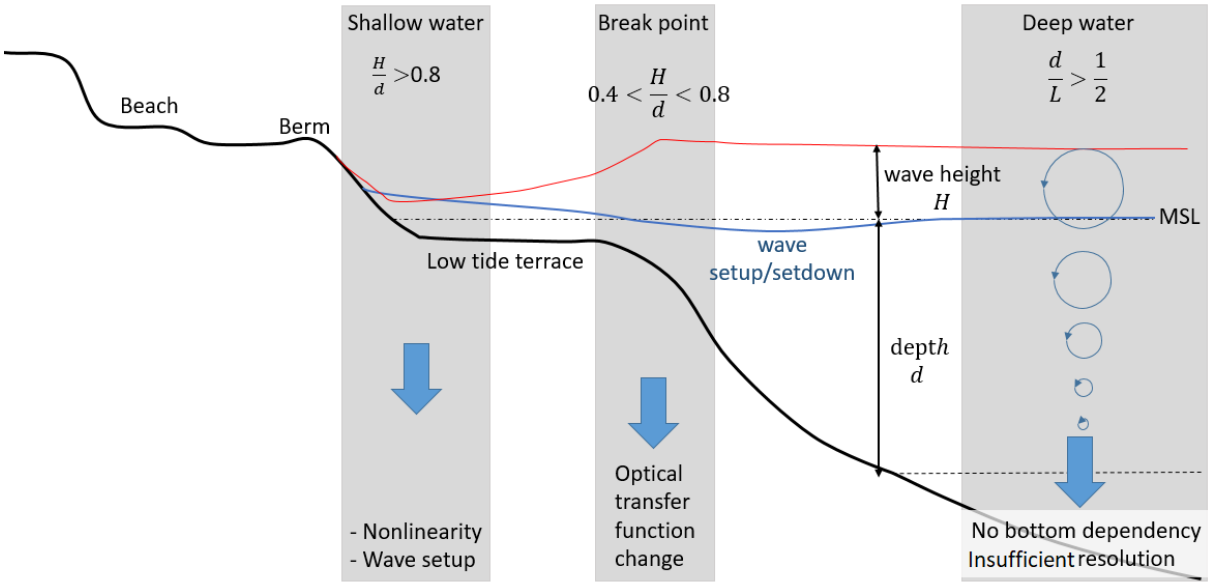

Figure 6.10: Description of the main sources of error for the use of video-based depth inversion methods. Namely, non-linearity and wave-setup in shallow area, optical modulation transfer function change at the breakpoint and relative deep water conditions for shortest waves.

not accounted for in current studies. This also tends to overestimate water depth.

6.4.2 Breakpoint optical effect

The sudden change of modulation transfer function between optical signal and actual wave phase from non-breaking to breaking waves (breakpoint) is a common problem of shore-based video camera systems. According to Bergsma and Almar (2018) in a recent study, a dominant uncertainty in video-based depth inversion stems from wave celerity detection. They suggest that the order of error in celerity detection may be twice larger than that from linear assumption of the dispersion relation. This is confirmed here with our new error estimate (at least in winter with bigger waves). The largest error in celerity detection occurs at breakpoint in both spectral and temporal methods, which means that it is intrinsic to the intensity images. This comes from a sudden change of the so-called modulation transfer function (Stockdon and Holman, 2000, Holman et al., 2017) at breakpoint. Prior to breakpoint, waves show a dark face and bright backface, but in the breaking zone, they have a bright roller and dark backface. The associated change in transfer function generates an apparent (spurious) increase of celerity. Usual methods ignore this issue or discard this specific region, but corrections were recently proposed relying on a different filter in the breaking and non-breaking zones Brodie et al. (2018).

6.4.3 Deep water asymptote

The third limitation is the largest, if not in magnitude, at least in space-time coverage. It stems from wave-bottom interactions that vanishes in deep waters, i.e., according to the linear theory, when $\frac{d}{L} > \frac{1}{5}$. Our study is particularly challenging in this respect because for a substantial part of the year (mostly summer), the sea state is composed of short wind waves for which video data is rarely accurate. Fortunately, we processed enough data in the inter-seasons to reveal

the seasonal evolution of the low tide terrace. However, our conclusion is that video-based depth inversion is generally not appropriate for wind wave conditions, at least for their shortest periods.

A synthesis of water wavelength as a function of depth is given in Figure 6.11 for winter and summer conditions. In summer, typically for $T \sim 3$ s, the deep water limit is 3 m, beyond which the wavelength reaches a deep water asymptote $L = \frac{gT^2}{2\pi} \sim 14$ m. Beyond this depth limit, the linear wave theory cannot be used for depth inversion. A second potential limitation associated with short waves is linked to the image resolution that increases with distance to the camera. The minimum wavelength that can be well resolved is $L > \sim 10\Delta x$ (Δx is the image resolution), which should limit the use of video cameras in the offshore zone. In Figure 6.11, we estimate the offshore resolution limit for summer wind waves to a maximum distance of ~ 250 m. Clearly, the resolution error is not dominant because even for a period of 3 s in summer, the physical deep water limit occurs much closer to shore than the resolution error (compare red and black lines in Figure 6.11). Depth inversion is invalid in this case. In winter (blue curve), with coastal wave periods closer to 5 s, the deep water asymptote is pushed much further offshore, although a domain of invalidity remains.

6.5 Conclusions

A video-based bathymetry inversion technique is applied to long-term data with varying wave environment from swell to local wind waves conditions. A main result is the overall stability but high resiliency demonstrated for the LTT beach, with rapid exchange of sediment between the terrace and the upper beach during typhoons, monsoon events or seasonal cycles. The high resiliency of these tropical environments may provide faster beach recovery compared with mid-latitude configurations.

At the same time, the study details the treatment techniques needed for a long-term dataset, and focuses on the limitations of the method in the case of wind waves. For the first time, a tide gauge is used to quantify the error produced by video estimates and produce a quality criterion. Three sources of error are exhibited in a single analysis. They are clearly identified (see diagram in Figure 6.10): 1) nonlinearities and wave setup localized in very shallow water; 2) change in the optical wave signature at breakpoint; 3) deep water limit for applying the linear dispersion relation, which is very restricting for wind waves ($D_{limit} \sim 3$ m for $T = 3$ s). The error types have contrasted spatial and temporal patterns, but the main error component in Nha Trang is deep water limitation. It has strong seasonality and is greatest in summer, when short wind waves are dominant, making depth inversion invalid. On the contrary, the second and third dominant error contributions at breakpoint and in the surf zone are maximum for large waves (during winter monsoon in Nha Trang). Corrections will probably be proposed for these errors in the future.

More generally, this study provides guidelines for users of video-based depth inversion methods and a base for standalone error assessment, which is essential for operational and data assimilation systems. For data assimilation, the estimation of error is required but generally not available (Wilson et al., 2012, Birrien et al., 2013). A comprehensive error estimate, such as the one proposed here, is thus an excellent step for improving the assimilation approach.

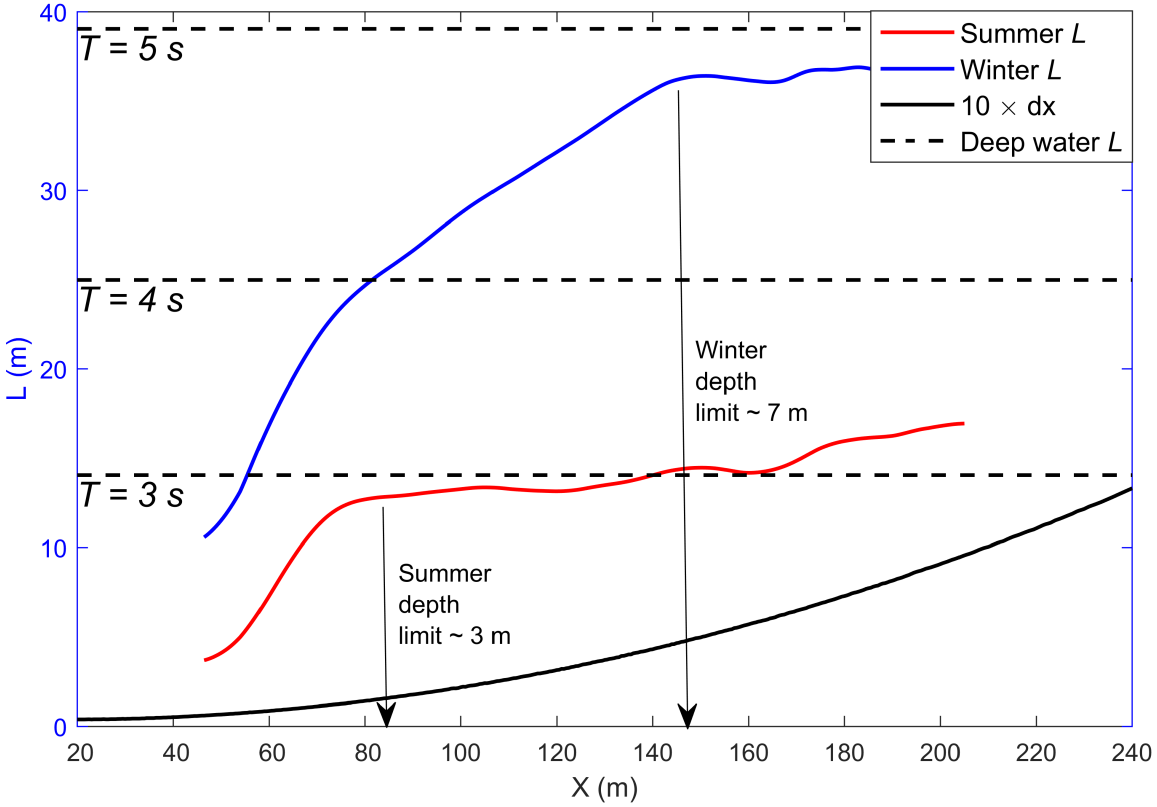

Figure 6.11: Seasonal deep water asymptotes off Nha Trang, used as critical condition for video-based bathymetry inversion. Time mean wavelength L profiles for summer (May-September; red line) and winter (December-February; blue line) are represented, along with deep water wavelengths for periods T = 3, 4 and 5 s for reference. Vertical arrows points to the deep water limits in each season, featuring a much shallower (and closer to shore) limit in summer that invalidates any attempt at depth inversion. The black line is the effective image resolution that limits the wavelength detection. It appears much less restrictive than physical limitations.

Chapter 7

Nearshore morphology using rotary wing Unmanned Aerial Vehicles-UAV

Contents

7.1 Background on the application of UAV in coastal areas

For over 20 years, video systems such as Argus has allowed to study the nearshore zone with significant results in various regions of the world, including in Vietnam during this PhD study. However, the shore-based camera system has a number of drawbacks Pennucci et al. (2007), Holman et al. (2011). It requires a high vantage point, e.g., a large tower, cliff, or a tall hotel adjacent to the beach. It also requires a power supply and internet connection. In addition, there are limits in the scope of the camera system and requirements about resolution lead to the

choice of multiple cameras for a long beach. This may be beyond the capability of developing countries. In addition, if there is no independent electrical system, monitoring during extreme events is not feasible (e.g., lightening problem at NT during tropical thunderstorm, power cut during typhoons). This increases the cost of setting up monitoring stations. These conditions are not always satisfactory, particularly with limited infrastructure as in Vietnam.

Recently, the rapid development of unmanned aerial vehicles (UAVs) or "drones" offer a viable alternative to conventional platform for acquiring high-resolution remote-sensing data at lower cost and increased operational flexibility. This technology can profit of the ability of drones to fly at low-level with stability and include ever better and cheaper camera systems. fixed-wing UAVs or rotary-wing UAVs are thus attractive alternatives. According to Turner et al. (2016), the coastal area is now in the drone era, so that UAV survey equipment and data processing methods are readily available for applications. However, it is clear that in their studies as well as in all of recent research related to UAV (see the review of Colomina and Molina (2014), Klemas (2015)), drones are only limited to topographic survey.

Civil (non-military) UAV systems, or drones, rapidly developed over the past decade, especially cheap drone systems ranging from a few hundred dollars to less than ten thousand dollars. These are cheap, flexible and easy to deploy. Owing to this progress, the application of drones is now widespread and include nearshore video monitoring (Dérian and Almar, 2017). Here, we limit the application of drones to the monitoring of nearshore morphology (aerial and submerged), hoping to produce an accurate representation of the land-sea continuum. Drones can be considered as an interesting tool for bridging the gap in spatial scales given by the local shore-based camera system (1 km^2) and aircraft or satellite systems (100 km^2) (Holman et al., 2017, Bergsma et al., 2018b).

Studies on the application of drones to near-shore monitoring are often divided into two categories: aerial topography with photogrammetry and bathymetry inversion from wave celerity:

- The first historical application is for upper aerial beach observation (Toth et al., 2015, Brunier et al., 2016). It is usually carried out by geomorphologists, and was actively developed in recent years (Carrivick et al., 2016). The method called 'Structure-from-Motion' (SfM) photogrammetry is often applied on images obtained from a low-cost drone. The results are extremely positive for geomorphology surveys compared with traditional in-situ measuring devices such as DGPS (James et al., 2017) or LiDAR (Cook, 2017). The accuracy of the position can reach a centimeter accuracy (Turner et al., 2016) but usually of the order of 10 cm (Brunier et al., 2016). The results depend largely on the terrain conditions and quality of the drone-mounted cameras (Cook, 2017). Accuracy will be improved with the constant improvement of drone sensors and stabilization.

- The second application for bathymetry inversion uses the drone as a portable shore-based camera station, which has the advantage that it can be installed anywhere at any time (Holman et al., 2011, 2017, Aarnink, 2017, Matsuba and Sato, 2018, Bergsma et al., 2018b), with an arbitrary altitude and without infrastructure. In principle, the drone system can use all the techniques developed for the shore-based camera system. However, this is only possible with a stable drone when acquiring images. Only a rotary wing UAV will satisfy this condition as fixed wing UAVs were found unsuitable (Holman et al., 2011).

In this chapter, I present some preliminary results on the combination of topography survey and nearshore bathymetry inversion with the drone system used in the NT4 field experiment as described in Section 4.1.4, and the drone system shown in Figure 4.18. The topography of the upper beach is based on the SfM technique mentioned above and the bathymetry inversion is based on the temporal version of the cross-correlation method described in Section 3.6. The bathymetry inversion method was presented in detailed and will not be presented again here, but the SfM method is introduced. Results on topography estimation will be compared with two cross-shore section measurements with RTK-DGPS. In the bathymetry part, two different camera calibration techniques are presented and their performance evaluated, then the bathymetry inversion is compared with measured profiles obtained during NT4 (see Section 4.1.4) with an echo-sounder. Finally some recommendations and guidelines are proposed.

7.2 UAV systems used during NT4

As mentioned in Section 4.1.4, and as shown in Figure 4.18, during the NT4 field trip we used two different drone systems for different purposes, which was due to the initial design of the project: the professional DJI Spreading Wings S800 (DJI-S800); and cheaper DJI Phantom 3 Pro (DJI-P3P).

- The DJI-S800 system is based on the original rotating wing hexacopter S800 system provided by DJI, after adding a variety of sensor configurations, including optical cameras, laser scanners, GPS receivers, IMU,...etc., similar to the system in Toth et al. (2015). However, during NT4, we did not install the LIDAR scanner. Similarly to Toth et al. (2015), the camera mounted on the DJI-S800 is the Nikon D800 full frame 36 Mpix DSLR camera with a fixed focal length 35 mm length, camera body rigidly fixed to the platform in nadir facing direction (Figure 4.18). The total system cost does not exceed ten thousand dollars. This system is used for topography surveys because of the image resolution up to 7360×4912 pixels, which with a flying height of about 100 m can give precision to the order of centimeters.

- The second UAV system used during the NT4 survey (Figure 4.18), is the DJI-P3P system. Unlike the customized system of the DJI-S800, this one is a complete product from the DJI manufacturer. At the time of this study, it was the most updated version of the Phantom product line of DJI Company. It contains an integrated 12,4MP camera (1/2.3 inch CMOS sensor) with 4096×2160 pixels Ultra-HD video recording at 24/25 fps on a micro-SD card and telemetry to a free Vision application (app) for iOS and Android. The Wi-Fi allows live, remote video streaming from up to 330 m away. It contains a 3D gimbal for the camera system and GPS position and gimbal information are automatically recorded and stored in the memory card. That information can be used directly for geo-rectification of images as presented later in this study. It can fly up to 25 minutes on a single charge using the included lithium polymer battery that is easily removable and contains a built-in charge-remaining indicator. In the course of this thesis, DJI released the latest Phantom product line, DJI Phantom 4 Pro Ver 2.0, with a camera CMOS sensor up to 1 inch, with 20Mp resolution and signal transmission between drone and controller up to 7 km. The

price of the new product remains similar to that of the DJI-P3P in 2015 at about 1300 $US.

There are many similar DJI drones on the market, but the DJI-P3P was chosen based on the quality of the acquired image and its popularity, which allows easy access. In addition, DJI products show stability in operation, the ability to communicate very well with peripherals such as phones or tablets with Android or iOS operating systems. This is very important because the risk of accident is high with drones – usually, every country requires a user to have a drone license.

7.3 Aerial beach topography by stereo photogrammetry

In this study, I used the SfM method applied to images obtained from the Nikon D800 camera mounted on the DJI-S800 drone system as mentioned above. In recent years, the SfM method proved suitable for a low-cost, topographic survey system that is comparable in accuracy to traditional in-situ measurements with DGPS, RTK-GPS or LiDAR.

SfM was developed in the 1990s in the field of computer vision, based on the Multi-View Stereo (MVS) methods to build 3D models from 2D images (Hartley and Zisserman, 2003). The principle of the SfM method is similar to stereoscopic analysis in photogrammetry. However, unlike traditional photogrammetry, SfM uses a variety of algorithms, such as a highly redundant, iterative bundle adjustment procedure to automatically find out the matching features in a collection of overlapping digital images and hence the geometry of the scene. Camera positions and orientation are solved automatically without the need to specify an a priori network of targets which have known 3D positions (Snavely, 2008, Westoby et al., 2012, Carrivick et al., 2016).

With traditional photogrammetry, building 3D coordinates of the points in the scene requires knowing the 3D location of the cameras, or the 3D coordinates of a given points. The SfM method does not need to know that information. Instead, the camera location and scene geometry is reconstructed simultaneously through automatically identifying the matching features in multiple images. The duplicate objects are defined from image to image, thus giving an initial estimate of the camera positions and object coordinates, and eventually it is refined iteratively using non-linear least-squares minimization (Westoby et al., 2012).

After this step, we get the 3D coordinates of point clouds in a relative 'image-space' coordinate system, due to the lack of scale and orientation provided by ground control coordinates. In most cases, the transformation of SfM image-space coordinates to a physical coordinate system can be achieved using a 3D similarity transform based on a small number of known ground control points (GCPs). The GCPs are generally selected so as to be accurately measured, easily identified on the images and distributed appropriately throughout the survey area. To ensure accuracy, we increase the contrast so that identifiable GCPs are usually made of artificial objects (e.g., reflective painted dots or crosses) and their real coordinates are measured by highly accurate in-situ methods such as DGPS. As shown in Figure 7.1, during the NT4 survey, GCPs (about 15 points) were generated by red painted plastic plates, allocated to three groups along the beach and their real location measured by RTK-DGP. The steps taken to process the image

Figure 7.1: This illustrates GCPs measurement using the RTK-GPS device for transformation of SfM image-space coordinates into a physical coordinate system of the DJI-S800 drone. Images obtained from NNT camera system.

obtained from the drone DJI-S800 and reconstruct the upper beach 3D topography are carried out following the flowchart in Figure 7.2. Detailed description of these steps can be found in Carrivick et al. (2016).

7.3.1 Flight protocol

With the altitude set to 100m (authorization required, see local regulations), the camera is set at the highest resolution of 7360x4912 pixels, the image has a coverage of up to 150m, while the upper beach in the study area is only about 50m wide, so the fly process is rather simple. The DJI-S800 is set to fly along the shoreline and the images obtained are similar to the one shown in Figure 7.3. The 5m/s flight speed is associated with the camera's acquisition frequency set to 5 frames per second and a 60% overlapping between consecutive images as required by the SfM method. During the NT4 field survey (see Section 4.1.4), each day at the lowest tide in the early morning, a flight with the DJI-S800 was conducted in combination with GCPs measured with a RTK-GPS. In principle, the Nikon D800 camera is capable of delivering RAW images, but for simplicity in this study, JPG images are produced. The JPG images were then used by the Agisoft PhotoScan Professional software to proceed to the reconstruction of the upper beach 3D topography. This is presented in the next section.

7.3.2 Photogrammetry and 3D beach reconstruction

In the field of geotechnical engineering, the use of the SfM method to reconstruct the 3D topography of the study area from the imaging of drone systems has become very common in the last few years. Taking advantage of recent developments in the field of computer vision, there are

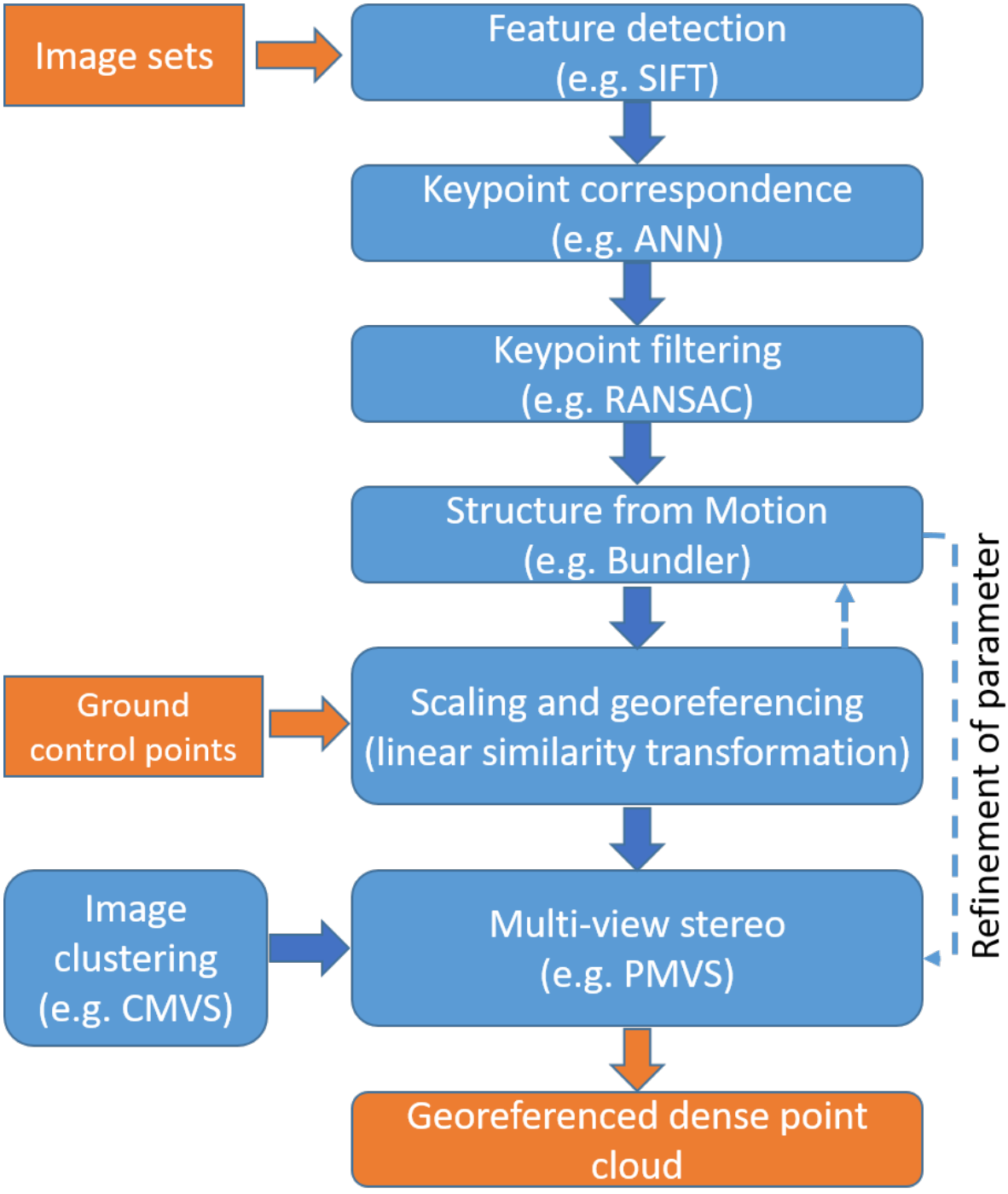

Figure 7.2: Typical workflow in the production of georeferenced dense point clouds from image sets and ground control points. Modified from Carrivick et al. (2016).

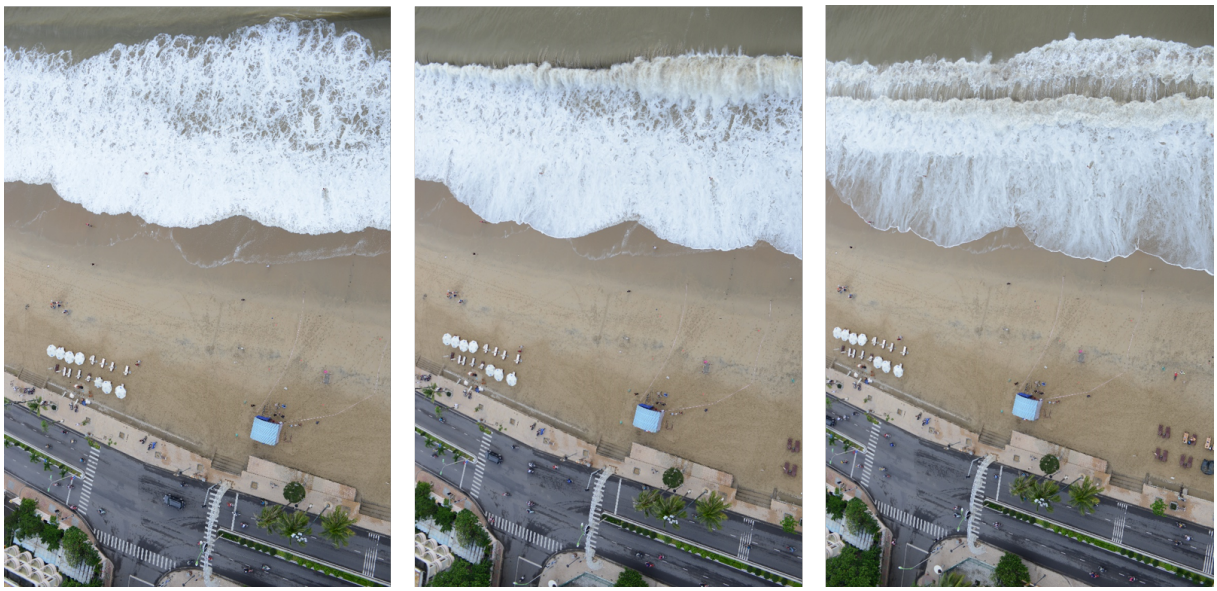

Figure 7.3: An example of photos used to build the upper beach 3D topography. The resolution of each image is 7360x4912 pixels and the two consecutive images have a mutual overlap greater than 60%.

many softwares based on this method, such as PhotoModeler (Micheletti et al., 2015), Photosynth (Fonstad et al., 2013), VisualSFM, Pix4D, and Agisoft PhotoScan (Javernick et al., 2014, Ouédraogo et al., 2014, Cook, 2017). Choosing a software generally depends on its accessibility rather than on differences in performances.

For this study, I used Agisoft PhotoScan Professional, commercially available SfM software that costs 550 $US for an educational license. While not being the lowest cost solution, PhotoScan Professional is becoming increasingly used in the geomorphology community. It includes all of the steps in model creation, beginning with the raw data (the photographs) and producing 3D point clouds, 3D triangulated meshes, DSMs, and orthophotos with a workflow that is simple and user-friendly, but allows for some user customization. PhotoScan Professional seamlessly incorporates GCPs in the workflow for georectification of the model, improving image alignment, and improving the calculation of the camera calibration parameters. All the processing was done on a Hp laptop with single Intel Core i7-5600U 3.20 GHz CPU, a built-in Intel HD 5500 graphics processing unit, and 16 GB of RAM. The whole process takes about 3-4 hours for one survey.

First, the images are aligned using a point matching algorithm that automatically detects matching points on overlapping photographs and uses these points to simultaneously solve for both the camera locations and the camera lens parameters (Figure 7.4a). With no independent position information for the photographs, this produces a rough 3D model of the scene with no information about the spatial scale of the model. After this initial scene construction, the ground control targets have to be located and manually marked on at least two photographs (Figure 7.4b); the software then predicts their locations in the model and on other photographs in which they appear. These predicted locations can be used to evaluate the success of the photograph alignment process. Achieving the best results in PhotoScan may require an iterative/manual process of aligning the photographs, marking ground control points, checking photograph alignment

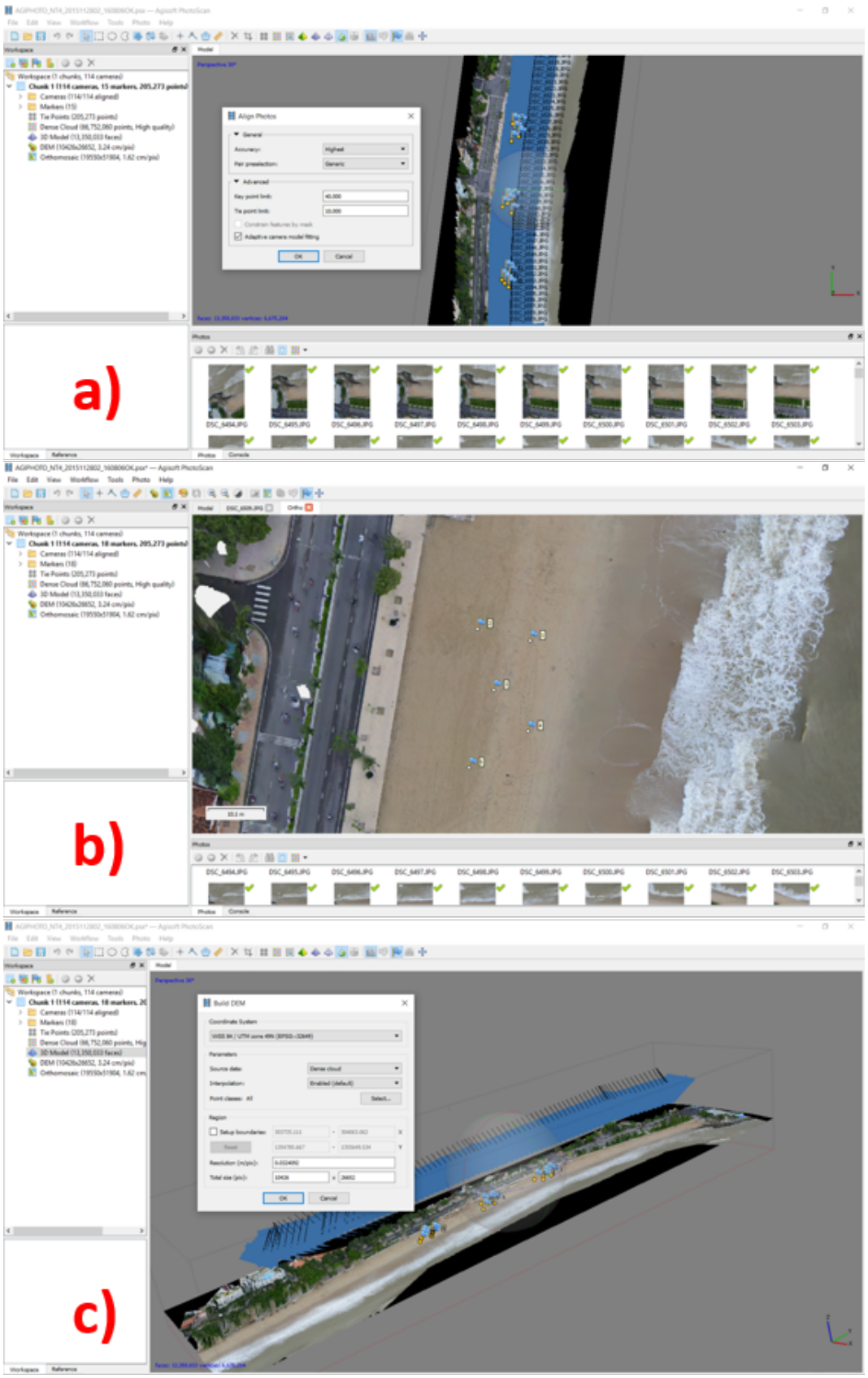

Figure 7.4: Steps using SfM Agisoft PhotoScan Professional software to reconstruct the 3D beach from the images taken by the Nikon D80 camera mounted on the DJI-S800 drone. An example is given for 9am on November 28, 2015. a) Choose the images that are aligned automatically using a point matching algorithm, calculating camera positions and orientation. b) GCPs data points were selected to serve for both automatic camera calibration and transformation of the 'image-space' coordinate reference to the real coordinate system . c) Development of a DEM model for the beach based on the actual 3D coordinates of point clouds. The end result is the export of the image to Google Earth Pro, shown in Figure 7.5.

based on predicted GCP locations, marking additional GCPs, and re-aligning the photographs. For the models presented here, the final alignment step was performed at the highest resolution. The software uses the measured locations of the GCPs to both georeference the model and refine the camera calibration by minimizing the error between the modeled locations of the points and the measured locations, increasing the model accuracy. PhotoScan reports the offset between calculated and measured control point locations, providing an initial estimate of model accuracy.

After aligning the photographs, PhotoScan calculates a dense point cloud at a range of "qualities" or resolutions (Figure 7.4c); lower quality dense clouds involve more subsampling of the original photographs. The results presented here are calculated with a mild depth filter and at medium quality, for which the photographs are subsampled by a factor of 4 in each dimension, to ensure reasonable processing times, given the large number of photographs. The point clouds were then cleaned manually by removing stray points and points below ground level in regions where points were poorly correlated.

The DEM model for 3D surface of the upper beach on the real coordinate system is then created with a resolution of up to 3.23 cm/pixel. Next, the orthomosaic image is created based on the DEM model in the previous step, with up to 1.62 cm/pixel. Orthomosaic image is then exported into the Google KMZ format to easily represent the study area in Google Earth Pro, shown in Figure 7.5a. To validate the SfM method on the image obtained from DJI-S800, the two profiles shown in Figure 7.5c were extracted from the DEM model and compared with with RTK-GPS measurements performed on the same day (Figure 7.6). The validation appears very satisfying.

7.4 Submerged beach inversion using wave celerity: stationary flight

The procedures to invert nearshore bathymetry from video images recorded by rotary wing unmanned aerial vehicles (drones) are presented here. Two effective simple methods for image rectification are discussed, together with image preprocessing before wave front trajectory tracking.

7.4.1 Motivation

The need for nearshore bathymetry (for understanding and modeling the dynamics and variability of the nearshore zone) has spurred extensive research into methods for cheap – and, for military purposes, inconspicuous – measurements of nearshore bathymetry. Some of these methods are in-situ such as traditional leveling, the use of bottom contacting vehicles such as the Coastal Research Amphibious Buggy (CRAB) (Birkemeier and Mason, 1984) or jet-skis equipped with global positioning system and fathometers (Dugan et al., 2001). These methods are accurate, but manpower intensive and expensive. Others are based on remote-sensing methods that exploit various depth signatures. For clear water where the bottom is visible, multi- or hyperspectral sensors show color variations that are correlated with depth (Mobley et al., 2005, Lyzenga et al., 2006) yielding approximate bathymetries from satellite or airborne data. The LIDAR has become a powerful and popular tool for airborne sensing of clear waters, providing

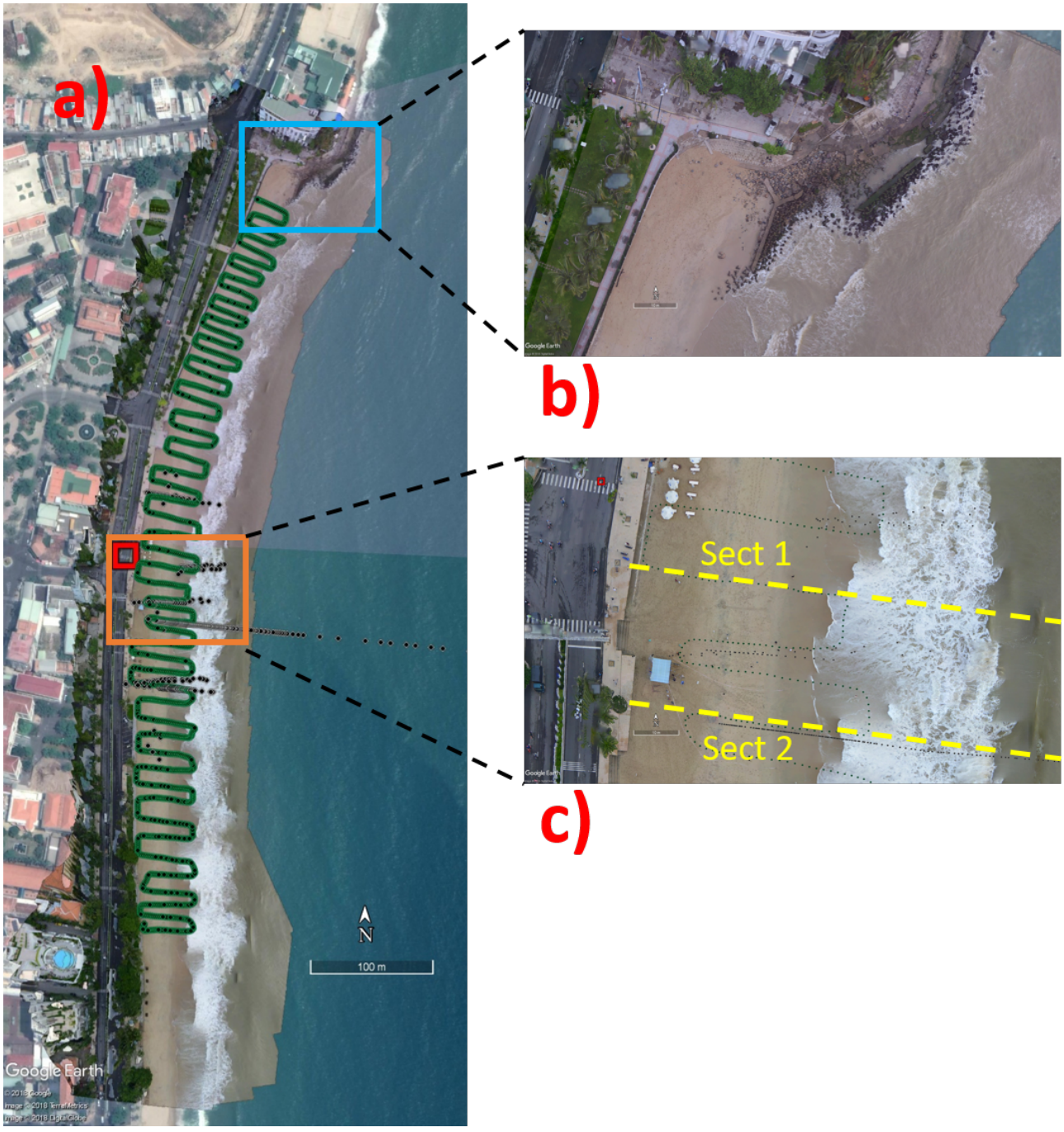

Figure 7.5: The projection of orthomosaic image generated by Agisoft software using the Nikon D800 mounted on the hexadrone during NT4 field campaign on the Google Earth Pro. a) The whole study area during NT4 field campaign presented in Section 4.1.4: the zigzag dot presents the walking RTK-GPS survey, the red rectangles show the shore-based camera system location. b) Zoom on the north end of the beach. c) Zoom on observation area of the NT4 survey, the dash yellow line showing the location of the cross-section used to validate the topography.

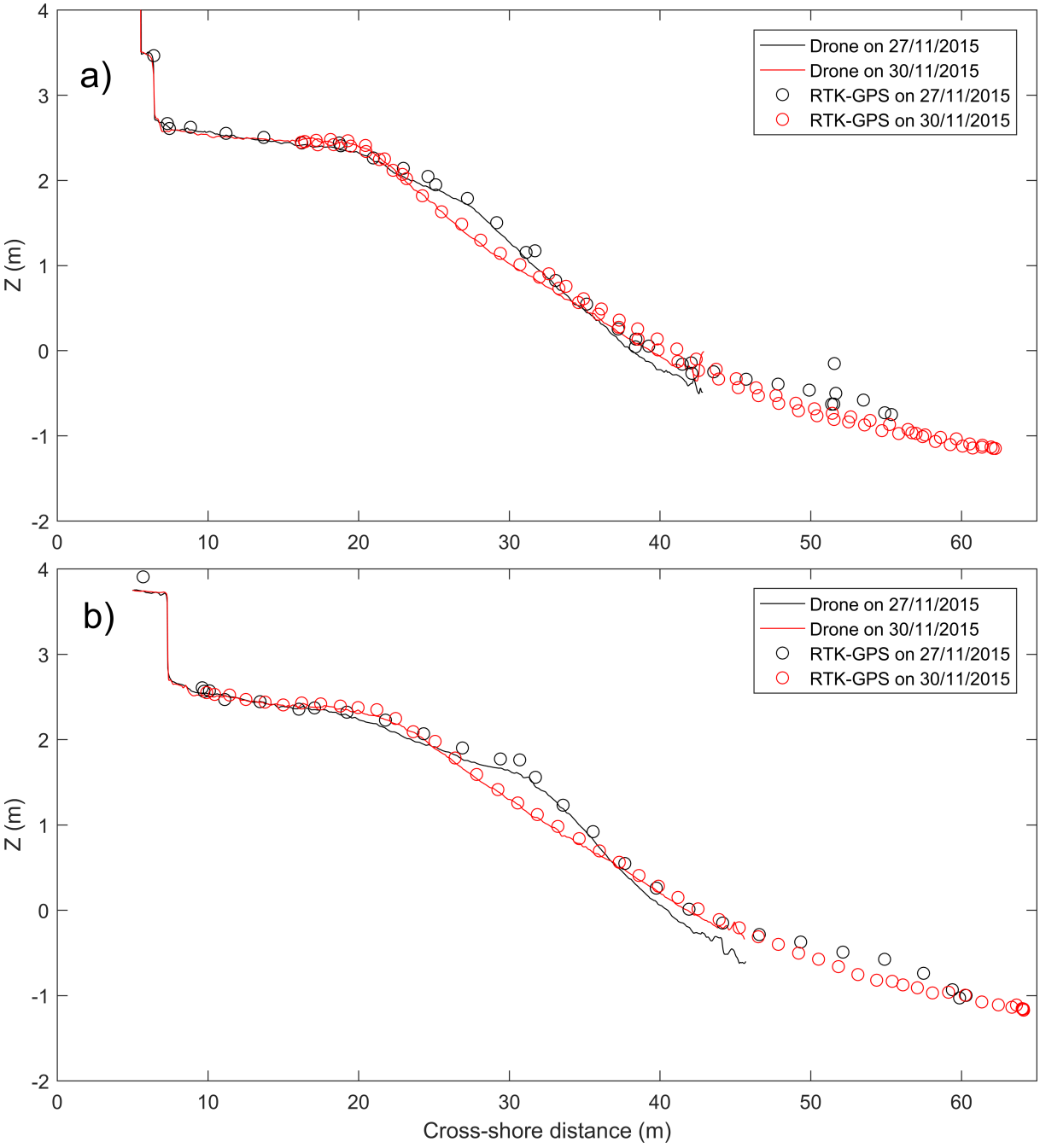

Figure 7.6: Comparison of upper beach profiles measured by RTK-GPS (solid lines) with topography calculated (dashed lines) from the Agisoft software using images from the Nikon D800 mounted on the hexadrone during the NT4 field campaign (day 29/11 and 30/11). a) at section 1 and b) at section 2.

accurate, albeit expensive, measurements for extensive areas each time an overflight is carried out (Irish and Lillycrop, 1999, Sallenger Jr et al., 2003). Remote sensing techniques using video cameras have the clear advantage of low cost.

In principle, what was developed for the shore-based camera system should be fully applicable to drone videos. This is what Holman et al. (2011) attempted to demonstrate. However, in their study they used a fixed-wing drone, which is not best suited for stationary applications and the accuracy was low. Depth-inversion using cBathy (Holman et al., 2013, Bergsma et al., 2016) with fixed-wing solutions confirmed that no positive results could be achieved. Therefore, in this study, we use a rotary-wing drone with a very-high resolution camera (12.4 megapixels). Only a few years ago, this type of drones were unavailable. The aim of this study is to show that the technique developed for shore-based video cameras can be successfully applied to a video system attached to a rotary-wing drone. To this end, drone estimates are compared with bathymetric surveys at Nha Trang.

7.4.2 Camera calibration for a drone camera-system

Similarly to the shore-based video system or any remote sensing system, the first step is camera calibration in order to assess the parameters needed to transform 2D image coordinates to 3D world coordinates (Holland et al., 1997). Whereas it has to be done once for fixed shore-based video cameras, it has to be done for each flight when using drones: this can be time-consuming. To conduct rectification, two methods were tested, one with GCPs and one without GCPs:

- With the development of photogrammetry (Kraus, 2011, Luhmann et al., 2007, Konecny, 2014) and computer vision (Hartley and Zisserman, 2003, Ponce et al., 2011) there are many different methods of calibration – for example, Tsai (1987), Heikkila and Silven (1997), Zhang (2000), Kannala and Brandt (2006). In addition, there are several ready-to-use toolboxes available, for example, "OpenCV toolbox" (OpenCV, 2018), "Camera Calibration Toolbox for Matlab" (Bouguet, 2015), "Fully Automatic Camera Calibration-FAUCCAL" (Ntouskos et al., 2009), "MetroVisionLab toolbox" (D. Samper, 2009), and so on. For the application of the Argus system in coastal areas, the 2D or 3D direct linear transformation (DLT) method (Abdel-Aziz and Karara, 1971) considering the lens distortion factors presented by Holland et al. (1997) is most widely used (Almar, 2009, Almar et al., 2012b, 2014, Bergsma et al., 2016). The conventional camera calibration process is carried out with a single photo and ground control points (GCPs), with a minimum of 4 points for the 2D case and 6 points for the 3D case. For a shore-based video as for a drone system, the camera calibration is carried out with GCPs to determine extrinsic parameters, namely the object coordinates of the camera and the rotations of the image. The intrinsic camera parameters are completely predetermined by conducting calibration in laboratory using available methods (Heikkila and Silven, 1997). Today the lens systems are increasingly thin (it is not necessary to use wide angle lens like fish eyes type), and the edges of the image, formerly neglected, can now be used. For example, ignoring the distortion of the lens, the principal point coincides with the center of the image, the effective focal length obtained according to the manufacturer manual are acceptable assumptions and widely used.

- Camera calibration without using GCP method for DJI-P3P

  Based on the definition of the relative angle of fly object, the three angles (Pitch, Yaw, Roll) are defined according to the gimbal manual. Comparing with the pin-hole model as mentioned in DLT method and following Kraus (2011), we determine for the real coordinates system (objective coordinates system) the Y-axis corresponding to the North, the X-axis corresponding to the East, and the Z-axis corresponding to the Elevation. The video recorded by DJI-P3P contains information such as GPS location (Latitude, Longitude, and Elevation), the pitch, yaw, and roll of the gimbal system. In the video information file, the string @xyz contains the location of the drone, assumed as the center of perspective location. And strings @gpt, @gyw, and @grl are the pitch angle, yaw angle, and roll angle of the gimbal of camera system, respectively. Therefore, the easiest step in image rectification is to directly use this information, ignoring the distortions. Then, the relationship between the coordinate (u, v) of an image point P' and the coordinates (X, Y, Z) of an objective point P is mathematically formulated as:

$$\begin{aligned} X &= X_0 - Z_0 \frac{r_{11}.u.S_x + r_{12}.v.S_y - r_{13}.f}{r_{31}.u.S_x + r_{32}.v.S_y - r_{33}.f} \\ Y &= Y_0 - Z_0 \frac{r_{21}.u.S_x + r_{22}.v.S_y - r_{23}.f}{r_{31}.u.S_x + r_{32}.v.S_y - r_{33}.f} \end{aligned} \tag{7.1}$$

  Where, (X_0, Y_0, Z_0) are the coordinates of the camera station (pose camera) obtained from @xyz information contained in the recorded video file, (Sx, Sy) is the scale factor estimated from the information of the sensor of the camera mounted on DJI-P3P (the drone uses the CMOS sensor IMX117CQT type with size 1/2.3 inch) with diagonal length of the CMOS approximately 7.81 mm, the video was setup at Full-HD 1920×1080 pixel, then, $Sx = \frac{7.81}{1000} \cdot \frac{4}{5} \cdot \frac{1}{1920}$ (m/pixel), $Sy = \frac{7.81}{1000} \cdot \frac{3}{5} \cdot \frac{1}{1080}$ (m/pixel), the effective focal length $f = 35$mm, and r_{ij} are the elements of the rotation matrix similar with $\mathbf{R}$ matrix in Equation 3.3, now re-calculated based on the three angles (pitch, yaw, roll) of the gimbal system as follow

$$\begin{aligned} \mathbf{R} = &\begin{bmatrix} \cos(-yaw) & -\sin(-yaw) & 0 \\ \sin(-yaw) & \cos(-yaw) & 0 \\ 0 & 0 & 1 \end{bmatrix} \times \begin{bmatrix} \cos(roll) & 0 & \sin(roll) \\ 0 & 1 & 0 \\ -\sin(roll) & 0 & \cos(roll) \end{bmatrix} \\ &\times \begin{bmatrix} 1 & 0 & 0 \\ 0 & \cos(pitch + 90^{\mathrm{O}}) & -\sin(pitch + 90^{\mathrm{O}}) \\ 0 & sin(pitch + 90^{\mathrm{O}}) & \cos(pitch + 90^{\mathrm{O}}) \end{bmatrix} \end{aligned} \tag{7.2}$$

  Using the available information we can completely transform the pixel coordinates (u, v) of the object on the image to the real coordinates without a camera calibration step, or in other words, we do not need any GCPs. This can be very important because the land part of the image (which has less interest) is often very narrow on the video frame and makes it difficult to conduct a high-resolution measurement for GCPs, requiring a survey team and extra costs.

- Camera calibration using GCPs method for DJI-P3P

As the drone system usually flies at a height of a few tens of meters to 150 meters, the GCPs that can easily be measured are usually located on the beach, so the altitude compared to the camera is very small. From that point of view, we can assume that the GCPs established on the beach would be coplanar points. With no loss of generality, we can set the altitude of the GCPs to zero. Then, we solve the system of Equations 3.7 for the real coordinates of points (u, v) on the image, we get an equation similar to Kraus (2011), Luhmann et al. (2007):

$$\begin{aligned} X &= \frac{a_1 u S_x + a_2 v S_y + a_3}{a_4 u S_x + a_5 v S_y + 1} \\ Y &= \frac{a_6 u S_x + a_7 v S_y + a_8}{a_4 u S_x + a_5 v S_y + 1} \end{aligned} \tag{7.3}$$

Where, the object has coordinates (u, v) on the image and the real coordinates are $(X, Y, 0)$. (S_x, S_y) is calculated as mentioned above. Eight parameters $a_{1..8}$ can be resolved if the number of GCPs is $(n \geq 4)$. The system of Equations 7.2 can be rewritten for n GCPs as follows:

$$\begin{bmatrix} u_1 S_x & v_1 S_y & 1 & 0 & 0 & 0 & -u_1 S_x X_1 & -v_1 S_y X_1 \\ 0 & 0 & 0 & u_1 S_x & v_1 S_y & 1 & -u_1 S_x Y_1 & -v_1 S_y Y_1 \\ & & & & & & & . \\ & & & & & & & . \\ & & & & & & & . \\ u_n S_x & v_n S_y & 1 & 0 & 0 & 0 & -u_n S_x X_n & -v_n S_y X_n \\ 0 & 0 & 0 & u_n S_x & v_n S_y & 1 & -u_n S_x Y_n & -v_n S_y Y_n \end{bmatrix} \times \begin{bmatrix} a_1 \\ a_2 \\ a_3 \\ a_6 \\ a_7 \\ a_8 \\ a_4 \\ a_5 \end{bmatrix} = \begin{bmatrix} X_1 \\ Y_1 \\ . \\ . \\ . \\ X_n \\ Y_n \end{bmatrix} \tag{7.4}$$

Equation 7.4 is of the type:

$$[\mathbf{A}] \times [\mathbf{C}] = [\mathbf{B}] \tag{7.5}$$

Usually n will be much larger than 4, and the solution of Equation 7.4 is given using a least squares method:

$$[\mathbf{C}] = \left[\mathbf{A}^T \times \mathbf{A}\right]^{-1} \times [\mathbf{A} \times \mathbf{B}] \tag{7.6}$$

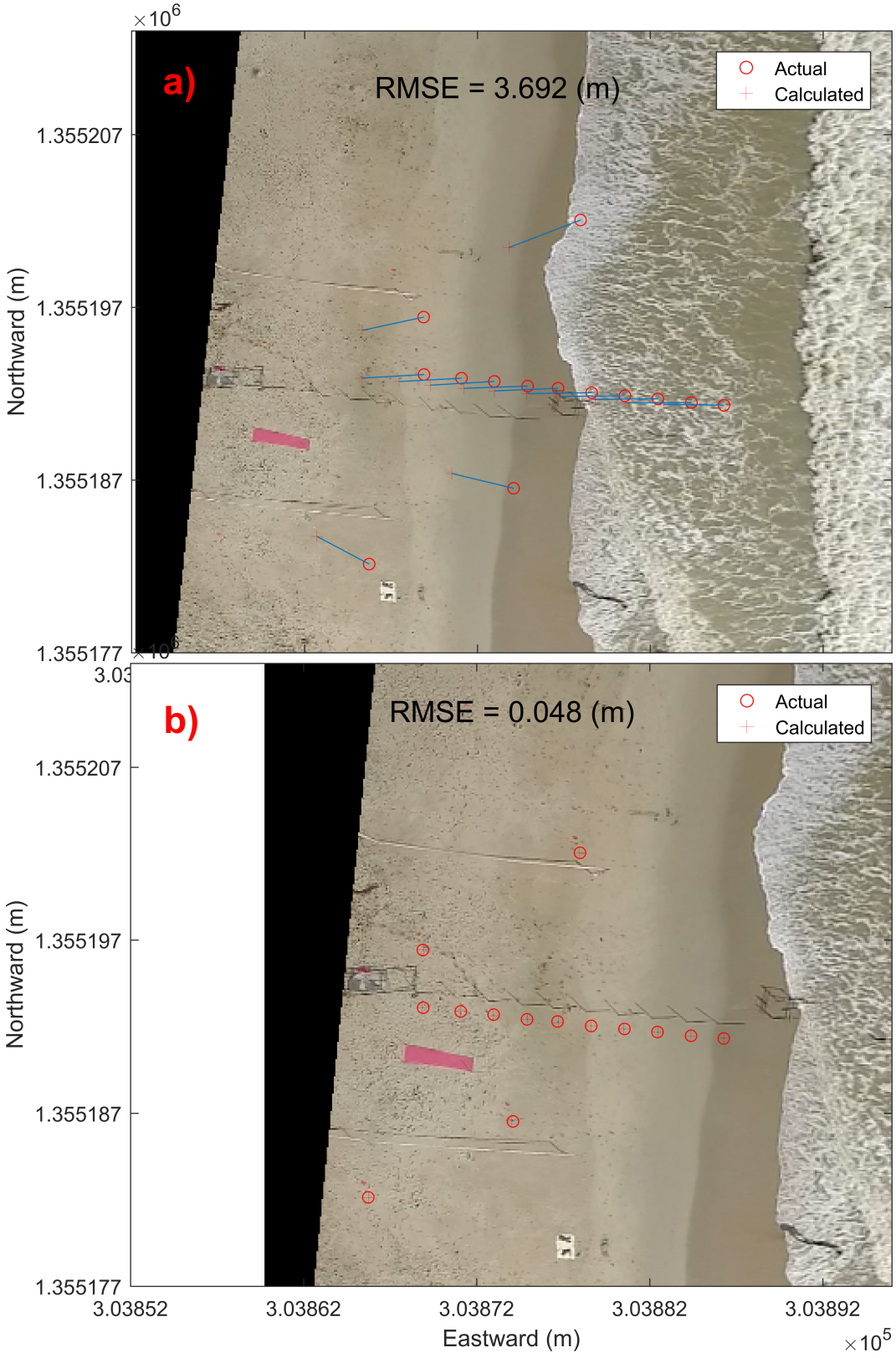

Figure 7.7: The rectification results of NT4 case using direct information (pitch, yaw, and roll of the gimbal of camera system) and the 2D direct linear transform method for the camera mounted on DJI P3P.

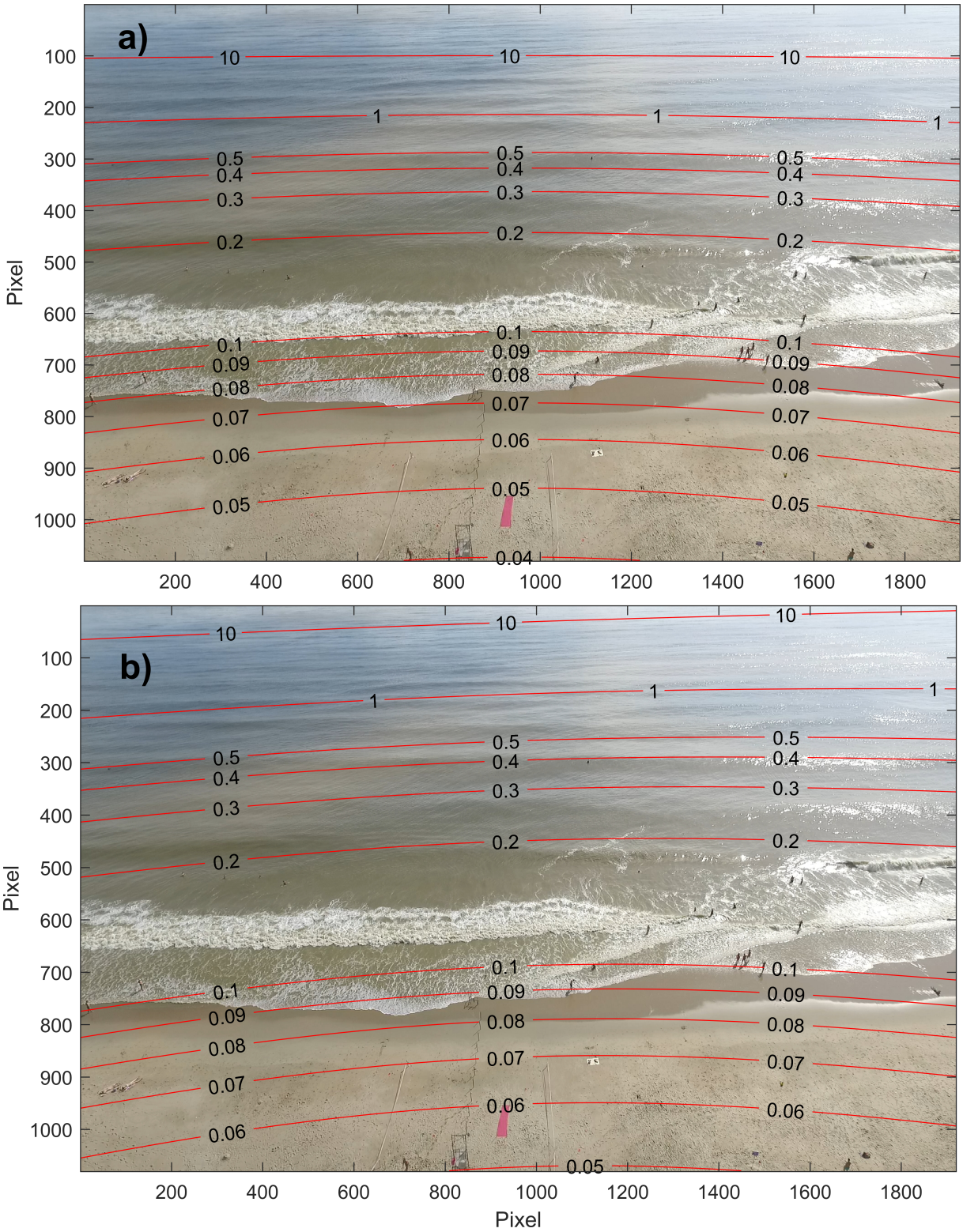

Figure 7.8: The footprint of the image for the camera system mounted on DJI P3P recorded during the NT4 field campaign. a) Represented for case without GCPs and b) for case using GCPs.

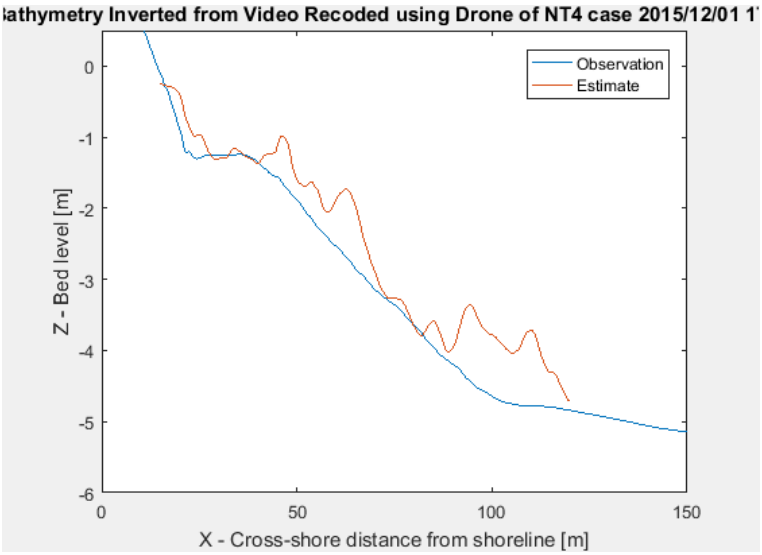

Figure 7.9: Comparison of video-based bathymetry inversion and in-situ profile measured in NT4 field campaign.

7.4.3 Results and discussion

7.4.3.1 Rectification with or without GCPs

The results of the camera rectification for the test case with and without GCPs are not shown in Figure 7.7. The results show that the difference in relative error is 4.8 cm for GCPs and 3.7 m for the cases with no GCPs. However, the footprint resolution shown in Figure 7.8 is very similar for both cases. This is interesting because in the video-based bathymetry inversion problem, the results are sensitive to accuracy in determining the relative distance between pixels, while the error with respect to the actual position of the pixels does not affect the final result.

This is quite consistent with Bergsma et al. (2018b). Bergsma et al. (2018b) find that high-accurate GCPs are unecessary, but instead can be replaced with features available on the frame and easily identified on freely available satellite imagery (e.g. Google map or Bing map). This is important because it is not always possible to measure GCPs with high accuracy and it is as we said an extra cost.

7.4.3.2 Bathymetry inversion along a measured profile

Since there is no bathymetry survey for the entire bay during NT4, the video-based bathymetry inversion was compared with a profile shown in Figure 7.9. The selected location for the section calculation in the image coincides with the surveyed transect. Despite being noisy, the results follow the main features of the profile, with an RMSE of 0.3 m and a bias of 0.8 m. It clearly shows the LTT morphology of Nha Trang beach. Because of the lack of surveyed data to compare with, the comparison is limited to a depth of about 4m, which corresponds anyway to our region of interest (i.e above the depth of closure) and to the limit of depth inversion with wind-waves in summer (Thuan et al., 2018).

7.4.3.3 Recommendations

In addition, as a guideline for future users, a preliminary sensitivity analysis suggests that the drone :

- Should fly more than 7 minutes to estimate properly the bulk wave characteristics due to their stochastics nature (Tissier et al., 2011),
- Should not use a too large yaw angle of camera (less than 70 degrees recommended) to have enough wave optical signature and maximize contrast,
- if using an embedded amateur camera with resolution less than 12MP, the drones should not fly higher than 100m to keep enough resolution and maintain less than a meter footprint.

Chapter 8

Conclusions, discussion and perspectives

Contents

The thesis had the clear objective of mounting a video system in Nha Trang, Vietnam, to diagnose the complex evolution of this low tide terraced beach under multi-scale ocean forcing. The implementation of video cameras and extraction of shoreline position needed careful adjustment of image processing. For shoreline position, the observations are very accurate and physically meaningful results could be rapidly obtained. The extraction of bathymetry was clearly more challenging and proper methods of identifying the limits of depth inversion were not available. Therefore a major methodological contribution of this thesis is in providing the first assessment of errors in video-based depth inversion.

Main contributions

8.0.1 Developing and operating remote sensing technique: shore-based coastal video system and drone

I conducted the installation of a video system in 2013 and operated it over the following years, including maintenance and transfer of images to the university server. I georectified images and corrected them from distortion using different state of the art methods (chessboard and ground control points). Therefore, I master every step of the process, from the design of a video system to its functioning and use for coastal applications. The same applies to quadricoptere monitoring for the nearshore. I used state of the art photogrammetry techniques to reconstruct the tridimentional topography of the beach dune and derived submerged bathymetry from stationary flight. These skills developed during my PhD will be useful for present and coming projects involving coastal monitoring in Vietnam (e.g., Mekong and Hoi An AFD projects).

8.0.2 Conducting field experiments to validate video estimates

4 field experiments were conducted at Nha Trang Beach withing the framework of this work funded by MOST1&2 projects and COASTVAR for the Vietnamese and French side, respectively. I participated to all these experiments and was in charge of organizing the field work, design and deployment of moorings, and beach and sea echo-sounder surveys. Besides their intrinsic interest, these field experiments were fundamental to validate video estimation of hydromorphodynamic parameters. Conducting a field experiment requires scientific and engineering skills that are currently in high demand in Vietnam. In this study, the evolution of Nha Trang shoreline is investigated with a high resolution (2Mp) and high frequency (2Hz) video camera system installed from May 2013 to present. The surfzone cross-shore profiles, shoreline positions and wave characteristics (height and period) extracted from the video data are calibrated with in-situ measurement from two field experiments (from 23/05 to 01/06 and 03/12 to 10/12 2013) and bathymetry measurement during the Haiyan typhoon event. This part provides some validation of the video data during field experiments before analyzing the shoreline evolution observed during the typhoon events of 2013 and recovery of the beach. This work is the first attempt at using video cameras in Vietnam for monitoring the evolution of coastal zones. Although further progress in data processing can still be made, our validation with field experiments give us some confidence on the accuracy of our techniques. The estimation of hydrodynamic variables appears satisfactory, while the mean accuracy of beach profiles is about 30 cm and locally higher.

8.0.3 Multi-scale shoreline evolution

In the first part of the manuscript describing the results of the PhD study, the problem of shoreline evolution in tropical Nha Trang beach is addressed for the particularly active 2013–2014 season. One of the most striking points of this study is the amount of wave energy provided by monsoon events and their dominant role on shoreline evolution. In contrast, while typhoons have large ephemeral impacts, our results show fast recovery of the shoreline. There is no evidence for a persistent influence, as suggested also for short-lived storms by Douglas and Crowell 2000 and

Zhang et al. 2002. This is confirmed here using the ShoreFor model that presents good skills at predicting intra-seasonal and seasonal scales but poorly describes short-term typhoon-induced dynamics. Recurrence of typhoons is more than 10 days so that they can be considered isolated and without cumulative effect (Ranasinghe et al., 2012). Winter monsoon events have impacts of similar magnitude to typhoons but with longer recovery, which is close to their observed recurrence period. Therefore, they can be considered as a sequence, as the beach cannot fully recover between events and is constantly moving towards high-energy equilibrium. Note that the ratio of erosion and accretion rates for typhoons is nearly constant over time, but not so for winter monsoons: while the erosion rate is constant, the accretion rate decreases after each new event. This result highlights the importance of wave event duration, to the extent that the erosive potential will be satisfied only if the event lasts the necessary time for the beach to reach new equilibrium (Kriebel and Dean, 1993). Therefore, for short-lived typhoons, full erosion potential is not achieved. Despite significant shoreline retreat, the beach profile is probably far from new equilibrium. As a consequence, shoreline recovery to its previous state (and shoreline position) occurs within a few days and does not affect longer term evolution (Hansen and Barnard, 2010). On the other hand, winter monsoon events have enough duration to achieve their full erosion potential, thus modifying the beach to a fully new equilibrium. The return of the shoreline to its previous position takes longer, leaving the beach more vulnerable.

It was previously observed that Nha Trang embayed beach has a seasonal rotation with modulation of wave incidence (Thuan et al., 2016), from northward in summer to southward transport in winter: the north end of the beach enlarges in summer and erodes in winter, the center of rotation being localized in the central part of the beach (Thanh et al., 2015). It is noteworthy that, even if summer monsoon is weak compared with high-energy winter monsoon, locally generated wind-waves can still induce a northward transport (Lefebvre et al., 2014). The shoreline near the central part of the beach – and close to the video system – mainly experiences translation due to cross-shore dynamics and is rather dominated by the event scale. This is similar to what has been observed elsewhere (Turki et al., 2013) where rotation and translation of the shoreline were quantified separately.

A main outcome of the study is the long lag (50–60 days) observed between monthly waves and shoreline location, while the envelope (Hilbert transform) of intra-seasonal monsoon events is in closer phase with the shoreline. This suggests that, contrarily to shoreline equilibrium model paradigms (Davidson et al., 2013, Yates et al., 2009), Nha Trang shoreline is actually in equilibrium with high-energy wave conditions. This is in line with observations by Jackson et al. 2002 of low-energy environments where the beach is assumed in equilibrium with previous high-energy wave events rather than with current conditions. The beach is considered inactive the rest of the time. Here, it is the particularly long duration of winter monsoon events that presumably drives most of the shoreline changes, with very gentle wave conditions in between that limit the recovery potential, as observed elsewhere by Karunarathna et al. 2014. In this sense, the phase-lag observed here between seasonal means and the intra-seasonal envelope is critical for shoreline equilibrium. To conclude on this chapter, the video camera has provided a long-term and quasi-continuous observation of the shoreline that was missing in Nha Trang beach. With relatively little effort compared to traditional monitoring, a reliable picture of

seasonal and intra-seasonal evolution is now possible in Vietnam and is very promising.

8.0.4 Bathymetry inversion with error estimate and time evolution analysis

Video-based bathymetry inversion is technically much more challenging than shoreline monitoring. There is still no video-based study showing time evolution of coastal bathymetry at scales ranging from daily to interanual. This is mainly because of lack of confidence on the results as no systematic error estimation was available. Here, we propose a solution to this probleme and apply a video-based bathymetry inversion technique in Nha Trang, using long-term data under swell to local wind-wave conditions. A main scientific result is the overall stability but high resiliency demonstrated for the LTT beach, with rapid exchange of sediment between the terrace and the upper beach during typhoons, monsoon events or seasonal cycles. The high resiliency of these tropical environments may provide faster beach recovery compared with mid-latitude configurations.

These results required careful examination of the method's validity. The treatment techniques needed for a long-term dataset is detailed, focusing on the method's limitations in the case of wind waves. For the first time, a tide gauge is used to quantify the error produced by video estimates and produce a quality criterion. Three sources of error are exhibited in a single analysis. They are clearly identified: 1) nonlinearities and wave setup localized in very shallow water; 2) change in the optical wave signature at breakpoint; 3) deep water limit for applying the linear dispersion relation, which is very restricting for wind waves ($D_{limit} \sim 3$ m for $T = 3$ s). The error types have contrasted spatial and temporal patterns, but the main error component in Nha Trang is deep water limitation. It has strong seasonality and is greatest in summer, when short wind waves are dominant, making depth inversion invalid. On the contrary, the second and third dominant error contributions at breakpoint and in the surf zone are maximum for large waves (during winter monsoon in Nha Trang). Corrections should and will probably be proposed for these errors in the future.

More generally, this study provides guidelines for users of video-based depth inversion methods and a base for standalone error assessment, which is essential for operational and data assimilation systems. For data assimilation, the estimation of error is required but generally not available (Wilson et al., 2012, Birrien et al., 2013). A comprehensive error estimate, such as the one proposed here, is thus an excellent step for improving the assimilation approach.

8.0.5 Guidelines for drone usage

The study is concluded with an exploratory chapter on the use of drones for remotely assessing a continuous profile of topography and bathymetry. Instead of using a fixed-wing drone, which is not best suited for stationary applications, in this study, we use a rotary-wing drone with a very-high resolution camera. The study shows that the technique developed for shore-based video cameras can be successfully applied to a video system attached to a rotary-wing drone. Drone estimates are successfully compared with bathymetric surveys in Nha Trang. In addition, a preliminary sensitivity analysis suggests some guideline for future users.

Future research

8.0.6 2D extension of cross-correlation method

With the development of video cameras and storage facilities, it is now possible to improve video system performances, namely spatial and temporal resolutions. For example, the system in Nha Trang – and most previous systems (e.g., Biscarrosse, SW France) – were designed to acquire pixel intensity along a few cross-shore and long-shore transects (timestacks). However, it is now possible to acquire full frame images at appropriate frequency. This was actually done at Nha Trang as it is now the routine mode of drone videos. The spectral method of cBathy (Holman et al., 2013) uses the 2D information of this image format in an optimal way, by computing coherence maps of phases (Bergsma et al., 2016). The temporal method used in this PhD study (Almar et al., 2008, Bergsma and Almar, 2018) can be extended in 2D based on the same principle. Random correlations with lagged timeseries can be done to retrieve both the distance traveled by waves during this lag and the direction of propagation. This will lift the assumption of 1D wave propagation, which is often justified in shallow waters (Tissier et al., 2011) but can cause projection errors in the shoaling area or with complex submerged bathymetry (Lerma et al., 2017).

8.0.7 Potential of video coastal network: ground truth for spatial studies and early warning systems

The results obtained in this study show that the video present good skills in observing the variability of sea level when compared with tide. But recent work by Abessolo Ondoa et al. (2018) shows that it can be extended at monthly, seasonal and even interranual scales. It is a low-cost technique suitable for nearshore areas where the installation of traditional measuring devices turns out delicate and expensive. Shore-based video systems can be used supplementary to existing tide gauges and altimetry. Video estimates of sea levels can be used to investigate processes related to storms surges and coastal flooding and support high-frequency and localized validation of wave forecasts and reanalysis of ocean forcing. This could make it possible to fill in the knowledge gap that exists between deep waters and the coast. A regional network of video cameras along the West African coast, for example, would densify the sea level monitoring network, provide long-term coastal sea level time series, and promote validation of the method to estimate the coastal contribution to sea levels proposed by Melet et al. (2018). It could be the backbone of a real-time, early warning systems for coastal disasters, as shown in Sembiring et al. (2017).

8.0.8 Data assimilation in a numerical model (CROCO)

Video-based bathymetry fields are noisy by nature but offer information on evolution that is critical for understanding the coastal system. Depth estimates can come with strong error and thus require careful selection and corrections. To optimize this process, depth-inversion methods based on data assimilation have recently emerged. Basically, video-based observed properties are compared with numerical model results, and the estimated bathymetry is adjusted to improve

the fit between model output and observations. The first work was carried out by Van Dongeren et al. (2008) with the development of Beach Wizard, a simple data assimilation module. Video-derived observations (dissipation, celerity, intertidal shoreline variation) are assimilated in the hydrodynamic model Delft3D through an optimal least-squares estimator applied to all points of the study field. Here, the method provides a balanced beach profile for each image at a given time but their is no prognostic equation for morphological evolution. Wilson et al. (2012) proposed a holistic approach using wave-current coupled models and heterogeneous data (wave heights and currents). Finally, Birrien et al. (2013) focused on bathymetry evaluation for sandy beaches with intermediate type bars (Wright and Short, 1984). They have developed a method applied to the 1D-Beach phase-resolving wave model. Their approach combines Van Dongeren et al. (2008)'s approach for the data used and Wilson et al. (2012)'s for the data assimilation method. The spatial distribution of observational error is given by a simple discrimination according to the study area, while considering a constant error amplitude. More generally, all these methods have limitations associated with lack of characterization of the observation error. That may lead to one of the largest error made by the assimilation method. Based on the characterization of observation error now available from this PhD study, we propose to lift this limitation.

Depth-inversion from different techniques and images together with tidal data can be used to estimate uncertainty and sensitivity of numerical simulations to observations. Data assimilation has so far been done with uncoupled hydrodynamic models but it could also be performed in a model like CROCO using coupled wave-current-sediment dynamics, in which bathymetry evolution is part of the prognostic equations. Ongoing data assimilation experiments using CROCO have started at LEGOS (LEFE project, Rachid Benshila) and are leading to the first interesting results. Eventually, the improved bathymetry fields will contribute to improved wave, current and flood modeling (runup, overtopping), as well as morphological evolution.

Conclusions en Français

L'objectif de la thèse était de monter un système vidéo à Nha Trang, au Vietnam, pour diagnostiquer l'évolution complexe de cette plage à terrasse soumis à un forçage océanique variable. La mise en place de caméras vidéo et l'extraction de la position du rivage nécessitaient un ajustement minutieux du traitement des images. Pour la position du rivage, les observations sont très précises et des résultats physiquement significatifs ont pu être obtenus rapidement. L'extraction de la bathymétrie était nettement plus difficile et il n'existait pas de méthodes appropriées pour déterminer les limites de l'inversion bathymétrique. Par conséquent, une contribution méthodologique majeure de cette thèse est de fournir une première évaluation systématique des erreurs dans l'inversion bathymétrique par vidéo.

Principales contributions

Mise au point et exploitation d'une technique de télédétection : système vidéo côtier à terre et drone

J'ai réalisé l'installation d'un système vidéo en 2013 et l'ai exploité au cours des années suivantes, y compris la maintenance et le transfert des images au serveur de l'université. J'ai geo-ajusté les images et les ai corrigé de la distorsion en utilisant différentes méthodes de pointe (échiquier et points de contrôle au sol). Je maîtrise donc toutes les étapes du processus, de la conception d'un système vidéo à son fonctionnement et à son utilisation pour des applications côtières. Il en va de même pour la surveillance des quadricoptères dans les eaux littorales. J'ai utilisé des techniques photogrammétriques de pointe pour reconstituer la topographie tridimensionnelle de la dune de plage et j'ai dérivé la bathymétrie submergée du vol stationnaire. Ces compétences développées au cours de mon doctorat seront utiles pour les projets actuels et à venir en matière de surveillance côtière au Vietnam (e.g., les projets AFD du Mékong et de Hoi An).

Réalisation d'expériences sur le terrain pour valider les estimations vidéo

4 expériences de terrain ont été menées à Nha Trang Beach dans le cadre de ce travail financé par les projets MOST1&2 et COASTVAR pour le Vietnam et la France respectivement. J'ai participé à toutes ces expériences et j'étais responsable de l'organisation du travail sur le terrain, de la conception et du déploiement des amarrages, ainsi que des relevés des échosondeurs de plage et de mer. Outre leur intérêt intrinsèque, ces expériences de terrain ont été fondamentales pour valider l'estimation vidéo des paramètres hydro-morphodynamiques. La réalisation d'une

expérience sur le terrain nécessite des compétences scientifiques et techniques qui sont actuellement très demandées au Vietnam. Dans cette étude, l'évolution du littoral de Nha Trang est étudiée en détail avec un système de caméra vidéo haute résolution (2Mp) et haute fréquence (2Hz) installé depuis mai 2013. Les profils transversaux de la zone de déferlement, les positions des rives et les caractéristiques des vagues (hauteur et période) extraits des données vidéo sont calibrés avec des mesures in situ de deux expériences sur le terrain (du 23/05 au 01/06 et du 03/12 au 10/12 2013) et des mesures bathymétriques pendant le typhon Haiyan, la section résultats fournit une validation des données vidéo pendant les expériences de terrain et analyse ensuite les évolutions observées pendant les typhons en 2013 et la récupération saisonnière de la plage.

Nous présentons la première tentative d'utilisation de caméras vidéo au Vietnam pour suivre l'évolution des zones estuariennes et côtières. Bien que des progrès puissent être réalisés dans le traitement des données, notre validation par des expériences sur le terrain nous donne une certaine confiance dans l'exactitude de nos techniques. L'estimation des variables hydrodynamiques semble satisfaisante, alors que la précision moyenne des profils de plage est d'environ 30 cm et localement supérieure.

Évolution multi-échelle du trait de côte

Dans la première partie du manuscrit, nous avons abordé le problème de l'évolution du littoral de la plage tropicale de Nha Trang, au Vietnam, au cours de la saison 2013-2014 particulièrement active. L'un des points les plus frappants de cette étude est la quantité d'énergie des vagues fournie par les moussons et leur rôle dominant sur l'évolution du littoral. Par contre, bien que les typhons aient des impacts éphémères importants, nos résultats montrent un rétablissement rapide du rivage. Il n'y a aucune preuve d'une influence persistante, comme le suggèrent également les tempêtes de courte durée de Douglas and Crowell 2000 et Zhang et al. 2002. Ceci est confirmé ici à l'aide du modèle ShoreFor qui présente de bonnes aptitudes à prédire les échelles intrasaisonnières et saisonnières mais qui décrit mal la dynamique à court terme induite par les typhons. La récurrence des typhons est supérieure à 10 jours de sorte qu'ils peuvent être considérés comme isolés et sans effet cumulatif (Ranasinghe et al., 2012). Les moussons d'hiver ont des impacts d'une ampleur similaire à ceux des typhons, mais avec une période de récupération plus longue, qui est proche de la période de récurrence observée. Par conséquent, ils peuvent être considérés comme une séquence, car la plage ne peut pas récupérer complètement entre les événements et se déplace constamment vers l'équilibre de haute énergie. Il est à noter que le rapport des taux d'érosion et d'accrétion des typhons est presque constant dans le temps, mais pas pour les moussons d'hiver : alors que le taux d'érosion est constant, le taux d'accrétion diminue après chaque nouvel événement. Ce résultat souligne l'importance de la durée de l'événement des vagues, dans la mesure où le potentiel érosif ne sera satisfait que si l'événement dure le temps nécessaire pour que la plage atteigne un nouvel équilibre (Kriebel and Dean, 1993). Par conséquent, pour les typhons de courte durée, le potentiel d'érosion n'est pas pleinement exploité. Malgré un recul important des rives, le profil de la plage est probablement loin d'être rééquilibré. Par conséquent, le rétablissement du rivage à son état antérieur (et à sa position sur le rivage) se produit en quelques jours et n'affecte pas l'évolution à long terme

(Hansen and Barnard, 2010). D'autre part, les épisodes de mousson hivernale ont une durée suffisante pour atteindre leur plein potentiel d'érosion, modifiant ainsi la plage vers un équilibre entièrement nouveau. Le retour du rivage à sa position antérieure prend plus de temps, ce qui rend la plage plus vulnérable.

On a observé précédemment que la plage en baie de Nha Trang a une rotation saisonnière avec modulation de l'incidence des vagues (Thuan et al., 2016), du nord en été vers le sud en hiver : l'extrémité nord de la plage s'élargit en été et s'érode en hiver, le centre de rotation étant localisé dans la partie centrale de la plage (Thanh et al., 2015). Il est à noter que, même si la mousson d'été est faible par rapport à la mousson d'hiver à haute énergie, les vagues de vent produites localement peuvent encore induire un transport vers le nord (Lefebvre et al., 2014). Le rivage près de la partie centrale de la plage et près du système vidéo subit principalement une translation due à la dynamique transverse du littoral et est plutôt dominé par les événements énergétiques. C'est similaire à ce qui a été observé ailleurs (Turki et al., 2013) où la rotation et la translation du littoral ont été quantifiées séparément.

L'un des principaux résultats de l'étude est le long décalage (50 à 60 jours) observé entre les vagues mensuelles et la position du rivage, tandis que l'enveloppe (transformée de Hilbert) des événements de mousson intrasaisonniers est en phase plus proche avec le rivage. Cela suggère que, contrairement aux paradigmes des modèles d'équilibre du littoral (Davidson et al., 2013, Yates et al., 2009), le littoral de Nha Trang est en fait en équilibre avec des conditions de vagues à haute énergie. Cela est conforme aux observations de Jackson et al. 2002 sur les environnements à basse énergie où la plage est supposée en équilibre avec les vagues à haute énergie antérieures plutôt qu'avec les conditions actuelles. La plage est considérée comme inactive le reste du temps. Ici, c'est la durée particulièrement longue des moussons hivernales qui est probablement à l'origine de la plupart des changements littoraux, avec des vagues très douces entre les deux qui limitent le potentiel de récupération, comme l'a observé Karunarathna et al. 2014 ailleurs. En ce sens, le décalage de phase observé ici entre la moyenne saisonnière et l'enveloppe intrasaisonnière est critique pour l'équilibre du littoral. Pour conclure ce chapitre, la caméra vidéo a fourni une observation à long terme et quasi-continue du littoral qui manquait sur la plage de Nha Trang. Avec relativement peu d'efforts par rapport à la surveillance traditionnelle, une image fiable de l'évolution saisonnière et intrasaisonnière est maintenant possible au Vietnam, ce qui semble prometteur.

Inversion bathymétrique avec estimation des erreurs et analyse de l'évolution temporelle

L'inversion bathymétrique par vidéo est techniquement beaucoup plus difficile que la surveillance du littoral. Il n'existe toujours pas d'étude vidéo montrant l'évolution temporelle de la bathymétrie côtière à des échelles allant de quotidienne à interanuelle. Cela s'explique principalement par un manque de confiance dans les résultats, car aucune estimation systématique des erreurs n'était disponible. Nous proposons ici une solution à ce problème et appliquons une technique d'inversion bathymétrique par vidéo à Nha Trang, en utilisant des données à long terme dans des conditions de houle et de vent local. L'un des principaux résultats scientifiques est la stabilité globale et la haute résilience démontrée pour la plage LTT, avec un échange

rapide de sédiments entre la terrasse et la plage supérieure pendant les typhons, les évènements de mousson ou les cycles saisonniers. La haute résilience de ces environnements tropicaux peut permettre une récupération plus rapide des plages par rapport aux configurations des latitudes moyennes.

Ces résultats ont nécessité un examen attentif de la validité de la méthode. Les techniques de traitement nécessaires pour un ensemble de données à long terme sont détaillées, en mettant l'accent sur les limites de la méthode dans le cas des vagues de vent. Pour la première fois, un marégraphe est utilisé pour quantifier l'erreur produite par les estimations vidéo et produire un critère de qualité. Trois sources d'erreur sont présentées dans une seule analyse. Ils sont clairement identifiés : 1) non-linéarités en eau très peu profonde ; 2) changement de la signature du signal optique au point de rupture ; 3) limite en eau profonde pour l'application de la relation de dispersion linéaire, ce qui est très restrictif pour les vagues de vent ($D_{limit} \sim 3$ m pour $T = 3$ s). Les types d'erreurs ont des distributions spatialles et temporelles contrastées, mais la principale composante d'erreur dans Nha Trang est la limitation en eau profonde. Elle est fortement saisonnière et est plus forte en été, lorsque les vagues de vent (courtes et de faible amplitude) sont dominantes, ce qui rend invalide l'inversion de la profondeur. Au contraire, les deuxième et troisième erreurs dominantes au point de rupture et dans la zone de déferlement sont maximales pour les grosses vagues (pendant la mousson d'hiver à Nha Trang). Des corrections devraient être et seront probablement proposées pour ces erreurs à l'avenir.

Plus généralement, cette étude fournit des lignes directrices pour les utilisateurs de méthodes d'inversion de profondeur basées sur la vidéo et une base pour l'évaluation autonome des erreurs, qui est essentielle pour les systèmes opérationnels et d'assimilation de données. Pour l'assimilation des données, l'estimation de l'erreur est requise mais généralement non disponible (Wilson et al., 2012, Birrien et al., 2013). Une estimation complète des erreurs, telle que celle proposée ici, est donc une excellente étape pour améliorer l'approche d'assimilation.

Recherches futures

Extension 2D de la méthode de corrélation croisée

Avec le développement des caméras vidéo et des installations de stockage, il est maintenant possible d'améliorer les performances des systèmes vidéo, notamment les résolutions spatiales et temporelles. Par exemple, le système de Nha Trang - et la plupart des systèmes précédents (e.g., Biscarrosse, sud-ouest de la France) - ont été conçus pour acquérir l'intensité des pixels le long de quelques transects transversaux et longitudinaux. Cependant, il est maintenant possible d'acquérir des images en plein cadre à une fréquence appropriée. Cela a été fait à Nha Trang car c'est maintenant le mode de routine des vidéos de drones. La méthode spectrale de cBathy (Holman et al., 2013)) utilise l'information 2D de ce format d'image de manière optimale, en calculant les cartes de cohérence des phases (Bergsma et al., 2016). La méthode temporelle utilisée dans cette thèse (Almar et al., 2008, Bergsma and Almar, 2018) peut être étendue en 2D selon le même principe. Des corrélations aléatoires avec les séries chronologiques retardées peuvent être faites pour récupérer à la fois la distance parcourue par les ondes pendant ce décalage et la direction de propagation. L'hypothèse de propagation de l'onde 1D, qui est

souvent justifiée dans les eaux peu profondes (Tissier et al., 2011) mais qui peut causer des erreurs de projection dans la zone de haut-fond ou avec une bathymétrie submergée complexe (Lerma et al., 2017), sera ainsi levée.

Potentiel du réseau vidéo côtier : vérité de terrain pour les études spatiales et les systèmes d'alerte précoce

Les résultats obtenus dans cette étude montrent que la vidéo présente de bonnes aptitudes à observer la variabilité du niveau de la mer par rapport à la marée. Mais les travaux récents de Abessolo Ondoa et al. (2018) montrent qu'elle peut être étendu à des échelles mensuelles, saisonnières et même interannuelles. Il s'agit d'une technique peu coûteuse adaptée aux zones littorales où l'installation d'appareils de mesure traditionnels s'avère délicate et coûteuse. Les systèmes vidéo à terre peuvent être utilisés en complément des marégraphes et de l'altimétrie existants. Les estimations vidéo du niveau de la mer peuvent être utilisées pour étudier les processus liés aux ondes de tempête et aux inondations côtières et appuyer la validation haute fréquence et localisée des prévisions de vagues et la réanalyse du forçage des océans. Cela pourrait permettre de combler le fossé des connaissances qui existe entre les eaux profondes et la côte. Un réseau régional de caméras vidéo le long de la côte ouest-africaine, par exemple, densifierait le réseau de surveillance du niveau de la mer, fournirait des séries chronologiques à long terme du niveau de la mer côtière et favoriserait la validation de la méthode proposée par Melet et al. (2018) pour estimer la contribution côtière au niveau de la mer. Il pourrait constituer l'épine dorsale d'un système d'alerte rapide en temps réel pour les catastrophes côtières, comme le montre l'exemple de Sembiring et al. (2017).

Assimilation de données dans un modèle numérique (CROCO)

Les champs de bathymétrie vidéo sont bruyants par nature mais offrent des informations sur l'évolution qui sont essentielles pour comprendre le système côtier. Les estimations de profondeur peuvent s'accompagner d'une forte erreur et donc nécessiter une sélection et des corrections minutieuses. Pour optimiser ce processus, des méthodes d'inversion de profondeur basées sur l'assimilation de données ont récemment vu le jour. Fondamentalement, les propriétés observées par vidéo sont comparées aux résultats du modèle numérique, et la bathymétrie estimée est ajustée pour améliorer l'ajustement entre la sortie du modèle et les observations. Le premier travail a été réalisé par Van Dongeren et al. (2008) avec le développement de Beach Wizard, un module simple d'assimilation de données. Les observations vidéo (dissipation, célérité, variation du rivage intertidal) sont assimilées dans le modèle hydrodynamique Delft3D grâce à un estimateur optimal des moindres carrés appliqué à tous les points du champ d'étude. Ici, la méthode fournit un profil de plage équilibré pour chaque image à un moment donné, mais il n'y a pas d'équation pronostique de l'évolution morphologique. Wilson et al. (2012) a proposé une approche holistique utilisant des modèles couplés vagues-courants et des données hétérogènes (hauteurs de vagues et courants). Enfin, Birrien et al. (2013) s'est concentré sur l'évaluation bathymétrique des plages de sable avec des barres de type intermédiaire (Wright and Short, 1984). Ils ont développé une méthode appliquée au modèle de vagues à résolution de phase 1D-Beach. Leur approche combine l'approche de Van Dongeren et al. (2008) pour les données

utilisées et celle de Wilson et al. (2012) pour la méthode d'assimilation des données. La distribution spatiale de l'erreur d'observation est donnée par une simple discrimination selon la zone d'étude, tout en considérant une amplitude d'erreur constante. Plus généralement, toutes ces méthodes ont des limites liées à l'absence de caractérisation de l'erreur d'observation. Cela peut conduire à l'une des plus grandes erreurs commises par la méthode d'assimilation. Sur la base de la caractérisation de l'erreur d'observation maintenant disponible dans cette étude doctorale, nous proposons de lever cette limitation.

L'inversion de la bathymétrie à partir de différentes techniques d'imagerie (drone et video) peut être combinée à des données de marées pour estimer l'incertitude et la sensibilité des simulations numériques aux observations. Jusqu'à présent, l'assimilation des données a été réalisée à l'aide de modèles hydrodynamiques découplés, mais elle pourrait également être réalisée dans un modèle comme CROCO en utilisant la dynamique couplée vague-courant-sédiment, dans laquelle l'évolution bathymétrique fait partie des équations pronostiques. Des expériences d'assimilation de données en cours avec CROCO ont débuté au LEGOS (projet LEFE, Rachid Benshila) et conduisent à des premiers résultats intéressants. À terme, l'amélioration des champs de bathymétrie contribuera à l'amélioration de la modélisation des vagues, des courants et des inondations (runup, overtopping), ainsi qu'à l'évolution morphologique.

Appendix A

Appendix I Article in JCR

Journal of Coastal Research	SI	75	263-267	Coconut Creek, Florida	2016

Typhoon Impact and Recovery from Continuous Video Monitoring: a Case Study from Nha Trang Beach, Vietnam

Duong H. Thuan[†§*], Le T. Binh[††], Nguyen T. Viet[†‡], Dong K. Hanh[†], Rafael Almar[§], and Patrick Marchesiello[§]

[†]Faculty of Civil Engineering
ThuyLoi University
Hanoi, Vietnam

[††]Vietnam Hydraulic Engineering Consultants Corporation
Hanoi, Vietnam

[‡]Central Region College of Technology, Economics, and Water Resources
Hoian, Vietnam

[§]IRD-LEGOS
Université Paul Sabatier/CNRS/CNES/IRD
Toulouse, France

www.cerf-jcr.org

www.JCRonline.org

ABSTRACT

Thuan, D.H.; Binh, L.T;Viet, N.T.; Hanh, K.D.; Almar, R., and Marchesiello, P., 2016. Typhoon impact and recovery from continuous video monitoring: a case study from Nha Trang beach, Vietnam. *In:* Vila-Concejo, A.; Bruce, E.; Kennedy, D.M., and McCarroll, R.J. (eds.), *Proceedings of the 14th International Coastal Symposium* (Sydney, Australia). *Journal of Coastal Research*, Special Issue, No. 75, pp. 263-267. Coconut Creek (Florida), ISSN 0749-0208.

Nha Trang beach in Vietnam is regarded as one of the most beautiful beaches in the world. However, its degradation in recent years is a serious problem for its economic development. Understanding the mechanisms of shoreline evolution is thus part of an integrated management strategy of the area. In this study, the evolution of Nha Trang shoreline is investigated in detail with a high resolution (2Mp) and high frequency (2Hz) video camera system installed from May 2013 to present. The surfzone cross-shore profiles, shoreline positions and wave characteristics (height and period) extracted from the video data are calibrated with in-situ measurement from two field experiments (from 23/05 to 01/06 and 03/12 to 10/12 2013) and bathymetry measurement during the Haiyan typhoon event. The study shows a marked seasonal evolution of the Nha Trang shoreline with accretion from March to September and cumulated seasonal amplitude of about 15 m. The impact of Nari and Haiyan typhoons to the shoreline is also dramatic with changes of 4 to 8 m in each case. The recovery to individual events is fast, of the order of one and half month.

ADDITIONAL INDEX WORDS: *Shoreline evolution, recovery, video monitoring, Nha Trang beach.*

INTRODUCTION

A beach located in a semi-enclosed bay, mostly sheltered from wave action or exposed to seasonal modulation of moderate energy waves, can be defined as a low energy environment (Jackson *et al.*, 2002). In such environment, major morphological changes are generally attributed to events of moderate to high-energy waves, with long periods of inactivity in between. Transfers between the subtidal region and upper beach are assumed weak or non-existent since the depth-of-closure (beyond which the depths do not change with time) is small. These assumptions have not been challenged until recently and low-energy environments have remained beyond the scope of major research interest. Yet, they raise important issues: how can a beach recover if the subtidal and upper beach sediment cells are disconnected? Are morphological features only generated during energetic events or do low-energy wave conditions have a role to play in the recovery process?

During extreme events, the beach is observed to evolve dramatically, dominated by surf processes that can rapidly lead to an up-state transition through offshore sediment transport by the undertow and sandbar formation. After such extreme event, the beach slowly evolves through transient states while recovering under low or moderate energy wave forcing (Coco *et al.*, 2014; Angnuureng *et al.*, 2015). There is as yet no consensus on whether these events have transient or persistent impact on beach evolution and on the crucial recovery processes leading to beach resilience (Anderson *et al.*, 2010). Resilience capacity would relate on the extent of departure from equilibrium driven by short events and on recovery timescale, which can be from days to years, depending on the site and severity of events. For isolated storm events, departure from equilibrium is related to storm intensity (Frazer *et al.*, 2009; Davidson *et al.*, 2013). However, no clear conclusion can be drawn when considering sequences of storms, since both enhanced and weakened effects are observed (Ferreira 2005; Karunarathna *et al.*, 2014; Splinter *et al.*, 2014). It seems that it is the interplay between recurrence interval of events and post-event (low-energy) recovery timescales that matters. For example, a sequence of events with recurrence interval shorter than recovery duration (*e.g.*, strong 2013-2014 winter events in Europe; Masselink *et al.*, 2014; Castelle *et al.*, 2015) shows greater impact than individual

DOI: 10.2112/SI75-053.1 received 15 October 2015; accepted in revision 15 January 2016.
*Corresponding author: duonghaithuan@gmail.com

events. The reason is that the system moves sequentially toward a new state of high-energy equilibrium.

The evolution of a beach can be characterized at different time scales, *i.e.*, interannual, seasonal or event scales. (Quartel *et al.*, 2008). The most dramatic changes occur occasionally during a storm event and high-frequency assessment is needed in this case. Traditional observation tools are designed for low frequency monitoring (bi-monthly with satellites and monthly with GPS) or are sporadic during measurement campaigns. Key parameters of coastal morphodynamics may be missed. To circumvent the problem, low cost systems of coastal video imaging (Holland *et al.*, 1997; Holman and Haller 2013) were designed. They are particularly well suited to monitor the shoreline evolution in various parts of the world, covering timescales from seconds to years and spatial scales from meters to kilometers. It allows a monitoring of beach morphology as well as hydrodynamic factors governing its evolution. Here, we present some analysis of shoreline seasonal evolution and typhoon impact in Nha Trang beach using the video camera technique. It will provide an example of the patterns and interplay between storm events and seasonal recovery in a low-energy environment.

DATA AND METHODS

The study site is Nha Trang Beach (12°N, 109°E), south-east of Vietnam in the Khanh Hoa Province, facing the fetch limited South China Sea (Figure 1). This beach has been identified by the Vietnamese government as a priority for the development of tourism. Wave climate is characterized by large seasonal variations. The wave regime is dominated by southerly wind waves during summer monsoon, from March to September, and by northeasterly swell during winter monsoon, from October to February. Vietnam lies within the most active cyclogenesis region in the world and 4 to 6 typhoons hit the coast every year (Nicholls *et al.*, 1999) from October to December. This rugged coastline is characterized by sandy/mud mixed environment.

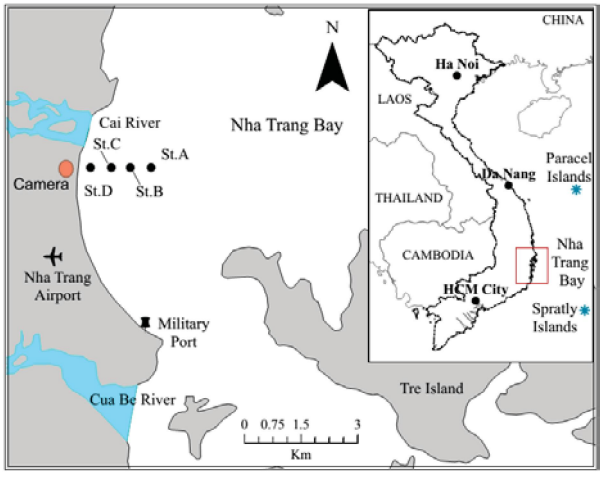

Figure 1. Study area of Nha Trang bay: location of the camera system (red dot) and field observation stations (St.A, B, C, D) in black dot.

The 7-km long Nha Trang embayed beach is orientated along a meridional axis (Figure 1), sheltered from southeasterly to southerly waves by Tre Island and disrupted at its center part by the Cai river mouth. Sediment on the shoreface is medium sized (D50 = 300 μm). The beach is a wave-dominated mixed micro-tidal environment (Relative Tidal Range, *i.e.*, tidal range modulated by wave height: RTR~1). The beach morphology presents strong variability but remains mostly in alongshore uniform, intermediate low-tide terrace, reflective upper beach state (Gourlay parameter Ω~1.5).

Field experiments

Two field experiments were conducted at Nha Trang Beach in 2013 (Figure 1), from May 26 to 30 and December 3 to 10. The first experiment (NT1) targeted the summer monsoon wind-wave dominated dynamics, and the other (NT2) the more energetic winter monsoon swell dominated dynamics. Deployments during the two experiments were similar: offshore wave and tidal forcing were given by 2 AWACs (acoustic Doppler profiler and directional wave gauge) in 10 m and 5-6 m depths and a current-meter in 3-m depth; refined surfzone and swash measurements were provided by swash video poles and a micro-profiler. A bathymetric survey was carried out at the beginning of each experiment while upper beach changes were monitored by daily theodolite surveys.

To complement these intensive short-term experiments, a two-camera permanent video system was deployed in March 2013 (Viet *et al.*, 2014a,b; Lefebvre *et al.*, 2014). Hydrodynamics (waves, currents, tides) and morphological parameters (upper beach morphology, bathymetry, shoreline, beach volume) are then extracted from processed secondary images.

Video processing

The video system consists of two high-resolution cameras (2Megapixel), which can cover a wide area of approximately 1.5 km by 1 km with a temporal resolution of 2 frames per second. Three types of images are generated: a snapshot to control image quality, a 15-min average to detect the shoreline position, and a radial time series of pixel intensity (timestacks).

The shoreline location can be obtained using various definitions (Boak and Turner, 2005). Here, it is derived from optical variables (Aarninkhof *et al.,* 2003) as the interface between water and beach in average images following the two-step method of Almar *et al.* (2012): a first detection of the red to blue and green pixel transition and refinement by minimizing the variation of shoreline length around its location. This method showed good skills at beaches with complex intertidal zones. Determination of the intertidal beach profile involved the delineation of the shoreline at different tidal levels (Aarninkhof *et al.*, 2003) and interpolation between low and high tides.

Breaker wave height (Almar *et al.*, 2012), period and surface elevation (inversed from celerity; see Stockdon and Holman, 2000; Catalán and Haller, 2008) were determined from space-time images.

RESULTS

The results section first provides some validation of the video data during the field experiments and then proceeds to analyze the shoreline evolution observed during the typhoon events of 2013 and seasonal recovery of the beach.

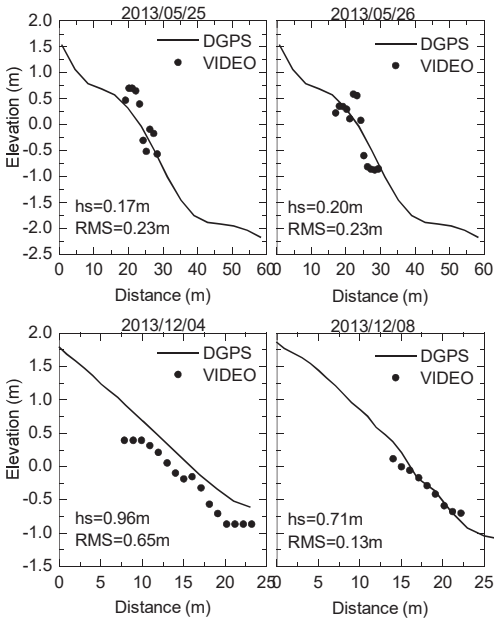

Figure 2. Comparison of beach profiles detected by camera and measured by DGPS.

Validation of video data during the fields experiments

During NT1, the tidal range varied from 0.8 to 1.5 m, while the southerly wind-waves remained roughly constant over the experiment with Hs=0.25 m, Tp=3.3 s, although there was diurnal modulation by the afternoon sea breeze. The beach profiles showed no substantial change, with a spring high-tide beach step and a rather linear swash zone, presenting a steep reflective slope of 0.17.

During NT2, the tidal range varied from spring to neap tide between 1.7 and 0.6 m. The swell showed quasi-constant characteristics with Hs~1 m and Tp~8 s from shore-normal incidence. It is noteworthy that the mega-typhoon Haiyan, which notoriously devastated central Philippines on November 8, hit the Vietnam coast on November 14, about 2 weeks before the beginning of our experiment. Even though wave energy during NT2 was moderate, the beach was recovering from the storm. The longshore-averaged beach profiles showed an almost constant slope of 0.15 throughout the experiment, but the morphology changed from a linear to convex shape.

In Figure 2, video-based and surveyed intertidal profiles are compared. The RMS error is 30 cm in average over NT1 and NT2, which is within the usual uncertainty shown by video techniques (*e.g.*, Aarninkhof *et al.,* 2003). In Figure 3, video estimates of hydrodynamic properties near the breaker point (wave height Hs and period Tp and tidal elevation) are compared with in-situ AWAC measurements during NT1 and NT2. An overall good agreement is found for tidal elevation (RMSE = 34 cm, bias 5 cm), Hs (RMSE = 6 cm, bias 2 cm) and Tp (RMSE = 1.18 s, bias 0.82 s). The skills are better for NT2, probably because of the clearer wave signature (swell waves during NT2 versus wind waves during NT1).

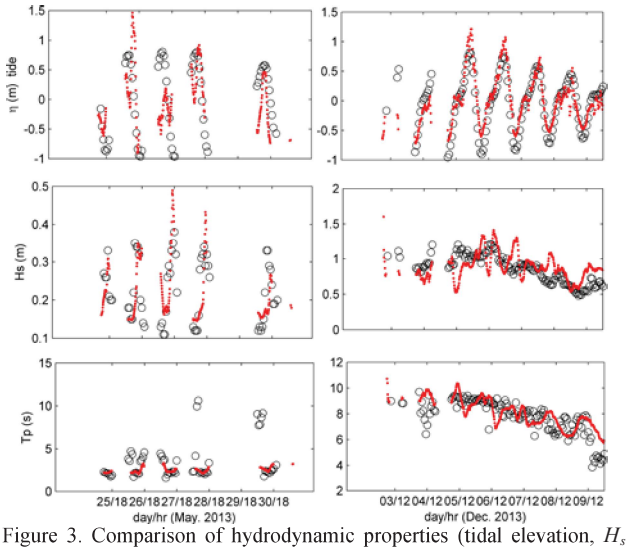

Figure 3. Comparison of hydrodynamic properties (tidal elevation, H_s and T_p), from video (red dots) and from in-situ measurements (black circles), for NT1 (left) and NT2 (right).

Typhoon impact and recovery

Our period of analysis covers a year of video data from June 2013 to June 2014 (Figure 4). Year 2013 was particularly rich in storm events in the South China Sea (up to 10 events affected Vietnam in various ways) and two typhoons most noticeably impacted the study site during this period: one from October 13 to 16 (Nari), the second from November 10 to 14 (Haiyan).

We computed the longshore-averaged shoreline location (Figure 4d), and analyzed it with respect to wave conditions (Figure 4c) and beach profile video estimates (not shown). In Figure 4c, only the seasonal wave conditions are apparent as the storm events are smoothed out and indicated as red arrows on the shoreline figure (Figure 4d). Two individual video images (Figure 4ab) of a calm summer monsoon day and of the Haiyan typhoon event, respectively, illustrate the contrasted conditions encountered in Nha Trang. The seasonal wave forcing is also very contrasted between winter and summer monsoons and correlated with shoreline evolution.

DISCUSSION

During summer, the reflective beach is in equilibrium with small wind-wave forcing. In the swell-dominated winter period, it evolves toward a more dissipative profile with formation of a low-tide terrace. Then, the first storm event (Nari) causes a marked erosion of the top of intertidal zone. The beach narrows in response to erosion and has a receding shoreline (about 4 m). The beach may also have developed sand bars during the storm and taken on a more dissipative profile. Following the first

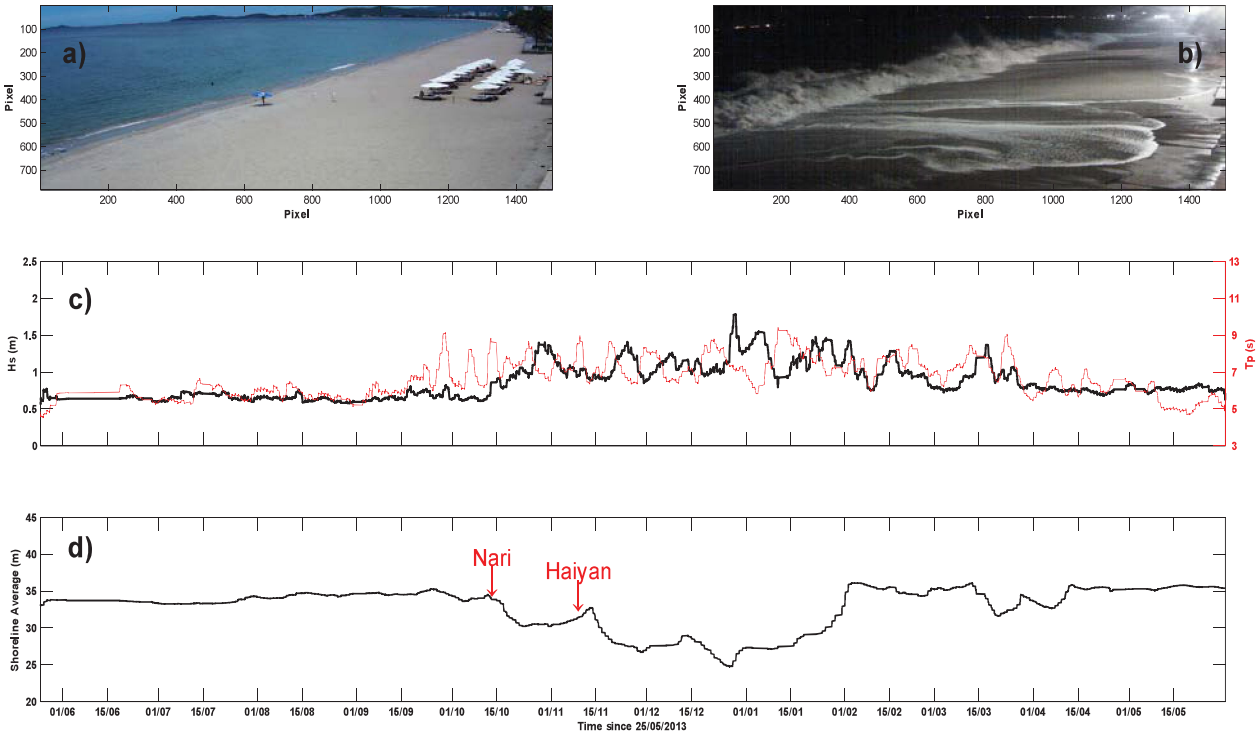

Figure 4. Typhoon impact on shoreline position. a) summer monsoon conditions with dominant south easterly waves; b) Haiyan event during the night of November 14; c) significant wave height (Hs) in black line and wave period (Tp) in red line extracted from video images during a year from June 2013 to June 2014; and d) corresponding average shoreline position compared with the embankment.

storm, the shoreline accreted rapidly. Then, the second storm (Haiyan) hit with greater impact, possibly because it had greater energy, or because it occurred in a sequence, or even because the tides were larger. After the second storm, wave forcing was generally intermediate with occasional occurrence of smaller storms. The shoreline alternated receding and accreting periods before it recovered by February. From Figure 4d, we clearly see that maximum erosion has occurred in January 2014, with 15 m difference in shoreline compared with August 2013. There is a marked seasonal evolution driven by the seasonal occurrence of storm events from August to November and recovery during northeasterly winter swell conditions.

It indicates that shoreline changes in Nha Trang beach are very significant at both storm and seasonal scales. Typhoon impact on shoreline is incremental with each strong event eroding 4 to 8 m of the beach. The cumulated shoreline variation over the season is about 15 m while the recovery to individual events is quite fast (about 1.5 month). In both cases, erosion is linked to high-energy wave forcing and accretion is important in the days following the storm, where the wave conditions are moderate. We assume that accretion relies on the presence of this moderate energy. Our results are in this sense very consistent with other studies. We suggest that the thresholds between beach accretion and erosion are as follows: Wind waves ($Hs < 0.4$ m & $T < 5$s) leads to a very low onshore transport; moderate swell (0.4 m $< Hs < 0.8$ m & $T > 5$s) causes accretion and swell ($Hs > 1$ m & $T > 5$s) causes erosion. Therefore, the winter monsoon regime that succeeds to the typhoon season has an important impact on beach recovery.

CONCLUSIONS

We present the first attempt at using video cameras in Vietnam for monitoring the evolution of estuarine and coastal zones. Although progress in data processing can be made, our validation with field experiments give us some confidence on the accuracy of our techniques. The estimation of hydrodynamics variables appears satisfactory, while the mean accuracy of beach profiles is about 30 cm and locally higher. After this validation step, our study presents results on shoreline evolution. This study clearly demonstrates the resilience capacities of the beach to a two-typhoon sequence, with recovery duration of about 1.5 month. The recovery timescale is a crucial parameter for predicting either erosive or accretive beach response and varies significantly with location, ranging from days to months and years. Here, the recovery timescale is close to the recurrence interval of typhoons, which would make prediction of beach evolution sensitive to climate modulation of storm occurrence. The study is limited to a small number of events. A conceptual model could be formulated from larger time series.

ACKNOWLEDGMENTS

Part of this study was supported by a Vietnamese Protocol research project: "Study on hydrodynamic regime and sediment transport in estuarine and coastal zones of Nha Trang bay, Khanh Hoa province" from the Ministry of Science and Technology (MOST). It has also received French support from ANR (COASTVAR: ANR-14-ASTR-0019).

LITERATURE CITED

Aarninkhof, S.G.J.; Turner, I.L.; Dronkers, T.D.T.; Caljouw, M., and Nipius, L., 2003. A video-based technique for mapping intertidal beach bathymetry. *Coastal Engineering*, 49, 275-289.

Almar, R. ; Cienfuegos, R. ; Catalán, P.A. ; Michallet, H. ; Castelle, B. ; Bonneton, P., and Marieu, V., 2012. A new breaking wave height direct estimator from video imagery, *Coastal Engineering*, 61, 42-48.

Anderson,T.R.; Frazer, L.N., and Fletcher, C.H., 2010. Transient and persistent shoreline change from a storm. *Geophys. Res. Lett.*, 37, p. L08401

Angnuureng, D.; Almar, R.; Sénéchal, N.; Castelle, B.; Appeaning Addo, K., and Marieu, V., 2015. Shoreline evolution under sequences of storms from video observations at a meso-macrotidal barred beach, in revision for *Geomorphology*

Boak, E.H. and Turner, I.L., 2005. Shoreline Definition and Detection: A Review. *Journal of Coastal Research*. 214, 688-703. doi:10.2112/03-0071.1

Castelle, B. ; Marieu, V. ; Bujan, S. ; Splinter, K.D.; Robinet, A. ; Sénéchal, N., and Ferreira, S., 2015. Impact of the winter 2013-2014 series of severe Western Europe storms on a double-barred sandy coast: beach and dune erosion and megacusp embayments. *Geomorphology*, 238, 135–148

Catalán, P., and Haller, M., 2008. Remote sensing of breaking wave phase speeds with application to nonlinear depth inversion, *Coastal Engineering*, 55, 93-11

Coco G.; Senechal N.; Rejas A.; Bryan K.; Capo S.; Parisot J.P.; Brown J.A., and MacMahan J.H.M., 2014. Beach response to a sequence of extreme storms, *Geomorphology*, 204, 493-501

Davidson, M.A.; Splinter, K.D., and Turner, I.L., 2013. A simple equilibrium model for predicting shoreline change. *Coastal Engineering*, 73, pp.191–202

Ferreira, O., 2005. Storm groups versus extreme single storms: predicted erosion and management consequences. *J. Coast. Res.* SI 42, 221– 227

Frazer, L.N.; Anderson, T.R., and Fletcher, C.H., 2009. Modeling storms improves estimates of long-term shoreline change. *Geophysical Research Letters*, 36, L20404

Holland, K.T.; Holman, R.A.; Lippmann, T.C.; Stanley, J., and Plant, N., 1997. Practical use of video imagery in nearshore oceanographic field studies. *IEEE Journal of Oceanic Engineering*, 22, 81-92.

Holman, R. and Haller, M., 2013. Remote sensing of the nearshore. Annual Review of Marine Science, 113, 5–95

Jackson, N.L.; Nordstrom, K.F.; Eliot, I., and Masselink, G., 2002. "Low energ1y" sandy beaches in marine and estuarine environments : a review. *Geomorphology*, 48, 147-162.

Quartel, S.; Kroon, A., and Ruessink, B.G., 2008. Seasonal accretion and erosion patterns of a microtidal sandy beach. *Marine Geology*, 250, 19-33.

Karunarathna, H.; Pender, D.; Ranasimghe, R.; Short A.D., and Reeve, D.E., 2014. The effects of storm clustering on beach profile variability, *Marine Geology*, 348, pp. 103-112

Lefebvre, J.P.; Almar, R.; Viet, N.T.; Uu, D.V.; Thuan, D.H.; Binh, L.T.; Ibaceta, R., and Duc, N.V., 2014. Contribution of swash processes generated by low energy wind waves in the recovery of a beach impacted by extreme events: Nha Trang, Vietnam. In: Green, A.N. and Cooper, J.A.G. (eds.), Proceedings 13th International Coastal Symposium (Durban, South Africa), *Journal of Coastal Research*, Special Issue No. 70, 663-668.

Masselink, G.; Austin, M.; Scott, T.; Poate, T., and Russell, P., 2014. Role of wave forcing, storms and NAO in outer bar dynamics on a high-energy, macro-tidal beach. *Marine Geology* 226, 76-93

Nicholls, R.J.; Hoozemans, F.M.J., and Marchand, M., 1999. Increasing flood risk and wetland losses due to global sea-level rise: regional and global analyses, *Global Environmental Change*, 9, 69-87.

Splinter, K.D.; Carley, J.T.; Golshani, A., and Tomlinson, R., 2014. A relationship to describe the cumulative impact of storm clusters on beach erosion. *Coast. Eng.* 83, 49–55

Stockdon, H.F. and Holman, R.A., 2000. Estimation of wave phase speed and nearshore bathymetry from video imagery. *Journal of Geophysical Research* 105 (C9):22,015–22,033

Viet, N.T.; Nguyen V.D.; Vo C.H.; Tanaka H.; Dinh V.U.; Tran T.T.; Almar R., and Lefebvre J.P., 2014. Investigation of Erosion Mechanics of Nha Trang Coast, Vietnam, *Proceedings of the 19th IAHR-APD, Hanoi, Vietnam*.

Viet,N.T.; Nguyen V.D.; Le T.B.; Duong H.T.; Tran T.T.; Nguyen V.T.; Dinh V.U.; Almar R.; Lefebvre J.P., and Tanaka, H., 2014. Seasonal Evolution of Shoreline Changes in Nha Trang Beach, Vietnam, *Proceedings of the 19th IAHR-APD, Hanoi, Vietna*

Appendix B

Appendix II Article in Water

water

MDPI

Article

Shoreline Response to a Sequence of Typhoon and Monsoon Events

Rafael Almar [1,*], Patrick Marchesiello [1], Luis Pedro Almeida [1], Duong Hai Thuan [1,2], Hitoshi Tanaka [3] and Nguyen Trung Viet [2]

1 LEGOS (Université de Toulouse/CNRS/CNES/IRD), 31400 Toulouse, France; Patrick.Marchesiello@legos.obs-mip.fr (P.M.); luis.pedro.almeida@legos.obs-mip.fr (L.P.A.); duonghaithuan@tlu.edu.vn (D.H.T.)
2 Faculty of Marine and Coastal Engineering, Thuyloi University, Hanoi, Vietnam; nguyentrungviet@tlu.edu.vn
3 Department of Civil and Environmental Engineering, Tohoku University, Sendai 980-8576, Japan; hitoshi.tanaka.b7@tohoku.ac.jp
* Correspondence: rafael.almar@ird.fr; Tel.: +33-05-6133-3006

Academic Editor: Maurizio Barbieri
Received: 11 April 2017; Accepted: 18 May 2017; Published: 23 May 2017

Abstract: Shoreline continuously adapts to changing multi-scale wave forcing. This study investigates the shoreline evolution of tropical beaches exposed to monsoon events and storms with a case study in Vietnam, facing the South China Sea, over the particularly active 2013–2014 season, including the Cat-5 Haiyan typhoon. Our continuous video observations show for the first time that long-lasting monsoon events have more persistent impact (longer beach recovery phase) than typhoons. Using a shoreline equilibrium model, we estimate that the seasonal shoreline behavior is driven by the envelope of intra-seasonal events rather than monthly-averaged waves. Finally, the study suggests that the interplay between intra-seasonal event intensity and duration on the one hand and recovery conditions on the other might be of key significance. Their evolution in a variable or changing climate should be considered.

Keywords: Vietnam; South China Sea; erosion; recovery; storminess; winter monsoon; typhoons

1. Introduction

It would be a mistake to consider the vulnerability of coastal regions as a simple response to sea level change, assuming static coastal morphology [1,2]. On the contrary, coastal morphology is in a constant process of equilibration at various timescales. It is generally assumed that waves are the main driver of coastal evolution but their role is strongly non-linear, and the coastal response to unsteady forcing is unclear [3].

Beach recovery to extreme events is also still debated as there is not even agreement on their transient or persistent impacts [4,5]. For isolated events, departure from equilibrium is related to the event's intensity and duration [2,6,7]. However, no clear conclusion can be drawn when considering a sequence of events, since both enhanced [8] and weakened effects are observed [9–11], e.g., during the particularly stormy winter of 2013–2014 in Europe, e.g., [12]. The timescales' interplay between recurring events and recovery conditions appears determinant.

Existing shoreline equilibrium models (among others: [2,13,14]) show appreciable skills in predicting shoreline location from wave energy at monthly or longer time-scales for mid-latitude, storm-dominated coasts. However, these skills may be at fault in a so-called low-energy environment as often encountered in the tropics. There, the beach is mostly active during occasional events and is generally found in equilibrium with the preceding energetic event rather than current conditions [15].

Existing equilibrium models might not be able to describe such behavior, in particular when energetic wave events do not occur concomitantly with the seasonal peak of wave energy.

Tropical beaches are exposed to infrequent short (1–3 days) but paroxysmal storms such as cyclones (typhoons in the western Pacific) and can rapidly adapt to these very energetic conditions [16]. They slowly recover under persisting low to moderate waves during the rest of the year. However, all the tropical environments are not strictly low-energy, and this is particularly true in Southeast Asia as it is affected by monsoons [17]. Typical winter monsoon events last from three days to three weeks and can bring strong persistent swells of somewhat lower energy but longer duration than tropical storms. There is substantial literature on the atmospheric cold intrusion affecting the Southeast Asian coastal states every winter, e.g., [18] but the role of these energetic events on shoreline evolution has not been investigated. Clearly, they are active processes for shoreline erosion and must be compared with the effect of short-term storms. Their particularly long duration may be a crucial element of their beach response as the beach may have sufficient time to adjust to the energetic conditions and reach equilibrium.

In this paper, we investigate the video-derived shoreline evolution of Nha Trang beach, Vietnam, over the particularly active 2013–2014 season, with numerous winter monsoon events and storms, including the Cat-5 Haiyan typhoon. We first investigate the role of monsoon events on shoreline evolution compared with storms, and secondly the seasonal behavior of the beach in response to both monthly-averaged wave forcing and wave events using a shoreline equilibrium model [2].

2. Study Site

Nha Trang is an embayed beach located in southeastern Vietnam coast, facing the South China Sea (Figure 1, upper panel). This 6 km bay is oriented north–south and is partially sheltered from waves by a group of islands at its southern end. This medium-sized (D_{50} = 0.4 mm) sandy beach is rather uniform along the shore, and is characterized by a steep (slope ~ 0.1) upper face and a flat low-tide terrace (~40 m wide). The tide is a mix of diurnal and semi-diurnal, with a small tidal range (<1.6 m).

2.1. Typhoons

The Northwest Pacific is the most cyclogenetic region on earth. Of the 16 tropical storms that turn into typhoons (JTWC 2013) annually, about one-third propagate westward to South China Sea [19]. Every year, 4–6 typhoons hit Vietnam [20], typically between August and December, but the risk of landfall varies strongly at seasonal and interannual scales, e.g., [19,21]. The year 2013 came after two years of La Niña conditions, resulting in strong sea surface temperatures, which favored cyclone generation [22]. As a consequence, 2013 was observed to be the most active typhoon season since 2004, and the one with most casualties since 1975. Among the 10 typhoons landing in Vietnam in 2013, Cat. 5 Haiyan in early November turned into one of the world strongest recorded tropical cyclones [23].

2.2. Monsoons

Summer monsoons (May to September) drive relatively weak, short-period southwesterly waves in the South China Sea. The inception of winter monsoon (October to April), caused by high-pressure systems in Siberia, drives strong northeast winds. Because these pressure systems form every three days to three weeks, wind pulses occur at these timescales. As a result, the winter monsoon generates energetic waves larger than 2.5 m off the Vietnamese coast [24], reaching values up to 4 m, which stands for the 10% exceedance level of wave climate [25].

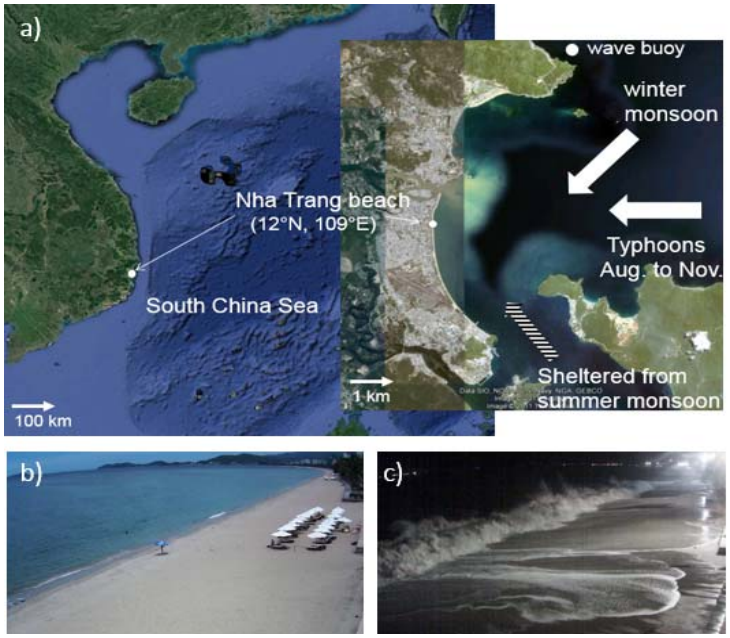

Figure 1. Study site, (**a**) Nha Trang each, Vietnam, facing the South China Sea. Images from the video system during (**b**) calm summer season and (**c**) Cat. 5 Haiyan typhoon.

From its orientation, Nha Trang region is mainly sheltered from summer monsoon which consists in very calm conditions. It can be considered that this stretch of coast is under the influence of winter monsoons and typhoons only [26,27].

3. Methods and Data

A video station was installed in May 2013 [26] in the central part of Nha Trang Bay, is considered far enough from the influence of the edges of the bay and is predominantly influenced by cross-shore rather than by longshore dynamics [27,28]. Hydrodynamic (waves, currents, tides) and morphology (intertidal and submerged bathymetry and shoreline) can be extracted from secondary images, timestack, and average images [27,29]. In this study, the shoreline was extracted manually at a single cross-shore section of the beach. It is estimated as the video-based average between maximum and minimum runup excursions over 15-min images and during daylight and night hours. Hourly tidal modulation of the shoreline location was averaged out using daily means. Wave fields were extracted from ERA-interim global reanalysis provided by the European Centre for Medium-Range Weather Forecasts (resolution of 0.5°, every 6 h [30]) at the closest node off Nha Trang, and validated over a two month period using a local wave gauge. This validation was successful (coefficient of determination R^2 = 0.87, RMSE = 0.26 m) down to event scale, which made it possible to extend our study over a full annual period, from 1 August 2013 to 1 August 2014. The period starts from summer monsoon conditions until October, and then winter monsoon lasts until April when a new summer monsoon begins.

Observations of waves and shoreline changes were used to calibrate the parametrical model of equilibrium shoreline position ShoreFor [2,31] accounting for cross-shore transport processes. This model was chosen as it was applied successfully at various sites for predicting the daily to seasonal shoreline response to waves compared to other models more dedicated to long-term interannual evolution [32]. This one-dimensional shoreline prediction model has the form

$$\frac{dx}{dt} = b + c\left(F^+ + rF^-\right) \quad (1)$$

where b and c are calibrated coefficients, r the ratio between erosive and accretive shoreline change, and $F^{\pm}$ is the shoreline forcing, which depends on disequilibrium with anteceding wave conditions

$$F^{\pm} = P^{0.5}(\Omega_{eq} - \Omega) \tag{2}$$

where P is wave power ($\propto Hs^2Tp$), with Hs and Tp as the deep water significant wave height and peak period, Ω and Ω_{eq} are the instant and time-varying dimensionless fall velocity such as

$$\Omega_{eq} = \left[\sum_{i=1}^{2\phi} \Omega_{eq} 10^{-i/\phi}\right] \tag{3}$$

with Ω defined as $\Omega = H_s/wT_p$, where w is the settling velocity and is a function of the site-specific median grain size (D_{50}). In Equation (3), i is the day prior to present, ϕ the number of past days where the decaying exponential function reaches 10% (more details in [2,14]).

4. Results

The offshore wave forcing for the one year study period is presented in Figure 2a. The southeast coast of Vietnam is partly sheltered from summer monsoon low-energy wind-waves ($Hs < 1$ m, $Tp < 4$s). The winter season presents more energetic swell ($Hs \sim 1.7$ m, $Tp = 7$–8 s) and larger variability, with largest values ($Hs \sim 3$ m, $Tp = 10$ s) during monsoon events. Waves during typhoon events have similar magnitude but shorter duration (<3 days). The shoreline (Figure 2a) is stable or even slightly in accretion till the end of summer monsoon in October, and then begins an erosive phase during winter monsoon until February when it reaches its most landward location, before migrating seaward again.

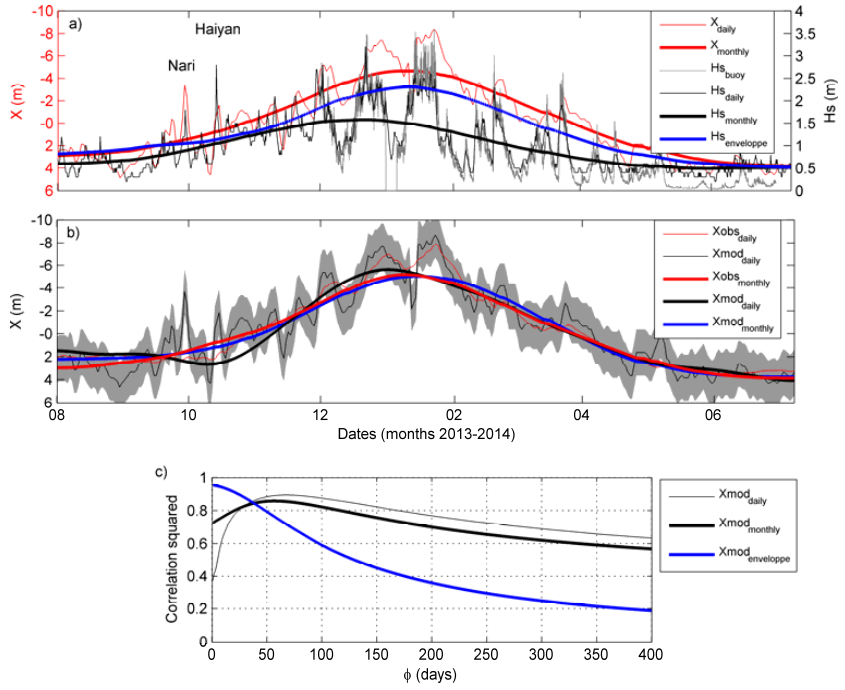

Figure 2. (**a**) Video-derived shoreline location X (red), wave height Hs from Era-Interim (black) and from buoy (gray) off Nha Trang, with the monthly envelope of intra-seasonal Hs (from 3 to 30 days) in blue. (**b**) Results from the shoreline equilibrium model ShoreFor (black, with uncertainty as shaded area), compared with the observed daily shoreline position (red) and in (**c**) the respective correlations squared for different ϕ values. In panels a,b, negative and positive X values stand for erosion and accretion from the mean, respectively. In a–c, thin and thick lines are daily and monthly data respectively.

This seasonal pattern (duration > 30 days) hides important intra-seasonal (or synoptic scale, i.e., winter monsoon events) variability with shoreline variations reaching 10 m during typhoon events and during long-lasting winter-monsoon events with durations from three days to three weeks. Even though the magnitude of shoreline retreat of these events is similar, Figure 2a shows that monsoon events have a more persistent impact with longer recovery (i.e., 10 to 20 days) than typhoons which takes a few days at most (sometimes within less than a day). While typhoon events were frequent at the beginning of the winter season, from October to December 2013, the magnitude of monsoon events increased and peaked in January to February of 2014. This coincided with already decreasing monthly-mean wave height but, surprisingly, the monthly-mean shoreline still eroded.

To investigate this two-month lag between monthly-mean waves and shoreline, the empirical shoreline equilibrium model ShoreFor (Equation (1)) was applied on daily wave and shoreline data. In Figure 2b the model shows good skills (R^2 = 0.8, RMS = 1.2 m) at intra-seasonal (larger than three days) and seasonal scales but miss short-lived storm impacts. The best correlation appears for a lag ϕ of 50 days (Figure 2c), which is much larger than the actual morphological response time of a few days observed at this beach. To investigate this point further, the model was forced with monthly-averaged waves and with the monthly envelop of intra-seasonal events (Figure 2b). The latter is done by means of the Hilbert transform, already applied successfully to study wave groupiness [33,34], $\left| Hs^{hf}(t) + \mathrm{H}\left\{ Hs^{hf}(t) \right\} \right|^{lf}$ where H denotes the Hilbert transform operator and $|\,|^{\mathrm{lf}}$ a low-pass filter operator, taking 30 days as the cutoff period separating short term (*hf*) and monthly (*lf*) timescales. Both monthly estimates well predict the seasonal shoreline behavior (Figure 2b), although that using the envelope gives more accuracy (R^2 = 0.8 and R^2 = 0.9, RMS = 0.5 and RMS = 0.3 m for monthly-averaged and envelope cases, respectively). Interestingly, the main difference rises from ϕ value in Figure 2c, which is similar (52 days) for monthly-averaged and daily data, but 0 for the envelope, indicating that the shoreline is in phase with the monthly envelope of energetic intra-seasonal events. Therefore, the shoreline is in better equilibrium with wave intra-seasonal events than monthly mean wave energy.

5. Discussion

One of the most striking points of this study is the wave energy provided by monsoon events and their dominant role on shoreline evolution. In contrast, while typhoons have large ephemeral impacts, our results show that the shoreline recovers rapidly. There is no evidence for a persistent influence, as suggested for short-lived storms by [35] and [36]. This is confirmed here using the ShoreFor model that presents good skills at predicting intra-seasonal and seasonal scales but poorly describes short-term typhoon-induced dynamics (see Figure 2b, October to November). Recurrence of typhoons is more than 10 days so that they can be considered isolated and without cumulative effect [5]. Winter monsoon events have impacts of similar magnitude to typhoons but with longer recovery, which is close to their observed recurrence period. Therefore, they can be considered as a sequence, as the beach cannot fully recover between events and is constantly moving towards a high energetic equilibrium. Note that the ratio of erosion and accretion rates for typhoons is nearly constant over time, but not so for winter monsoons: while the erosion rate is constant, the accretion rate decreases after each new event. This result highlights the importance of the wave event duration, to the extent that the erosive potential will be satisfied only if the event lasts the necessary time for the beach to establish a new equilibrium [6]. Thus for short-lived typhoons, the full erosion potential is not achieved. Despite the significant shoreline retreat, the beach profile is likely to be far from a new equilibrium. As a consequence, the shoreline recovery to its previous state (and shoreline position) occurs within a few days and does not affect longer term evolution [37]. On the other hand, winter monsoon events have enough duration to achieve their full erosion potential, thus modifying the beach to a fully new equilibrium. The return of the shoreline to its previous position takes longer, leaving the beach more vulnerable and for longer.

It was previously observed that Nha Trang's embayed beach has a seasonal rotation with modulation of waves incidence [27], from northward summer to winter southward transport: the north end of the beach enlarges in summer and erodes in winter, the center of rotation being localized in the central part of the beach [38]. It is noteworthy that, even if summer monsoon has only a weak influence compared to the energetic winter monsoon, locally generated wind-waves induce this northward transport [26]. The shoreline at the central part of the beach close to the video system mainly experiences translation due to cross-shore dynamics and is rather dominated by event scale. This is similar to what has been observed elsewhere [39] where rotation and translation of the shoreline were quantified separately.

A main outcome of this study is the long lag (50–60 days) observed between monthly waves and shoreline location, while the envelope (Hilbert transform) of intra-seasonal monsoon events is in closer phase with the shoreline. This suggests that, contrarily to shoreline equilibrium model paradigms [2,13], the Nha Trang shoreline is actually in equilibrium with energetic wave conditions. This is in line with observations by [15] at low-energy environments where the beach is assumed to be in equilibrium with previous energetic wave events rather than with current conditions. The beach is considered inactive the rest of the time. Here, it is the particularly long duration of winter monsoon events that presumably drives most of the shoreline changes, with very gentle wave conditions in between which limit the recovery potential, as observed elsewhere by [10]. In this sense, the phase-lag observed here between seasonal means and the intra-seasonal envelope is crucial for shoreline equilibrium.

6. Conclusions

In this paper, we addressed the shoreline evolution of the tropical Nha Trang beach, Vietnam, over the particularly active 2013–2014 season. Our results show for the first time that long-lasting (3–10 days) monsoon events have more persistent impact than typhoons (less than 3 days), of similar amplitude but rather transient with fast recovery. The ShoreFor shoreline equilibrium model shows good skills in predicting seasonal shoreline behavior. The seasonal shoreline appears driven by the intra-seasonal event envelope (from Hilbert transform) rather than monthly-averaged waves. Finally, this paper suggests that the interplay between intra-seasonal event intensity and duration, on the one hand, and recovery conditions, on the other, might be of key significance. Therefore, their evolution in a variable or changing climate should be considered.

Acknowledgments: This work was supported by Vietnamese grant (MOST2/216/QD/BKHCN-No2994) and French ANR project COASTVAR (ANR-14-ASTR-0019). We acknowledge use of the ECMWF ERAInterim dataset (www.ECMWF.Int/research/Era). DHT PhD supported by ARTS-IRD program.

Author Contributions: Rafael Almar, Patrick Marchesiello, Nguyen Trung Viet and Luis Pedro Almeida designed the project and conducted analyses. Duong Hai Thuan analyzed the video images and Hitoshi Tanaka provided expertise on shoreline dynamics. All authors wrote the paper.

Conflicts of Interest: The authors declare no conflict of interest.

References

1. Ashton, A.D.; Evans, R.L.; Donnelly, J.P. Discussion of the Potential Impacts of Climate Change on the Shorelines of the Northeastern USA. *Mitig. Adapt. Strateg. Glob. Chang.* **2008**, *13*, 719–743. [CrossRef]
2. Davidson, M.A.; Splinter, K.D.; Turner, I.L. A simple equilibrium model for predicting shoreline change. *Coast. Eng.* **2013**, *73*, 191–202. [CrossRef]
3. Cooper, J.A.G.; Pilkey, O.H. Sea-level rise and shoreline retreat: Time to abandon the Bruun Rule. *Glob. Planet. Chang.* **2004**, *43*, 157–171. [CrossRef]
4. Anderson, T.R.; Frazer, L.N.; Fletcher, C.H. Transient and persistent shoreline change from a storm. *Geophys. Res. Lett.* **2010**, *37*. [CrossRef]
5. Ranasinghe, R.; Holman, R.; de Schipper, M.A.; Lippmann, T.; Wehof, J.; Minh Duong, T.; Roelvink, D.; Stive, M.J.F. Quantification of nearshore morphological recovery time scales using Argus video imaging: Palm Beach, Sydney and Duck, NC. *Coast. Eng. Proc.* **2012**, *1*, 24.

6. Kriebel, D.L.; Dean, R.G. Convolution method for time dependent beach profile response. *J. Waterw. Port. Coast. Ocean Eng.* **1993**, *119*, 204–226. [CrossRef]
7. Frazer, L.N.; Anderson, T.R.; Fletcher, C.H. Modeling storms improves estimates of long-term shoreline change. *Geophys. Res. Lett.* **2009**, *36*. [CrossRef]
8. Ferreira, Ó. Storm groups versus extreme single storms: Predicted erosion and management consequences. *J. Coast. Res.* **2005**, *21*, 221–227.
9. Coco, G.; Senechal, N.; Rejas, A.; Bryan, K.R.; Capo, S.; Parisot, J.P.; Brown, J.A.; MacMahan, J.H.M. Beach response to a sequence of extreme storms. *Geomorphology* **2014**, *204*, 493–501. [CrossRef]
10. Karunarathna, H.; Pender, D.; Ranasinghe, R.; Short, A.D.; Reeve, D.E. The effects of storm clustering on beach profile variability. *Mar. Geo.* **2014**, *348*, 103–112. [CrossRef]
11. Splinter, K.D.; Carley, J.T.; Golshani, A.; Tomlinson, R. A relationship to describe the cumulative impact of storm clusters on beach erosion. *Coast. Eng.* **2014**, *83*, 49–55. [CrossRef]
12. Masselink, G.; Scott, T.; Poate, T.; Russell, P.; Davidson, M.; Conley, D. The extreme 2013/14 winter storms: Hydrodynamic forcing and coastal response along the southwest coast of England. *Earth Surf. Proc. Landf.* **2016**, *41*, 378–391. [CrossRef]
13. Yates, M.L.; Guza, R.T.; O'Reilly, W.C. Equilibrium shoreline response: Observations and modeling. *Geophys. Res.* **2009**, *114*. [CrossRef]
14. Splinter, K.D.; Turner, I.L.; Davidson, M.A.; Barnard, P.; Castelle, B.; Oltman-Shay, J. A generalized equilibrium model for predicting daily to interannual shoreline response. *J. Geophys. Res. Earth Surf.* **2014**, *119*, 1936–1958. [CrossRef]
15. Jackson, N.L.; Nordstrom, K.F.; Eliot, I.; Masselink, G. "Low energy" sandy beaches in marine and estuarine environments: A review. *Geomorphology* **2002**, *48*, 147–162. [CrossRef]
16. Chen, S.S.; Curcic, M. Ocean surface waves in Hurricane Ike (2008) and Superstorm Sandy (2012): Coupled modeling and observations. *Ocean Mod.* **2016**, *103*, 161–176. [CrossRef]
17. Chang, C.-P.; Wang, Z.; Hendon, H. *The Asian Monsoon*; Springer: Heidelberg, Germany, 2006; pp. 89–128.
18. Wu, M.C.; Chan, J.C.L. Surface features of winter monsoon surges over South China. *Mon. Wea. Rev.* **1995**, *123*, 662–680. [CrossRef]
19. Camargo, S.J.; Robertson, A.W.; Gaffney, S.J.; Smyth, P.; Ghil, M. Cluster analysis of typhoon tracks, Part I: General properties. *J. Clim.* **2007**, *20*, 3635–3653. [CrossRef]
20. Nicholls, R.J.; Hoozemans, F.M.; Marchand, M. Increasing flood risk and wetland losses due to global sea-level rise: Regional and global analyses. In *Global Environmental Change*; Elsevier: Amsterdam, The Netherlands, 1999; Volume 9, pp. 69–87.
21. Chan, J.C.L. Tropical cyclone activity in the northwest Pacific in relation to El Niño/Southern Oscillation phenomenon. *Mon. Weather Rev.* **1985**, *113*, 599–606. [CrossRef]
22. Nakamura, T.; Yamazaki, K.; Iwamoto, K.; Honda, M.; Miyoshi, Y.; Ogawa, Y.; Tomikawa, Y.; Ukita, J. The stratospheric pathway for Arctic impacts on midlatitude climate. *Geophys. Res. Lett.* **2016**, *43*, 3494–3501. [CrossRef]
23. Nakamura, R.; Shibayama, T.; Esteban, M.; Iwamoto, T. Future typhoon and storm surges under different global warming scenarios: Case study of typhoon Haiyan (2013). *Nat. Hazards* **2016**, *82*, 1645–1681. [CrossRef]
24. Chu, P.C.; Qi, Y.; Chen, Y.; Shi, P.; Mao, Q. South China Sea wind- wave characteristics. Part I: validation of Wavewatch-III using TOPEX/Poseidon data. *J. Atmos. Ocean Technol.* **2004**, *21*, 1718–1733. [CrossRef]
25. Mirzaei, A.; Tangang, F.; Juneng, L.; Mustapha, M. A.; Husain, M. L.; Akhir, M. F. Wave climate simulation for southern region of the South China Sea. *Ocean Dyn.* **2013**, *63*, 961–977. [CrossRef]
26. Lefebvre, J.-P.; Almar, R.; Viet, N.T.; Uu, D.V.; Thuan, D.H.; Binh, L.T.; Ibaceta, R.; Duc, N.V. Contribution of swash processes generated by low energy wind waves in the recovery of a beach impacted by extreme events: Nha Trang, Vietnam. *J. Coast. Res.* **2014**, *70*, 663–668. [CrossRef]
27. Duong, H.T.; Binh, L.T.; Viet, N.T.; Hanh, K.D.; Almar, R.; Marchesiello, P. Typhoon impact and shoreline recovery from continuous video monitoring: a case study from Nha Trang beach, Vietnam. Proceedings of the 14th International Coastal Symposium (Sydney, Australia). *J. Coast. Res.* **2016**, *75*, 263–267.
28. Almeida, L.P.; Almar, R.; Marchesiello, P.; Blenkinsopp, C.; Martins, K.; Sénéchal, N.; Floc'H, F.; Bergsma, E.; Benshila, R.; Caulet, C.; et al. Swash zone dynamics of a reflective beach with a low tide terrace. *Mar. Geol.* **2017**, submitted for publication.

29. Abessolo, O.G.; Almar, R.; Kestenare, E.; Bahini, A.; Houngue, G.H.; Jouanno, J.; Du, P.Y.; Castelle, B.; Melet, A.; Messignac, B.; et al. Potential of video cameras in assessing event and seasonal coastline behaviour: Grand Popo, Benin (Gulf of Guinea). *J. Coast. Res.* **2016**, *75*, 442–446. [CrossRef]
30. Dee, D.P.; Uppala, S.M.; Simmons, A.J.; Berrisford, P.; Poli, P.; Kobayashi, S.; Andrae, U.; Balsamo, G.; Bauer, P.; Bechtold, P. The ERA-Interim reanalysis: Configuration and performance of the data assimilation system. *Q. J. R. Meteorol. Soc.* **2011**, *137*, 553–597. [CrossRef]
31. Davidson, M.A.; Turner, I.L. A behavioral template beach profile model for predicting seasonal to interannual shoreline. *J. Geophys. Res.* **2009**, *114*, F01020. [CrossRef]
32. Ruggiero, P.; Buijsman, M.; Kaminsky, G.M.; Gelfenbaum, G. Modeling the effects of wave climate and sediment supply variability on large-scale shoreline change. *Mar. Geol.* **2010**, *273*, 127–140.
33. Veltcheva, A.D. Wave and group transformation by a Hilbert spectrum. *Coast. Eng. J.* **2002**, *44*, 283–300. [CrossRef]
34. Ortega, J.; Smith, G.H. Hilbert-Huang transform analysis of storm waves. *Appl. Ocean Res.* **2009**, *31*, 212–219. [CrossRef]
35. Douglas, B.C.; Crowell, M. Long-Term Shoreline Position Pre diction and Error Propagation. *J. Coast. Res.* **2000**, *16*, 145–152.
36. Zhang, K.; Douglas, B.C.; Leatherman, S.P. Do Storms Cause Long-Term Beach Erosion along the U.S. East Barrier Coast? *J. Geol.* **2002**, *110*, 493–502. [CrossRef]
37. Hansen, J.E.; Barnard, P.L. Sub-weekly to interannual variability of a high-energy shoreline. *Coast. Eng.* **2010**, *57*, 959–972. [CrossRef]
38. Thanh, T.M.; Tanaka, H.; Viet, N.T.; Mitobe, Y.; Hoang, V.C. Evaluation of longshore sendiment transport on Nha Trang coast considering influence of Northeast monsoon waves. *J. Jpn. Soc. Civ. Eng.* **2015**, *71*, 1681–1686.
39. Turki, I.; Medina, R.; Gonzalez, M.; Coco, G. Natural variability of shoreline position: Observations at three pocket beaches. *Mar. Geol.* **2013**, *338*, 76–89. [CrossRef]

Bibliography

Duong H Thuan, Le T Binh, Nguyen T Viet, Dong K Hanh, Rafael Almar, and Patrick Marchesiello. Typhoon impact and recovery from continuous video monitoring: a case study from nha trang beach, vietnam. *Journal of Coastal Research*, 75(sp1):263–267, 2016.

Rafael Almar, Patrick Marchesiello, Luis Pedro Almeida, Duong Hai Thuan, Hitoshi Tanaka, and Nguyen Trung Viet. Shoreline response to a sequence of typhoon and monsoon events. *Water*, 9(6):364, 2017.

Gerhard Masselink and Michael G Hughes. *An introduction to coastal processes and geomorphology*. Routledge, 2014.

Robert G Dean and Robert A Dalrymple. *Coastal processes with engineering applications*. Cambridge University Press, 2004.

Paul D Komar. *Beach processes and sedimentation (2nd edition)*. Prentice Hall, 1999.

Dominic Reeve, Andrew Chadwick, and Christopher Fleming. *Coastal engineering: processes, theory and design practice*. CRC Press, 2012.

Andrew D Short. Australian beach systems—nature and distribution. *Journal of Coastal Research*, pages 11–27, 2006.

Ali Mirzaei, Fredolin Tangang, Liew Juneng, Muzneena Ahmad Mustapha, Mohd Lokman Husain, and Mohd Fadzil Akhir. Wave climate simulation for southern region of the south china sea. *Ocean Dynamics*, 63(8):961–977, 2013.

Adam J Bechle, Chin H Wu, Wen-Cheng Liu, and Nobuaki Kimura. Development and application of an automated river-estuary discharge imaging system. *Journal of Hydraulic Engineering*, 138(4):327–339, 2011.

Rafael Almar, Rodrigo Cienfuegos, Patricio A Catalán, Hervé Michallet, Bruno Castelle, Philippe Bonneton, and Vincent Marieu. A new breaking wave height direct estimator from video imagery. *Coastal Engineering*, 61:42–48, 2012a.

Jeseon Yoo. *Nonlinear bathymetry inversion based on wave property estimation from nearshore video imagery*. PhD thesis, Georgia Institute of Technology, December 2007.

Rafael Almar, Jean-Pierre Lefebvre, Natalie Bonneton, Philippe Bonneton, Dinh Van Uu, Nguyen Trung Viet, Le Thanh Binh, and Nguyen Viet Duc. Swash hydro-morphodynamics

at a low-tide terrace beach during post-typhoon recovery period, nha trang bay, vietnam. In *Proc. of the 19th Congress of the Aisa and Pacific Division of the International Association of Hydraulic Engineering and Research*. IAHR-APD, 2014.

Olivier Morio, Thierry Garlan, and Patrick Guyomard. Etude dánalyse granulométrique de prélévements sédimentaires effectués lors de la campagne coastvar vietnam 2015. Sedimentation Report, 2016.

Jonathan L Carrivick, Mark W Smith, and Duncan J Quincey. *Structure from Motion in the Geosciences*. John Wiley & Sons, 2016.

Giovanni Coco, Nadia Senechal, A Rejas, Karin R Bryan, S Capo, JP Parisot, Jenna A Brown, and Jamie HM MacMahan. Beach response to a sequence of extreme storms. *Geomorphology*, 204:493–501, 2014.

Donatus Bapentire Angnuureng, Rafael Almar, Nadia Senechal, Bruno Castelle, Kwasi Appeaning Addo, Vincent Marieu, and Roshanka Ranasinghe. Shoreline resilience to individual storms and storm clusters on a meso-macrotidal barred beach. *Geomorphology*, 290:265–276, 2017.

Tiffany R Anderson, L Neil Frazer, and Charles H Fletcher. Transient and persistent shoreline change from a storm. *Geophysical Research Letters*, 37(8), 2010.

L Neil Frazer, Tiffany R Anderson, and Charles H Fletcher. Modeling storms improves estimates of long-term shoreline change. *Geophysical Research Letters*, 36(20), 2009.

MA Davidson, KD Splinter, and IL Turner. A simple equilibrium model for predicting shoreline change. *Coastal Engineering*, 73:191–202, 2013.

Óscar Ferreira. Storm groups versus extreme single storms: predicted erosion and management consequences. *Journal of Coastal Research*, pages 221–227, 2005.

Harshinie Karunarathna, Douglas Pender, Roshanka Ranasinghe, Andrew D Short, and Dominic E Reeve. The effects of storm clustering on beach profile variability. *Marine Geology*, 348:103–112, 2014.

Kristen D Splinter, Ian L Turner, Mark A Davidson, Patrick Barnard, Bruno Castelle, and Joan Oltman-Shay. A generalized equilibrium model for predicting daily to interannual shoreline response. *Journal of Geophysical Research: Earth Surface*, 119(9):1936–1958, 2014a.

Gerd Masselink, Tim Scott, Tim Poate, Paul Russell, Mark Davidson, and Daniel Conley. The extreme 2013/2014 winter storms: hydrodynamic forcing and coastal response along the southwest coast of england. *Earth Surface Processes and Landforms*, 41(3):378–391, 2016.

Bruno Castelle, Vincent Marieu, Stéphane Bujan, Kristen D Splinter, Arhur Robinet, Nadia Sénéchal, and Sophie Ferreira. Impact of the winter 2013–2014 series of severe western europe storms on a double-barred sandy coast: Beach and dune erosion and megacusp embayments. *Geomorphology*, 238:135–148, 2015.

Nancy L Jackson, Karl F Nordstrom, Ian Eliot, and Gerdhard Masselink. 'low energy'sandy beaches in marine and estuarine environments: a review. *Geomorphology*, 48(1-3):147–162, 2002.

JR Miles and PE Russell. Dynamics of a reflective beach with a low tide terrace. *Continental Shelf Research*, 24(11):1219–1247, 2004.

Robin Davidson-Arnott. *Introduction to coastal processes and geomorphology*. Cambridge University Press, 2010.

Gerhard Masselink, Paul Russell, Chris Blenkinsopp, and Ian Turner. Swash zone sediment transport, step dynamics and morphological response on a gravel beach. *Marine Geology*, 274 (1-4):50–68, 2010.

Leo H Holthuijsen. *Waves in oceanic and coastal waters*. Cambridge university press, 2010.

Michael R Gourlay and T Meulen. Beach and dune erosion tests (i). *M0935*, 1968.

LD Wright and Andrew D Short. Morphodynamic variability of surf zones and beaches: a synthesis. *Marine Geology*, 56(1-4):93–118, 1984.

TC Lippmann and RA Holman. The spatial and temporal variability of sand bar morphology. *Journal of Geophysical Research: Oceans*, 95(C7):11575–11590, 1990.

Gerhard Masselink and Andrew D Short. The effect of tide range on beach morphodynamics and morphology: a conceptual beach model. *Journal of Coastal Research*, pages 785–800, 1993.

Bruno Castelle, Rafael Almar, Matthieu Dorel, Jean-Pierre Lefebvre, Nadia Sénéchal, Edward J Anthony, Raoul Laibi, Rémy Chuchla, and Yves du Penhoat. Rip currents and circulation on a high-energy low-tide-terraced beach (grand popo, benin, west africa). *Journal of Coastal Research*, 70(sp1):633–638, 2014.

Rafael Almar, Alexandre Nicolae Lerma, Bruno Castelle, and Timothy Scott. On the influence of reflection over a rhythmic swash zone on surf zone dynamics. *Ocean Dynamics*, pages 1–11, 2018.

Julian D Orford, Donald L Forbes, and Simon C Jennings. Organisational controls, typologies and time scales of paraglacial gravel-dominated coastal systems. *Geomorphology*, 48(1-3): 51–85, 2002.

Donatus Bapentire Angnuureng, Rafael Almar, Nadia Senechal, Bruno Castelle, Kwasi Appeaning Addo, and Vincent Marieu. Shoreline evolution under sequences of storms from 6-year video observation at a mesomacrotidal beach. In *The Proceedings of the Coastal Sediments 2015*. World Scientific, 2015.

S Quartel, Aart Kroon, and BG Ruessink. Seasonal accretion and erosion patterns of a microtidal sandy beach. *Marine Geology*, 250(1-2):19–33, 2008.

K Todd Holland, Robert A Holman, Thomas C Lippmann, John Stanley, and Nathaniel Plant. Practical use of video imagery in nearshore oceanographic field studies. *IEEE Journal of oceanic engineering*, 22(1):81–92, 1997.

Rob Holman and Merrick C Haller. Remote sensing of the nearshore. *Annual Review of Marine Science*, 5:95–113, 2013.

Damodharan Padmalal and K Maya. *Sand mining: environmental impacts and selected case studies*. Springer, 2014.

G Mathias Kondolf. Profile: hungry water: effects of dams and gravel mining on river channels. *Environmental management*, 21(4):533–551, 1997.

James PM Syvitski, Albert J Kettner, Irina Overeem, Eric WH Hutton, Mark T Hannon, G Robert Brakenridge, John Day, Charles Vörösmarty, Yoshiki Saito, Liviu Giosan, et al. Sinking deltas due to human activities. *Nature Geoscience*, 2(10):681, 2009.

D INMAN and RW Harris. Oceanographic and engineering report on investigation of sedimentation, silting and dredging requirements. *Saigon: Daniel Mann Johnson & Mendenhall*, 1966.

Anna Dahlström and Susanna Böös. Coastal evolution at nha trang bay, vietnam. mathesis, Lund University, 2015.

Peter C Chu, Yiquan Qi, Yuchun Chen, Ping Shi, and Qingwen Mao. South china sea wind-wave characteristics. part i: validation of wavewatch-iii using topex/poseidon data. *Journal of atmospheric and oceanic technology*, 21(11):1718–1733, 2004.

Liew Juneng and Fredolin T Tangang. Evolution of enso-related rainfall anomalies in southeast asia region and its relationship with atmosphere–ocean variations in indo-pacific sector. *Climate Dynamics*, 25(4):337–350, 2005.

Johnny CL Chan. Tropical cyclone activity in the northwest pacific in relation to the el niño/southern oscillation phenomenon. *Monthly Weather Review*, 113(4):599–606, 1985.

Chang-Hoi Ho, Jong-Jin Baik, Joo-Hong Kim, Dao-Yi Gong, and Chung-Hsiung Sui. Interdecadal changes in summertime typhoon tracks. *Journal of Climate*, 17(9):1767–1776, 2004.

Suzana J Camargo, Andrew W Robertson, Scott J Gaffney, Padhraic Smyth, and Michael Ghil. Cluster analysis of typhoon tracks. part i general properties. *Journal of Climate*, 20(14): 3635–3653, 2007a.

Suzana J Camargo, Kerry A Emanuel, and Adam H Sobel. Use of a genesis potential index to diagnose enso effects on tropical cyclone genesis. *Journal of Climate*, 20(19):4819–4834, 2007b.

Nguyen Nguyet Minh, Marchesiello Patrick, Lyard Florent, Ouillon Sylvain, Cambon Gildas, Allain Damien, and Dinh Van Uu. Tidal characteristics of the gulf of tonkin. *Continental Shelf Research*, 91:37–56, 2014.

Ngo Ngoc Cat, Pham Huy Tien, DD Sam, and NN Binh. Status of coastal erosion of viet nam and proposed measures for protection. *This volume*, 2006.

Nguyen Trung Viet. Study of hydrodynamics and sediment transport in estauries and coastal zone of nha trang bay, khanh hoa province. *Hanoi: Water Resources University*, 2014.

Le Dinh Mau. Overview of natural geographical conditions of nha trang bay. Technical report, Nha Trang Institute of Oceanography, 2014.

Jean-Pierre Lefebvre, Rafael Almar, Nguyen T Viet, Duong H Thuan, Le T Binh, Raimundo Ibaceta, and Nguyen V Duc. Contribution of swash processes generated by low energy wind waves in the recovery of a beach impacted by extreme events: Nha trang, vietnam. *Journal of Coastal Research*, 70(sp1):663–668, 2014.

Rob A Holman and John Stanley. The history and technical capabilities of argus. *Coastal Engineering*, 54(6-7):477–491, 2007.

Stefan GJ Aarninkhof, Ian L Turner, Thomas DT Dronkers, Mark Caljouw, and Leann Nipius. A video-based technique for mapping intertidal beach bathymetry. *Coastal Engineering*, 49 (4):275–289, 2003.

Rafael Almar, Roshanka Ranasinghe, Nadia Sénéchal, Philippe Bonneton, Dano Roelvink, Karin R Bryan, Vincent Marieu, and Jean-Paul Parisot. Video-based detection of shorelines at complex meso–macro tidal beaches. *Journal of Coastal Research*, 28(5):1040–1048, 2012b.

Carline Bos. Wave characteristics derived from video. Master's thesis, 2006.

Rafael Almar, Philippe Bonneton, Nadia Senechal, and Dano Roelvink. Wave celerity from video imaging: a new method. *Coastal Engineering Proceedings*, pages 661–673, 2008.

Miguel Angel Nieto, Bartolomé Garau, Salvador Balle, Gonzalo Simarro, Gustavo A Zarruk, Alberto Ortiz, Joaquín Tintoré, Amaya Álvarez-Ellacuría, Lluís Gómez-Pujol, and Alejandro Orfila. An open source, low cost video-based coastal monitoring system. *Earth Surface Processes and Landforms*, 35(14):1712–1719, 2010.

English version Vivotek User's Manual IP7361. *Vivotek User's Manual IP7361 Network Camera, English version*. Vivotek Inc Company. URL http://download.vivotek.com/downloadfile/downloads/usersmanuals/ip7361manual_en.pdf.

Tom C Lippmann and Robert A Holman. Quantification of sand bar morphology: A video technique based on wave dissipation. *Journal of Geophysical Research: Oceans*, 94(C1):995–1011, 1989.

C Pianca, R Holman, and E Siegle. Shoreline variability from days to decades: Results of long-term video imaging. *Journal of Geophysical Research: Oceans*, 120(3):2159–2178, 2015.

G Abessolo Ondoa, Rafaël Almar, Elodie Kestenare, A Bahini, GH Houngue, Julien Jouanno, Y Du Penhoat, B Castelle, A Melet, B Meyssignac, et al. Potential of video cameras in

assessing event and seasonal coastline behaviour: Grand popo, benin (gulf of guinea). *Journal of coastal research*, 75(sp1):442–446, 2016.

Grégoire Abessolo Ondoa, Frédéric Bonou, Folly Serge Tomety, Yves du Penhoat, Clément Perret, Cossi Georges Epiphane Degbe, and Rafael Almar. Beach response to wave forcing from event to inter-annual time scales at grand popo, benin (gulf of guinea). *Water*, 9(6):447, 2017a.

Christien E Huisman, Karin R Bryan, Giovanni Coco, and BG Ruessink. The use of video imagery to analyse groundwater and shoreline dynamics on a dissipative beach. *Continental shelf research*, 31(16):1728–1738, 2011.

Troels Aagaard and Jörgen Holm. Digitization of wave run-up using video records. *Journal of Coastal Research*, pages 547–551, 1989.

Rob A. Holman, Asbury H. Sallenger Jr., Tom C. Lippmann, and John W. Haines. The application of video image processing to the study of nearshore processes. *Oceanography*, 6, 1993. URL https://doi.org/10.5670/oceanog.1993.02.

Hilary F Stockdon, Rob A Holman, Peter A Howd, and Asbury H Sallenger Jr. Empirical parameterization of setup, swash, and runup. *Coastal Engineering*, 53(7):573–588, 2006.

Hilary F Stockdon, David M Thompson, Nathaniel G Plant, and Joseph W Long. Evaluation of wave runup predictions from numerical and parametric models. *Coastal Engineering*, 92: 1–11, 2014.

Rafael Almar. *Morphodynamique littorale haute frequence par imagerie video.* PhD thesis, University of Bordeaux 1, 2009.

Muhammad Zikra. *Development of video image analysis methods for estimating bathymetry and the directional wave spectrum in shallow water areas.* PhD thesis, Kyushu University, 2012.

Umberto Andriolo. *Nearshore hydrodynamics and morphology derived from video imagery.* PhD thesis, UNIVERSIDADE DE LISBOA, 2018.

Richard Hartley and Andrew Zisserman. *Multiple view geometry in computer vision.* Cambridge university press, 2003.

Karl Kraus. *Photogrammetry: geometry from images and laser scans.* Walter de Gruyter, 2011.

Thomas Luhmann, Stuart Robson, Stephen Kyle, and Ian Harley. *Close range photogrammetry.* Wiley, 2007.

Y.I Abdel-Aziz and H.M. Karara. Direct linear transformation from comparator coordinates into object space coordinates in close-range photogrammetry. In *Proceedings of the ASP Symposium on Close-Range Photogrammetry, 1971*, pages 1–18. American Society of Photogrammetry, 1971.

Janne Heikkila and Olli Silven. A four-step camera calibration procedure with implicit image correction. In *Computer Vision and Pattern Recognition, 1997. Proceedings., 1997 IEEE Computer Society Conference on*, pages 1106–1112. IEEE, 1997.

Jean-Yves Bouguet. Camera calibration toolbox for matlab, 2015. URL http://www.vision.caltech.edu/bouguetj/calib_doc/.

Nguyen Viet Duc, Nguyen Trung Viet, Duong Hai Thuan, Le Thanh Binh, Dao Van Hung, Nguyen Thai Binh, Jean-Pierre Lefebvre, and Rafael Almar. Evaluation of long term variation of intertidal topography of nha trang beach based on high frequency video processing. In *Proc. of the 19th Congress of the Aisa and Pacific Division of the International Association of Hydraulic Engineering and Research*. IAHR-APD, 2014a.

Nguyen Trung Viet, Nguyen Viet Duc, Le Thanh Binh, Duong Hai Thuan, Tran Thanh Tung, Nguyen Van Thin, Dinh Van Uu, Jean-Pierre Lefebvre, Rafael Almar, and Hitoshi Tanaka. Seasonal evolution of shoreline changes in nha trang bay, vietnam. In *Proc. of the 19th Congress of the Aisa and Pacific Division of the International Association of Hydraulic Engineering and Research*. IAHR-APD, 2014.

Tran Minh Thanh, Hitoshi Tanaka, Yuta Mitobe, Nguyen Trung Viet, and Rafael Almar. Seasonal variation of morphology and sediment movement on nha trang coast, vietnam. *Journal of Coastal Research, Special Issue, Tropical coastal and estuarine dynamics*, 81:22–31, 2018.

Elizabeth H Boak and Ian L Turner. Shoreline definition and detection: a review. *Journal of coastal research*, pages 688–703, 2005.

Nathaniel G. Plant and Rob A. Holman. Intertidal beach profile estimation using video images. *Marine Geology*, 140(1):1 – 24, 1997. ISSN 0025-3227. doi: https://doi.org/10.1016/S0025-3227(97)00019-4. URL http://www.sciencedirect.com/science/article/pii/S0025322797000194.

Ian Turner, Vince Leyden, Graham Symonds, John McGRATH, Angus Jackson, Tony Jancar, SGJ Aarninkhof, and IE Elshoff. Comparison of observed and predicted coastline changes at the gold coast artificial (surfing) reef, sydney, australia. In *Proceedings of the International Conference on Coastal Engineering*, 2001.

Tyson Hilmer. *Measuring breaking wave height using video*. PhD thesis, University of Hawai'i at MANOA, 2005.

Baeck Oon Kim, Hong Yeon Cho, Dhong Il Lim, Gil Lim Yoon, Im Sang Oh, and Yong Ahn Park. Nearshore wave measurement using single-video images of buoy motions. *Journal of Coastal Research*, pages 1481–1486, 2008.

Yaniv Gal, Matthew Browne, and Christopher Lane. Long-term automated monitoring of nearshore wave height from digital video. *IEEE Transactions on Geoscience and Remote Sensing*, 52(6):3412–3420, 2014.

B. Robertson, I. Nistor, K. Hall, and B. Buckham. Remote measurement and prediction of breaking wave parameters. *Coastal Engineering Proceedings*, 1(34):41, 2014. ISSN 2156-1028. doi: 10.9753/icce.v34.waves.41. URL https://journals.tdl.org/icce/index.php/icce/article/view/7290.

Donatus Bapentire Angnuureng. *Shoreline response to multi-scale oceanic forcing from video imagery*. PhD thesis, Université de Bordeaux, 2016.

Grégoire Abessolo Ondoa, Rafael Almar, Bruno Castelle, Magnus Larson, Minette Tomedi Eyango, Frédéric Bonou, Yves Du Penhoat, Ibrahima Camara, Moussa Sall, Raphaël Onguéné, and Gael Alory. Development of a west and central africa regional video camera network to monitor coastal response to multiscale ocean forcing. In *Proceedings of Coastal Dynamics 2017*, pages 1540–1550. COASTAL DYNAMICS 2017, 2017b.

PA Catalán, MC Haller, RA Holman, and WJ Plant. Optical and microwave detection of surf zone breaking waves. *IEEE Trans. Geosci. Remote Sens*, 49(6):1879–1893, 2011.

Patricio A Catálan and Merrick C Haller. Remote sensing of breaking wave phase speeds with application to non-linear depth inversions. *Coastal Engineering*, 55(1):93–111, 2008.

Tom C Lippmann and Rob A Holman. Phase speed and angle of breaking waves measured with video techniques. In *Coastal Sediments*, pages 542–556. ASCE, 1991.

Hilary F Stockdon and Rob A Holman. Estimation of wave phase speed and nearshore bathymetry from video imagery. *Journal of Geophysical Research: Oceans*, 105(C9):22015–22033, 2000.

Nathaniel G Plant, K Todd Holland, and Merrick C Haller. Ocean wavenumber estimation from wave-resolving time series imagery. *IEEE Transactions on Geoscience and Remote Sensing*, 46(9):2644–2658, 2008.

Rob Holman and John Stanley. cbathy bathymetry estimation in the mixed wave-current domain of a tidal estuary. *Journal of Coastal Research, Special Issue 65*, pages 1391–1396, 2013. doi: 10.2112/SI65-235.1.

Erwin WJ Bergsma and Rafael Almar. Video-based depth inversion techniques, a method comparison with synthetic cases. *Coastal Engineering*, 138:199–209, 2018.

M Tissier, P Bonneton, R Almar, B Castelle, N Bonneton, and A Nahon. Field measurements and non-linear prediction of wave celerity in the surf zone. *European Journal of Mechanics-B/Fluids*, 30(6):635–641, 2011.

Nguyen Danh Thao, Hiroshi Takagi, and Miguel Esteban. *Coastal Disasters and Climate Change in Vietnam: Engineering and Planning Perspectives*. Elsevier, 2014.

Nguyen Viet Duc, Nguyen Trung Viet, Nguyen Chien, Duong Hai Thuan, Dinh Van Uu, and Hitoshi Tanaka. Study on hydrodynamics of nha trang bay by using fvcom model. In *Proc. of the 19th Congress of the Aisa and Pacific Division of the International Association of Hydraulic Engineering and Research*. IAHR-APD, 2014b.

Nguyen Viet Duc. *Investigation of mechanism of morphological changes in coastal zone and structural solutions for stabilization - application for Xuong Huan beach region in Nha Trang bay.* PhD thesis, THUYLOI University, 2016.

Tran Hai Yen. *Modeling long term shoreline evolution and coastal erosion.* PhD thesis, Université Grenoble Alpes, 2018.

Le Thanh Binh. *Study on shoreline evolution and structural measures for beach protection in Nha Trang city.* PhD thesis, THUYLOI University, 2017.

Luis Pedro Almeida, Rafael Almar, Chris Blenkinsopp, Kévin Martins, Nadia Sénéchal, France Floc'H, Erwin Bergsma, Patrick Marchesiello, Rachid Benshila, Charles Caulet, Melanie Biausque, Duong Hai Thuan, Le Thanh Binh, and Nguyen Trung Viet. Tide control on the swash dynamics of a steep beach with low-tide terrace. *Marine Geology*, –(–):xxx–xxx, 2016a.

Luis Pedro Almeida, Rafael Almar, Chris Blenkinsopp, Kevin Martins, Rachid Benshila, and Christopher Daly. Swash dynamics of a sandy beach with low tide terrace. In *Proceedings of Coastal Dynamics 2017*. COASTAL DYNAMICS 2017, 2017.

Raimundo Ibaceta, Rafael Almar, Patricio A Catalán, Chris E Blenkinsopp, Luis P Almeida, and Rodrigo Cienfuegos. Assessing the performance of a low-cost method for video-monitoring the water surface and bed level in the swash zone of natural beaches. *Remote Sensing*, 10(1): 49, 2018.

Paul D Komar and Douglas L Inman. Longshore sand transport on beaches. *Journal of geophysical research*, 75(30):5914–5927, 1970.

Paolo Ciavola, Rui Taborda, Óscar Ferreira, et al. Field observations of sand-mixing depths on steep beaches. *Marine Geology*, 141(1-4):147–156, 1997.

Edith L Gallagher, Jamie MacMahan, AJHM Reniers, Jenna Brown, and Edward B Thornton. Grain size variability on a rip-channeled beach. *Marine Geology*, 287(1-4):43–53, 2011.

Luis Pedro Almeida, Rafael Almar, Patrick Marchesiello, Rachid Benshila, Kevin Martins, Chris Blenkinsopp, France Floc'h, Jeromme Ammann, Philippe Grandjean, Nguyen Trung Viet, Duong Hai Thuan, Le Thanh Binh, Nadia Senechal, Guillaume Detandt, Melanie Biausque, Thierry Garlan, Erwin Bergsma, Charles Caulet, and Hai-Yen Tran. Swash zone dynamics of a sandy beach with low tide terrace during variable wave and tide conditions. *Proceedings Journées Nationales Génie Côtier-Génie Civil*, 2016b.

Umberto Andriolo, Luis Pedro Almeida, and Rafael Almar. Coupling terrestrial lidar and video imagery to perform 3d intertidal beach topography. *Coastal Engineering*, 140:232–239, 2018.

Andrew D Ashton, Jeffrey P Donnelly, and Rob L Evans. A discussion of the potential impacts of climate change on the shorelines of the northeastern usa. *Mitigation and Adaptation Strategies for Global Change*, 13(7):719–743, 2008.

J Andrew G Cooper and Orrin H Pilkey. Sea-level rise and shoreline retreat: time to abandon the bruun rule. *Global and planetary change*, 43(3-4):157–171, 2004.

Roshanka Ranasinghe, Rob Holman, Matthieu de Schipper, Tom Lippmann, Jennifer Wehof, Trang Minh Duong, Dano Roelvink, and Marcel Stive. Quantifying nearshore morphological recovery time scales using argus video imaging: Palm beach, sydney and duck, north carolina. *Coastal Engineering Proceedings*, 1(33):24, 2012.

David L Kriebel and Robert G Dean. Convolution method for time-dependent beach-profile response. *Journal of Waterway, Port, Coastal, and Ocean Engineering*, 119(2):204–226, 1993.

Kristen D Splinter, James T Carley, Aliasghar Golshani, and Rodger Tomlinson. A relationship to describe the cumulative impact of storm clusters on beach erosion. *Coastal engineering*, 83:49–55, 2014b.

ML Yates, RT Guza, and WC O'reilly. Equilibrium shoreline response observations and modeling. *Journal of Geophysical Research Oceans*, 114(C9), 2009.

Shuyi S Chen and Milan Curcic. Ocean surface waves in hurricane ike (2008) and superstorm sandy (2012): Coupled model predictions and observations. *Ocean Modelling*, 103:161–176, 2016.

C-P Chang, Zhuo Wang, and Harry Hendon. The asian winter monsoon. In *The Asian Monsoon*, pages 89–127. Springer, 2006.

MC Wu and Johnny CL Chan. Surface features of winter monsoon surges over south china. *Monthly Weather Review*, 123(3):662–680, 1995.

Robert J Nicholls, Frank MJ Hoozemans, and Marcel Marchand. Increasing flood risk and wetland losses due to global sea-level rise: regional and global analyses. *Global Environmental Change*, 9:S69–S87, 1999.

Tetsu Nakamura, Koji Yamazaki, Katsushi Iwamoto, Meiji Honda, Yasunobu Miyoshi, Yasunobu Ogawa, Yoshihiro Tomikawa, and Jinro Ukita. The stratospheric pathway for arctic impacts on midlatitude climate. *Geophysical Research Letters*, 43(7):3494–3501, 2016a.

Ryota Nakamura, Tomoya Shibayama, Miguel Esteban, and Takumu Iwamoto. Future typhoon and storm surges under different global warming scenarios: case study of typhoon haiyan (2013). *Natural Hazards*, 82(3):1645–1681, 2016b.

MA Davidson and IL Turner. A behavioral template beach profile model for predicting seasonal to interannual shoreline evolution. *Journal of Geophysical Research: Earth Surface*, 114(F1), 2009.

Peter Ruggiero, Maarten Buijsman, George M Kaminsky, and Guy Gelfenbaum. Modeling the effects of wave climate and sediment supply variability on large-scale shoreline change. *Marine Geology*, 273(1-4):127–140, 2010.

Albena Dimitrova Veltcheva. Wave and group transformation by a hilbert spectrum. *Coastal Engineering Journal*, 44(4):283–300, 2002.

J Ortega and George H Smith. Hilbert–huang transform analysis of storm waves. *Applied Ocean Research*, 31(3):212–219, 2009.

Bruce C Douglas and Mark Crowell. Long-term shoreline position prediction and error propagation. *Journal of Coastal Research*, pages 145–152, 2000.

Keqi Zhang, Bruce Douglas, and Stephen Leatherman. Do storms cause long-term beach erosion along the us east barrier coast. *The journal of Geology*, 110(4):493–502, 2002.

Jeff E Hansen and Patrick L Barnard. Sub-weekly to interannual variability of a high-energy shoreline. *Coastal Engineering*, 57(11-12):959–972, 2010.

TM Thanh, H Tanaka, NT Viet, Y Mitobe, and VC Hoang. Evaluation of longshore sendiment transport on nha trang coast considering influence of northeast monsoon waves. *J. Jpn. Soc. Civ. Eng*, 71:1681–1686, 2015.

I Turki, R Medina, M Gonzalez, and G Coco. Natural variability of shoreline position: Observations at three pocket beaches. *Marine Geology*, 338:76–89, 2013.

ANDREW D Short. The role of wave height, period, slope, tide range and embaymentisation in beach classifications: a review. *Revista Chilena de Historia Natural*, 69(4):589–604, 1996.

AD Short and DWT Jackson. Beach morphodynamics. *Treatise on Geomorphology*, 10:106–129, 2013.

Harshinie Karunarathna, Jose M Horrillo-Caraballo, Roshanka Ranasinghe, Andrew D Short, and Dominic E Reeve. An analysis of the cross-shore beach morphodynamics of a sandy and a composite gravel beach. *Marine Geology*, 299:33–42, 2012.

David Fuhrman Troels Aagaard, Rolf Deigaard, editor. *Transient surf zone circulation induced by rhythmic swash zone at a reflective beach*, number 131, Kulturværftet, Allegade 2, 3000 Helsingør, Denmark, June 2017.

Rafael Almar, Pedro Almeida, Chris Blenkinsopp, and Patricio Catalan. Surf-swash interactions on a low-tide terraced beach. *Journal of Coastal Research*, 75(sp1):348–352, 2016.

Katherine L Brodie, Margaret L Palmsten, Tyler J Hesser, Patrick J Dickhudt, Britt Raubenheimer, Hannah Ladner, and Steve Elgar. Evaluation of video-based linear depth inversion performance and applications using altimeters and hydrographic surveys in a wide range of environmental conditions. *Coastal Engineering*, 136:147–160, 2018.

EWJ Bergsma, DC Conley, MA Davidson, and TJ O'Hare. Video-based nearshore bathymetry estimation in macro-tidal environments. *Marine Geology*, 374:31–41, 2016.

Rob A Holman, K Todd Holland, Dave M Lalejini, and Steven D Spansel. Surf zone characterization from unmanned aerial vehicle imagery. *Ocean Dynamics*, 61(11):1927–1935, 2011.

Janbert Aarnink. Bathymetry mapping using drone imagery. mathesis, Delft University of Technology, July 2017.

Erwin W.J. Bergsma, Daniel C. Conley, Mark A. Davidson, Tim J. O'Hare, and Rafael Almar. Multi-scale coastal monitoring through video-based bathymetry estimation). *Sub to Marine Geology*, XX(X):XX–XX, 2018a.

Haijiang Liu, Makoto Arii, Shinji Sato, and Yoshimitsu Tajima. Long-term nearshore bathymetry evolution from video imagery: a case study in the miyazaki coast. *Coastal Engineering Proceedings*, 1(33):60, 2012.

DP Dee, SM Uppala, AJ Simmons, P Berrisford, P Poli, S Kobayashi, U Andrae, MA Balmaseda, G Balsamo, dP Bauer, et al. The era-interim reanalysis: Configuration and performance of the data assimilation system. *Quarterly Journal of The Royal Meteorological Society*, 137 (656):553–597, 2011.

G Abessolo Ondoa, R Almar, B Castelle, L Testut, F Leger, F Bonou, E Bergsma, B Meyssignac, and M Larson. On the use of shore-based video camera to monitor sea level at the coast: A case study in grand popo, benin (gulf of guinea, west africa). *Sub to Journal of Geophysical Research: Ocean*, XX(X):XX–XX, 2018.

William Dorsch, Tom Newland, David Tassone, Samuel Tymons, and David Walker. A statistical approach to modelling the temporal patterns of ocean storms. *Journal of Coastal Research*, 24(6):1430–1438, November 2008. ISSN 07490208.

Paul S Bell. Shallow water bathymetry derived from an analysis of x-band marine radar images of waves. *Coastal Engineering*, 37(3):513–527, 1999. ISSN 0378-3839. doi: https://doi.org/10.1016/S0378-3839(99)00041-1. URL http://www.sciencedirect.com/science/article/pii/S0378383999000411.

Rob Holman, Nathaniel Plant, and Todd Holland. cbathy: A robust algorithm for estimating nearshore bathymetry. *Journal of Geophysical Research: Oceans*, 118(5):2595–2609, 2013.

Rob A Holman, Katherine L Brodie, and Nicholas J Spore. Surf zone characterization using a small quadcopter: Technical issues and procedures. *IEEE Transactions on Geoscience and Remote Sensing*, 55(4), 2017.

Greg Wilson, Tuba Özkan-Haller, Robert Holman, and Alexander Kurapov. Remote sensing and data assimilation for surf zone bathymetric inversion. *Coastal Engineering Proceedings*, 1(33):44, 2012. ISSN 2156-1028. doi: 10.9753/icce.v33.waves.44. URL https://journals.tdl.org/icce/index.php/icce/article/view/6725.

Florent Birrien, Bruno Castelle, Vincent Marieu, and Benjamin Dubarbier. On a data-model assimilation method to inverse wave-dominated beach bathymetry using heterogeneous video-derived observations. *Ocean Engineering*, 73:126–138, 2013.

G Pennucci, DC Conley, and R Holman. Rapid environmental assessment from small unmanned aerial vehicles. In *Proc. 22nd Int. Conf. Unmanned Aerial Vehicle Syst.*, pages 8–1, 2007.

Ian L. Turner, Mitchell D. Harley, and Christopher D. Drummond. Uavs for coastal surveying. *Coastal Engineering*, 114:19–24, 2016.

Ismael Colomina and Pere Molina. Unmanned aerial systems for photogrammetry and remote sensing: A review. *ISPRS Journal of Photogrammetry and Remote Sensing*, 92:79–97, 2014.

Victor V Klemas. Coastal and environmental remote sensing from unmanned aerial vehicles: An overview. *Journal of Coastal Research*, 31(5):1260–1267, 2015.

Pierre Dérian and Rafael Almar. Wavelet-based optical flow estimation of instant surface currents from shore-based and uav videos. *IEEE Transactions on Geoscience and Remote Sensing*, 55(10):5790–5797, 2017.

Erwin Willem Johan Bergsma, Rafael Almar, Luis Pedro Melo de Almeida, and Moussa Sall. On the operational use of uavs for video-derived bathymetry. *Coastal Engineering*, –(–):xxx–xxx, 2018b.

Charles Toth, Grzegorz Jozkow, and Dorota Grejner-Brzezinska. Mapping with small uas: a point cloud accuracy assessment. *Journal of Applied Geodesy*, 9(4):213–226, 2015.

Guillaume Brunier, Jules Fleury, Edward J Anthony, Antoine Gardel, and Philippe Dussouillez. Close-range airborne structure-from-motion photogrammetry for high-resolution beach morphometric surveys: Examples from an embayed rotating beach. *Geomorphology*, 261:76–88, 2016.

Michael Richard James, Stuart Robson, Sebastian d'Oleire Oltmanns, and Uwe Niethammer. Optimising uav topographic surveys processed with structure-from-motion: Ground control quality, quantity and bundle adjustment. *Geomorphology*, 280:51–66, 2017.

Kristen L Cook. An evaluation of the effectiveness of low-cost uavs and structure from motion for geomorphic change detection. *Geomorphology*, 278:195–208, 2017.

Yoshinao Matsuba and Shinji Sato. Nearshore bathymetry estimation using uav. *Coastal Engineering Journal*, 60(1):51–59, 2018.

Keith Noah Snavely. *Scene recostruction and visualization from internet photo collections*. PhD thesis, University of Washington, 2008.

Matthew J Westoby, James Brasington, Niel F Glasser, Michael J Hambrey, and JM Reynolds. 'structure-from-motion'photogrammetry: A low-cost, effective tool for geoscience applications. *Geomorphology*, 179:300–314, 2012.

Natan Micheletti, Jim H Chandler, and Stuart N Lane. Investigating the geomorphological potential of freely available and accessible structure-from-motion photogrammetry using a smartphone. *Earth Surface Processes and Landforms*, 40(4):473–486, 2015.

Mark A Fonstad, James T Dietrich, Brittany C Courville, Jennifer L Jensen, and Patrice E Carbonneau. Topographic structure from motion: a new development in photogrammetric measurement. *Earth Surface Processes and Landforms*, 38(4):421–430, 2013.

L Javernick, J Brasington, and B Caruso. Modeling the topography of shallow braided rivers using structure-from-motion photogrammetry. *Geomorphology*, 213:166–182, 2014.

Mohamar Moussa Ouédraogo, Aurore Degré, Charles Debouche, and Jonathan Lisein. The evaluation of unmanned aerial system-based photogrammetry and terrestrial laser scanning to generate dems of agricultural watersheds. *Geomorphology*, 214:339–355, 2014.

William A. Birkemeier and Curtis Mason. The crab: A unique nearshore surveying vehicle. *Journal of Surveying Engineering*, 110(1):1–7, 1984.

JP Dugan, WD Morris, KC Vierra, CC Piotrowski, GJ Farruggia, and DC Campion. Jetski-based nearshore bathymetric and current survey system. *Journal of Coastal Research*, pages 900–908, 2001.

Curtis D Mobley, Lydia K Sundman, Curtiss O Davis, Jeffrey H Bowles, Trijntje Valerie Downes, Robert A Leathers, Marcos J Montes, William Paul Bissett, David DR Kohler, Ruth Pamela Reid, et al. Interpretation of hyperspectral remote-sensing imagery by spectrum matching and look-up tables. *Applied Optics*, 44(17):3576–3592, 2005.

David R Lyzenga, Norman P Malinas, and Fred J Tanis. Multispectral bathymetry using a simple physically based algorithm. *IEEE Transactions on Geoscience and Remote Sensing*, 44(8):2251–2259, 2006.

Jennifer L Irish and W Jeff Lillycrop. Scanning laser mapping of the coastal zone: the shoals system. *ISPRS Journal of Photogrammetry and Remote Sensing*, 54(2-3):123–129, 1999.

AH Sallenger Jr, WB Krabill, RN Swift, J Brock, J List, Mark Hansen, RA Holman, S Manizade, J Sontag, A Meredith, et al. Evaluation of airborne topographic lidar for quantifying beach changes. *Journal of Coastal Research*, pages 125–133, 2003.

Gottfried Konecny. *Geoinformation: Remote Sensing, Photogrammetry and Geographic Information Systems*. CRC Press, 2014.

Jean Ponce, David Forsyth, Equipe-projet Willow, S Antipolis-Méditerranée, R d'activité RAweb, L Inria, and I Alumni. Computer vision: a modern approach. *Computer*, 16(11), 2011.

Roger Y. Tsai. A versatile camera calibration technique for high-accuracy 3d machine vision metrology using off-the-shelf tv cameras and lenses. *IEEE Journal on Robotics and Automation*, 3(4):323–344, 1987.

Zhengyou Zhang. A flexible new technique for camera calibration. *IEEE Transactions on pattern analysis and machine intelligence*, 22, 2000.

Juho Kannala and Sami S. Brandt. A generic camera model and calibration method for conventional, wide-angle, and fish-eye lenses. *IEEE transactions on pattern analysis and machine intelligence*, 28(8):1335–1340, 2006.

OpenCV. Open source computer vision library - opencv, 2018. URL https://opencv.org/.

Valsamis Ntouskos, Lazaros Grammatikopoulos, Ilias Kalisperakis, George Karras, and Elli Petsa. Fauccal: An open source toolbox for fully automatic camera calibration. In *XXII CIPA*

Symposium on Digital Documentation, Interpretation & Presentation of Cultural Heritage, Kyoto, Japan, 2009.

J.J. Aguilar et al. D. Samper, J. Santolaria. Metrovisionlab toolbox for camera calibration and simulation, 2009. URL http://metrovisionlab.unizar.es.

Duong Hai Thuan, Rafael Almar, Patrick Marchesiello, and Nguyen Trung Viet. Video sensing of nearshore bathymetry evolution with error estimate. *Remote Sensing*, –(–):xxx–xxx, 2018.

Alexandre Nicolae Lerma, Rodrigo Pedreros, Arthur Robinet, and Nadia Sénéchal. Simulating wave setup and runup during storm conditions on a complex barred beach. *Coastal Engineering*, 123:29–41, 2017.

Angélique Melet, Benoit Meyssignac, Rafael Almar, and Gonéri Le Cozannet. Under-estimated wave contribution to coastal sea-level rise. *Nature Climate Change*, 8(3):234, 2018.

L Sembiring, M Van Ormondt, AR Van Dongeren, and JA Roelvink. Operational prediction of rip currents using numerical model and nearshore bathymetry from video images. In *AIP Conference Proceedings*, volume 1857, page 080004. AIP Publishing, 2017.

Ap Van Dongeren, Nathaniel Plant, Anna Cohen, Dano Roelvink, Merrick C Haller, and Patricio Catalán. Beach wizard: Nearshore bathymetry estimation through assimilation of model computations and remote observations. *Coastal engineering*, 55(12):1016–1027, 2008.